Boundary Element Method for Fast Solution of Acoustic Problems: Active and Passive Noise Control

by

Alessandro Brancati



Thesis submitted for the degree of Doctor of Philosophy of the Imperial College London

Department of Aeronautics
Imperial College London
2010

To my sister Emanuela

Acknowledgments

I would like to acknowledge the strong support given to this thesis by the SEAT European research project.

A great deal is owed to my supervisor, Prof. M.H. Ferri Aliabadi, for the opportunity to undertake this challenge during this period of my life and for his patience and his enlightening advice. He taught me to be either professional during my research studies and, at the same time, demonstrated a profound sense of humanity that I will never forget.

Similarly, I wish to thank Prof. John Hughes for his willingness and patience during our English lessons and for both encouraging and believing in me.

I would also like to show my appreciation to Dr. Vincenzo Mallardo and Dr. Pedro Baiz Villafranca for our lasting and always fruitful conversations, as well as for their career advice.

I wish to thank Dr. Joaquim Peiro for the Falcon mesh.

Thanks to Prof. Alberto Milazzo and Dr. Ivano Benedetti for the fundamental call.

Special thanks must go to my colleagues: Gaurav, Lucio, Mark, Matthew, Neil, Nelson and Zahra for their friendship and all their valuable discussions.

I would like to thank Alessandra for her support during this difficult period of my life.

Thanks also to my parents, who have always been so full of love for me.

Finally, I would like to thank the person to whom this thesis is dedicated: my sister Emanuela. Thank you for everything that you taught me during all the time we spent together. I am honored to have grown with you at my side and to have had the happiness from sharing this part of my life with the love and gaiety of such an older sister. You have been and always will be, my wisest councilor and confident.

Abstract

This thesis presents boundary element formulations for three-dimensional acoustic problems of active (ANC) and passive (PNC) noise control.

A new boundary element strategy, referred to as RABEM (Rapid Acoustic Boundary Element Method), has been formulated and implemented for acoustic problems. The assembly time for both the system matrix and the right hand side vector is accelerated using a Hierarchical-matrix approach based on the Adaptive Cross Approximation (ACA). Two different H-matrix-GMRES solvers (one without preconditioners and one with a block diagonal preconditioner) are developed and tested for low and high frequency problems including noise emanated by aircraft approaching an airport.

A new formulation for solving the ANC based on attenuating the unwanted sound in a control volume (CV) rather than cancelling it at a single point is presented. The noise attenuation is obtained by minimising the square modules of two acoustic quantities - the potential and one component of the particle velocity - within the CV. The two formulations presented include a single and a double secondary source, respectively. Several examples are presented to demonstrate the efficiency of the proposed technique.

A new approach, based on sensitivity analysis, for determining the optimum locations of the CV and the optimum location/orientation of the secondary source is presented. The optimisation procedure is based upon a first order method and minimises a suitable cost function by using its gradient. The procedure to calculate the cost function gradients is explained in detail.

Finally, a PNC strategy applied to the interior of an aircraft cabin is investigated. A lower noise level is achieved through the introduction of a new textile with a higher noise absorbing coefficient than a conventional textile, especially at low frequencies. The so-called "bubble concept", which consists of adding cap insertions at the sides of the passenger head, is also investigated.

Declaration of Originality

I confirm that the work presented in this thesis is the personal work of the author and all else is appropriately referenced.

Contents

1 Introduction **33**

1.1 General 33

1.2 Active and Passive Noise Control 35

1.2.1 Numerical Simulations 37

1.3 Numerical Method 38

1.3.1 The Boundary Element Method 38

1.4 Thesis Overview 40

1.5 Author Published Work 43

1.5.1 Conference Proceedings 44

2 Fundamentals of Acoustics **45**

2.1 Origin of Sound 46

2.2 Acoustic Equations 49

2.2.1 Acoustic Model 49

2.2.2 Equation of State for an Ideal Fluid 51

2.2.3 Conservation of Mass 52

2.2.4 Equation of Motion for an Ideal Fluid 54

2.2.5 Linearisation 56

2.2.6 Uniform Medium 58

2.2.7 One-dimensional General Solution 60

2.3 Acoustic Quantities 62
2.3.1 Speed of Sound 62
2.3.2 Acoustic Energy 64
2.3.3 Acoustic Intensity 64
2.3.4 Sound Pressure Level 65
2.3.5 Impedance 66
2.4 Planewaves and Monopole Sources 67
2.4.1 Planewave 68
2.4.2 Monopole 69
2.5 Human perception 71
2.6 Noise Control Strategies 74
2.6.1 Passive Noise Control (PNC) 75
2.6.2 Active Noise Control (ANC) 80

3 The Boundary Element Method **84**
3.1 Helmholtz Equation 86
3.2 Boundary Conditions 87
3.3 Gauss' Theorem and Green's Identities 88
3.4 Fundamental Solutions 90
3.5 Boundary Integral Equation 92
3.6 Numerical Implementation 96
3.6.1 Boundary Discretisation using Shape Functions 96
3.6.2 Matrix Assembly using the Collocation Method 99
3.7 Internal Points 102
3.8 Fictitious Frequency and Spurious Eigenvalue Problems 104
3.9 Benchmark Examples 105
3.9.1 Pulsating Sphere 105

3.9.2 Spherical Cavity 110
3.9.3 Plane-wave Scattering from a Sphere 111
3.10 Summary 117

4 Hierarchical Adaptive Cross Approximation GMRES Procedure 119
4.1 Hierarchical-ACA 122
4.1.1 Cluster Tree 124
4.1.2 Block Tree 126
4.1.3 ACA 129
4.1.4 H-matrix 133
4.2 Boundary Conditions and Right Hand Side Setting 135
4.2.1 Optimisation Procedure for the Right Hand Side Vector 140
4.3 System Solution 141
4.3.1 GMRES 142
4.3.2 Internal Points 146
4.4 Numerical Results 146
4.5 Summary 166

5 Active Noise Attenuation in a Control Volume 168
5.1 Noise Attenuation by Using a Single Control Source 171
5.2 Results for a Single Control Source 173
5.2.1 Primary Noise and Secondary Source Model 174
5.2.2 Results for Different CV Dimensions 176
5.3 Faulty ANC System 181
5.4 Noise Attenuation Using Two Control Sources 186
5.4.1 Mathematical Model 186
5.5 Results for Two Control Sources 189
5.5.1 Standard Procedure 190

5.5.2 Simplified Procedure 192
5.5.3 Modified Procedure 194
5.6 Practical Aspects of the Proposed Control Volume Approach 195

6 A Sensitivity Formulation for Three Dimensional Active Noise Control 198

6.1 Optimisation 201
6.2 Implicit Differentiation of the Boundary Integral Equation 206
6.3 Sensitivity Analysis 208
6.3.1 Optimum Control Source and Control Volume Locations 209
6.3.2 Optimum Control Source Orientation 210
6.4 Equation Assembly 214
6.5 Numerical Aspects 216
6.5.1 Matrix Update 216
6.5.2 Rapid Solver 217
6.6 Numerical Examples 218
6.6.1 CV optimum location 220
6.6.2 Optimisation of the secondary source location 221
6.6.3 Optimisation of the secondary source orientation 225
6.6.4 Optimisation of the secondary source location in a large-scale engineering problem 228

7 Passive Noise Control 235

7.1 Experimental Tests 237
7.2 Cabin Model 240
7.2.1 Microphones 242
7.2.2 Noise Source 243
7.2.3 Boundary Condition Setting 245

7.2.4 Nanofibres 246
7.2.5 Bubble Concept 247
7.3 Numerical Results for the SEAT Project 249
7.3.1 Comparison with the Experimental Results 250
7.3.2 Noise Reduction Acting on Seat Covers and on Headrest Shape 252
7.3.3 Bubble Caps Sensitivities 261

8 Conclusion and Future Work 265
8.1 Conclusions 265
8.2 Future Research 269

A Preliminary Validations 271
A.1 Preliminary Validation: Garcia-Bonito Results 271
A.2 Integration Process Validation 274

B Optimisation Methods 276
B.1 Non-linear Optimisation Problem 277
B.1.1 A General Algorithm 277
B.1.2 Search Direction and Step Size 279
B.2 Quasi-Newton Method 280

C Benchmark Results for the Optimum Location of the Control Volume 283

List of Algorithms

4.1 Recursive Subroutine SplitClusterTree($P(t_i)$) 126

4.2 Recursive Subroutine SplitBlockTree($P(t_1)$,$P(t_2)$) 128

4.3 Adaptive Cross Approximation (ACA). 131

4.4 GMRES. 145

List of Figures

2.1 Bas-relief of Gandhara (100 b.c.) from Marcello Dubois. 47

2.2 A music lesson: particular in a Hydra of V b.c.[131] 49

2.3 A schematic wave. 51

2.4 Cone speaker. 67

2.5 Human ear internal structure. [126] 71

2.6 ISO standard 226:2003. Acoustics – Normal Equal Loudness Level Contours: Fletcher & Munson curve. 73

2.7 A (blue), B (yellow), C (red), and D weighting (black) [127]. 74

2.8 Mass law validity. [130] 76

2.9 Coincident frequency. 78

2.10 Perforated material. 79

3.1 Boundary divided into two parts: Γ_ε, hemi-sphere centred at $\mathbf{x}'$; $\Gamma_\varepsilon - \Gamma$, remaining geometry. 93

3.2 Triangular/quadrilateral elements: constant, linear and quadratic. . . 97

3.3 Border nodes belonging to two different elements. 100

3.4 Sphere discretised into: a) 24 isoparametric quadratic quadrilateral elements and b) 1126 constant elements. 106

3.5 Pulsating sphere under prescribed uniform flux. Real part of the potential for the internal points with $1 \leq r \leq 3$, k =1.2. 107

3.6 Pulsating sphere under prescribed uniform flux. Real part of the potential for the internal points with $1 \leq r \leq 3$, k =4.0. 108
3.7 Pulsating sphere under prescribed uniform flux. Real part of the potential for the internal points with $1 \leq r \leq 3$, k =6.0. 108
3.8 Potential around a pulsating sphere: a) real part; b) imaginary part; c) amplitude; d) phase. 109
3.9 Potential within pulsating spherical cavity ($k = 8$): a) real part; b) imaginary part; c) amplitude; d) phase. 112
3.10 Plane-wave scattering from a rigid sphere: potential amplitude in a 20×20 m square constituted by 101×101 points at a single wavenumber value (k =7); P_{inc}, incident plane-wave. 113
3.11 Plane-wave scattering from a rigid sphere: a) real part , b) imaginary part, c) amplitude, d) phase of the incident plane-wave potential. . . . 115
3.12 Plane-wave scattering from a rigid sphere: a) real part , b) imaginary part, c) amplitude, d) phase of the scattered wave potential. 116
3.13 Plane-wave scattering from a rigid sphere: a) real part , b) imaginary part, c) amplitude, d) phase of the total (incident + scattered) wave potential. 117

4.1 Low rank approximation: a few entries of the original block represent the entire block. 120
4.2 A schematic of the first two iterations of the cluster tree creation: 1) the whole geometry is divided 2) into two parts, each of which is then subdivided again 3) into two parts. 125
4.3 A schematic presentation of the first three iterations that form the block tree [14]. 128
4.4 A schematic presentation of the ACA algorithm[25]. 131

4.5 Hierarchical matrix. 135
4.6 Substitution of the k^{th} values of each row with zero, addition of the k^{th} column of the **G** block matrix and of a zero row with *1* at the k^{th} element. 137
4.7 Addition of the k^{th} column of the **G** block matrix multiplied by the artificial admittance ζ opposite in sign and of a zero row with *1* at the k^{th} element. 137
4.8 Multiplication of the k^{th} row of the **G** block matrix by the artificial admittance ζ opposite in sign, addition of the k^{th} column of the **H** block matrix and of a zero row with *1* at the k^{th} element. 138
4.9 Substitution of the k^{th} values of each row with zero, addition of the columns of the **G** block matrix multiplied by the artificial admittance opposite in sign and of its rows where the k^{th} elements are divided by ζ. 139
4.10 Cabin geometry. 148
4.11 Influence on the assembly time, solution time and total time ratios due to the cardinality for a pulsating sphere. 149
4.12 Influence on the assembly time, solution time and total time ratios due to the cardinality for an aircraft cabin. 150
4.13 Influence on the assembly time, solution time and total time ratios due to η for a pulsating sphere. 151
4.14 Influence on the assembly time, solution time and total time ratios due η for an aircraft cabin. 152
4.15 Block-wise representation of the ACA generated matrix for $\eta = 1$, $\eta = 2$, $\eta = 4$ and $\eta = 10$. 153
4.16 Speed up ratio for a scattered rigid sphere by a plane wave - LMS/RABEM. 155

4.17 Speed up ratios relates to four different groups of internal points for a pulsating sphere discretised with 3240 super-parametric triangular elements. 156
4.18 CPU time ratios for different angular frequencies for a pulsating sphere meshed with 10340 triangular elements. 157
4.19 Surface of an airplane seat row meshed with 27,284 triangular elements. 158
4.20 Comparison between the unpreconditioned, the diagonal preconditioned and block diagonal preconditioned GMRES for an airplane seat row meshed with 27,284 triangular elements. 159
4.21 Real part of the potential for the aircraft seats when a monopole acts at 100Hz. 160
4.22 Qantas Boeing 747 approaching runway 27L at London Heathrow Airport, England [128]. 161
4.23 53,074 triangular elements Dassault Falcon mesh. 162
4.24 Sound pressure level at 25Hz generated by a Dassault Falcon. 163
4.25 Sound pressure level at 100Hz generated by a Dassault Falcon approaching in an airport at different altitudes: a) 250 m; b) 200 m; c) 150 m; d) 125 m. 164
4.26 Sound pressure level at 100Hz generated by a Dassault Falcon approaching in an airport at different altitudes: a) 100 m; b) 75 m; c) 50 m. . . 165

5.1 The problem configuration including vibrating surface, secondary source and control volume. 172
5.2 SEAT headrest with two speakers. 174
5.3 Mathematical model of the problem: Γ_S vibrating surface, Γ_z case of the speaker, D control volume, primary noise plane waves. 175
5.4 Spheres with active segments of 120^0 (a) and 90^0 (b) degree. 176

5.5 Average noise reduction area generated by a rigid sphere with an active segment of 120^0 degree and by the point cancellation strategy at the point (19.4, 0.0, 0.0) cm. 178
5.6 Average noise reduction area generated with the small CV. 179
5.7 Average noise reduction area generated with the medium CV. 180
5.8 Average noise reduction area generated with the large CV. 181
5.9 Adaptive feed-forward ANC system. 182
5.10 Superposition (continuous line) of a primary sinusoidal field with a secondary source without variations (a); with a variation of 20% of the potential amplitude (b) and 10% π of the phase (c). 184
5.11 Noise reduction area when the secondary field is varied in percentage ($\pm$5%, $\pm$10%, $\pm$20%) from its optimal value that minimises the noise level. 185
5.12 Noise reduction area when the secondary field is varied in percentage ($\pm$5%, $\pm$10%, $\pm$20% π) from its optimal value that minimises the noise level. 185
5.13 The three configurations tested: (a) configuration 1, (b) configuration 2, (c) configuration 3. 190
5.14 Average noise reduction area for the first configuration. 191
5.15 Average noise reduction area for the second configuration. 192
5.16 Average noise reduction area for the third configuration. 192
5.17 Average noise reduction area of the simplified procedure. 193
5.18 Average noise reduction area when the component of the particle velocity is along the x_2-direction instead of the x_1-direction. 194

6.1 Optimisation process applied to the control source: a) optimum location; b) optimum orientation; c) fixed control volume. 202

6.2 Optimisation process applied to the control volume: a) optimum CV location; b-c) fixed control sources. 202
6.3 Geometry of the problem: secondary source with the vibrating surface, remaining boundary, CV, position vectors of the CV $\mathbf{a} \equiv a_l = (a_1, a_2, a_3)$ and of the secondary source $\mathbf{b} \equiv b_m = (b_1, b_2, b_3)$. 204
6.4 Secondary source modelled as a rigid sphere with a 120° active segment. 211
6.5 Secondary source section: the x_1 and x_3-local axes 211
6.6 Secondary source section: the x_1 and x_2-local axes 213
6.7 Matrix division. 217
6.8 Example 1. Different locations of the CV at a frequency of 1092 Hz: a) initial guess; b) first iteration; c) second iteration. 221
6.9 Example 1. The cost function f_c for four different frequencies. 222
6.10 Example2. Room geometry, CV and primary noise locations. 223
6.11 Example 2. Different locations of the secondary source in the optimisation procedure. 224
6.12 Example 2. SPL distribution (dB) inside a 4×3×2.5 m room of a) the pure primary noise, and b) the total field generated by the primary noise and the speaker. 224
6.13 Example 2. SPL distribution (dB) inside a 2×1×1.2 m CV of a) the pure primary noise, and b) the total field generated by the primary noise and the speaker. 225
6.14 Example 3. Geometry of the problem. 226
6.15 Example 3. SPL distribution (dB) inside the box of the total field generated by the primary noise and the speaker a) initial guess, and b) optimal value. 227

6.16 Example 3. SPL distribution (dB) inside the CV of the total field generated by the primary noise and the speaker: a) initial guess, and b) optimal value. 227
6.17 Example 5. Geometry of the cabin: Origin of the coordinate system, CV, secondary source and primary noise (monopole outside the cabin) locations. 229
6.18 Example 5. Particular of the seat of the cabin: row and CV meshes, secondary source with the vibrating segment. 230
6.19 Example 5. A few different secondary source locations at optimisation procedure iterations at 70 Hz: a) initial guess; b) locations of a first group of iterations; c) next to the last iteration; d) final optimal position. 231
6.20 Example 5. SPL and optimum secondary source location at 70 Hz. . . . 232
6.21 Example 5. SPL and optima secondary source locations, highlighted in red, for the six frequencies: a) 100 Hz, b) 130 Hz, c) 160 Hz, d) 170 Hz, e) 180 Hz, f) 200 Hz. 234

7.1 Experimental mock-up: a) microphones at the seat headrests; b) front panel [86]. 238
7.2 Thales mock-up [86]. 238
7.3 Experimental signal spectrum: takeoff. 239
7.4 Experimental signal spectrum: landing. 239
7.5 Experimental signal spectrum: cruise. 240
7.6 Initial cabin model [86]. 241
7.7 Final cabin models [86]. 242
7.8 Location of the four microphones in the model [86]. 243
7.9 Noise source: a) experimental dodecahedral speaker; b) numerical monopole [86]. 244

7.10 Relation between the absorbing coefficient α and the real part of the impedance z. 246
7.11 A microscope view of the nanofibre [129]. 247
7.12 Acoustic performance of the nanofibre textile compared with a typical textile [86]. 248
7.13 Bubble concept [86]. 248
7.14 Model with lateral caps located at the headrests: coarse mesh (a), fine mesh (b) [86]. 249
7.15 Comparison between experimental and numerical results at the microphones [86]. 252
7.16 Noise reduction at the microphone locations: 10% more absorptive textile; 20% more absorptive textile; headrests with lateral caps [86]. . . . 254
7.17 SPL for the experimental signal over the range 125-1000 Hz: a) standard textile; b) 10% more absorptive textile; c) 20% more absorptive textile; d) headrests with lateral caps [86]. 255
7.18 SPL for the experimental signal over the range 500-1000 Hz: a) standard textile; b) 10% more absorptive textile; c) 20% more absorptive textile; d) headrests with lateral caps [86]. 256
7.19 Location of the point close to the passengers' ears [86]. 257
7.20 SPL for the white noise over the range 500-1000 Hz: a) standard textile; b) 10% more absorptive textile; c) 20% more absorptive textile; d) headrests with lateral caps [86]. 259
7.21 SPL for the white noise over the range 500-1000 Hz: a) standard textile; b) 10% more absorptive textile; c) 20% more absorptive textile; d) headrests with lateral caps [86]. 260
7.22 Design of the new cap for the bubble concept. 262

7.23 SPL for the experimental signal over the range 8-1000 Hz: a) SEAT project configurations; b) separated caps; c) 5^o degree ; d) 10^o degree; e) -5^o degree; f) -10^o degree. 263

A.1 Noise reduction area generated by a rigid sphere with an active segment of 45^0 degree considered to be uniform (a) and produced by a function of Legendre polynomial and the spherical Hankel function (b). 272

A.2 Average noise reduction area generated by a rigid sphere with a vibrating segment of different sizes when kd=0.5: (a) 360^0, (b) 180^0, (c) 45^0. . . . 273

A.3 Average noise reduction area generated by a rigid sphere with different values of kd: (a) $kd = 0.2$, (b) $kd = 0.5$, (c) $kd = 1.0$. 273

A.4 Average noise reduction area generated by a rigid sphere with an active segment of 120^0 degree and by the point cancellation strategy at the point (19.4, 0.0, 0.0) cm. 274

A.5 Integration Process Validation: a) minimisation obtained by a CV of volume equal to 3,125 $10^{-8}m^3$; b) cancellation point strategy. 275

C.1 Primary diffuse noise amplitude created by 72 planewaves distributed in all directions of the space for four different frequencies: a) 109Hz; b) 273 Hz; c) 546Hz; d) 1092 Hz. 284

C.2 Secondary field amplitude created by a rigid sphere with an active segment of 120^0 degree and radius 8 cm for four different frequencies: a) 109Hz; b) 273 Hz; c) 546Hz; d) 1092 Hz. 285

C.3 Total amplitude potential for the optimum CV x_1-locations corresponding to the trough of the cost function in figure 6.9: a) 109Hz; b) 273 Hz; c) 546Hz; d) 1092 Hz. 286

C.4 Total amplitude potential of the worst CV x_1-locations corresponding to the crests of the cost function in figure 6.9: a) 109Hz; b) 273 Hz; c) 546Hz; d) 1092 Hz. 286

List of Tables

3.1 Pulsating sphere under prescribed uniform flux for four wave numbers (k =1, 2, 3, 4). 107

3.2 Pulsating spherical cavity under prescribed uniform flux for four wavenumbers (k =1, 2, 3, 4) 111

3.3 Plane-wave scattering from a rigid sphere for three wavelength (λ =10, 100, 1000). 113

4.1 Speed up ratio between the RABEM, SBEM and LMS. 154

5.1 Values of the terms in equation (5.5). 173

5.2 Characteristics of the CVs. 178

5.3 Values of the terms in equations. (5.12-5.15). 189

6.1 Numerical examples. 219

6.2 Example 2. Optimum location of the secondary source centre, level of noise attenuation (dB) and number of iterations for four different initial orientation values (0, $\pi/2$, π, $3\pi/2$) in radians. 223

6.3 Example 4. Optimisation of the speaker's orientation for different initial guesses. 226

6.4 Example 5. Optima secondary source locations for seven different frequencies (70, 100, 130, 160, 170, 180, 200 Hz) and the corresponding reduction at the initial and optima locations, respectively. 230

7.1 Microphone coordinates in the mathematical model [86]. 242
7.2 Values of the absorption coefficient over the range 8-50 Hz [86]. 250
7.3 Values of the absorption coefficient over the range 63-400 Hz [86]. . . . 251
7.4 Values of the absorption coefficient over the range 500-1000 Hz [86]. . . 251
7.5 SPL in dB at the passengers' ears over the range 125-1000 Hz [86]. . . . 258
7.6 SPL in dB at the passengers' ears over the range 500-1000 Hz [86]. . . . 258
7.7 SPL in dB at the passengers' ears over the range 500-1000Hz. 262

Nomenclature

α	anlge
	constant for ANC
β	constant for ANC
δ	Dirac delta
δ_{ij}	Kronecker delta
η	variables
	local coordinates
	parameter influencing the ACA admissible blocks
Γ	domain boundary
γ	gas constant
$\hat{e}_k$	planewave versor
κ	kernel of the integrand operator
λ	wavelength
$\overline{\mathbf{G}}$	coefficient matrix to evaluate internal point potential
$\overline{\mathbf{G}}'$	coefficient matrix to evaluate internal point particle velocity

$\overline{\mathbf{H}}$ coefficient matrix to evaluate internal point potential

$\overline{\mathbf{H}}'$ coefficient matrix to evaluate internal point particle velocity

$\mathbf{\Psi}$ vector of shape functions

$\mathbf{A}$ system matrix

column matrix block in ACA

$\mathbf{a}$ position vector

$\mathbf{a}_i$ $i-th$ column in ACA

$\mathbf{B}$ row matrix block in ACA

$\mathbf{b}$ position vector

$\mathbf{b}_i$ $i-th$ row in ACA

$\mathbf{C}$ admissible block in ACA

$\mathbf{C}_k$ approximated block in ACA

$\mathbf{F}$ right hand side vector

$\mathbf{G}$ coefficient matrix multiplying flux

$\mathbf{H}$ coefficient matrix multiplying potential

$\mathbf{H}_m$ Hessenberg matrix

$\mathbf{I}$ acoustic intensity

$\mathbf{J}$ Jacobian

$\mathbf{M}$ generic matrix

$\mathbf{n}$ element normal vector

$\mathbf{P}$ monopole-planewave vector at internal points

$\mathbf{p}$ monopole-planewave vector

$\mathbf{q}$ flux vector

$\mathbf{r}$ position vector

$\mathbf{r}_i$ GMRES residual at the $i-th$ iteration

$\mathbf{R}_k$ error matrix in ACA

$\mathbf{u}$ potential vector

$\mathbf{V}$ vector field

$\mathbf{v}$ fluid velocity

$\mathbf{X}$ coordinates of field points

$\mathbf{x}$ point coordinates

coordinates of boundary points

$\mathbf{X}'$ coordinates of source points

$\mathbf{x}'$ collocation point at the boundary

$\mathbf{Y}$ unknown vector

∇ Nable operator

∇^2 Laplacian operator

Ω domain volume

ω angular frequency

$\Omega_{r/c}$ group of elements

ϕ velocity potential

generic potential function

ψ generic potential function

angle

shape function

ρ medium density

σ stress tensor

θ angle

ε infinitesimal radius

φ potential function

angle

ϱ surface density

ξ variable

potential or flux of the integrand operator

ζ artificial admittance

ζ_{ij} generic matrix coefficient

* fundamental solution

$'$ perturbed value

$_{,i}$ $\partial(\cdot)/\partial x_i$

$_{,n}$ $\partial(\cdot)/\partial x_n$

$_0$ initial quantity

$_I$ imaginary part

$_p$ primary source quantity

$_R$ real part

$_s$ secondary source quantity

a specific sphere radius

B complex monopole-planewave amplitude

b strength of noise source

c wave speed

BEM constant

c_j Coordinates of the centre of spherical control source

c_p specific heat for constant pressure

c_v specific heat for constant volume

D control volume

d generic distance

D/Dt material derivative

E internal energy

f frequency

generic function

f_Γ force per unit mass acting on fluid surface

f_Ω force per unit mass acting on fluid mass

g gravity acceleration

generic function

H Hierarchical

$H_0^{(1)}$ Henkel function of the first kind of order zero

I set of indices

i index

imaginary unit

I_L intensity level

j index

J_i $i-th$ Jacobian component

k wave number

index

order of the ACA approximated block

l, L indices

m number of matrix rows

design variable generic direction

N degrees of freedom

total number of nodes

n element normal

number of matrix columns

N_p total number of points

Ne number of elements

Nn number of nodes at the $i-th$ element

NP total number of extra sources

p pressure

subset of $P(t)$

$P(t)$ initial set of element indices for the cluster tree in ACA

P_t potential of the $t-th$ extra source

q flux

R gas constant

r generic distance

distance between collocation and field points

r_p reflection coefficient

S entropy

T period

temperature

t time

group subset indices for cluster tree

U potential at internal point

u time-harmonic velocity potential

U' particle velocity at internal point

v normal velocity

W power

z specific surface impedance

Z_j impedance

2D two dimensional

3D three dimensional

ACA Adaptive Cross Approximation

ANC Active Noise Control

BEM Boundary Element Method

BIE Boundary Integral Equation

CHEEF Combined Helmholtz Exterior Integral Equation Formulation

CHIEF Combined Helmholtz Integral Equation Formulation

CV Control Volume

det determinant

dof degree of freedom

DSP Digital Signal Processor

FDM Finite Difference Method

FEM Finite Element Method

FMM Fast Multiple Method

GMRES Generalized minimal residual method

PNC Passive Noise Control

RABEM Rapid Acoustic Boundary Element Method

SBEM Standard BEM

SEAT Smart tEchnologies for stress free Air Travel

SP Signal Processing

SPL Sound Pressure Level

SQP Sequential Quadratic Programming

Chapter 1

Introduction

1.1 General

Noise comfort is one of the main factors in passengers' acceptance of a transportation system and a fundamental aspect of improving the global perceived comfort. Intercontinental and other long flights require passengers to remain seated at the same seat and subjected to the same acoustic disturbance for hours, which can result in a stressful journey especially for those seated close to aircraft engines. Modern aircraft are quieter than their predecessors. However, noise still remains an irritating factor for passengers. Additionally, air vibrations that are not perceived, between 2 Hz and 10 Hz, also affect passengers' perception of comfort, since they tend to resonate with the natural frequencies of different part of the human body [132].

In aircraft, noise comes from different sources that can be classified as follows [46, 74]:

1. propulsion system (including fans, jets, etc.);
2. airframe (including lift devices, speed brakes, landing gear, etc.);
3. other passengers (crying babies, loud music, etc.);
4. vibrations of system malfunctions.

Noises generated by aircraft are mainly periodic, whereas, noises produced by the passengers themselves are non-periodic sounds. Periodic noises are of particular interest in noise control since they can be controlled more easily than random ones.

Noise is transmitted into the cabin through several vibroacoustic paths [74]. The influence on the sound field of such paths varies with frequencies and flight conditions, and they have to be carefully examined to avoid disturbing annoyance that can be easily eliminated utilising simple expedients. Nonetheless, some annoyances can not be avoided and to reduce them engineers utilise noise control strategies.

On the side of these objective considerations, it should be highlighted that sound perception by human beings is strongly subjective and the level of noise tolerance depends on age, temperamental characteristics, health status, etc., of a person. For instance, human beings tend to lose high frequency perception with age. In this regard, Fletcher and Munson [47] succeed in obtaining an average behaviour of the human ear through experimental tests. They published in 1933 a paper where they reported equal-loudness contours for the human ear. These curves are nowadays utilised in the ISO Standard [133]. One of the most important findings of their study was that humans perceive high frequency sounds (above 1 kHz) better than bass sounds. The most sensitive frequency range is from 1 to 6 kHz. This implies that the energy content of a disturbing treble noise is lower than for a bass noise, hence different noise control approaches are required. Besides, it should be noted that sounds that are perceived as an annoyance are not only those with high sound pressure levels, but also non-constant in time sounds that are generated by shocks, e.g., hammer blow, vibrating impacts, unannounced crashes.

1.2 Active and Passive Noise Control

In the last few decades many studies [36, 38, 91, 112] have been focused in new technologies to improve noise comfort sponsored especially by the airline and aircraft industries.

Noise control includes a variety of strategies to attenuate unwanted noises. They can be classified into several groups and subgroups. A first classification divides them into global strategies, that act to reduce the noise in the overall sound field, and local strategies, that involve techniques for reducing noise in a particular location often increasing the level of noise at other places. Another classification subdivides noise control techniques into passive noise control (PNC) and active noise control (ANC). From this point of view both of them can *i*) eliminate or reduce the cause of noise or *ii*) attenuate the existing noise.

The PNC provides a noise reduction by altering the acoustic field of the noise source. It includes almost the totality of noise control technique since it is cheap, simple to implement and the governing physical principles are commonly understood. The PNC is effective for high frequencies and it does not require any power supply. This category includes *i*) noise absorbing materials to be placed inside the cabin and reflecting materials to be located outside, *ii*) materials that reduce the volume velocity of noise sources (vibration attenuation) and *iii*) techniques that modify the acoustic impedance.

The PNC technologies are in constant evolution due to the fact that the market regularly offers new materials with high absorbing or high reflecting coefficients, equipment for high damping systems and various design solution to attenuate undesired noise.

On the other side, ANC aims to attenuates bass sounds by attenuating or cancelling the unwanted acoustic waves with a second group of acoustic waves mainly generated electronically (with loudspeaker for instance) that interfere destructively with the primary disturbance (same amplitude but opposite phase). The noise attenuation achieved

with this approach is effective due to the fact that the acoustic field is linear, hence the superposition principle can be applied.

The complementary application of the two approaches provides an opportunity to utilise both the ANC and PNC at the same time.

The ANC takes its origins from the pioneering works of Paul Lueg [84] in 1933 and Conover [37] in 1956, but only recently it has begun to be part of our daily life. Traditionally, the physical principles for ANC were deeply understood by researchers, but a robust system to be sold on the market was not easily implemented due to the lack in technologies and the associated costs. Such problems have been overcome in the last 15-20 years thanks to more accurate electronic components, also involving microphones and loudspeakers, and the evolutions of the theory of the signal processing (SP). Such developments contribute to progress in different areas of acoustics, e.g., communication, psychology, medical aspects. For instance, today, in many airports, stores sell headphones with an integrated system of ANC.

Nevertheless, the ANC application in enclosed space is strongly limited by a series of physical problems. In fact, effective global noise attenuation can be provided by an ANC system only if the response is tonal and in resonance (or close to the resonance frequency) with one of the mode of the enclosure, otherwise it can be attenuated only in local sense.

Some of the modern propeller-driven aircraft and helicopters have the possibility to integrate an ANC system (for instance Commander 690, various models of Cessna, etc.). In jet aircraft, applying ANC technologies is limited since the noise frequency content is not modal. However, a local approach, that attenuates noise at the passenger ear level only, can still be applied.

In general, the performances of a noise control system vary with the internal design of aircraft cabins and they can be evaluated with numerical simulations.

1.2.1 Numerical Simulations

Simulations are commonly used in noise control and they are performed for both passive and active control.

In active strategies, simulations are aimed at mainly two goals, i.e., to evaluate the performance of an active system for noise suppression and to optimise the control source and microphone locations to achieve the highest noise reduction level.

Early research on ANC was focused on a global approach [17, 70, 92, 103], whereas local strategies were introduced in 1994 by Joseph *et. al* [75] and David and Elliot [44], and further developed by many researchers (see for instance Garcia-Bonito and Elliot [50, 51] and Rafaely *et al.* [99]).

Techniques aimed at maximising the noise reduction level by means of the optimisation of the actuator locations have been explored only in the last couple of decades. Many researchers [29, 63, 105] focused their efforts in evaluating the optimum location of actuators to reduce the source of noise. The researches of Baek and Elliot [7] and Martin and Roure [88] represent two pioneering studies in optimising the location of direct actuators, i.e., the speakers. A possible and valid optimisation technique is the Quasi Newton method that requires the first order derivatives of the physical variables with respect to the design variables. However, the computational effort of the optimisation method based upon the first order derivative represents the main drawback of this analysis and only a few papers [49, 59, 94] have studied this problem.

Another important group of simulations are for the PNC. Such simulations are in general required to prove the performance of a new absorbing material, to evaluate appropriate locations and shapes for such materials, to obtain the optimum design of a mechanical component, a room, a duct, that maximises the noise attenuation level. The computational effort of PNC simulations is in generating the model, in setting the boundary conditions and in providing the final solution. The geometry should

be reproduced as faithfully as possible by the discretised surface otherwise simulation results could not coincide with real circumstances. The absorbing coefficient of each material, if unknown, should be evaluated by experimental tests or using the data in the literature and the disturbing noise needs to be carefully chosen. A particular solution, in fact, can be effective for a given primary disturbance and fruitless for other noises.

1.3 Numerical Method

Analytical solutions of the acoustic equation are available only for simple problems with regular geometries and numerical techniques are required for the solutions for irregular geometries. In the literature there are many techniques for modelling both internal and external sound fields, including modal expansions, finite difference method (FDM), meshfree method, and finite element (FEM) and boundary element (BEM) methods. The modal expansion method [71, 90] is a technique especially developed for internal acoustic problems since the solution is obtained using the acoustic modes for enclosures. The FDM [2] has been mainly adopted for seismic prediction. The meshfree method [4, 20, 113] is a promising and novel strategy for solving acoustic problems that still requires to be fully developed. The FEM [111, 125] and the BEM [45, 123] are both effective techniques for solving acoustic problems. The FEM is one of the most popular techniques and it is utilised in various areas of engineering and industries for its accurate results and its adaptability to practical applications. However, the numerical method selected in this thesis is the BEM for a series of advantages that are highlighted below.

1.3.1 The Boundary Element Method

Probably, the most effective of numerical techniques for solving three dimensional acoustic problems, especially for wide range of acoustic simulations involving infinite domains, is the BEM. Leading acoustic commercial software such as LMS, Ansys, Beasy all utilise

BEM for acoustic modelling.

The BEM takes its origin from the Integral Equation Method, a general technique for solving partial differential equation. The method started to be developed at the beginning of 1960 by the pioneering studies of Shaw and Friedman (1962), Banaugh and Goldsmith (1963), Chen and Schweikert (1963) and Schenck (1967). The period between 1960 and 1975 was prolific for the BEM development especially in potential theory and acoustics research. The first conference was organized in June 1975 by Tom Cruse and Frank Rizzo [40] with name of "Boundary Integral Equation Method: Computational Application in Applied Mechanics". In 1976, Brebbia [24] organized a conference with the name "Boundary Element Methods" in Southampton, U.K., and in 1978 he published a teaching text with the name "The Boundary Element Method for Engineers" [23]. These two episodes established the name of the method as the Boundary Element Method.

One of its main advantages among other numerical techniques is related to the mesh required. Several techniques, in fact, necessitate to discretise the entire medium, whereas the BEM requires to discretise only the surfaces of a given geometry. In addition the technique is particularly effective for unbounded domains and sped up the model setting also in case of enclosed space problems. An important aspect of the BEM integral equation is that the Sommerfeld radiation condition is automatically satisfied [45, 123]. Moreover, the BEM formulation involves (as in other numerical techniques) not only the problem variables, but also their derivatives, i.e., pressure and flux in acoustics, and the solution requires the knowledge of the Green's functions (or fundamental solutions) of the examined problem, which make this numerical technique more accurate than other methods based on polynomial expansion.

On the other hand, the BEM formulation is not without drawbacks. In general, the formulation requires the integration of functions that, in some cases, contain singularities that need elaborate procedures that complicate the method. Moreover, the

BEM, unlike other methods such as the FEM and FDM, generates fully populated and non-symmetric matrices that limit the benefits in using iterative solvers and memory storage management schemes. Several techniques have been investigated to overcome this drawback including block-based solvers [39, 101], lumping techniques [76], iterative solvers [87] and Fast Multipole Method (FMM) [5, 28, 35, 58, 102]. One of the most popular of these techniques is the Adaptive Cross Approximation (ACA) [10, 13], that is an effective technique that reduces both the assembly time and the storage requirements. The ACA in conjunction with Hierarchical matrix (H-matrix) format [60, 61] can be easily implemented with iterative solvers since it strongly speeds up the matrix-vector product. The most popular iterative solver for non symmetric linear systems is the Generalized Minimal Residual Method (GMRES). The method has been proposed by Saad and Schultz (1986) [106] and further developed by other authors [3, 81, 89]. A BEM based code that utilises the ACA, the H-matrix format and the GMRES is very competitive and can strongly speed up the time required for simulations.

1.4 Thesis Overview

The objective of the work is to formulate and implement an efficient three-dimensional boundary element method for modelling ANC and PNC. Upon successful implementation of the method, the numerical tool can be used to model relatively large scale acoustic problems.

The following is a short description of the organization of the thesis.

In the second chapter a brief description of fundamental concepts of the acoustic theory is presented. The history of sound in primordial populations and of the acoustic theory are described. The sound propagation phenomenon is mathematically formulated to obtain the linear wave equation in uniform and non-uniform mediums and a few important acoustic quantities are introduced. Human sense of perception and noise

control strategies for both PNC and ANC are also addressed.

Chapter three presents an overview of the mathematical formulation for the 3D acoustic boundary element method. The Helmholtz equation, that reduces the number of independent variables by one, is obtained. The three boundary conditions, i.e., Neumann, Dirichlet and Robin mixed conditions, are presented as well as the Gauss' theorem and the Green's identities. Fundamental solutions for 2D and 3D acoustic problems are introduced. The boundary integral equation is obtained and numerically implemented using shape functions of any order and kind. The system matrix is assembled by the collocation method. The well known fictitious frequency and spurious eigenvalue problems are briefly mentioned. The chapter is concluded by comparing the solution of two BEM formulations, i.e., superparametric and isoparametric formulations, utilising constant-linear and quadratic elements, respectively, with the solutions of three benchmark problems whose analytical solution is well known, i.e., pulsating sphere, vibrating spherical cavity and plane wave scattering from a sphere.

In chapter four the adaptive cross approximation using the hierarchical matrix format and in conjunction with the GMRES solver is presented for 3D boundary element solution of Helmholtz problems. The procedure and all the mathematical aspects of the technique are described paying particular attention to implementation of different types of boundary conditions into the solution algorithm. A superparametric formulation is implemented and assessed for constant unknown and linear geometry elements. The procedure has been also formulated to evaluate the potential and particle velocity at selected internal points. Numerical results compare the solution time of the presented formulation with the standard BEM, a commercial code, i.e., LMS virtual Lab, that uses the BEM formulation and a code based on the FMM. A parametric study over two quantities is presented. Two simple benchmark problems of the pulsating sphere and of the scattering of a plane wave from a rigid sphere are investigated and the solution times compared. Finally, a row of three seats representing the seats in an aircraft cabin

and noise emanating from engines of the Dassault Falcon aircraft are examined as large scale applications.

Chapter five presents a new approach to the ANC. The strategy is to attenuate the primary noise in a confined zone by minimising the square modulus of the potential and the square modulus of the total particle velocity in one direction in a defined volume, called control volume (CV), rather than cancelling those quantities at discrete points. The strategy results in a more extended and homogeneous noise attenuated area. Simulations presented aim at evaluating the extension of the quiet zone including the addition of second control source. A series of considerations for a practical implementation of this strategy in a noise control system has been also described.

In the sixth chapter a novel Boundary Element (BE) formulation for sensitivity analysis of local ANC in a three-dimensional field for monotone frequencies is presented. The primary noise is attenuated in the above introduced control volume. The optimisation procedure identifies the best location of the control volume and of the control source and, overall, the best orientation of the control source. Moreover, the procedure is sped up by a formulation based on the ACA, the H-matrix format and the GMRES solver. The ACA is utilised to evaluate the system matrix, the internal point quantities and the derivative of the system matrix with respect to the design variables. All the matrices have been stored in the H-matrix format and the GMRES solve the direct as well as the differential system matrix. Several examples conclude the chapter to highlight the efficiency and accuracy of the proposed formulation, i.e., optimum CV location in an infinite unbounded domain; optimum secondary source location inside a room; optimum secondary source orientation inside a box and a room; optimum secondary source locations at different frequencies in an aircraft cabin.

The seventh chapter is devoted to the PNC analysis. The main purpose is to numerically investigate the noise reduction due to the insertion of a new textile as upholstery in aircraft seats. Such a textile is a fiber, called nanofiber, highly porous with excel-

lent absorptive properties especially in the low frequency range. In general, aircraft seat foams have excellent performance at high frequencies and poor at low frequencies. Hence, the nanofiber opens new scenarios in PNC and for this reason the analysis has been focused on the frequency range 8-1000 Hz. All the numerical results are obtained by LMS Virtual.Lab commercial code [82] and compared with the code developed in this thesis (RABEM). The numerical simulations have been aimed at reducing the effort of the experimental tests of the project and to evaluate the practical influence of the nanofiber and different headrest geometries on the sound distribution inside an aircraft cabin. First, some experimental tests have been recovered. Second, various textile properties, diverse locations of the nanofiber and different shapes of the headrest geometries have been investigated, and, third, a sensitivity analysis on the new headrest shape is presented.

The thesis finishes with some concluding remarks and suggestions for future research.

1.5 Author Published Work

In this section a list of the author published or submitted or in press works related to the author's PhD is presented.

1. A. Brancati, M.H. Aliabadi, I. Benedetti. Hierarchical Adaptive Cross Approximation GMRES Technique for Solution of Acoustic Problems Using the Boundary Element Method. *CMES: Computer Modeling in Engineering & Sciences* **43**, 149-172, 2009.

2. A. Brancati, M.H. Aliabadi. Active Noise Attenuation in a Control Volume. (in press)

3. A.Brancati, M.H.Aliabadi, V.Mallardo. A BEM Sensitivity Formulation for three Dimensional Active Noise Control. (in press)

4. V. Mallardo, M.H. Aliabadi, A. Brancati, V. Marant. Noise control in the aircraft cabin.(in press)

1.5.1 Conference Proceedings

1. A. Brancati, M. H. Aliabadi. Active Noise Attenuation Modelling Using the Boundary Element Method. International Conference in Boundary Element Technique IX (BeTeq 2008), July 2008, Sevilla, Spain. (poster)

2. A. Brancati, M. H. Aliabadi. Rapid Solver for 3D Acoustic Simulation Using Boundary Element Method. Mathematics of Finite Elements and Applications (MAFELAP 09), thirteenth conference, June 2009, London, United Kingdom.

3. A. Brancati, M.H. Aliabadi, I. Benedetti. Rapid acoustic boundary element method for solution of 3D problems using hierarchical adaptive cross approximation GMRES approach. International Conference in Boundary Element Technique X (BeTeq 2009), July 2009, Athens, Greece.

This thesis has been carried out with the support of the European research project with acronym SEAT (Smart tEchnologies for stress free Air Travel AST5-CT-2006-030958) under the 6th Framework Programme. The SEAT project has been focused on developing a smart seat to improve the comfort in the economy class of aircraft.

Chapter 2

Fundamentals of Acoustics

Acoustics is a science discovered many centuries ago, but its study has greatly evolved in the last two decades due to two fundamental factors: the first is the development of new technologies more reliable and accurate than in the past and, second, the evolution of the theory of signal processing (SP). On the other side SP has been strongly developed due to the acoustic studies because it can be simply and quickly verified through hearing. The theory of the SP has the drawback of being very complicated, but the mathematical model matches the reality well.

Acoustics is the science of sound (related to one of the five senses) and also a mechanical phenomenon that requires a medium (solid, liquid, gas). It covers many fields of human life: communication (e.g., speech, telephony, music, etc.); higher comfort level (e.g., architectural acoustic, noise control); medical aspects (e.g., stethoscope, phonendoscope); engineering control (e.g., indestructible control on structures); psychology (e.g., neurosis due to extended exposure on noise); etc.

This chapter presents an overview of the fundamentals of acoustics, providing the mathematical description of sound propagation phenomenon and noise control considering human sense perception. Next, a brief review of the history of sound in primordial populations and the efforts to comprehend and study acoustics are presented. The

sound propagation is formulated in terms of the linear wave equation in uniform and non-uniform mediums in the second section. A series of acoustic quantities, i.e., speed of sound, acoustic energy and intensity, the sound pressure level and the impedance, is introduced in the third section. Next, the human sense of sound perception and noise control strategies are described. A summary concludes the chapter.

2.1 Origin of Sound

The phenomenon of acoustic is fascinating and has been widely investigated especially in the last two centuries. However, sound generation was an important aspect of human life for several centuries or maybe millennia, perhaps since humans appeared on the planet earth.

In primordial populations music represented a fundamental part of life, related more on existence than on religious and cultural aspects [107]. Musics and rhythmic sounds are the human way to manifest emotional impulses. In all five continents, musical instruments and artistic objects representing people in their act of playing have been found. Only a few tribes of Patagonia do not show any sense of rhythm and music interest.

The first approach in sound generation is somehow related on striking with hands and feet different parts of the body, ground or trees, generating various tones and effects. The first musical instruments take their origins from hunting and they can be dated back to around 15000 b.c. or even before [21]. In fact, they were often built using wood, bones or reeds, hence a very few exhibits have been found in excavations. Historical researchers often observe the populations that actually live in primitive conditions to imagine and know secrets of prehistoric instruments. Holes on the ground covered with wood, clapped bones and hollow trunks represent first examples of percussion. The sound created by the vibrations of bows after twanging an arrow can be considered the

father of the lute, lira and other string instruments. Hollow bones and horns were used as modern trumpets, flutes and air instruments.

In the Bronze age, people had the opportunity to build more accurate musical instruments with different length, size and material creating different acoustic effects.

The first historical orchestra can be traced back in the IV century b.c. with Nabucodonosor. In the Egypt, the dried conditions of the ground as well as the presence of several bas-reliefs constitute a great source of information to discover the music habits of ancient Egyptians. Flutes, harps, clarinets, lyres, lutes were their favorite musical instruments and they give evidence on Egyptian deep knowledge on resonators and sonorous cases [9, 107] (see for instance figure 2.1).



Figure 2.1: Bas-relief of Gandhara (100 b.c.) from Marcello Dubois.

In India and China musics was a fundamental part of the social life. The first harp, dated 2800 b.c., has been discovered in India, whereas in China music was greatly

connected to the social behaviour of various tribes. Confucius (551-478 b.c.) asserted that in order to have a tidy society, a "sane" music was required. Notes, colours, flavours, seasons, hearth elements, cardinals points were strictly connected to each other and orchestras were the sound bridge between macro and micro-cosmos, death and life [97].

The knowledge of the acoustic transmission phenomenon in solids was utilised not only in music generation, but also for other purposes, e.g., American Indians detected the presence of incoming trains by the sound produced on the rail by their vibrations.

In the literature many experiments reproducible at home can be found to better understand the nature of sound. For example, hitting glasses differently filled (for instance with water) generates various notes that confirms the wave nature of sound and suggests that different sounds are generated by different velocities of vibrations. These concepts are well-known in our society, so they surprise nobody, but much effort was spent to understand the sound phenomenon.

Despite their vast knowledge on scales and notes, Greeks did not invent any new musical instruments. The music, utilised to accompany poetry, was generated by instruments coming from other countries in contact with Greece [21]. Moreover, ancient Greek philosophers comprehended the wave nature of sound, but only with Aristotle and Pythagoras the sound production was interpreted as an air vibration. The theologian, mathematician Marin Mersenne and the scientist Galileo Galilei are the pioneers of acoustics and they introduced the octave frequencies and discovered that sound has a finite speed. The need of a medium was highlighted by Boyle. Reynold and Rayleigh emphasized on the diffraction and reflection phenomena and suggested the ray theory to study the sound propagation. Newton was the first to utilise mathematics to study acoustics, but his poor knowledge of the sound basis constricts his enlighten work to be accurately revisited. Euler, Lagrange and d'Alembert developed the sound theory as it can be read in modern books on acoustics [38, 90, 95, 116].

The effect of the progress on sound theory are visible and audible in many historical building and theatres, such as the Royal Albert Hall of London or the Teatro Massimo of Palermo, in medical instruments, such as the stethoscope and phonendoscope, and in many other fields. As evident, sound dispersion, collection and absorption phenomena play a fundamental role in developing engineering to increase the sound comfort. For instance modern sound systems are focused on creating at home a theatre like environment. On the other hand, sound comfort means also reduction of unwanted noise. The present thesis contributes towards both passive and active noise control.

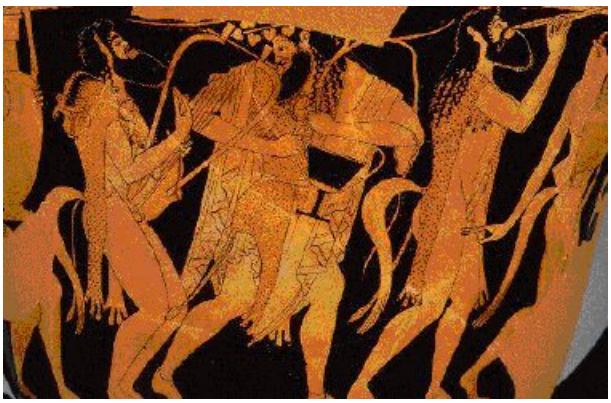


Figure 2.2: A music lesson: particular in a Hydra of V b.c.[131]

2.2 Acoustic Equations

In the present section the wave equation for acoustic is obtained starting from the basic equations of gases and fluids.

2.2.1 Acoustic Model

Sound propagation requires a medium to be transmitted. The experiment of an alarm clock inside a vacuum bell that rings without any noise is well known. The acoustic

medium is considered to be continuum for a large range of frequency. Hence, when one considers a point in the medium it should be considered as a small volume constituted by millions of molecules of fluid in such a way that the sound transmission characteristics are not varied from the macro to the micro model [90, 116].

The fluid is constituted by millions of molecules that counteract each other, bounding and pushing. The mean distance between two of them is called *mean free path*, Λ, that in air has a value around $\Lambda = 6 \times 10^{-5}\, cm$. For very high frequencies, more than 5 million Hz, the wavelength is of the same order of Λ, so the continuum model falls.

The oscillatory nature of the sound motion can be characterized by a sinusoidal function, where crests (highs) and troughs (lows) represent the compression and rarefaction phase, respectively. The distance between two consecutive peaks is the wavelength (λ) and the difference between the crest and trough values is double the amplitude of the sound (see figure 2.3). Three other sound quantities are the frequency f

$$f = \frac{1}{\hat{T}} = \frac{c}{\lambda} \tag{2.1}$$

the angular frequency ω

$$\omega = 2\pi f \tag{2.2}$$

and the wave number k

$$k = \frac{\omega}{c} = \frac{2\pi}{\lambda} \tag{2.3}$$

where c is the wave speed, depending on the medium and $\hat{T}$ is the time between two consecutive instants crests. Wave-number can be interpreted as the number of the peaks within a unit wavelength.

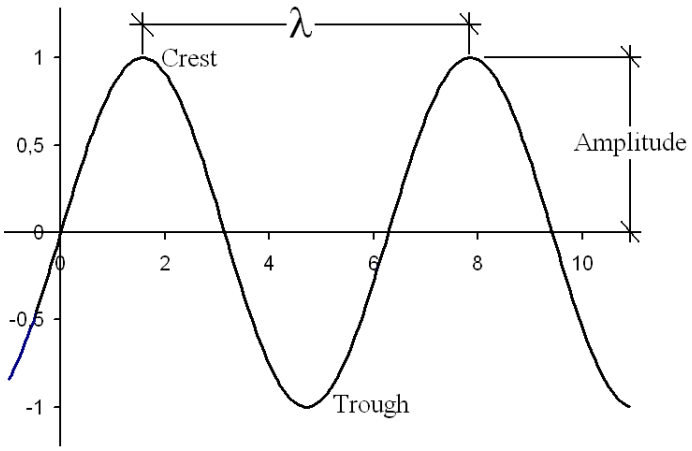


Figure 2.3: A schematic wave.

2.2.2 Equation of State for an Ideal Fluid

The equation of state relates the physical condition of the matter by a mathematical equation between physical quantities such as pressure, volume, temperature and internal energy. In the literature there are many equations for the different states of the matter, i.e., solid, liquid, gas, and for different substances. Currently, a single equation of state that describes the properties of all the substance at different conditions does not exist and for each particular state of the matter different equation is required [90, 116].

In this section the equation of state for an ideal fluid is presented. The pressure p is related to the density ρ and temperature T by a constant R as follows

$$p = R\rho T \tag{2.4}$$

where the value of R depends upon the gas characteristics. A fluid that satisfies the above equation is called *perfect gas* and, in general, it has low pressure and high temperature. Moreover, this equation can be utilised to evaluate the fluid internal energy E, which hence depends upon only two quantities. On the other hand, the pressure

can be expressed in terms of the density and the internal energy

$$p = p(\rho,\, E) \tag{2.5}$$

or, using the entropy S yields

$$p = p(\rho,\, S) \tag{2.6}$$

2.2.3 Conservation of Mass

The total mass contained in a volume Ω depends upon the density ρ of the fluid that can vary with position, $\mathbf{x}$, and time, t, and it can be evaluated as follows [90, 116]

$$\int_{\Omega} \rho\left(\mathbf{x},\, t\right)\, d\Omega(\mathbf{x}) \tag{2.7}$$

In general, the quantity of fluid mass inside the volume can be modified by adding or eliminating a certain amount of fluid mass. This amount depends on the fluid that passes through the boundary Γ of the volume Ω with velocity $\mathbf{v}\left(\mathbf{x},\, t\right)$;

$$\int_{\Gamma} \rho\left(\mathbf{x},\, t\right) \mathbf{v}\left(\mathbf{x},\, t\right) \cdot \mathbf{n}\left(\mathbf{x}\right)\, d\Gamma(\mathbf{x}) \tag{2.8}$$

with dot being the scalar product operator and $\mathbf{n}\left(\mathbf{x}\right)$ the outward normal at the point $\mathbf{x}$ of the boundary.

The well-known Gauss's theorem, also known as the divergence theorem, is here recalled. The Gauss's theorem establishes that the divergence of a given vector field $\rho\mathbf{V}$ inside the volume Ω and the flux across the surface Γ corresponds to

$$\int_{\Omega} \nabla\cdot \left(\rho\left(\mathbf{x},\, t\right) \mathbf{V}\left(\mathbf{x},\, t\right)\right)\, d\Omega = \int_{\Gamma} \rho\left(\mathbf{x},\, t\right) \mathbf{V}\left(\mathbf{x},\, t\right) \cdot \mathbf{n}\left(\mathbf{x}\right)\, d\Gamma(\mathbf{x}) \tag{2.9}$$

where

$$\nabla = \left[\frac{\partial}{\partial x_1}, \frac{\partial}{\partial x_2}, \frac{\partial}{\partial x_3} \right] \tag{2.10}$$

where x_1, x_2, x_3 is the Cartesian coordinate system. It should be noted that (2.9) can be seen as a conservation law in which the volume integral of the divergence is equal to the net flow across the volume's boundary.

The mass conservation law establishes that the variation of the mass within the volume Ω is equal to the fluid that crosses the boundary Γ, that is

$$\frac{d}{dt} \int_{\Omega} \rho\left(\mathbf{x},\, t\right)\, d\Omega(\mathbf{x}) = - \int_{\Gamma} \rho\left(\mathbf{x},\, t\right) \mathbf{v}\left(\mathbf{x},\, t\right) \cdot \mathbf{n}\left(\mathbf{x}\right)\, d\Gamma(\mathbf{x}) \tag{2.11}$$

By considering the volume Ω fixed in space and time, the left hand side becomes

$$\frac{d}{dt} \int_{\Omega} \rho\left(\mathbf{x},\, t\right)\, d\Omega(\mathbf{x}) = \int_{\Omega} \frac{\partial}{\partial t} \rho\left(\mathbf{x},\, t\right)\, d\Omega(\mathbf{x}) \tag{2.12}$$

whereas the right hand side can be rewritten by using the divergence theorem

$$\int_{\Gamma} \rho \mathbf{v} \cdot \mathbf{n}\, d\Gamma = \int_{\Omega} \nabla \cdot \left(\rho \mathbf{v}\right)\, d\Omega \tag{2.13}$$

which implies that

$$\int_{\Omega} \left(\frac{\partial}{\partial t} \rho + \nabla \cdot \left(\rho \mathbf{v}\right) \right)\, d\Omega = 0 \tag{2.14}$$

The above equation is valid inside the volume Ω, but it can be also considered to be valid at each point of the domain, such that

$$\frac{\partial}{\partial t} \rho + \nabla \cdot \left(\rho \mathbf{v}\right) = 0 \tag{2.15}$$

or, written in an equivalent form as

$$\frac{\partial}{\partial t}\rho + \mathbf{v}\cdot\nabla\rho + \rho\nabla\cdot\mathbf{v} = 0 \tag{2.16}$$

The above relation is the well known conservation of mass equation.

2.2.4 Equation of Motion for an Ideal Fluid

The basic concept of the equilibrium equation for a fluid is that the external body and surface forces acting on a fluid mass yield an acceleration of the mass that can be expressed as [90, 116]

$$\frac{d}{dt}\int_\Omega \rho\mathbf{v}\, d\Omega = \int_\Gamma \mathbf{f}_\Gamma\, d\Gamma + \int_\Omega \mathbf{f}_\Omega\, d\Omega \tag{2.17}$$

where $\mathbf{f}_\Gamma$ and $\mathbf{f}_\Omega$ are the forces per unit area and unit volume acting on the fluid surface and mass, respectively. In general, the body forces acting on the mass are long range forces such as gravity force, whereas the surface forces are caused by surrounding particles. The above equation is valid since the mass fluid particles are constant in the considered volume, hence the mass multiplied to its acceleration is just the time rate of the variation of the momentum of the particle, defined as the volume integral of $\rho\mathbf{v}$.

The left-hand-side contribution of (2.17) can be modified as follows

$$\frac{d}{dt}\int_\Omega \rho\mathbf{v}\, d\Omega = \int_\Omega \frac{\partial}{\partial t}\left(\rho\mathbf{v}\right)\, d\Omega + \int_\Gamma \rho\mathbf{v}\left(\mathbf{v}\cdot\mathbf{n}\right)\, d\Gamma \tag{2.18}$$

where the first contribution is given by the local changes of $\rho\mathbf{v}$, and the second is generated by the variation of the volume with time and for which the divergence theorem yields

$$\int_\Gamma \rho\mathbf{v}\left(\mathbf{v}\cdot\mathbf{n}\right)\, d\Gamma = \int_\Omega \left(\nabla\cdot\rho\mathbf{v}\right)\mathbf{v}\, d\Omega \tag{2.19}$$

Substituting the above expression into the equation (2.18) produces

$$\frac{d}{dt}\int_{\Omega}\rho\mathbf{v}\,d\Omega=\int_{\Omega}\frac{\partial}{\partial t}\left(\rho\mathbf{v}\right)\,d\Omega+\int_{\Omega}\left(\nabla\cdot\rho\mathbf{v}\right)\mathbf{v}\,d\Omega=\int_{\Omega}\rho\frac{D\mathbf{v}}{Dt}\,d\Omega \tag{2.20}$$

where

$$\frac{D}{Dt}=\frac{\partial}{\partial t}+\mathbf{v}\cdot\nabla \tag{2.21}$$

is the material derivative.

The motion of a fluid can be examined by a fixed observer (Eulerian observer) or by an observer that follows the fluid in its motion (Lagrangian observer). The above quantity refers to this last approach where the fluid changes in time and space.

As afore-mentioned, the right hand side term of (2.17) is composed by body and surface forces. The former forces can be neglected since the gravity does not interfere with the acoustic behaviour of the medium. The gravity can influence only low frequency sounds where the wavelength is of the same order as the ratio between the gravity acceleration and the sound speed, i.e., g/c.

The surface forces can now be written as follows

$$\int_{\Gamma}\mathbf{f}_{\Gamma}\,d\Gamma=\int_{\Gamma}\sigma_{ij}n_{j}\,d\Gamma \tag{2.22}$$

where σ_{ij} is the stress tensor defined as follows

$$\sigma=\begin{bmatrix}\sigma_{11} & \sigma_{12} & \sigma_{13}\\ \sigma_{21} & \sigma_{22} & \sigma_{23}\\ \sigma_{31} & \sigma_{32} & \sigma_{33}\end{bmatrix} \tag{2.23}$$

The σ_{ij} components correspond to force along the i-axis that acts on the fluid mass surface perpendicular to the j-axis. If $i=j$ the force is normal to the surface and it is a pure tension/compression for a positive/negative value, respectively. If $i\neq j$ the stress is tangential to the surface and the forces acting on the mass are due to the viscosity of

the fluid. For an ideal fluid the tangential stresses are neglected and the stress tensor is isotropic and given in terms of the mechanical pressure as follows

$$\sigma = \begin{bmatrix} -p & 0 & 0 \\ 0 & -p & 0 \\ 0 & 0 & -p \end{bmatrix} \tag{2.24}$$

The above matrix can be substituted by a vector of the type $\sigma = -p\mathbf{n}$, where $\mathbf{n}$ denotes the unit outward normal, so that by substituting it in (2.22) and applying the divergence theorem yields

$$\int_\Gamma \mathbf{f}_\Gamma \, d\Gamma = -\int_\Gamma p\mathbf{n} \, d\Gamma = \int_\Omega \nabla p \, d\Omega \tag{2.25}$$

Equation (2.17) can now be rewritten as follows

$$\int_\Omega \left(\rho \frac{D\mathbf{v}}{Dt} + \nabla p \right) d\Omega = 0 \tag{2.26}$$

that is valid at each point of the volume Ω such that

$$\rho \frac{D\mathbf{v}}{Dt} = -\nabla p \tag{2.27}$$

This equation is the well-known Euler's equation for an ideal fluid.

2.2.5 Linearisation

Sound is created by a perturbation of an acoustic medium that is in equilibrium state. Under this hypothesis the initial quantities, indicated with subscript "$_0$", i.e., p_0, ρ_0, T_0, $\mathbf{v}_0$, have a finite value, with $\mathbf{v}_0 = 0$ and satisfy equations (2.4), (2.16) and (2.27). The medium is considered to be homogeneous, thus all the quantities are independent with respect to location within the medium.

The perturbation, which is an isentropic compression, introduces extra terms in the pressure, density and velocity values such that [90, 116]

$$p(\mathbf{x},\, t) = p_0(\mathbf{x}) + p'(\mathbf{x},\, t); \qquad \rho(\mathbf{x},\, t) = \rho_0(\mathbf{x}) + \rho'(\mathbf{x},\, t); \qquad \mathbf{v}(\mathbf{x},\, t) = \mathbf{v}'(\mathbf{x},\, t) \tag{2.28}$$

where $|p'| \ll p_0$ and $|\rho'| \ll \rho_0$.

The infinitesimal fluctuation from the equilibrium state can be considered in (2.6) and the pressure can be written as follows

$$dp = \left(\frac{\partial p}{\partial \rho}\right)_S d\rho + \left(\frac{\partial p}{\partial S}\right)_\rho dS \tag{2.29}$$

that in case of isentropic transformation yields

$$dp = c^2 d\rho \tag{2.30}$$

where the velocity of sound c is defined as follows

$$c^2 = \left(\frac{\partial p}{\partial \rho}\right)_{S_0} \tag{2.31}$$

The above quantity can thus be expanded by a Taylor series

$$c^2 = \left[\left(\frac{\partial p}{\partial \rho}\right)_{S_0}\right]_{\rho=\rho_0} + \left[\left(\frac{\partial^2 p}{\partial \rho^2}\right)_{S_0}\right]_{\rho=\rho_0} (\rho - \rho_0) + ... \tag{2.32}$$

or in an equivalent form

$$c^2 = c_0^2 + d_0^2 \rho' + ... \tag{2.33}$$

with

$$c_0^2 = \left[\left(\frac{\partial p}{\partial \rho}\right)_{S_0}\right]_{\rho=\rho_0} \qquad d_0^2 = \left[\left(\frac{\partial^2 p}{\partial \rho^2}\right)_{S_0}\right]_{\rho=\rho_0} \tag{2.34}$$

The linearisation process (also well-known as the acoustic approximation) considers only the linear terms of the Taylor series eliminating the second and higher order terms so that (2.6), (2.16) and (2.27) can be written as following

$$p' = c_0^2 \rho' \tag{2.35a}$$

$$\frac{\partial \rho'}{\partial t} + \rho_0 \nabla \cdot \mathbf{v}' = 0 \tag{2.35b}$$

$$\rho_0 \frac{\partial \mathbf{v}'}{\partial t} = -\nabla p' \tag{2.35c}$$

Substituting (3.5a) in (3.5b) and differentiating with respect to the time yields

$$\frac{1}{c_0^2}\frac{\partial^2 p'}{\partial t^2} + \rho_0 \nabla \cdot \frac{\partial \mathbf{v}'}{\partial t} = 0 \tag{2.36}$$

The second term of the left hand side of the above equation can be substituted into (3.5c) to give

$$\nabla^2 p' - \frac{1}{c_0^2}\frac{\partial^2 p'}{\partial t^2} = 0 \tag{2.37}$$

where ∇^2 is the Laplacian operator. The above relation is the well-known *wave equation* for a medium that is not uniform.

2.2.6 Uniform Medium

The relation (2.37) is valid for a not uniform medium, such as atmosphere or sea water, where the sound characteristics, e.g., sound velocity, pressure, depend upon

various factors, e.g., altitude, air temperature, wind. The hypothesis that the acoustic propagation takes place in a limited area (a room for instance) yields an important idealization [90, 116].

Evaluating the curl of the Euler equation for the linearised model, equation (3.5c), and observing that $\nabla \times \nabla p = 0$ (the curl of a scalar quantity gradient is zero), gives

$$\frac{\partial}{\partial t}(\nabla \times \mathbf{v}') = 0 \tag{2.38}$$

which means that the vorticity is constant in time.

In case this constant is zero, the fluid is uniform and called *irrotational*, for which $\nabla \times \mathbf{v}' = 0$, hence a function $\phi = \phi(\mathbf{x}, t)$, called *velocity potential*, can be introduced to evaluate the velocity $\mathbf{v}'$ as follows

$$\mathbf{v}' = \nabla\phi \tag{2.39}$$

This implies that the value of the sound perturbation velocity can be evaluated through a single scalar quantity. Moreover, substituting this last relation into (3.5c) yields

$$\nabla\left(\rho_0 \frac{\partial \phi}{\partial t} + p'\right) = 0 \tag{2.40}$$

which means that the velocity potential ϕ also evaluates the pressure variation within the uniform domain.

Another important aspect of the velocity potential is that it satisfies the wave equation. To demonstrate it equations (2.35) are rewritten by using the function ϕ as

$$p' = c_0^2 \rho' \tag{2.41a}$$

$$\frac{\partial \rho'}{\partial t} + \rho_0 \nabla^2 \phi = 0 \tag{2.41b}$$

$$\rho_0 \frac{\partial \phi}{\partial t} = -p' \tag{2.41c}$$

Equations (2.41a), (2.41b) and (2.41c) can be rearranged to yield

$$\nabla^2 \phi - \frac{1}{c_0^2} \frac{\partial^2 \phi}{\partial t^2} = 0 \tag{2.42}$$

which is the well known d'Alembert equation of wave motion for a uniform field.

2.2.7 One-dimensional General Solution

The solution of the wave motion equation for a uniform field (2.42) for one-dimensional case can be achieved by using two variables ξ and η functions of space (x_1) and time (t), as follows [116]

$$\xi = x_1 - c_0 t; \qquad \eta = x_1 + c_0 t \tag{2.43}$$

The first derivative of ϕ with respect to the space is

$$\frac{\partial \phi}{\partial x_1} = \frac{\partial \phi}{\partial \xi} \frac{\partial \xi}{\partial x_1} + \frac{\partial \phi}{\partial \eta} \frac{\partial \eta}{\partial x_1} \tag{2.44}$$

or

$$\frac{\partial \phi}{\partial x_1} = \frac{\partial \phi}{\partial \xi} + \frac{\partial \phi}{\partial \eta} \tag{2.45}$$

The second derivative can now be written as

$$\frac{\partial^2\phi}{\partial x_1^2} = \frac{\partial}{\partial\xi}\left(\frac{\partial\phi}{\partial\xi} + \frac{\partial\phi}{\partial\eta}\right) + \frac{\partial}{\partial\eta}\left(\frac{\partial\phi}{\partial\xi} + \frac{\partial\phi}{\partial\eta}\right) = \frac{\partial^2\phi}{\partial\xi^2} + 2\frac{\partial^2\phi}{\partial\xi\partial\eta} + \frac{\partial^2\phi}{\partial\eta^2} \tag{2.46}$$

Differentiating ϕ with respect to time yields

$$\frac{\partial\phi}{\partial t} = c_0\left(\frac{\partial\phi}{\partial\eta} - \frac{\partial\phi}{\partial\xi}\right) \tag{2.47}$$

and the second derivative

$$\frac{\partial^2\phi}{\partial t^2} = c_0^2\left(\frac{\partial^2\phi}{\partial\eta^2} + \frac{\partial^2\phi}{\partial\xi^2}\right) - 2\frac{\partial^2\phi}{\partial\xi\partial\eta} \tag{2.48}$$

Substituting (2.46) and (2.48) into (2.42) gives

$$\frac{\partial^2\phi}{\partial\xi\partial\eta} = 0 \tag{2.49}$$

A solution of the above equation can be obtained by the product of two equations $f(\xi)$ and $g(\eta)$

$$\phi = f(\xi) + g(\eta) = f(x_1 - c_0 t) + g(x_1 + c_0 t) \tag{2.50}$$

These two functions can be interpreted as two different waves that travel with opposite directions ($f(\xi)$ toward a positive x_1) and same velocity c_0. The amplitudes of both functions are constant with respect to space and depend only upon the time, which means that at two different points the amplitude is the same and the two front-waves occur at different times depending on the distance between the two points.

Under the hypothesis that $f(\xi)$ and $g(\eta)$ yield two symmetrical waves with same amplitudes, combining the two waves gives a standing wave that simply oscillates and does not travel toward any direction. In fact, when the two waves are opposite in phase

(180° degree) the combined wave is cancelled, whereas when the two waves have same phase, the amplitude is the double of each single amplitude. Finally, for any phase value the wave oscillates between zero and the maximum amplitude.

As evident, a travelling wave can be simply created by setting one of the two functions $f(\xi)$ or $g(\eta)$ equal to zero.

2.3 Acoustic Quantities

In this section some important sound quantities that are used in the next chapter are introduced. They include speed of sound, acoustic energy and intensity, decibel and sound pressure level, impedance.

2.3.1 Speed of Sound

As introduced above, speed of sound varies with the medium. In gases this value is lower than in fluids or solids. Equation (2.31) gives the isentropic speed of sound, but its value cannot be calculated with common measurable quantities. Hence, in the present contribution the speed of sound for perfect gas is evaluated.

For an ideal gas, equation (2.4) describes its state and its internal energy, under the hypothesis of constant volume, depends only upon the temperature [90]

$$dE = c_v dT \tag{2.51}$$

where c_v is the specific heat for constant volume, a quantity that indicates the ability of a system, with fixed volume, to increase its temperature T by an addition of heat dE. As evident, a high value of c_v indicates that the system needs a great amount of heat to increase its temperature. The value of c_v depends upon the temperature and it can be demonstrated that for an isentropic change (S constant) its value can be evaluated

as follows

$$c_v(T) = \frac{p}{\rho^2}\frac{d\rho}{dT} \tag{2.52}$$

A specific heat for a transformation at constant pressure, indicated with c_p, is related with the above quantity by the constant of gases R as follows

$$R = c_p - c_v \tag{2.53}$$

Now, the differential form of equation (2.4) gives

$$dp = R(Td\rho + \rho dT) \tag{2.54}$$

Substituting this relation into (2.31) yields

$$c_0^2 = RT_0 + R\rho_0 \left(\frac{\partial T}{\partial \rho}\right)_{S_0} \tag{2.55}$$

where the subscript $_0$ indicates initial quantities of an isentropic transformation. This relation can be modified by (2.52) as follows

$$c_0^2 = RT_0 \left(1 + \frac{R}{c_{v0}}\right) \tag{2.56}$$

and by considering another constant $\gamma = c_p/c_v$, the sound speed can be easily evaluated with the following relation

$$c_0 = \sqrt{\gamma RT} \tag{2.57}$$

As evident, from the above equation, the sound velocity for an ideal gas depends only upon the temperature. The importance of (2.57) is on the fact that it agrees with experimental tests on real gases, such as the air. This means that the passage of sound

waves does not vary the temperature of the gas. This assumption is valid for an ideal fluid that has zero thermal conductivity as well as for a real gas that has a finite value of this quantity. This can be explained considering that (2.57) has been derived using an adiabatic transformation. Further details on this subject are beyond the scope of this thesis and can be found in [116].

2.3.2 Acoustic Energy

The equation of the acoustic energy for uniform fluids is obtained by combining the internal energy equation of gases, the Euler's equation (2.27) and the equation of mass conservation (2.16) under the hypothesis of small variation from the equilibrium state and isentropic transformation. The acoustic energy equation can be written as follows [90, 116]

$$\frac{\partial}{\partial t}\left(\frac{1}{2}\rho_0 q^2 + \frac{1}{2}\frac{c_0^2}{\rho_0}\rho'^2\right) = -\nabla\cdot(p'\mathbf{v}') \tag{2.58}$$

where $q^2 = \mathbf{v}'\cdot\mathbf{v}'$. The left hand side quantity is the total acoustic energy contained in a unitary volume. Integrating the above equation over a volume Ω helps to interpret its significance

$$\frac{\partial}{\partial t}\int_\Omega \frac{1}{2}\left(\rho_0 q^2 + \frac{c_0^2}{\rho_0}\rho'^2\right)\, d\Omega = -\int_\Gamma p'\mathbf{v}'\cdot\mathbf{n}\, d\Gamma \tag{2.59}$$

where, the left hand side term is the acoustic energy contained in the volume and the left hand side term is the variation of the acoustic energy within the same volume that is the acoustic power.

2.3.3 Acoustic Intensity

The acoustic intensity is a time average vector defined as follows [90]

$$\mathbf{I} = \langle p'\mathbf{v}' \rangle = \frac{1}{\tau} \int_0^\tau \mathbf{I}(t)\, dt \tag{2.60}$$

measured in $Watt/m^2$. It is the power crossing a unit area, with τ denoting a time interval. The acoustic power crossing any surface with normal $\mathbf{n}$ can be evaluated by the integral of $\mathbf{I}$ over the surface

$$W = \int_\Gamma \mathbf{I} \cdot \mathbf{n}\, d\Gamma \tag{2.61}$$

2.3.4 Sound Pressure Level

The human perception of sound varies in a wide range of pressure (measured in Pascal), of order of a hundred million, namely [38]

$$2 \cdot 10^{-5} < p < 2 \cdot 10^3\, Pa \tag{2.62}$$

and the ear response is almost logarithmic. This suggests utilising a similar approach for sound measurements. Therefore a dimensionless quantity, i.e., the intensity level, is introduced now

$$I_L = \log \frac{I}{I_{ref}} \tag{2.63}$$

where I is the intensity level component along a single direction, and $I_{ref} = 10^{-12}$ $Watt/m^2$ is the threshold of audibility used as reference level at 1 kHz. This dimensionless quantity is measured in Bel, in honour of Alexander Graham Bell that can be considered as the first inventor of a speaker. A similar quantity is the Sound Pressure Level (SPL) defined as follows

$$SPL = 10 \log_{10} \frac{|p|^2}{|p|^2_{ref}} \tag{2.64}$$

where $p_{ref} = 2 \cdot 10^{-5}\, Pa$ is the reference sound at 1 kHz. The above relation has the advantage to be evaluated using measurable quantities. The SPL is measured in decibel (dB). It should be noted that 0 dB means that the medium fluctuations create a pressure equal or inferior than $2 \cdot 10^{-5}\, Pa$.

2.3.5 Impedance

The impedance originates from the word "impede", or to stop from moving, and indicates how a field reacts to an applied source. In engineering and science, it is common to refer phenomena that involve to the movement of some substance in terms of three quantities: potential difference (or pressure), flow (or velocity) and impedance (or its inverse, admittance). In particular, impedance indicates how much flow is generated by the potential difference

$$\text{impedance} = \text{potential difference/flow} \tag{2.65}$$

or in terms of acoustic quantities

$$Z_j = \frac{p'}{v'_j} \tag{2.66}$$

with $j = 1, 2, 3$. It is measured in $\frac{Pa}{m/s}$ that is called *Rayl* in honour of John William Strutt Rayleigh, an English scientist who received the Nobel price in 1904. In air the impedance value is approximately 415 Rayl. The impedance has a complex value. The real part is called resistance and the imaginary part reactance.

A low value of Z_j implies a situation in which the flow of acoustic waves away from the source will be high. For instance, in a cone amplifier the initial impedance value Z_A is higher than the final one Z_B. This represents an advantageous situation since the sound created by the membrane with high pressure and low flow (treble sound) is transformed by the cone shape in a sound with low pressure and high flow (a bass

sound), more suitable for the motion of acoustic waves in air.

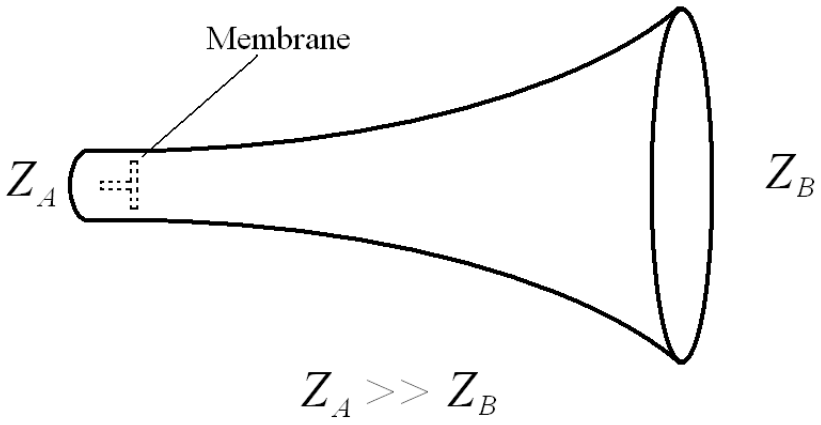


Figure 2.4: Cone speaker.

In case of a conventional speaker cone, the impedance is a measure of the sound pressure level that can be generated. The power of speakers, in fact, is realised by the speaker impedance. To make an automobile analogy, a sport car (like a Ferrari) cannot be fast with bicycle wheel (low impedance). The same happens in sound generation. A sound system with high power requires an high speaker impedance value. Speaker cones have constant volume velocity and the acoustic impedance is directly related to the sound pressure level. For high/low impedance the SPL is also high/low. Moreover, if the potential difference and the flow velocity are in phase the impedance has the highest performance, whereas if they are out of phase the energy transportation is not optimal.

2.4 Planewaves and Monopole Sources

Two general idealizations of the sound sources for a uniform three dimensional field are planewaves and monopoles. The former could be created inside pipe organs, or

exhaust gas duct, and it reproduces the effects of a source located far away from the observation point. On the contrary, monopole idealizes the effect of a common source such a loudspeaker especially at low frequencies.

2.4.1 Planewave

The planewave is a plane sound where all the molecules of the same plane move at the same direction with same phase, velocity and pressure. It can be created by an infinite piston that moves at a single direction.

The medium motion is governed by the wave equation for uniform medium, equation (2.42), and the pressure and acoustic velocity are obtained by the velocity potential ϕ by equations (2.41c) and (2.39).

If the piston is moving with sinusoidal behaviour and the medium particles move with the same motion of the piston (sinusoidal), the value of velocity potential can be evaluated as follows

$$\phi(\mathbf{x},\, t) = \phi_{max}\, e^{i(\omega t - k\hat{e}_k \cdot \mathbf{x})} \tag{2.67}$$

where k is the wave number, ω is the angular frequency and $\hat{e}_k$ is the unitary direction of the planewave. It should be noted that only the real part of the above relation has a physical meaning.

As indicated previously the acoustic field is linear, which means that each wave is not modified when it interacts with other waves. Non linearity would have created a field with oscillating waves having frequency multiple to the original [116].

In the present thesis the acoustic field is always linear. In practical applications, e.g., electrical transducer, non linearity is undesirable. For instance a speaker with non linear behaviour is not able to perfectly recreate and amplify an incoming sound. In other context, non linearity could be a desirable characteristic as in case of string

musical instruments, e.g., violin, guitar, that have complex and harmonic sounds, where harmonic means that a sound is generated by the fundamental note and other treble notes that produce the characteristic sound of a musical instrument.

Considering the planewave proceeding along the x_1-axis and combining equation (2.67) with (2.41c) and (2.39), pressure and velocity can be expressed, respectively, as follows

$$\begin{aligned} p' &= -i\rho_0\omega\phi_{max}\, e^{i(\omega t - kx_1)} \\ v_1' &= \frac{\partial\phi}{\partial x_1} = -ik\phi_{max}\, e^{i(\omega t - kx_1)} \end{aligned} \tag{2.68}$$

where v_1' is the component of the velocity along the x_1-axis, and v_2' and v_3' are both zero.

2.4.2 Monopole

The monopole is a spherical source with spherical symmetry where all the points on the sphere surface vibrate with same value of phase, pressure and velocity. It is also a basic function of the boundary element formulation, i.e., potential fundamental solution, hence its behaviour is really important for what follows.

By using spherical coordinates, equation (2.42) can be rewritten as follows [116]

$$\frac{\partial^2\phi}{\partial r^2} + \frac{2}{r}\frac{\partial\phi}{\partial r} = \frac{1}{c^2}\frac{\partial\phi}{\partial t^2} \tag{2.69}$$

with r distance from the origin of the spherical source. To evaluate the solution, the particle velocity at the surface of the source ($r = R_0$) can be used as the required boundary condition

$$\mathbf{v}(R_0,\, t) = v_{max}\, e^{i\omega t}\, \hat{e}_r \tag{2.70}$$

where $\hat{e}_r$ is the radial direction of the sound propagation.

The solution can be now written as follows

$$\phi = \frac{\kappa}{r} e^{i(\omega t - kr)} \tag{2.71}$$

where κ is a constant evaluated by imposing the velocity at the source surface. The velocity can be calculated by the gradient of the potential as follows

$$\mathbf{v}(r,\, t) = \nabla\phi(r,\, t) = \frac{-(1+ikr)\kappa\, e^{i(\omega t - kr)}}{r^2} \tag{2.72}$$

that yields the value of the constant κ

$$\kappa = -v_{max} \frac{R_0^2}{1+ikR_0}\, e^{ikR_0} \tag{2.73}$$

The value of the pressure can be evaluated using the solution (2.71) and equation (2.41c) as follows

$$p'(r,\, t) = -\rho_0 \frac{\partial\phi(r,\, t)}{\partial t} = -\rho_0 \frac{i\omega\kappa\, e^{i(\omega t - kr)}}{r^2} \tag{2.74}$$

The monopole impedance can be calculated as

$$Z(r) = \frac{i\omega\rho_0}{1+ikr} \tag{2.75}$$

Now, when $r \to 0$ the angle of complex vector is $\arg(Z(r)) = 90°$, whereas when $r \to \infty$, $Z(r) \to \rho_0 c$, which is the air impedance and means that at infinity there are no effects of the monopole presence.

Moreover, if $r \gg \lambda$ the impedance is real and its phase is zero, and this is the case of planewave. In the case $r \ll \lambda$, the impedance can be vanished and $\arg(Z(r)) = 90°$, which means that pressure and velocity are 180° out of phase, determining a low

radiation efficiency and part of the radiation energy returns to the source.

Considering two speakers with characteristic dimensions $d_1 \ll \lambda$ and $d_2 \gg \lambda$, respectively, the first has pressure and velocity 180° out of phase and a low efficiency, whereas in the second speaker pressure and phase have same phase and a higher efficiency.

2.5 Human perception

The human ear is a complex electron-mechanical instrument able to transform the air fluctuation in perception of sound. It also identifies the sound quality, power and provenance. The internal structure of a human ear, shown in figure 2.5, is now presented to explain the human different perceptions at various frequencies [38].

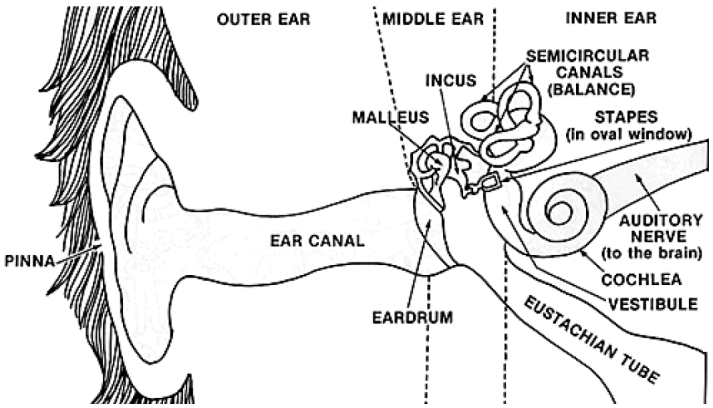


Figure 2.5: Human ear internal structure. [126]

The ear can be divided into three parts each of which has a different task: external, middle and internal ear.

The external (pinna and ear canal) ear collects and canalizes the surrounding sounds that are transferred to the middle ear. The middle ear is constitutes by the tympanic membrane that vibrates with incoming sounds. Its mechanical motion is reduced by three small bones, i.e., malleus, incus and stapes. The last bone is attached to the inner

ear by the oval window. The sound is then transferred to the cochlea that transforms the pressure variation into a proper code to be sent to the brain. The spiral shape of the cochlea is the key for its behaviour at different frequencies. The treble sounds, which have a short wavelength and a low penetrating capability, are kept in its initial part, whereas the bass sounds, with long wavelength and more penetrating power than the former, arrive in the internal part of the cochlea, where the treble sounds are almost totally cancelled. Due to this fact, the treble sound takes less time to be heard and so they are heard better than the bass.

The frequency range that human can hear is between 20 Hz and 16-20 kHz. Children are, in general, more sensitive to the treble sounds than bass sound, whereas an older person's ear loses first the treble sound perception due to infections on the cochlea initial part.

Figure 2.6 shows the ISO Standard 226 [133] and summarizes the human ear behaviour. On the x-axis the frequency is marked, on the y-axis the SPL in dB. Each curve is made using a statistic calculus based on a series of tests on a sample of people. The frequency of 1 kHz is the reference frequency, so each curve, measured in *phons*, delineates the sound perceived with the same loudness level of a 1 kHz frequency. For example the sound having 20 dB at 20 Hz has the same perceived power of a sound of 80 dB at 1 kHz and of 90 dB at 5 kHz. Again, in order to have a sound of 30 dB at 20 Hz, the same power of a 100 dB sound of 5 kHz is needed.

For this reason the sound pressure level measured by a sound acquisition system is weighted by a series of curves defined in the International standard IEC 61672:2003 [134] and various national standards, the so called "A-B-C-D-Z-weightings", to evaluate the sound pressure level perceived by humans (see figure 2.7). A-weighting is the most common curve and its decibels are abbreviated dB(A) or dBA. As evident, its shape has been approximately achieved by the inverse of the Fletcher-Munson curves.

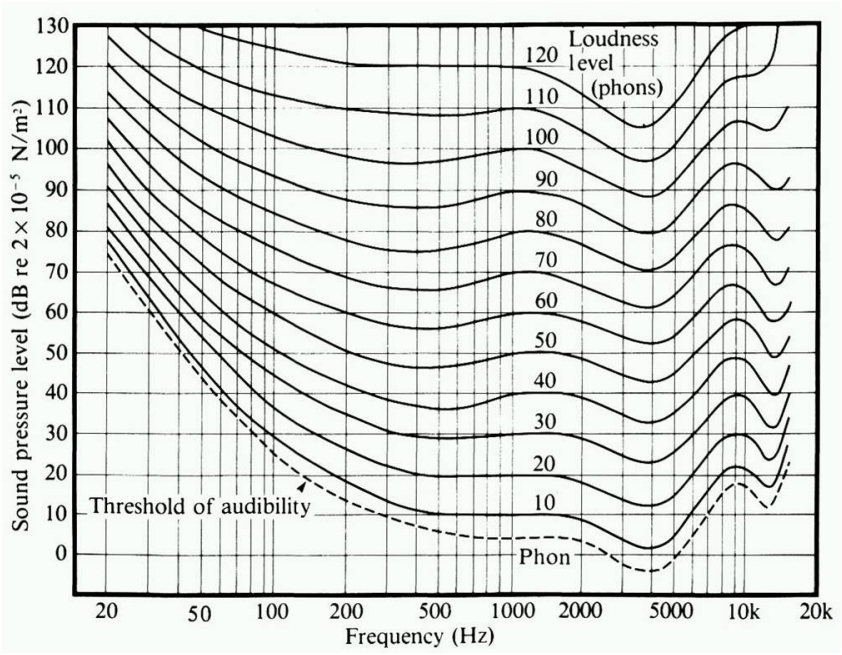


Figure 2.6: ISO standard 226:2003. Acoustics – Normal Equal Loudness Level Contours: Fletcher & Munson curve.

The threshold of audibility also depends upon the frequency. The maximum sound pressure level a person can hear is around 120 dB. At a higher level the pain threshold is reached and, with any further increase, the level of injury will occur. The level of sound for each activity of the human life takes a location on this graph, e.g., for speech is between 30 dB and 80 dB and 150 Hz to 3000 Hz.

Another significant difference between treble and bass sounds is the perception of the source location in a closed space. The distance of treble source is detected based on its intensity and the difference between the perception of the right and left ears gives the exact position of a source. On the contrary, a bass sound has a wavelength comparable to the characteristic length of a room, hence the primary sound interfering with the rebounded sound so that the source intensity varies with locations inside the room. Hence, sound perception is based upon reflections and statistical behaviour of the room, at high frequencies, and upon room modes, at low frequencies. The crossover

frequency between the low- and the high-frequency is known as the *Schroeder frequency*. More details on these regards are presented next.

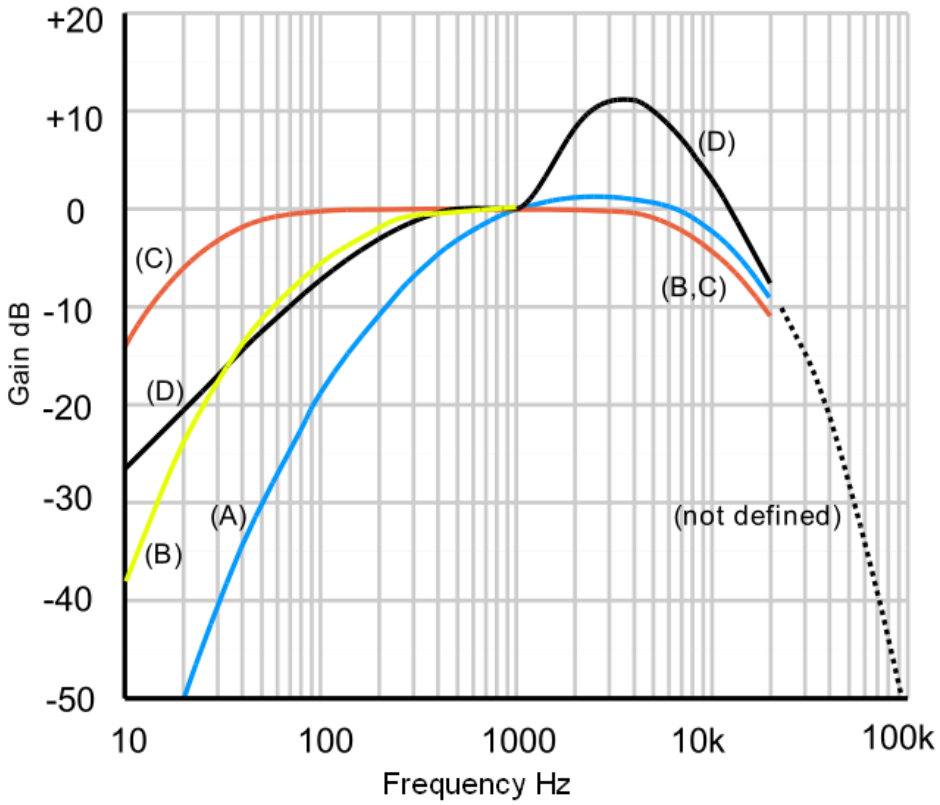


Figure 2.7: A (blue), B (yellow), C (red), and D weighting (black) [127].

A complete description of the behaviour of the human ear is beyond the scope of this thesis and can be found in [104].

2.6 Noise Control Strategies

In the present section two of the main techniques to reduce unwanted noise are presented: passive noise control (PNC) and active noise control (ANC).

Noise control is simply the reduction in amplitude of unwanted noise. The noise control approaches can be divided into two general categories: *i*) reduction in the total

sound power flowing away from the source, and *ii*) redirect the acoustic flow energy such that the SPL directed on humans is attenuated. The former approach often provides global reduction, whereas the latter yields an attenuation of primary disturbs at one location and in response the noise level can be higher in other locations.

Both categories can be further divided into several subgroups. A first group includes techniques which aim to "absorb" sound energy and turn it in a very small amount of heat. A second group aims to reduce the volume velocity of the noise source by attenuating vibrations and the third group target in varying the acoustic impedance.

A further classification divides the noise reduction techniques into two categories, i.e., PNC and ANC. PNC and ANC employments depend upon the frequency of the undesirable noise. As afore-mentioned sound is a wave travelling in a medium. Treble sounds have high frequency values, hence low wavelengths, whereas bass sounds have high wavelengths and low frequencies. A treble sound is created by rapid variations of few air molecules and the energy contained in it is quite low compared to that contained in a bass sound, generated by a low motion of a great quantity of air molecules. PNC is utilised to reduce treble sounds, whereas ANC is used to attenuate bass sounds [64, 91].

2.6.1 Passive Noise Control (PNC)

The PNC consists of utilising foams or sound absorbing materials to dissipate the acoustic energy. As evident, the quantity of absorbing material required for bass sounds is higher than for treble sounds. This concept is in general expressed by the mass law, known also as the Sabine's law, where the absorbent ratio R_a, indicating the noise reduction, in dB, of a sound travelling through a material, is evaluated as follows [38]

$$R_a = 20 \log (\varrho f) - 42.5 \tag{2.76}$$

where ϱ is the surface density of a material expressed in kg/m^2 and f is the frequency. As evident, R_a rises up 6 dB per octave.

The above formula is generally used for evaluating the absorbent coefficient in an enclosure, but it should be noted that it cannot be applied to all the audible frequency range. In figure 2.8 this range is divided into three regions.

The first region is characteristic for frequencies that are in resonance with the enclosures, and the dominant pattern of wave travel at those frequencies are the associated mode shape. To visualize the modes let consider a rectangular box where three types of modes can exist: *i*) axial mode, that exist between two parallel walls (1D modes); *ii*) tangential modes, that involve reflection from two sets of walls at one time (2D modes); *iii*) oblique mode, that involve reflections of all walls (3D modes). The minimum sound reduction index corresponds to the first associated mode, that, in general, is axial and with frequency having double wavelength with respect to the longest direction of extension. The limit of this region is the afore-mentioned Schroeder frequency which in general is around 10-20 Hz, and in any case below 100 Hz.

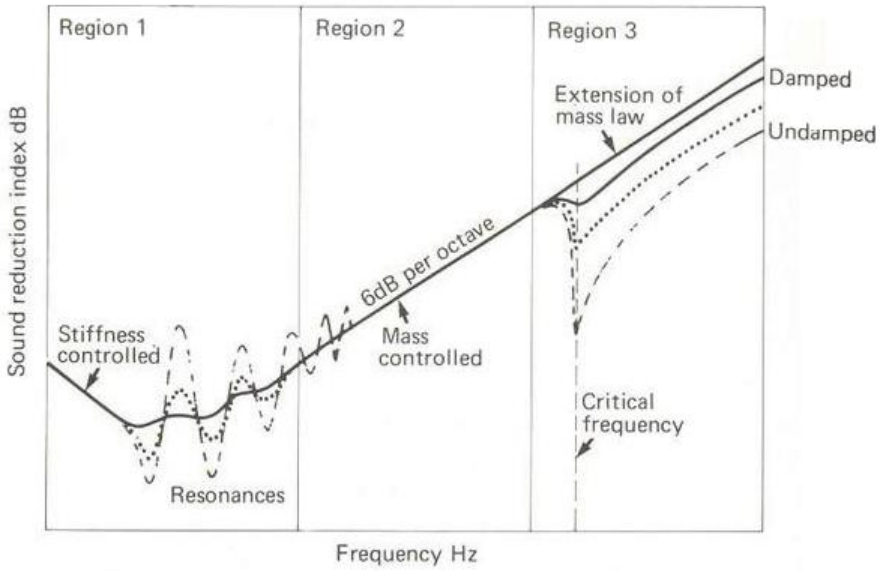


Figure 2.8: Mass law validity. [130]

The second region is where the mass law is valid with acceptable approximation.

In the last region the mass law is not valid anymore due to the coincidence of the bending wave velocity to the sound speed. This concept can be explained considering a wall response at different frequencies. In the second region, the wall under the effect of an acoustic field behaves as a big piston that pumps air to the other side without any particular vibration frequencies and the mass law is valid. At higher frequencies, the vibrations of the wall start to be in resonance with the air on the opposite side and the absorbing coefficient is strongly reduced. The *coincidence frequency* is a particular frequency that coincides with the beginning of the third region and indicates that the bending waves of the wall have same velocity as the speed of sound, so that a sound is generated on the other side of the wall. In other words this is the frequency where the wavelength of structural waves is the same as the wavelength of acoustic waves. The value of this frequency depends upon the Young's modulus, the thickness, the density of the panel, the sound speed of air and the presence of a damping system that reduces this effect and increase the reduction index. At higher frequencies the sound propagation is completely resonant and this phenomenon is repeated. An interesting area to study the coincidence frequency is on space-craft panels, where the variation of speed sound with altitude and the employment of honeycomb sandwich panels make it a complex phenomenon [100].

Figure 2.9 shows a schematic draft of the creation of the coincidence frequency. It should be noted that the incident and the bending wave sounds have different wavelengths, thus the noise perceived to the other side of the panel is different from the incoming noise.

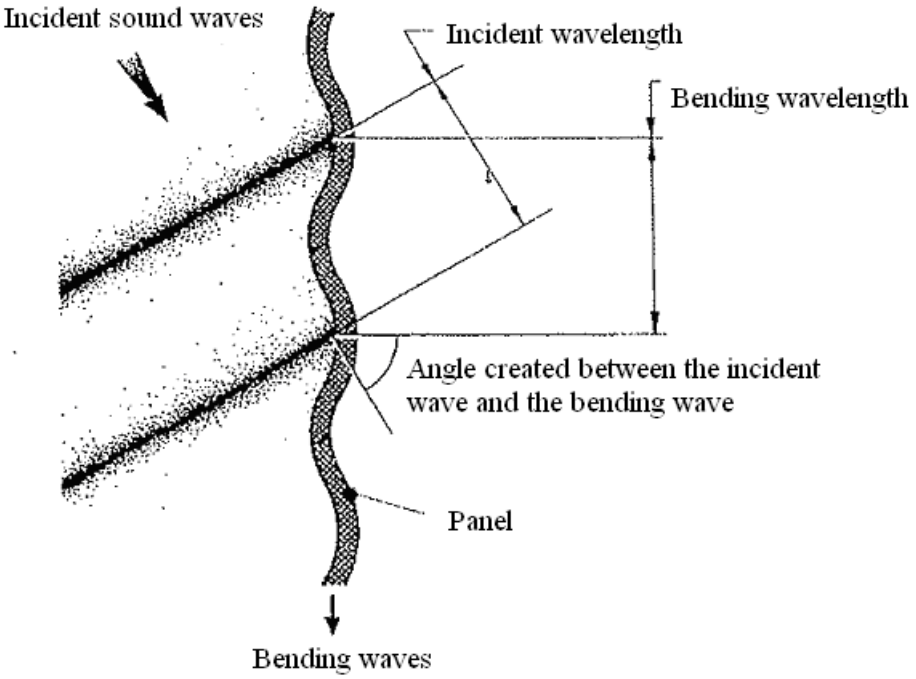


Figure 2.9: Coincident frequency.

Concerning the variety of absorbing materials, on the market there are three different options:

i) porous materials;

ii) vibrating panels;

iii) perforated materials.

The former are the most common materials used in industry and they include glass wool, foams and absorbent textiles. The incoming sound penetrates into the pores and the air contained vibrates. The acoustic energy is dissipated by the air viscosity and its contact with the boundary. The absorbing capability of a porous material depends upon its thickness that should be of the same order of the wavelength of the disturbance to be effective. An inadequate thickness yields an inefficient sound absorption. In aircraft

porous materials are inserted inside the structural frame in the trim panels. As evident, constraints limit this approach to be effective at bass frequencies such those generated by an engine.

The second kind is constituted by a regular shape panel installed at an appropriate distance from a wall. The system panel-air-wall constitutes a mass-spring like system that can reduce even bass sounds for appropriate dimensions of panel.

The last type of system is a panel where the surface is pierced and it is constituted by a series of layers: perforated material, porous materials, air and wall (see figure 2.10). The dimension, number and distance of the holes will characterize the behaviour of the panel that is selective at certain frequencies. Again the system constitutes a mass- spring like system.

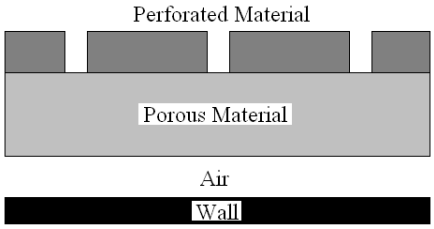


Figure 2.10: Perforated material.

Placing noise absorbing materials in optimal locations can significantly reduce the noise level. For instance, if there is an enclosure is disturbed by a noise with a particular mode, better performance is obtained if the absorbing material is located on the walls which form the end boundaries of the mode rather than on the side waveguide walls.

More details in PNC approach regards are given in Chapter 7.

2.6.2 Active Noise Control (ANC)

The ANC is a technique to reduce the unwanted noise at bass frequencies by altering the acoustic field in which the sound source operates.

Compression and rarefaction phases make up the sound wave components. The phenomenon generated by the interaction of the two wave sounds is called *interference*. As most commonly used, this term refers to the interaction of waves with similar frequencies and amplitudes. The noise reduction is achieved in the area where destructive interferences take place (the primary wave amplitude is around 180° degree out of phase respect to the secondary wave) at the expense of other areas where the noise level is higher due to constructive interferences (the primary and secondary source amplitudes have similar phase). Moreover, ANC feasibility and performance depends upon a series of variables that can be classified as follows:

1. control source arrangement;
2. error sensor placement;
3. reference signal quality;
4. quality of the controller software and hardware.

These variables are more relevant if noise reduction is required in global sense.

Control source arrangement mainly depends upon the field environment. In the free field case with primary noise emanated by a point source, the maximum possible acoustic power attenuation is given by Nelson *et al.* [93]. They established that a significant noise reduction level (more that 10 dB) can be achieved only if the distance between primary noise and secondary source, intended also as a point source, is less than $\lambda/10$. Practically, in free space ANC can be applied only to problems with periodic sounds, since a non-periodic noise requires the ANC system to be really fast in providing control field. However, even the fastest system requires at least 4-10 millisecond to

acquire the primary noise, evaluate the control field and create it. During this amount of time, well known as *group delay*, the sound wave covers a certain distance that is around 2 m considering the speed of sound 343 m/s. This means that 2 m is also the minimum distance between the microphone and loudspeaker, which makes such an approach almost unfeasible for non-periodic noises.

In enclosed space, ANC has the potential to provide global sound attenuation only if the response is classified as modal and the noise is tonal. Moreover, the control source does not have to be located close to the unwanted noise source and it can be located at almost any location (nodes of the modes must be avoided). This is quite different form the free field case. In cars, global ANC is not really effective due to the fact that the modal response ends at lower frequency than would be expected by dimensions alone because of the high level of acoustic damping inside the vehicle. This consideration limits the potential for active noise control to provide useful levels of global sound attenuation. A local approach is hence preferable and gives better results, even though 5-6 dB is the best reduction level achieved.

Noise reduction inside aircraft has driven research on ANC. In propeller-driver aircraft, rotating blades generate tonal and low disturbing noise, so that the response inside airplanes can still be classified as modal. In jet aircraft, the main limitation on applying active control technologies is that the frequency content of the noise is higher than that of propeller aircraft and so the response inside airplanes cannot be classified as modal. However, ANC can still be applied using a local approach by putting loudspeakers into passenger headrests.

Recently, many brand companies start to produce and sell active headphones. The control source is a small embed loudspeaker. The microphone is located inside the headphone, thus close to the control source. Hence, there is not the required minimum distance between control source and microphone to utilise such a system for random noise. However, headphones are effective, especially for periodic noises, since the cavity

between ear and headphone creates a regular sound field.

Finally, the number of error microphones and control sources that should be utilised for global ANC in enclosed space depends upon the specific application. However, an upper limit on the minimum number of source is equal to the number of modes which are excited in the target frequency band. On the other side, microphones have not to be located at the modal nodes and an effective approach is often to place them randomly.

The quality of the reference signal and the controller software and hardware are fundamental aspect of an ANC system. Nevertheless, a more complete description of the active noise control is beyond the scope of this chapter and can be found in [64, 91].

Summary

The linearised wave equation, also well-known as the equation of d'Alembert, has been obtained for an ideal fluid. In the present thesis the acoustic medium is considered to be continuum and only its macro-mechanic behaviour is considered. The frequency, the wave number, the angular frequency and the wavelength have been introduced as parameters that characterize the waves. The equation of state, the equation for the conservation of mass and the motion equation for ideal fluids have been presented and their explicit forms have been obtained. The linearised equation that describes the wave motion has been accomplished by considering a sound as a small perturbation in a fluid in its equilibrium state. Moreover, the medium has been hypothesized to be irrotational, hence uniform, and a potential function, i.e., the velocity potential, has been utilised to evaluate pressure and velocity of the fluid particle. The velocity potential also satisfies the wave motion that is then described by a single quantity. The sound propagation solution for one dimensional problem has been achieved. A series of important acoustic quantities, i.e., speed of sound, acoustic energy and intensity, sound pressure level and impedance have been introduced. Due to their fundamental

importance for the following chapters, the monopole and planewave sources have been presented. The human ear has been analysed and its different way of responding at different frequencies have been also explained. Finally, the noise control strategies for a direct reduction of noise, i.e., active and passive noise control, have been introduced.

In the Chapter 3, the wave equation of linear acoustics is recalled and utilised to formulate the boundary element method. In Chapter 5, the ANC is formulated to reduce unwanted noise using a local strategy, since a global noise attenuation is limited only for propeller-driven aircraft under certain conditions. Practical aspects for the proposed formulation are described based upon the considerations of this chapter. Finally, the basic concepts of passive noise strategies presented before are utilised in Chapter 7 for the numerical analysis, since the textile with high absorbing coefficient utilised as upholstery in the SEAT project is classified as porous material. Moreover, the performances at different frequencies of such a material follow the considerations described in figure 2.8.

Chapter 3

The Boundary Element Method

The development and proliferation of computer technologies in the last decades increased research interest in numerical methods to reduce the costs associated with experimental tests. In this regard, there are several techniques for solving both internal and external acoustic problems including modal expansions [71, 90], finite difference methods (FDM) [2] and meshfree methods [4, 20, 113]. However, the most popular and efficient techniques for engineering analyses are the Finite Element Method (FEM) and the Boundary Element Method (BEM).

The main advantage of the BEM over the FEM is related to the reduction in modelling effort. The FEM discretisation includes the whole domain of the problem, while the BEM requires only the discretisation of the boundary. Hence, the finite element leads to bigger system matrix than the BEM, but symmetric, sparse and banded, that grows almost linearly with the size of the problem. On the contrary, boundary element matrices are non-symmetric and fully populated and require N^2 storage, where N is the degree of freedom (d.o.f.) of the problem. A cost comparison between BEM and FEM in acoustics can be found in [66], where the FEM appears to possess a certain computational advantage. Nevertheless, the BEM seems to be more efficient than the FEM particularly if coupled with fast procedures such as the Fast Multipole Method

(FMM) and the Adaptive Cross Approximation (ACA).

Moreover, the case of unbounded problems makes the FEM prohibitive. Several techniques to overcome this drawback and to represent the infinite boundary condition have been investigated [65, 117]. By contrast, the BEM approach makes the method attractive, especially for problems with infinite domains. For this reason, one of the first development of the BEM was to lead with three dimensional acoustic problems.

Another substantial difference between FEM and BEM is based on evaluating the internal point quantities. In the FEM, these values are obtained directly by calculating the solution and they are located at the mesh points, whereas in the BEM they are evaluated after the analysis as post-processing and they can be located anywhere inside the domain without any restrictions.

The BEM and, in general, integral equation methods of boundary-value problems require the knowledge of the Green's functions (or fundamental solutions) of the examined problem. Their evaluation is obtained by the solution of the physical problem with infinite domain perturbed by a point source. The solution obtained is consequentially more accurate than other numerical methods that utilise polynomial expansions, such as the FEM.

The BEM takes its origin from the Integral Equation Method that was used for several decades to solve partial differential equations (PDE). The main limitation of the integral equation methods consists in the fact that only a limited class of problems with regular and elementary geometries can be solved by this analysis. The discretisation process and the use of matrix analyses, taken from the FEM, was the main innovation that permitted the evolution of the integral equation into the BEM.

A partial differential equation, relating variables of a physical problem in the domain and on its boundary, is mathematically represented by the Boundary Integral Equation Method (BIEM or BIE method) to integral equations governed only by boundary quantities. It should be noted that the BIE and BEM equations involve not only the

problem variables, but also their derivatives. Therefore the problem is solved by the boundary quantities and the values of quantities at domain points are evaluated with a post-processing stage.

Development of the BEM for acoustic application can be traced back to the early 1960s. Some of the pioneering works in this area are due to Shaw and Friedman (1962), Banaugh and Goldsmith (1963), Chen and Schweikert (1963) and Schenck (1967). During the period from 1960 and 1975, BEM or, BIEM, was developed by many researchers in two main areas, i.e., potential theory in perfect fluid flow for the aerospace industry and acoustics research, especially for underwater acoustics, supported by the U.S. Navy. The first conference was organized in June 1975 by Tom Cruse and Frank Rizzo [40] with name of "Boundary Integral Equation Method: Computational Application in Applied Mechanics". The "integral equation" nomenclature was maintained until 1978 after that Brebbia [24] organized a conference in 1976 with the name "Boundary Element Methods" in Southampton, U.K., and then a teaching text with the name "The Boundary Element Method for Engineers" [23].

In this chapter an overview of key mathematical expressions for the application of 3D Boundary Element Method to acoustics is presented. For further information the reader is referred to any of the general books on Acoustic BEM [23, 36, 123].

3.1 Helmholtz Equation

The wave equation (2.42) of linear acoustics is recalled

$$\nabla^2\phi - \frac{1}{c^2}\frac{\partial^2\phi}{\partial t^2} = \frac{1}{c^2}b \tag{3.1}$$

where ∇^2 is the Laplacian operator and b may contain the effect of noise source in the domain.

For time-harmonic wave motion we have

$$\phi(\mathbf{X},\, t) = u(\mathbf{X})e^{i\omega t} \tag{3.2}$$

where ω is the angular frequency, $u(\mathbf{X})$ is the velocity potential, a complex quantity, called here simply potential, and is related to the pressure by the following relation

$$p = -i\rho\omega u \tag{3.3}$$

The assumption (3.2) yields a simplification of the problem that can be studied only in terms of the space quantity $u(\mathbf{x})$ that transforms equation (3.3) into the *Helmholtz* equation

$$\nabla^2 u(\mathbf{X}) + k^2 u(\mathbf{X}) = \frac{1}{c^2} b \tag{3.4}$$

where $k = \omega/c$, with c sound velocity, is the wave number. The main advantage of the Helmholtz equation is that the number of independent variables is reduced by one. The above simplification is valid since in a real problem the transient effect is irrelevant due to the high speed of the sound velocity. Moreover, the time-space domain problem is transformed into a simply frequency space problem where the phase of a sound is referred to the origin and the whole sound distribution can be imagined by a combination of frozen waves. Then the presence of the quantity $e^{i\omega t}$ in equation (3.2) gives back the motion to the medium.

3.2 Boundary Conditions

In acoustics the boundary conditions (BCs) can be divided into three groups as follows

$$u(\mathbf{x}) = \overline{u}(\mathbf{x}) \qquad \mathbf{x} \in \Gamma_1 \tag{3.5a}$$

$$q(\mathbf{x}) = u(\mathbf{x})_{,n} = \overline{q}(\mathbf{x}) \qquad \mathbf{x} \in \Gamma_2 \tag{3.5b}$$

$$\overline{\alpha} u(\mathbf{x}) + \overline{\beta} q(\mathbf{x}) = \overline{\gamma} \qquad \mathbf{x} \in \Gamma_3 \tag{3.5c}$$

where Γ_1, Γ_2 and Γ_3 are three non-intersecting surfaces such that $\Gamma_1 \cup \Gamma_2 \cup \Gamma_3 = \Gamma$ with Γ boundary of the domain Ω under analysis, $\mathbf{n}(\mathbf{x})$ is the outward normal to the boundary at $\mathbf{x}$, q is the flux, comma indicates partial derivative and the barred quantities indicate prescribed values. The boundary condition (3.5a) is called Dirichlet, and can be referred to soft surfaces when $\overline{u}(\mathbf{x}) = 0$, the boundary condition (3.5b) Neumann, and can be referred to hard surfaces if $\overline{q}(\mathbf{x}) = 0$, and the boundary condition (3.5c) is the Robin mixed condition with $\overline{\alpha}$, $\overline{\beta}$ and $\overline{\gamma}$ non-zero constants that depend on the value of the impedance of the surfaces. Relationship (3.5c) can be also expressed as follows

$$q = -i\rho\omega \frac{u}{z} \tag{3.6}$$

with ρ the density of the medium and z the specific surface impedance.

3.3 Gauss' Theorem and Green's Identities

Before introducing the boundary integral equation a couple of well-known mathematical concepts are recalled, i.e., the Gauss' theorem, also known as the divergence theorem, introduced in the previous chapter, and the first two Green's identities.

Let us consider a vector field $\mathbf{V}$ and a volume Ω with boundary Γ. The Gauss' theorem establishes that the divergence of the vector $\mathbf{V}$ inside the volume Ω and the flux across the surface Γ are related as

$$\int_{\Omega} (\nabla \cdot \mathbf{V})\, d\Omega = \int_{\Gamma} (\mathbf{V} \cdot \mathbf{n})\, d\Gamma \tag{3.7}$$

This theorem can be seen as a conservation law in which the volume integral of the divergence is equal to the net flow across the volume's boundary.

The Green's identities are two corollaries of such a theorem. Assuming that the vector field can be expressed by the product between two potential functions in Ω yields

$$V_i = \phi \frac{\partial \psi}{\partial x_i}\,, \qquad\qquad i = 1,\, 2,\, 3 \tag{3.8}$$

where V_i is a component along one of the axes of the vector field, ϕ and ψ are the two potential functions that are twice and once continuously differentiable, respectively. By substituting equation (3.8) into equation (3.7) one obtains

$$\int_{\Omega} \frac{\partial}{\partial x_i} \left(\phi \frac{\partial \psi}{\partial x_i} \right) d\Omega = \int_{\Gamma} \phi \frac{\partial \psi}{\partial x_i}\, n_i\, d\Gamma \tag{3.9}$$

The integrand in the left hand side term of the above expression can be rewritten by utilising the chain rule as follows

$$\frac{\partial}{\partial x_i} \left(\phi \frac{\partial \psi}{\partial x_i} \right) = \frac{\partial \phi}{\partial x_i} \frac{\partial \psi}{\partial x_i} + \phi \nabla^2 \psi \tag{3.10}$$

hence the Green's first identity in (3.9) can be written as

$$\int_{\Omega} \frac{\partial \phi}{\partial x_i} \frac{\partial \psi}{\partial x_i} d\Omega + \int_{\Omega} \phi \nabla^2 \psi d\Omega = \int_{\Gamma} \phi \frac{\partial \psi}{\partial x_i}\, n_i\, d\Gamma \tag{3.11}$$

By considering that the potential function ψ is twice differentiable, the two functions ϕ and ψ can be interchanged in the above identity

$$\int_{\Omega} \frac{\partial \psi}{\partial x_i} \frac{\partial \phi}{\partial x_i} d\Omega + \int_{\Omega} \psi \nabla^2 \phi d\Omega = \int_{\Gamma} \psi \frac{\partial \phi}{\partial x_i} n_i \, d\Gamma \tag{3.12}$$

and by subtracting equation (3.11) from (3.12), i.e.,

$$\int_{\Omega} (\psi \nabla^2 \phi - \phi \nabla^2 \psi) d\Omega = \int_{\Gamma} \left(\psi \frac{\partial \phi}{\partial n} - \phi \frac{\partial \psi}{\partial n} \right) d\Gamma \tag{3.13}$$

the well known Green's second identity is obtained, where the partial derivative of the two functions ϕ and ψ with respect to x_i in the right hand side term multiplied by the i-component of the normal n has been substituted by the partial derivative of the same quantity with respect to n.

3.4 Fundamental Solutions

The fundamental solution to the Helmholtz differential equation corresponds to the field generated by a unit concentrated harmonic source.

Consider the Helmholtz differential equation where the following right hand side term b is a Dirac delta function δ centred in $\mathbf{X}'$, i.e.,

$$\nabla^2 u^*(\mathbf{X}', \mathbf{X}) + k^2 u^*(\mathbf{X}', \mathbf{X}) = -\delta(\mathbf{X}', \mathbf{X}) \tag{3.14}$$

where upper case $\mathbf{X}'$ and $\mathbf{X}$ denote source and field point, respectively, inside the domain.

In mathematics the solution of an inhomogeneous differential equation, such as (3.14), over an unbounded domain perturbed by a Dirac delta function δ is the so-called fundamental solution. In the wave propagation problem, which is a potential problem, over a unbounded, homogeneous and isotropic medium, the fundamental solution produces a spherical wave centred at the point source which can be written as [45, 123]

$$u^*(\mathbf{X}', \mathbf{X}) = -\frac{i}{4} H_0^{(1)}(kr) \tag{3.15}$$

for a two dimension (2D) domain, where $H_0^{(1)}$ is the Hankel function of the first kind of order zero, and

$$u^*(\mathbf{X}', \mathbf{X}) = \frac{1}{4\pi r}\, e^{-ikr} \tag{3.16}$$

for the three dimension (3D) case. In both fundamental solutions (3.15) and (3.16) r is the distance between the field point and the point source, i.e., $r = |\mathbf{X} - \mathbf{X}'|$. In case $\mathbf{X} \in \Gamma$, a normal derivative of the potential fundamental solution, the flux, can be evaluated as follows

$$q^*(\mathbf{X}', \mathbf{X}) = \frac{\partial u^*(\mathbf{X}', \mathbf{X})}{\partial n} = \frac{ik}{4} H_1^{(1)}(kr) r_{,n} \tag{3.17}$$

for 2D problems,

$$q^*(\mathbf{X}', \mathbf{X}) = \frac{\partial u^*(\mathbf{X}', \mathbf{X})}{\partial n} = -\frac{1}{4\pi r} \left(ik + \frac{1}{r} \right) e^{-ikr} r_{,n} \tag{3.18}$$

for 3D problems, where $H_1^{(1)}$ is the Hankel function of the first kind of order one and $r_{,n}$ is the partial derivative of r with respect to the normal n that is defined as follows

$$r_{,n} = \frac{\partial r}{\partial n} = \frac{r_i n_i}{r} \tag{3.19}$$

The present thesis is focused on the 3D wave propagation problem. The above fundamental solutions are equally valid for the source and field point on the boundary.

3.5 Boundary Integral Equation

In order to evaluate the boundary integral equation, the second Green's identity is written for two potential functions u and u^*, which are the generic potential solution of the homogeneous Helmholtz equation in any domain and the fundamental solution, respectively, as

$$\int_\Omega (u\nabla^2 u^* - u^*\nabla^2 u)\, d\Omega = \int_\Gamma \left(u\frac{\partial u^*}{\partial n} - u^*\frac{\partial u}{\partial n} \right) d\Gamma \tag{3.20}$$

Substituting equations (3.14) and (3.4) with $b = 0$ into the left hand side of the above identity yields the following

$$\int_\Omega (u\nabla^2 u^* - u^*\nabla^2 u)\, d\Omega = \int_\Omega u(\nabla^2 u^* + k^2 u^*)\, d\Omega = -\int_\Omega u\, \delta(\mathbf{X}', \mathbf{X})\, d\Omega = -u(\mathbf{X}') \tag{3.21}$$

Hence equation (3.20) can be written as follows

$$u(\mathbf{X}') = \int_\Gamma u^*(\mathbf{X}', \mathbf{x}) \frac{\partial u(\mathbf{x})}{\partial n}\, d\Gamma - \int_\Gamma u(\mathbf{x}) \frac{\partial u^*(\mathbf{X}', \mathbf{x})}{\partial n}\, d\Gamma \tag{3.22}$$

or

$$u(\mathbf{X}') = \int_\Gamma u^*(\mathbf{X}', \mathbf{x}) q(\mathbf{x})\, d\Gamma - \int_\Gamma u(\mathbf{x}) q^*(\mathbf{X}', \mathbf{x})\, d\Gamma \tag{3.23}$$

The above equation is the Boundary Integral Equation (BIE). The value of the potential at any point requires the potential $u(\mathbf{x})$ and flux $q(\mathbf{x})$ at the point $\mathbf{x}$ and to calculate the fundamental solutions. In a generic problem these last values are chosen to be the values at the boundary points. The boundary conditions (3.5) provide half of these values, hence the problem is now focused on finding the unknown values. Equation (3.23) can be written at the boundary points $\mathbf{x}'$, but some singularities, that need special

treatments, arise due to the fundamental solutions. Therefore, let us consider the case as $\mathbf{X}' \to \mathbf{x}'$ on the boundary. The boundary is divided into two parts, i.e., a hemi-sphere of radius "ε" and the remaining boundary, as shown in figure 3.1.

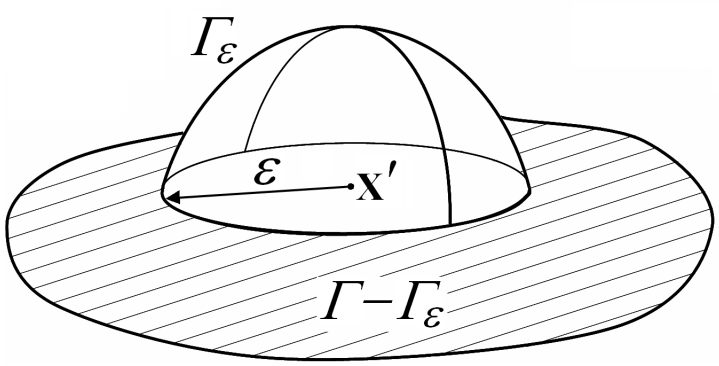


Figure 3.1: Boundary divided into two parts: Γ_ε, hemi-sphere centred at $\mathbf{x}'$; $\Gamma_\varepsilon - \Gamma$, remaining geometry.

The point $\mathbf{x}'$ is considered to be at the centre of the hemi-sphere, so that the radius "ε" tends to zero for $\mathbf{X}' \to \mathbf{x}'$ and $\mathbf{x} \to \mathbf{x}'$. In the following derivation for simplicity a smooth boundary is assumed. Each integral in equation (3.23) is analysed separately and decomposed into two parts, one being the integral at the boundary $\Gamma - \Gamma_\varepsilon$ and the other at the boundary Γ_ε. Hence, the first integral can be written as follows

$$\lim_{\varepsilon \to 0} \int_{\Gamma - \Gamma_\varepsilon + \Gamma_\varepsilon} u^*(\mathbf{x}', \mathbf{x}) q(\mathbf{x})\, d\Gamma = \lim_{\varepsilon \to 0} \left(\int_{\Gamma - \Gamma_\varepsilon} u^*(\mathbf{x}', \mathbf{x}) q(\mathbf{x})\, d\Gamma + \int_{\Gamma_\varepsilon} u^*(\mathbf{x}', \mathbf{x}) q(\mathbf{x})\, d\Gamma \right) \tag{3.24}$$

The second integral on the right hand side of (3.24), however, contains a singularity and must be evaluated by using a limiting form as

$$\lim_{\varepsilon \to 0} \int_{\Gamma_\varepsilon} u^*(\mathbf{x}', \mathbf{x}) q(\mathbf{x})\, d\Gamma = \lim_{\varepsilon \to 0} \int_{\Gamma_\varepsilon} \frac{1}{4\pi\varepsilon}\, e^{-ik\varepsilon} q(\mathbf{x}')\, d\Gamma = q(\mathbf{x}') \lim_{\varepsilon \to 0} \int_{\Gamma_\varepsilon} \frac{1}{4\pi\varepsilon}\, e^{-ik\varepsilon}\, d\Gamma \tag{3.25}$$

where the value of the flux at the point $\mathbf{x}'$ has been placed outside the integral for being constant. Integrating over the hemi-sphere requires a change of the integral variables, from the Cartesian to the polar system, and generates a Jacobian of order ε^2 that vanishes the integral value.

$$q(\mathbf{x}') \lim_{\varepsilon \to 0} \int_{\Gamma_\varepsilon} \frac{1}{4\pi\varepsilon} e^{-ik\varepsilon} \, d\Gamma = q(\mathbf{x}') \lim_{\varepsilon \to 0} \int_0^\pi \int_0^\pi \frac{1}{4\pi\varepsilon} e^{-ik\varepsilon} \varepsilon^2 \sin\varphi \, d\theta \, d\varphi = 0 \tag{3.26}$$

The second right hand side integral of equation (3.23) can now be evaluated and written as follows

$$\lim_{\Gamma_\varepsilon \to 0} \int_{\Gamma - \Gamma_\varepsilon + \Gamma_\varepsilon} u(\mathbf{x}) q^*(\mathbf{x}', \mathbf{x}) \, d\Gamma = \lim_{\varepsilon \to 0} \left(\int_{\Gamma - \Gamma_\varepsilon} u(\mathbf{x}) q^*(\mathbf{x}', \mathbf{x}) \, d\Gamma + \int_{\Gamma_\varepsilon} u(\mathbf{x}) q^*(\mathbf{x}', \mathbf{x}) \, d\Gamma \right) \tag{3.27}$$

where the first resulting integral is not singular and its value is understood in the sense of the Cauchy principal value.

The value of the second integral in equation (3.27) can be calculated as previously seen by the explicit value of the fundamental solution

$$\lim_{\varepsilon \to 0} \int_{\Gamma_\varepsilon} u(\mathbf{x}) q^*(\mathbf{x}', \mathbf{x}) \, d\Gamma = -u(\mathbf{x}') \lim_{\varepsilon \to 0} \left(\int_{\Gamma_\varepsilon} \frac{1}{4\pi\varepsilon} ik e^{-ik\varepsilon} \varepsilon_{,n} \, d\Gamma + \int_{\Gamma_\varepsilon} \frac{1}{4\pi\varepsilon^2} e^{-ik\varepsilon} \varepsilon_{,n} \, d\Gamma \right) \tag{3.28}$$

The first resulting integral is zero since it has the same order of the integral in equation (3.26), and the last integral is evaluated as follows

$$-u(\mathbf{x}') \lim_{\varepsilon \to 0} \int_{\Gamma_\varepsilon} \frac{1}{4\pi\varepsilon^2} e^{-ik\varepsilon} \varepsilon_{,n} \, d\Gamma = -u(\mathbf{x}') \lim_{\varepsilon \to 0} \int_0^\pi \int_0^\pi \frac{1}{4\pi\varepsilon^2} e^{-ik\varepsilon} \varepsilon_{,n} \, \varepsilon^2 \sin\varphi \, d\theta \, d\varphi \tag{3.29}$$

Now, the limit of $\varepsilon_{,n}$ is equal to one, hence the relation

$$u(\mathbf{x}') \lim_{\varepsilon \to 0} \frac{e^{-ik\varepsilon}}{4\pi} \left[\cos\varphi\right]_0^{\pi} \left[\theta\right]_0^{\pi} = -\frac{1}{2} u(\mathbf{x}') \tag{3.30}$$

Finally, the BIE at the boundary points is written as follows

$$\frac{1}{2} u(\mathbf{x}') = \int_{\Gamma} u^*(\mathbf{x}', \mathbf{x}) q(\mathbf{x})\, d\Gamma - \int_{\Gamma} u(\mathbf{x}) q^*(\mathbf{x}', \mathbf{x})\, d\Gamma \tag{3.31}$$

that is valid on a smooth boundary and can be generalized at any point of the boundary Γ with any smoothness by introducing a coefficient $c(\mathbf{x}')$

$$c(\mathbf{x}') u(\mathbf{x}') = \int_{\Gamma} u^*(\mathbf{x}', \mathbf{x}) q(\mathbf{x})\, d\Gamma - \int_{\Gamma} u(\mathbf{x}) q^*(\mathbf{x}', \mathbf{x})\, d\Gamma \tag{3.32}$$

where

$$c(\mathbf{x}') = \tfrac{\alpha}{4\pi} \quad with \quad 0 \leq \alpha \leq 4\pi \tag{3.33}$$

with α being the internal solid angle of the boundary at the point $\mathbf{x}'$.

An extra term, $P_t(\mathbf{x}', \mathbf{X}^s)$, can be included into both equations (3.23) and (3.32) to include the presence of extra-sources inside the domain Ω such as monopole, with

$$P_t(\mathbf{x}', \mathbf{X}^s) = B\, u^*(\mathbf{x}', \mathbf{X}^s) \tag{3.34}$$

or plane-waves, with

$$P_t(\mathbf{x}') = B\, e^{ik\hat{e}_k \cdot \mathbf{x}'} \tag{3.35}$$

where B is the strength of the source, $\hat{e}_k$ is the unitary direction of the plane-wave and $\mathbf{X}^s$ is the location of the monopole.

3.6 Numerical Implementation

A convenient method of solution for the boundary integral equation is point collocation. Here, the integral equation is evaluated at the point $\mathbf{x}'_j$ to give equation (3.32), where $j = 1, \ldots N_p$ and N_p is the total number of points.

For application of BEM to complex problems it is necessary to discretise the geometry using shape functions or interpolating function similar to those used in the finite element method. Depending on the choice of shape function representation for the geometry parameter $\mathbf{x}$ and the unknown functions $u(\mathbf{x})$ and $q(\mathbf{x})$, different formulations are achieved. In isoparametric formulation the same shape function is used for both the geometry and the unknown functions. If the shape function used for the geometry is higher order polynomial than that used for the geometry the formulation is referred as superparametric and in the contrary case one refers to subparametric formulation.

Dividing the surface of the problem into Ne elements yields the following

$$c(\mathbf{x}'_j)u(\mathbf{x}'_j) = \sum_{i=1}^{Ne} \left(\int_{\Gamma_i} u^*(\mathbf{x}'_j, \mathbf{x}_i) q_i(\mathbf{x})\, d\Gamma(\mathbf{x}_i) - \int_{\Gamma_i} u_i(\mathbf{x}) q^*(\mathbf{x}'_j, \mathbf{x}_i)\, d\Gamma(\mathbf{x}_i) \right) \tag{3.36}$$

3.6.1 Boundary Discretisation using Shape Functions

In this thesis constant elements for unknown functions with linear elements for the geometry are considered as superparametric formulation and nine node quadratic elements are used for isoparametric formulation.

In the literature there are different shapes and orders that are utilised for the discretisation process. For example figure 3.2 shows six different types of elements, divided into two different shapes, i.e., triangular/quadrilateral, and three orders, i.e., constant/linear/quadratic. The constant element is constituted only by a single node, the linear and the quadratic by 3 and 6 nodes, respectively, in case of triangular ele-

ments, and by 4 and 9 nodes for quadrilateral elements, respectively.

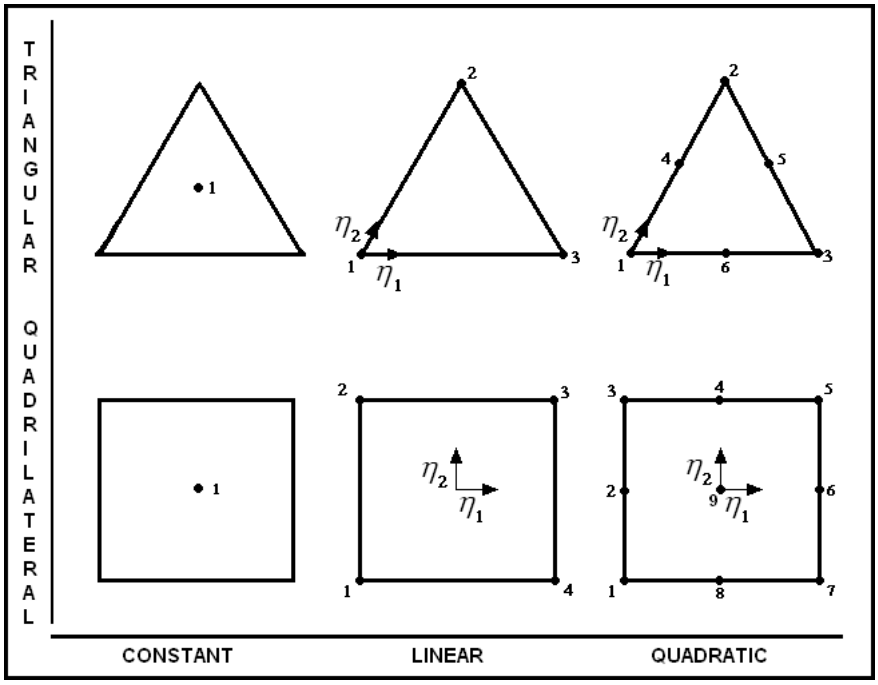


Figure 3.2: Triangular/quadrilateral elements: constant, linear and quadratic.

In acoustic simulations, the order and number of elements that discretise the variables depends upon the frequency. For quadratic elements at least two elements per wavelength are required, for linear at least four elements and for constant at least eight elements per wavelength [38].

Superparametric Constant Elements The superparametric constant elements are utilised when the geometry is discretised using linear elements and the field variables are constant along each element and referred to the centre of the element. Hence, equation (3.36) can be rewritten as follows

$$c(\mathbf{x}'_j)u(\mathbf{x}'_j) = \sum_{i=1}^{Ne} \left(q_i \int_{\Gamma_i} u^*(\mathbf{x}'_j, \mathbf{x}_i)\, d\Gamma_i - u_i \int_{\Gamma_i} q^*(\mathbf{x}'_j, \mathbf{x}_i)\, d\Gamma_i \right) \tag{3.37}$$

The evaluation of the two integrals in the above equation requires a local coordinate system (η_1, η_2). For quadrilateral elements the local system is defined as $-1 \leq \eta_1 \leq 1$ and $-1 \leq \eta_2 \leq 1$, whereas for triangular as $0 \leq \eta_1 \leq 1$ and $0 \leq \eta_2 \leq 1$. The resulting right hand side integral of equation (3.37) can be evaluated as follows

$$c(\mathbf{x}'_j)u(\mathbf{x}'_j) = \sum_{i=1}^{Ne} \left(q_i \int_{\eta_2} \int_{\eta_1} u^*(\mathbf{x}'_j, \mathbf{x}(\eta_1, \eta_2)) \mathbf{J}(\eta_1, \eta_2)\, d\eta_1 d\eta_2 \right) - \sum_{i=1}^{Ne} \left(u_i \int_{\eta_2} \int_{\eta_1} q^*(\mathbf{x}'_j, \mathbf{x}(\eta_1, \eta_2)) \mathbf{J}(\eta_1, \eta_2)\, d\eta_1 d\eta_2 \right) \quad (3.38)$$

where $\mathbf{J}(\eta_1, \eta_2)$ is the Jacobian of the transformation can be in general be written as

$$\mathbf{J}(\eta_1, \eta_2) = \sqrt{J_1^2 + J_2^2 + J_3^2} \quad (3.39)$$

with

$$J_1 = \frac{\partial x_2}{\partial \eta_1}\frac{\partial x_3}{\partial \eta_2} - \frac{\partial x_3}{\partial \eta_1}\frac{\partial x_2}{\partial \eta_2}, \qquad J_2 = \frac{\partial x_1}{\partial \eta_1}\frac{\partial x_3}{\partial \eta_2} - \frac{\partial x_3}{\partial \eta_1}\frac{\partial x_1}{\partial \eta_2}, \qquad J_3 = \frac{\partial x_1}{\partial \eta_1}\frac{\partial x_2}{\partial \eta_2} - \frac{\partial x_2}{\partial \eta_1}\frac{\partial x_1}{\partial \eta_2}$$

It should be noted that the Jacobian is constant for constant elements, hence, it does not depend upon η_1 and η_2.

The component of the outward normal can be evaluated by these values, i.e., $n_j = J_j/\mathbf{J}$. Equation (3.38) can be rewritten in a compact form

$$c(\mathbf{x}'_j)u(\mathbf{x}'_j) + \sum_{i=1}^{Ne} H_{ji} u_i = \sum_{i=1}^{Ne} G_{ji} q_i \quad (3.40)$$

where H_{ji} and G_{ji} correspond to the integrals of equation (3.38).

Iso-Sub-Super-parametric Linear and Quadratic Elements The right hand side integrals in equation (3.36) can be evaluated by utilising different order shape functions for both the geometry and field variables.

Let us assume that the $i{-}th$ element is composed by Nn nodal points. Thus the potential $u_i(\mathbf{x})$ and flux $q_i(\mathbf{x})$ can be evaluated using the nodal values as follows

$$u_i = \varphi^k(\eta)\, u_i^k \tag{3.41a}$$

$$q_i = \varphi^k(\eta)\, q_i^k \tag{3.41b}$$

with $k = 1, 2, \ldots Nn$, u_i^k and q_i^k are the value of the potential and flux at the $k{-}th$ nodal point, respectively, and $\varphi^k(\eta)$ is the interpolation of the shape function. Any location, $\mathbf{x}_i$, in the $i{-}th$ element may be approximated by a similar procedure

$$\mathbf{x}_i = \varphi^k(\eta)\, \mathbf{x}_i^k \tag{3.42}$$

where $\mathbf{x}_i^k$ is the location of the $k{-}th$ nodal point.

The shape functions for 2D and 3D problems with different orders (zero, one, two, etc.) can be easily found in the literature and are referred to the local coordinate system (η_1, η_2). As previously seen for the superparametric constant elements, the final integral values of equation (3.36) are evaluated through the Jacobian.

Nevertheless, the nodes of each element are assigned in a particular order. With reference to figure 3.2, the nodes must be numbered as shown for external problems, whereas for internal problems the number order must be anticlockwise.

3.6.2 Matrix Assembly using the Collocation Method

The isoparametric boundary element formulation for linear and higher order elements can be written as

$$c(\mathbf{x}'_j)u(\mathbf{x}'_j) = \sum_{i=1}^{Ne}\left(\sum_{k=1}^{Nn} q_i^k \int_{\eta_2}\int_{\eta_1} \varphi^k u^*(\mathbf{x}'_j, \mathbf{x}_i^k(\eta_1,\eta_2))\mathbf{J}_i(\eta_1,\eta_2)\, d\eta_1 d\eta_2\right)$$

$$-\sum_{i=1}^{Ne}\left(\sum_{k=1}^{Nn} u_i^k \int_{\eta_2}\int_{\eta_1} \varphi^k q^*(\mathbf{x}'_j, \mathbf{x}_i^k(\eta_1,\eta_2))\mathbf{J}_i(\eta_1,\eta_2)\, d\eta_1 d\eta_2\right) \tag{3.43}$$

where Nn is the total number of nodes in $i-th$ element.

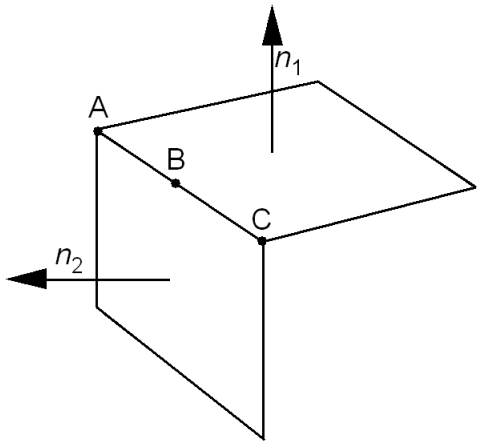


Figure 3.3: Border nodes belonging to two different elements.

The 3D fundamental solutions (3.16) and (3.18) are evaluated at each of the Nn nodes and at each of the Ne elements of the boundary. In assembly of the system of equations, some care must be taken with the values of flux at corners. The double sum in (3.43) must be evaluated considering that some nodes are shared between elements, and the potential values are uniquely defined at these nodes so that they are combined to give a sum over all the nodes, whereas the flux values are not uniquely defined at corners (see figure 3.3) and take a different value depending on the element orientation. The different value of flux is due to the non-uniqueness of the outward normal at corners. There have been developed different methods to overcome this problem [45, 123]. Here, we adopt an assembly strategy that would allow, for different prescribed values of flux,

to collect the flux values at an element by the element bases. Following the above strategy equation (3.43) can be rewritten as follows

$$c(\mathbf{x}'_j)u(\mathbf{x}'_j) + \sum_{\gamma=1}^{N} \tilde{H}_{j\gamma} u_\gamma = \sum_{i=1}^{Ne} G_{ji} q_i \,, \qquad j = 1, \ldots N \tag{3.44}$$

where N is the total number of nodes that constitute the discretised boundary, $\tilde{H}_{jk}$ is made up from the first integral in the double sum in (3.43) and G_{jk} represents the second double integral in (3.43).

Calling

$$H_{j\gamma} = \tilde{H}_{j\gamma} + \delta_{j\gamma}\, c(\mathbf{x}'_j) \tag{3.45}$$

with δ_{ji} Kronecker delta, one obtains

$$\sum_{\gamma=1}^{N} H_{j\gamma} u_\gamma = \sum_{i=1}^{Ne} G_{ji} q_i \tag{3.46}$$

that is valid for the node j and it is similar to equation (3.40).

A collocation technique can now be applied to all the nodal points and elements of the discretised boundary and yields a system of N equations that can be written under the following matrix notation

$$\mathbf{Hu} = \mathbf{Gq} \tag{3.47}$$

where $\mathbf{H}$ is a $N \times N$ square matrix, $\mathbf{G}$ a $N \times Ne$ rectangular matrix, $\mathbf{u}$ a $N \times 1$ potential vector and $\mathbf{q}$ a $Ne \times 1$ flux vector. The presence of extra sources as in equations (3.34) and (3.35) can be also included by adding a $N \times 1$ vector $\mathbf{p}$ that collects all contributions of such sources to all the collocation nodes.

$$\mathbf{Hu} = \mathbf{Gq} + \mathbf{p} \tag{3.48}$$

Substituting the boundary conditions (3.5) into the above system results in a new system of algebraic equation that can be written in a matrix form as follows

$$\mathbf{AY} = \mathbf{F} \tag{3.49}$$

where $\mathbf{Y}$ is the vector containing the unknown boundary potentials and fluxes, $\mathbf{A}$ is a coefficient matrix which is non-symmetric and densely populated, and $\mathbf{F}$ is obtained by multiplying the prescribed BCs by the corresponding columns of the $\mathbf{G}$ and $\mathbf{H}$ matrices.

The system of equations (3.49) can be solved by a direct approach evaluating the value of the inverse of $\mathbf{A}$. The drawback of this approach is that it is time consuming, requiring $O(N^3)$ operations, where N denotes the total degrees of freedom of the problem, and $O(N^2)$ storage space. To overcome these difficulties different approaches have been investigated using block-based solvers [39, 101], lumping technique [76] and iterative solvers [87]. A more detailed discussion on this subject is presented in the next chapter.

3.7 Internal Points

Once the system (3.49) is solved, the value of the potential and particle velocity (defined as the derivative of the potential along three axes of the coordinate system) at the internal points ($\mathbf{X}'_j$) can be calculated.

From now on the upper case U indicates the potential at internal points. Using the boundary values of the potential and flux, and using the discretised form of equation (3.23) this value is evaluated as follows

$$U(\mathbf{X}'_j) = -\sum_{\gamma=1}^{N} \overline{H}_{j\gamma} u_\gamma + \sum_{i=1}^{Ne} \overline{G}_{ji} q_i + P(\mathbf{X}'_j, \mathbf{X}^{\mathbf{s}}) \tag{3.50}$$

where $\overline{H}_{ji}$ and $\overline{G}_{jk}$ correspond to the integrals involving the potential and flux funda-

mental solutions, respectively, and $P(\mathbf{X}'_j,\, \mathbf{X^s})$ refers to the presence of extra sources. Furthermore, the potential vector $\mathbf{U}$ at NI internal points can be evaluated by NI equations as follows

$$\mathbf{U} = -\overline{\mathbf{H}}\mathbf{u} + \overline{\mathbf{G}}\mathbf{q} + \mathbf{P} \tag{3.51}$$

where $\overline{\mathbf{H}}$ and $\overline{\mathbf{G}}$ are similar to $\mathbf{H}$ and $\mathbf{G}$, but evaluated at internal points and $\mathbf{P}$ is a $NI \times 1$ vector that collects the contribution of the extra sources to the potential at the internal points.

The particle velocity at an internal point $\mathbf{X}'_j$ can be evaluated by differentiating equation (3.23) as follows

$$\frac{\partial}{\partial \mathbf{X}'_i} U(\mathbf{X}'_j) = \int_\Gamma \frac{\partial u^*(\mathbf{X}', \mathbf{x})}{\partial \mathbf{X}'_i}\, q(\mathbf{x})\, d\Gamma - \int_\Gamma u(\mathbf{x})\, \frac{\partial q^*(\mathbf{X}', \mathbf{x})}{\partial \mathbf{X}'_i}\, d\Gamma + P'(\mathbf{X}'_j,\, \mathbf{X^s})\,, \qquad i = 1,\, 2,\, 3 \tag{3.52}$$

where $P'(\mathbf{X}'_j,\, \mathbf{X^s})$ refers to the contribution of the extra sources to the particle velocity at the internal points. The derivative of the two fundamental solutions for the 3D case can be evaluated as follows

$$\frac{\partial}{\partial \mathbf{X}'_i} u^*(\mathbf{X}', \mathbf{x}) = \frac{\partial u^*}{\partial r}\frac{\partial r}{\partial \mathbf{X}'_i} = -\frac{1}{4\pi r^2}(1 + ikr)\mathbf{e}^{-ikr}\frac{\partial r}{\partial \mathbf{X}'_i}$$

$$\frac{\partial}{\partial \mathbf{X}'_i} q^*(\mathbf{X}', \mathbf{x}) = \frac{\partial q^*}{\partial r}\frac{\partial r}{\partial \mathbf{X}'_i} = \frac{1}{4\pi r^3}[(2 + 2ikr - k^2r^2)r_{,n}\frac{\partial r}{\partial \mathbf{X}'_i} - (r + ikr^2)\frac{\partial r_{,n}}{\partial \mathbf{X}'_i}]\mathbf{e}^{-ikr} \tag{3.53}$$

Thus, the particle velocities vector $\mathbf{U}'$ at NI internal points can be evaluated as follows

$$\mathbf{U}' = -\overline{\mathbf{H}}'\mathbf{u} + \overline{\mathbf{G}}'\mathbf{q} + \mathbf{P}' \tag{3.54}$$

where $\overline{\mathbf{H}}'$ and $\overline{\mathbf{G}}'$ are $NI \times N$ and $NI \times Ne$ matrices, respectively, containing the derivatives of the fundamental solutions with respect to $\mathbf{X}'_i$ and $\mathbf{P}'$ is a $NI \times 1$ vector generated by $P'(\mathbf{X}'_j, \mathbf{X}^{\mathbf{s}})$.

It should be noted that the coefficients of the matrices in the systems (3.51) and (3.54) are evaluated by the standard Gaussian quadrature.

3.8 Fictitious Frequency and Spurious Eigenvalue Problems

The integral equation methods of boundary-value problems governed by the Helmholtz equation are well-known to have non-unique solutions at certain wavenumbers. In this regard one refers to fictitious frequency, for exterior acoustics, and spurious eigenvalue, for internal acoustics [27, 108]. Both problems stem from the rank deficiency of the matrix.

Schenck [108] showed that the fictitious frequency occurs when solving the boundary Helmholtz integral equation at the natural frequencies of the associated interior Dirichlet problem. At the fictitious frequencies both matrices $\mathbf{H}$ and $\mathbf{G}$ of equation (3.47) are singular and the solution is not unique [34]. In order to remove the non-uniqueness at the fictitious frequencies, Burton and Miller [27] proposed to solve the problem by combining singular and hypersingular equations with an imaginary number. The hypersingular integrals involving the formulation are the main difficulty for this approach. To avoid this computation effort, Schenck [108] proposed an alternative method that adds some additional Helmholtz integral relations evaluated in the interior region. The method is commonly referred to with the acronym CHIEF (Combined Helmholtz Integral Equation Formulation). In the BIEM discretised form, the CHIEF consists of adding an auxiliary constraint to promote the rank of influence matrices by

collocating at a point outside the domain, where the potential is zero. Nodal points of the corresponding interior eigenmode should be avoided, which in general is not difficult as pointed out by Seybert and Rengarajan [109].

Spurious eigenvalues are not present for the complex-valued BEM in a simply connected problem [33, 115]. However, in multiply connected domains spurious eigenvalues always appear, even for a complex-valued BEM formulation. Many approaches have been successfully applied to deal with the spurious solution, including residue method [32], generalized singular value decomposition [80], singular value decomposition updating terms [57], combined Helmholtz exterior integral equation formulation (CHEEF) method [30] and Burton-Miller method considering only the real-part formulation [31].

For further information the reader can find in [16] a complete overview of such methods with accuracy and efficiency comparisons.

In the present thesis, fictitious frequencies are simply avoided, whereas spurious eigenvalues never appear since no multiply connected domains are utilised for interior problems.

3.9 Benchmark Examples

In this section the boundary element method presented in earlier sections is tested against some simple benchmark problems to assess its accuracy and efficiency.

3.9.1 Pulsating Sphere

The analytical solution in terms of pressure p for the sound radiated by a uniform radiating pulsating sphere with velocity q_r at a point with distance d from the centre of the sphere with radius a is given as follows [95]

$$p(d) = \frac{a}{d} q_r \rho_0 c \frac{-ika}{1+ika} e^{ik(d-a)} \tag{3.55}$$

where ρ_0 is the medium density. To determine the pressure on the surface of the sphere and to make the study as simple as possible, the radius a, distance d, normal uniform radial vibrating velocity q_r and acoustic impedance $\rho_0 c$ are all considered equal to unity. Henceforth (and if not otherwise specified) the other simulations use identical values.

Two different superparametric and isoparametric meshes are used. The first has 1126 triangular elements with linear variation for geometry and constant for the unknown functions (T1126) and the second has 24 quadrilateral elements with 98 nodes (S24) (see figure 3.4). The maximum wave number k that can be studied by both meshes, T1126 and S24, is almost the same [38].

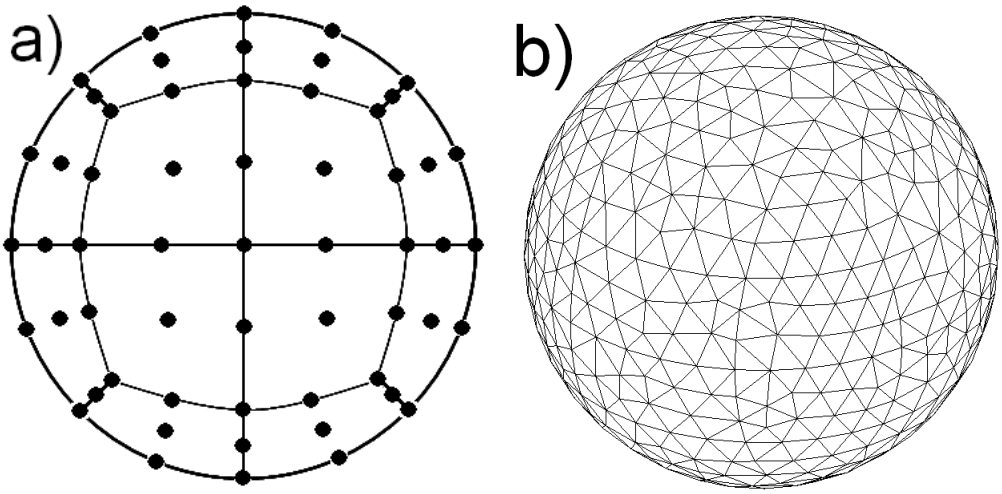


Figure 3.4: Sphere discretised into: a) 24 isoparametric quadratic quadrilateral elements and b) 1126 constant elements.

The effect of a pulsating sphere can be described by the BEM using the Neumann BCs with unitary value for all the boundary elements.

In table 3.1 the pressure obtained by the BEM approach using constant T1126 and quadratic elements S24 are presented. As expected both BEM solutions are in close agreement with the analytical values for all the wave numbers k. It should be noted that the solution of the S24 is obtained 35 time faster than the solution of the T1126.

Wave	Analytical Solution		Quadratic BEM S24		Constant BEM T1126	
num. k	Real part	Imag. part	Real part	Imag. part	Real part	Imag. part
1	0.5000	0.5000	0.5000	0.4999	0.4983	0.5005
2	0.8000	0.4000	0.8011	0.3997	0.7986	0.4010
3	0.9000	0.3000	0.9124	0.2992	0.8909	0.2930
4	0.9412	0.2353	0.9402	0.2394	0.9422	0.2396
5	0.9615	0.1923	0.9625	0.1887	0.9600	0.1957

Table 3.1: Pulsating sphere under prescribed uniform flux for four wave numbers (k =1, 2, 3, 4).

Figures 3.5, 3.6 and 3.7 compare the real part of the potential values of the analytical solution and the constant and quadratic BEM approaches for the internal points with $1 \leq d \leq 3$ and for three wave number values (k =1.2, 4.0, 6.0). Again good agreement is observed. This means that both meshes have sufficient number of elements to reach an accurate solution.

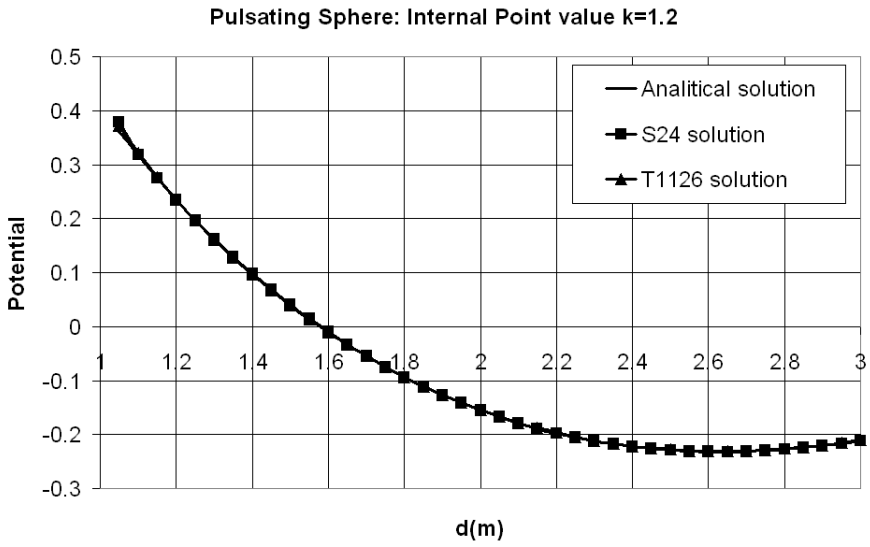


Figure 3.5: Pulsating sphere under prescribed uniform flux. Real part of the potential for the internal points with $1 \leq r \leq 3$, k =1.2.

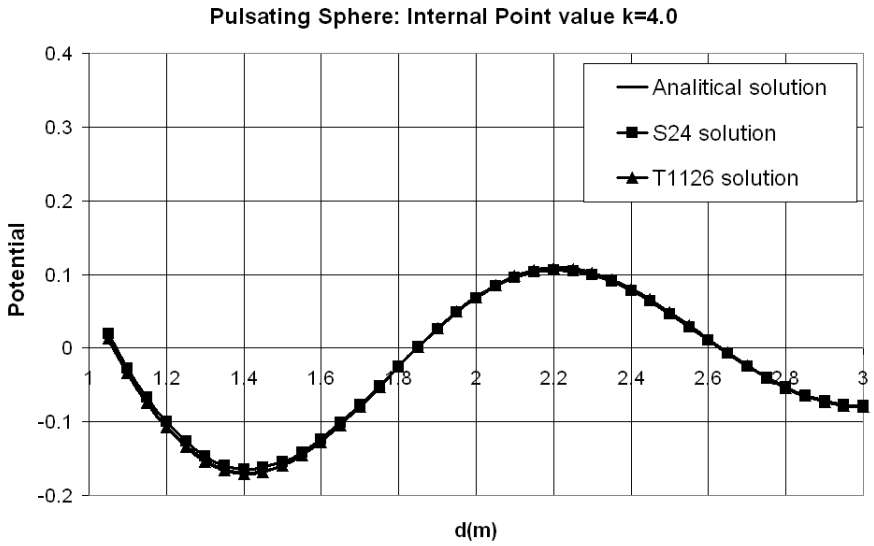


Figure 3.6: Pulsating sphere under prescribed uniform flux. Real part of the potential for the internal points with $1 \leq r \leq 3$, k =4.0.

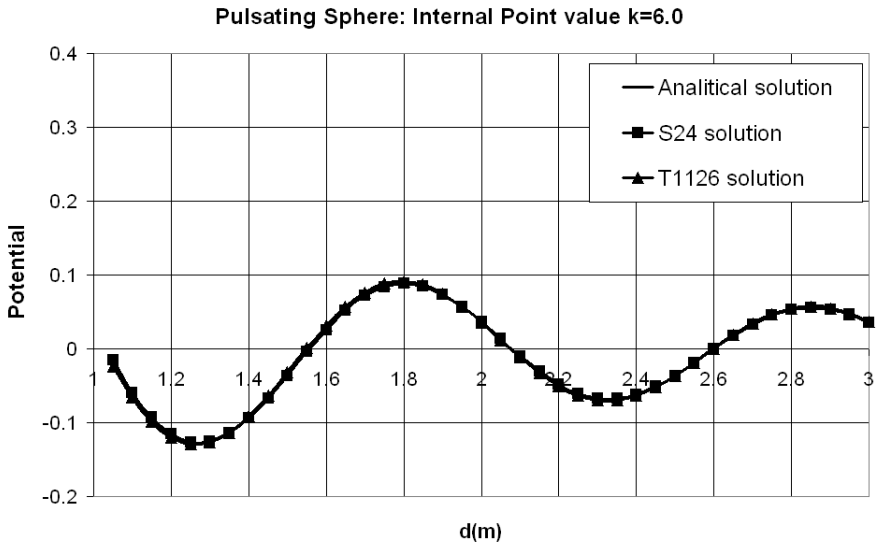


Figure 3.7: Pulsating sphere under prescribed uniform flux. Real part of the potential for the internal points with $1 \leq r \leq 3$, k =6.0.

Figure 3.8 shows the trend of the real part (a), the imaginary part (b), the amplitude (c) and phase (d) of the potential around the pulsating sphere in a 20×20 m square

constituted by 101×101 points for a single wavenumber value (k =2). In particular the peaks/throats of the former two quantities are reduced as the distance from the sphere increases, due to the Sommerfeld radiation condition. This condition can also be noted to be valid when observing the amplitude trend (c). On the contrary the phase trend is not reduced with the distance and it is repeated along the plane, where its values are contained between -π/2 and π/2, as expected. The phase assumes a fundamental role in the time domain solution. In a sound system, if the phase is badly set, the sound could reverberate generating an annoying perception. The active noise control, for instance, is based on creating a secondary wave with the same amplitude, but with opposite phase. In Chapter 5 it is shown how even a small phase variation from its optimal value can strongly reduce the whole system performance.

Notice that each section of figure 3.8 has been obtained by scaling separately each quantity in order to have a better view of the quantity variations between π/2 and -π/2.

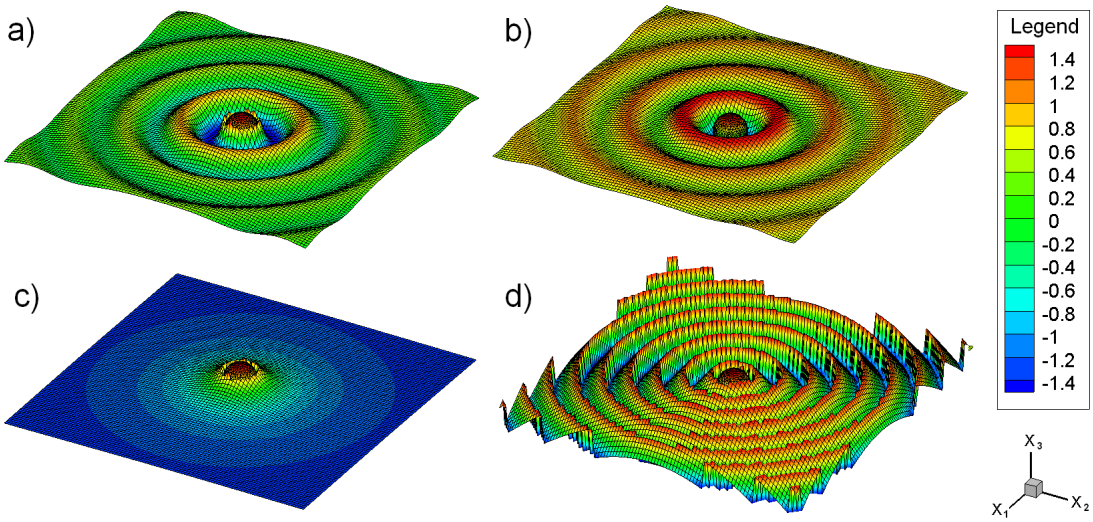


Figure 3.8: Potential around a pulsating sphere: a) real part; b) imaginary part; c) amplitude; d) phase.

3.9.2 Spherical Cavity

The case of a vibrating pulsating spherical cavity, whose analytical solution is well-known, is studied.

The analytical solution for a wave motion inside a rigid-walled spherical cavity of radius a at a distance d from the sphere centre is given by [116] in terms of potential as follows

$$U(kd,\, t) = \left[A j_0(kd) + \tilde{B} y_0(kd)\right] e^{-i\omega t} \tag{3.56}$$

where j_0 and y_0 are the spherical Bessel functions of the first kind and second kind of order zero, respectively. In order to constrain the potential $U(kd,\, t)$ to a finite value for a point in the centre of the sphere (d=0), $\tilde{B}$ must be equal to zero. Thus the above equation can be written as follows

$$U(kd,\, t) = A j_0(kd)\, e^{-i\omega t} = A \frac{\sin(kd)}{kd}\, e^{-i\omega t} \tag{3.57}$$

By assuming that the cavity walls vibrate with a constant velocity $\tilde{b}$ over the entire surface, the constant A can be evaluated as follows

$$\tilde{b} = \left(\frac{\partial u}{\partial d}\right)_{d=a} = A\, e^{-i\omega t} \frac{\partial}{\partial d} \frac{\sin(kd)}{kd} = A \frac{ka\cos(ka) - \sin(ka)}{ka^2}\, e^{-i\omega t} \tag{3.58}$$

where the radius and the outward normal to the sphere coincide. Table 3.2 compares the results obtained from four values of wavenumber (k =1, 2, 3, 4) for the analytical solution and the constant and quadratic BEM approaches. The close agreement of the results confirms again the precision of the BEM approach.

k	Analytical Solution	Quadratic BEM S24	Constant BEM T1126
1	-2.7940	-2.8132	-2.8058
2	-0.5221	-0.5198	-0.5243
3	-0.0453	-0.0416	-0.0448
4	0.4073	0.3994	0.4036

Table 3.2: Pulsating spherical cavity under prescribed uniform flux for four wavenumbers (k =1, 2, 3, 4) .

Figure 3.9 shows the trend of the real part (a), the imaginary part (b), the amplitude (c) and phase (d) of the potential around the pulsating cavity in a $\sqrt{2}\times\sqrt{2}$ m square constituted by 101×101 points for a single wavenumber value (k =8). Due to the fact that the surfaces of the cavity are hard, the sound is not absorbed and stands inside the cavity all the time without any reductions. Again, value of the legend refers to scaled quantities for a better view of the quantity variations.

3.9.3 Plane-wave Scattering from a Sphere

The effect of the presence of a plane-wave on a rigid sphere is investigated. The plane wave propagates along the negative direction x_1 (see figure 3.10).

As explained previously in section 3.5 extra sources such as plane-waves create an additional term of known values which can be included in the BEM formulation as shown in equation (3.48). This term depends upon the geometry of the problem, the directions and the complex amplitude (amplitude and phase) value of the plane-wave (see equation (3.35)).

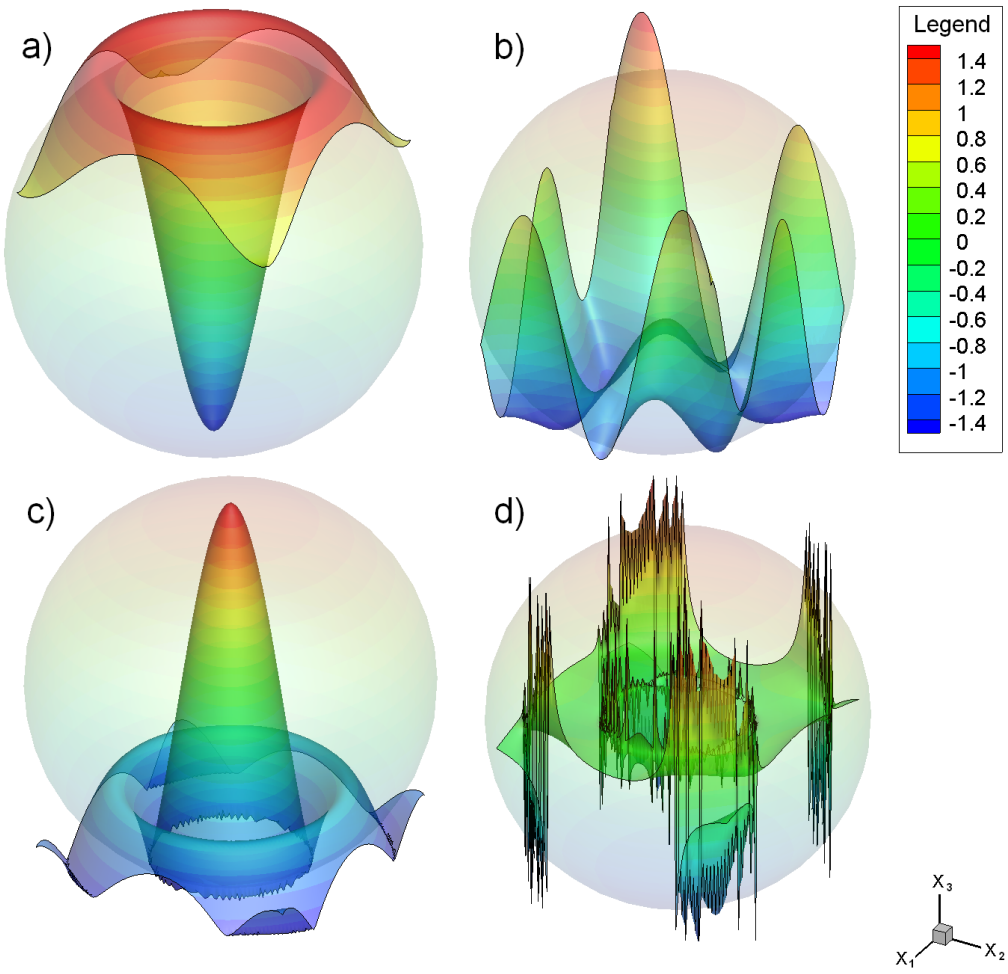


Figure 3.9: Potential within pulsating spherical cavity ($k = 8$): a) real part; b) imaginary part; c) amplitude; d) phase.

The analytical solutions for a plane-wave scattering by the presence of an object, with characteristic dimension a, for low and high frequencies, is well-known and can be found in the literature [90, 95]. For a constant frequency, the pressure is obtained by multiplying equation (3.35) to $-i\omega\rho$. The scattered complex pressure for low frequencies at a point with distance r from the plane-wave origin, for a sphere with radius a and with $ka \ll 1$ is provided by Pierce [95] and reported below

$$p_{sc} = \frac{k^2}{4\pi r}\frac{8a^3}{3}B\cos\theta\left(1+\frac{i}{kr}\right)e^{ikr} \tag{3.59}$$

where B is the complex plane-wave amplitude and θ the angle between the plane-wave direction and the position vector $\mathbf{r}$. Table 3.3 compares the values for three values of wavelength (λ =10, 100, 1000) of the analytical solution and the constant and quadratic BEM approaches at a point placed at a distance of $2m$ from the sphere centre along the plane-wave propagation direction (point A in figure 3.10). As evident, the BEM is able to reach an accurate solution.

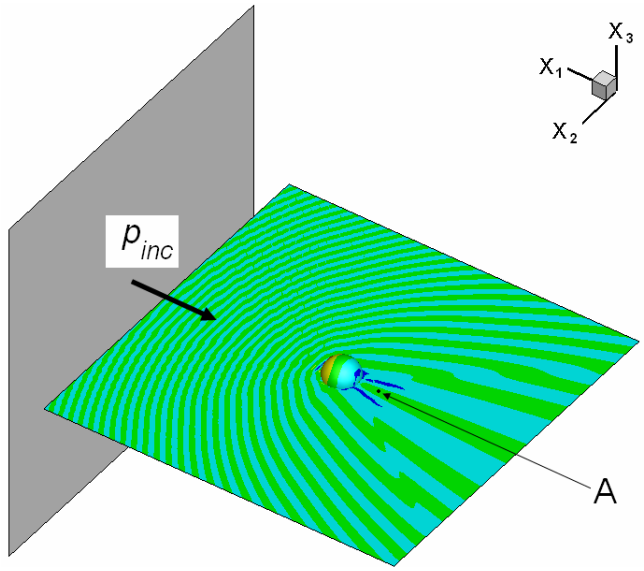


Figure 3.10: Plane-wave scattering from a rigid sphere: potential amplitude in a 20×20 m square constituted by 101×101 points at a single wavenumber value (k =7); P_{inc}, incident plane-wave.

	Analytical Solution		Quadratic BEM S24		Constant BEM T1126	
λ	Real part	Imag. part	Real part	Imag. part	Real part	Imag. part
10	0.2903	1.001	0.2920	1.015	0.2889	1.047
100	0.9921	0.1287	0.9918	0.1299	0.9918	0.1291
1000	0.9999	0.0123	0.9999	0.0111	0.9999	0.0125

Table 3.3: Plane-wave scattering from a rigid sphere for three wavelength (λ =10, 100, 1000).

Figure 3.11 shows the real part (a), the imaginary part (b) and the amplitude (c) and phase (d) of the potential value due simply by the presence of the incident wave in plane constitutes by 101×101 points at a single wavenumber value (k =7). In particular, the real and imaginary parts create characteristic waves, similar to those generated on the water surface, the amplitude is constant along the whole domain and the phase is nullified at the origin since the complex plane-wave amplitude B of equation (3.35) is (1, 0) and its phase refers to the origin. By maintaining the same amplitude, a different phase α can be easily obtained by solving the following system of equation

$$\begin{aligned} \sqrt{B_R^2 + B_I^2} &= 1 \\ \arctan \tfrac{B_L}{B_R} &= \alpha \end{aligned} \tag{3.60}$$

Figures 3.12 and 3.13 are similar to figure 3.11, but the values displayed are referred to the scattered waves and the total (incident plus scattered waves) potential, respectively.

It can be noted that solutions obtained by the constant element sphere are slightly more accurate than the quadratic BEM approach. This is not due to the fact that the former approach is more accurate than the latter, but on the mesh density that constitutes the sphere. In fact, the maximum frequencies that can be studied by the T1126 sphere is slightly higher that the maximum frequency of the S24.

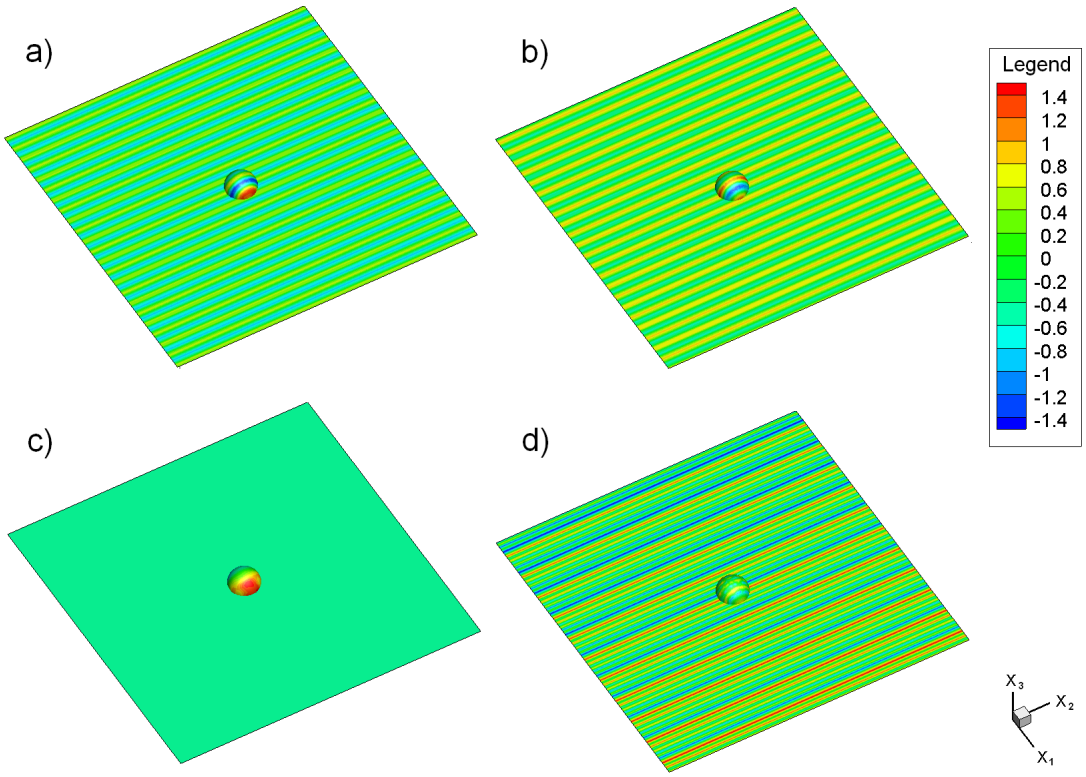


Figure 3.11: Plane-wave scattering from a rigid sphere: a) real part , b) imaginary part, c) amplitude, d) phase of the incident plane-wave potential.

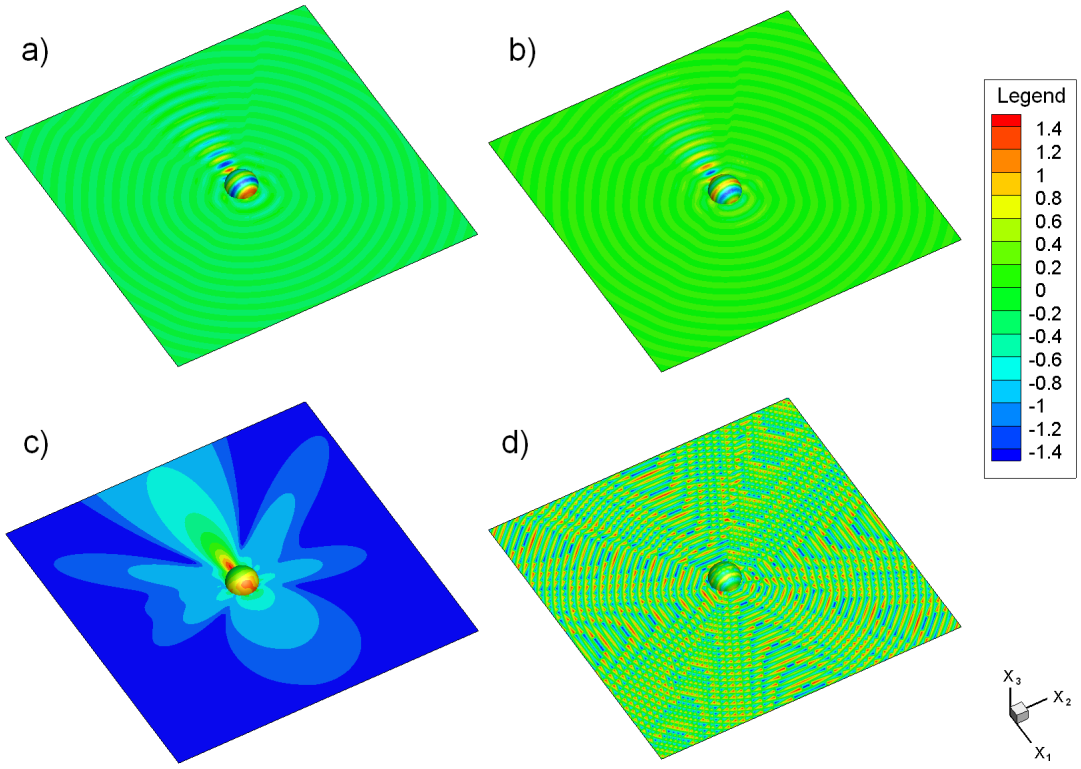


Figure 3.12: Plane-wave scattering from a rigid sphere: a) real part , b) imaginary part, c) amplitude, d) phase of the scattered wave potential.

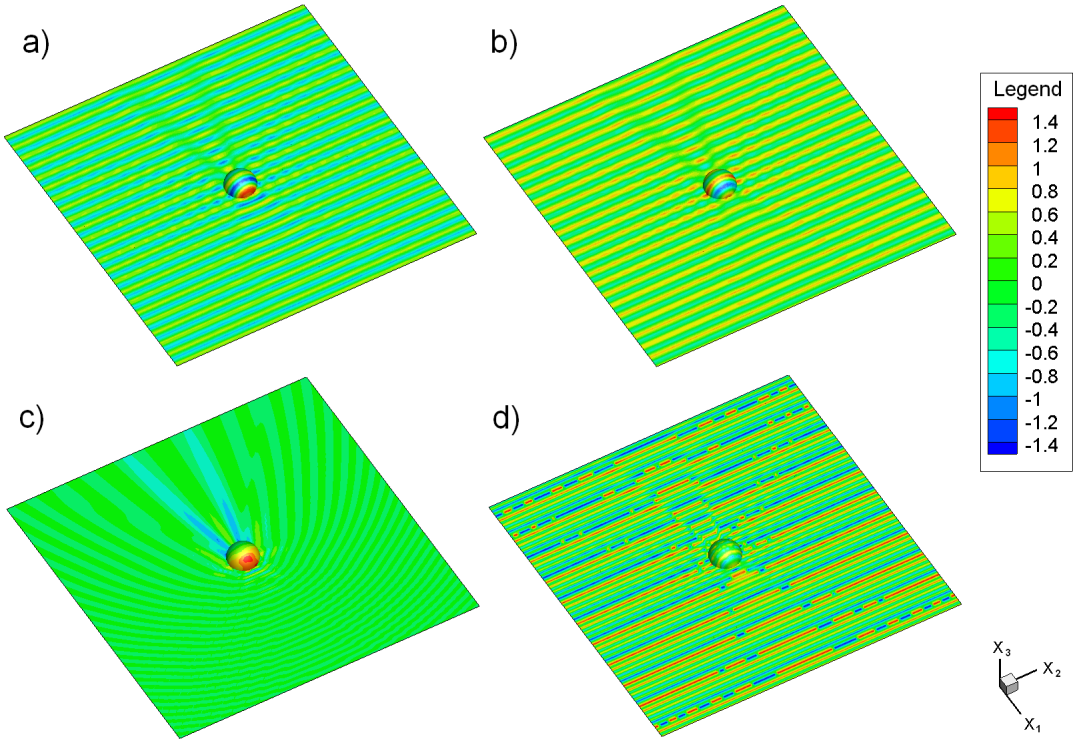


Figure 3.13: Plane-wave scattering from a rigid sphere: a) real part , b) imaginary part, c) amplitude, d) phase of the total (incident + scattered) wave potential.

3.10 Summary

The fundamental concepts and derivation of the boundary element method using the collocation method for acoustic problems governed by the Helmholtz equation have been examined.

Different discretisation strategies involving constant and quadratic elements have been also reviewed and their accuracy and efficiency have been assessed by solving several benchmark examples where analytical solutions are available. Both discretisations have given accurate results, thus both strategies are comparable. The number and order of the discretising elements depend upon the frequency. If quadratic elements are used at least two elements per wavelength are required and in case of constant element

at least eight elements are required. The dimension of the system matrix depends upon the degree of freedom (d.o.f.) of a problem. For constant elements the d.o.f. coincide with the number of elements, whereas for quadratic elements the **H** matrix size depends upon the number of nodes and the **G** matrix size upon the number of elements. Also, the matrices **H** and **G** depend on the frequency. Moreover, constant elements require an easier integration process that can be implemented in a simpler way. For this reason, the fast method, based on the Adaptive Cross Approximation in conjunction with the *Hierarchical Matrix* format and the GMRES solver presented in the next chapter, has been developed, implemented and assessed for the superparametric (linear geometries and constant unknown) formulation.

The fictitious frequency and spurious eigenvalue problems have been briefly reviewed. Both of them are due to the fact that boundary-value problems governed by the Helmholtz equation do not have non-unique solutions at certain wavenumbers that generate a rank deficiency of the solving matrix. In the simulations presented in the following chapters fictitious frequencies are simply avoided and spurious eigenvalues never arise.

Moreover, it should be pointed out that the matrices **H** and **G** depend only upon the geometry of the discretised problem. This is an important task if different simulations with same geometries and various boundary conditions are required as in the case of the active noise control presented in Chapter 5.

Chapter 4

Hierarchical Adaptive Cross Approximation GMRES Procedure

In chapter 3 it has been highlighted that the BEM formulation leads to a non-symmetric and fully populated system matrix. For a standard formulation both the memory storage and the setting up of the system matrices are of $O(N^2)$, where N denotes the number of degrees of freedom. Moreover, direct solvers require $O(N^3)$ operations while iterative solvers $O(kN^2)$, where k is the number of iterations.

To overcome the difficulties related to storage and solution time a number of techniques have been proposed which include block-based solvers [39, 101], lumping techniques [76] and iterative solvers [87]. The Adaptive Cross Approximation (ACA) is an effective technique for populating non-symmetric and fully populated matrices and, in conjunction with iterative solvers, decreases the CPU time significantly [13]. The ACA has been applied to the Helmholtz equation by, for example, Von Estorff *et al.* [119]. The assembly time of a linear system of equations is accelerated by calculating only a few entries of the original matrix. The basic idea is to divide the whole matrix into two rank (*low* and *full rank*) blocks based on size and distance between a group of collocation points and a group of boundary elements. Low rank blocks require only a

few entries of the original block to represent the entire block (see figure 4.1). Therefore, the ACA algorithm is applied to the low rank blocks achieving approximately O(N) for both storage and matrix-vector multiplication [14, 62].

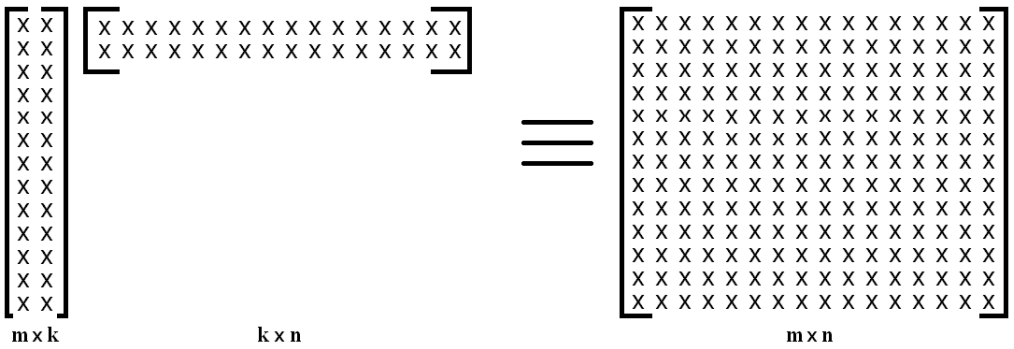


Figure 4.1: Low rank approximation: a few entries of the original block represent the entire block.

Another popular approach to speed up the solution time is the Fast Multipole Method (FMM) (see for example [5, 28, 35, 58, 68, 102, 121, 122]). Although FMM techniques are efficient for fast solutions of boundary element problems, knowledge of the kernel expansion is required to carry out the integration process and this represents its main drawback; all the terms of the series needed to reach a given accuracy must be computed in advance and then integrated, which can lead to a significant modification of the integration procedures in standard BEM codes. From an algebraic point of view however, the integration of a degenerate kernel, i.e., of a kernel expanded in series, over a cluster of elements corresponds to the approximation of the corresponding matrix block by a low rank block. Comparisons between the FMM and ACA method were made by Wang *et al.* [120] for three-dimensional Laplace problems. In their study a fully pivoted ACA was shown to require considerably more computational effort than FMM. Nevertheless, it must be noted that the full pivoted approach is well known to be much slower than partially pivoted approach used by Wang. The main reason behind

this is that fully pivoted approach requires the knowledge of the full matrix whereas the partially pivoted approach would only require generation of individual matrix entries. Indeed, in this thesis the partially pivoted ACA approach for acoustic problems is shown to be superior to the FMM for an example considered.

Developing iterative solvers for non symmetric linear systems has been widely investigated. One of the most popular is the generalized minimal residual method (GMRES) proposed by Saad and Schultz [106] in 1986 and further developed by other authors [3, 81, 89].

In this chapter a new hierarchical adaptive cross approximation technique coupled with GMRES is presented for the 3D boundary element solution of Helmholtz problems. Next, the Hierarchical-ACA procedure as well as the mathematical aspect of the ACA technique are described. In the second section particular attention is paid to the implementation of different types of boundary conditions (i.e., Dirichlet, Neumann and mixed Robin). The ACA and the H-Matrix format are also employed for the post processing steps required to evaluate the values of the potential and particle velocity at the internal points and this procedure is presented in the third section. Numerical results are presented in the fourth section. The superparametric formulation with constant and linear elements is utilised to solve the problem. Initially, a parametric study over two quantities is presented. Then, two simple benchmark problems of a pulsating sphere and the scattering of a plane wave from a rigid sphere are investigated. Next, large scale applications involving a row of three seats representing the seats in an aircraft cabin and noise emanating from engines of the Dassault Falcon aircraft are presented. The tests carried out show that the new assembly and solution technique can achieve CPU times of almost $O(N)$ for low frequency and $O(N \log N)$ for high frequency problems. A summary concludes the chapter.

4.1 Hierarchical-ACA

In this section a brief introduction to the hierarchical matrix (H-matrix) format, originally introduced by [60, 61], and an introduction to the ACA [10, 13] are presented. These two approaches have been chosen in the present thesis because in conjunction with iterative solvers they significantly speed up the solution time due to three efficient principles, i.e., the hierarchical partitioning of the matrix into blocks, the block-wise restriction to low rank blocks (see figure 4.1) and the matrix-vector multiplication with almost linear complexity.

By this procedure the system matrix is represented as a collection of blocks divided into two groups, *low rank* and *full rank blocks*, based on their representation. The former blocks admit an approximated representation that reduces the required storage and accelerate the matrix-vector multiplication [62], whereas the latter are fully computed and stored entirely.

The low rank block representation is based on a suitable expansion of the kernel of the continuous integral operator, i.e., the potential and flux fundamental solutions. The analytical existence and sufficient condition of the low rank representation is based on the *asymptotic smoothness* of the kernel functions, i.e., the kernels are singular only if the collocation point and the field point coincide [10, 13, 53, 118].

The subdivision into low and full rank blocks is based upon a geometrical criterion on the problem geometry and discretised mesh. At a starting stage, the matrix indices are hierarchically partitioned to collect indices corresponding to contiguous nodes and elements and stored in a binary tree, i.e., the *cluster tree*. The cluster tree is the basis for the following evaluation of the block subdivision and for building a quaternary tree, i.e., the *block tree*, where all blocks are stored [15]. Low rank blocks are detected by an *admissible criterion*, based on geometrical consideration.

The approximation of the low rank blocks is performed by the ACA. Two subsets

of contiguous collocation points and contiguous field points, that fulfill the admissible criterion, constitute a block of coefficients (ς_{ij}) in the system matrix evaluated by a series of integrals of the kind [13]

$$\varsigma_{ij}(\mathbf{x}'_j,\, \mathbf{x}_i) = \int_{\Gamma_i} \kappa(\mathbf{x}'_j,\, \mathbf{x}_i)\chi_i(\mathbf{x})\, d\Gamma_i \tag{4.1}$$

where $\kappa(\mathbf{x}'_j,\, \mathbf{x}_i)$ is the kernel and $\chi_i(\mathbf{x})$ is the potential or flux value evaluated at i-th field point with coordinates $\mathbf{x}_i$. At this stage, only a few entries of the original block are calculated and the remaining matrix coefficients are evaluated by them. In other words, the terms of the kernel expansion of some coefficients are evaluated by the value of other kernel that refers to contiguous nodes and elements. It should be highlighted that the ACA approximates adaptively a low rank block with *a priori* selected accuracy. These features make such a technique particularly appealing, as it is not necessary to modify or rewrite the routines for the boundary integration in previously developed codes. To summarize, the idea behind this technique is based on the consideration that the integrals of contiguous elements due to a single collocation point are almost identical, especially for high density meshes. The same consideration is valid for the integrals of a single element due to a number of collocation points.

The H-matrix approach for the representation of BEM system of equations are described in the papers [19, 60, 61] and in conjunction with Krylov subspace methods in these papers [81, 89]. In the present thesis the H-matrix approach is extended to BEM acoustic problems with different boundary conditions.

In this section, the cluster tree formation, the block tree evaluation, including some analytical considerations for the approximation existence, the ACA procedure and the H-matrix strategy are presented.

4.1.1 Cluster Tree

As afore-mentioned, the hierarchical representation of a boundary element matrix can be regarded as a subdivision of the matrix itself into a collection of blocks, some of which, called *low rank blocks*, allow a special compressed representation, while others, called *full rank blocks* are represented in their entirety. The subdivision and the subsequent classification are achieved starting from the boundary element mesh and are based on the grouping of the nodes and elements into clusters of close nodes and elements. The process leading to the subdivision in sub-blocks and to their further classification is based on a preliminary hierarchical partition of the matrix index set aimed at grouping subsets of indices corresponding to contiguous nodes and elements.

The process starts from the complete set of indices $I = \{1, 2, ..., N\}$ where N denotes the number of elements. This initial set constitutes the root of the tree. Each cluster in the tree, called *tree node* (not to be confused with geometrical discretisation nodes) is split into pairwise disjoint subsets $P(t) = \{(t_1, t_2) : t_1, t_2 \subset I\}$, called *sons*, on the basis of some selected criterion. For this study the longest extended dimension of the whole geometry (step 1 of the figure 4.2) is detected first and its central point calculated. This point divides the mesh into two tree nodes (step 2). The geometries of the mesh of each of these blocks are then divided into two other tree nodes by following the same procedure (step 3). Such an iterative procedure is repeated until each tree node is constituted by a minimum number of elements, called *cardinality*. At this point the cluster tree contains a hierarchical partition of I. As evident, the total number of subsets p of a set $P(t)$ yields

$$t = \bigcup_{p \in P(t)} p, \qquad \text{If } \#t > cardinality \tag{4.2}$$

with $t \subset I$. The common tree node from which two sets originate is called the *parent*. The tree nodes that cannot be further split are the *leaves* of the tree. The number

of elements of each leaf is equal to or less than the cardinality, previously fixed. This partition is stored in a binary tree of index subsets, or cluster tree, that constitutes the basis for the subsequent construction of the hierarchical block subdivision, which will be stored in a quaternary *block tree*.

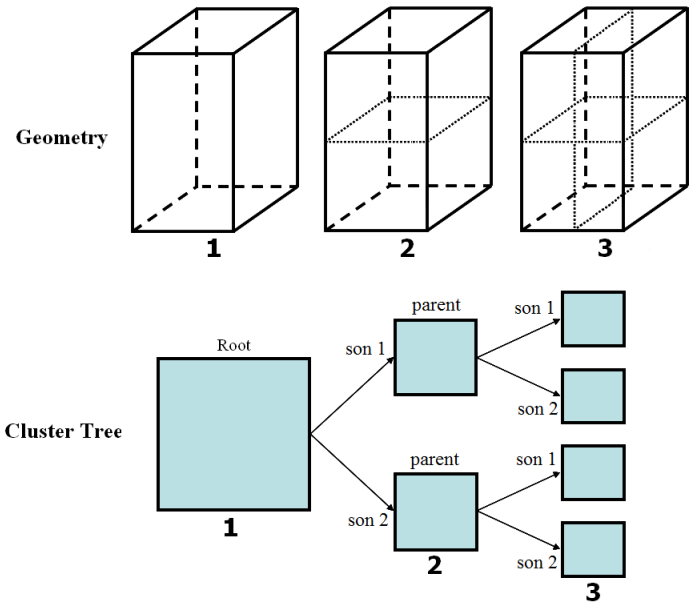


Figure 4.2: A schematic of the first two iterations of the cluster tree creation: 1) the whole geometry is divided 2) into two parts, each of which is then subdivided again 3) into two parts.

The algorithm for generating the cluster tree is shown below. t_i indicates the number of elements of a subset of nodes $p \in P(t)$; S_c collect the central node of the constant element along the three coordinates (x_1, x_2, x_3), hence it is a $N \times 3$ matrix; the coordinates (x_1, x_2, x_3) with maximum extensions of the subset p is evaluated and stored in $j_{max} = 1, 2, 3$; c_j the value of the central point along the maximum extension.

Algorithm 4.1 Recursive Subroutine SplitClusterTree($P(t_i)$)

If $t_i \leq cardinality$ **Then**

j_{max}=max loc(arg max($S_c(t_i,:)$,1) - arg min($S_c(t_i,:)$,1),1)

c_j=(arg max($S_c(t_i,j_{max})$,1) + arg min($S_c(t_i,j_{max})$,1)) / 2

If $S_c(t_i,j_{max})<c_j$ **Then** $t_1 = t_i$ **Else** $t_2 = t_i$

Call SplitClusterTree($P(t_1)$)

Call SplitClusterTree($P(t_2)$)

End If

4.1.2 Block Tree

The block tree is recursively built starting from the complete index $I \times I$ (both rows and columns) of the collocation matrix and the previously found cluster tree. The objective of this process is to split hierarchically the matrix into sub-blocks and to classify the leaves of the tree into admissible (low-rank) or non admissible (full-rank) blocks. The classification is based on a geometrical criterion that assesses the separation of the clusters of boundary elements associated to the considered block. A block populated by integrating over a cluster of elements whose distance, suitably defined, from the cluster of collocation nodes is above a certain threshold is called admissible and it can be represented in the low rank format. The remaining blocks are generated and stored in their entirety.

Let Ω_r denote the cluster of elements containing the discretisation nodes corresponding to the row indices of the considered block and Ω_c the set of elements over which the integration is carried out to compute the coefficient corresponding to the column indices. The admissibility condition can be written as

$$\min(diam\,\Omega_r,\, diam\,\Omega_c) \leq \eta\, dist(\Omega_r,\, \Omega_c) \tag{4.3}$$

where *diam* and *dist* indicate the diameter and the distance of the two clusters, respectively, and $\eta > 0$ is a parameter influencing the number of admissible blocks on one hand and the convergence speed of the adaptive approximation of low rank blocks on the other hand [19].

Since the actual diameters and the distance between two clusters are generally time consuming to be exactly computed, the condition is usually assessed with respect to bounding boxes parallel to the reference axes [52, 55]. In this case Ω_r and Ω_c in the equation (4.3) are replaced by the boxes Ω_{r_0} and Ω_{c_0}. The bounding box clustering technique adopted in the present work is generally used for its simplicity. The distance of two clusters is intended as the minimum length between two corner points of two boxes. The value of the distance is negative if two clusters penetrate, i.e., a few collocation nodes of a cluster belongs to elements of the other cluster. In this case the admissible criterion is never fulfilled and a block is full rank.

The algorithm is graphically illustrated in the figures (4.3). Starting from the root (the entire matrix), each block is subdivided into four sub-blocks until either the admissibility condition is satisfied or the block is sufficiently small that it cannot be further subdivided. The clear grey boxes represent low rank blocks while the dark grey boxes are the full rank ones.

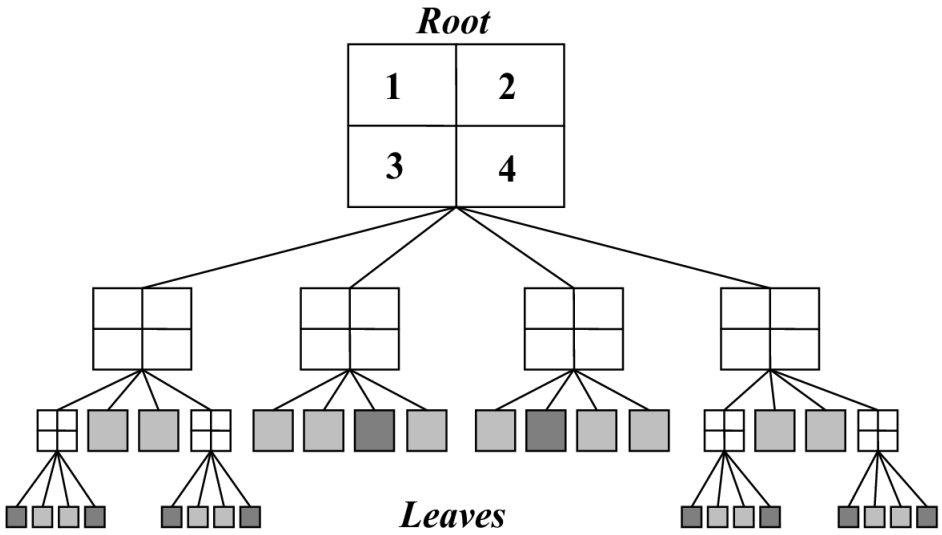


Figure 4.3: A schematic presentation of the first three iterations that form the block tree [14].

The algorithm for evaluating the block tree is shown below.

Algorithm 4.2 Recursive Subroutine SplitBlockTree($P(t_1)$,$P(t_2)$)

Check Admissibility ($P(t_1)$, $P(t_2)$, admiss)

If (admiss is true) **Then**

  Call ACA

ElseIf ($P(t_1) \leq$ *cardinality* or $P(t_2) \leq$ *cardinality*) **Then**

  Evaluate the full-rank block

Else

  Call SplitBlockTree($P(t_1)$%son1,$P(t_2)$%son1)

  Call SplitBlockTree($P(t_1)$%son1,$P(t_2)$%son2)

  Call SplitBlockTree($P(t_1)$%son2,$P(t_2)$%son1)

  Call SplitBlockTree($P(t_1)$%son2,$P(t_2)$%son2)

End If

4.1.3 ACA

An admissible block can be represented in low rank format. Such representation constitutes an approximation of the discrete integral operator based, from the analytical point of view, on a suitable expansion of the kernel of the continuous integral operator [10, 13, 53, 118] as in equation (4.1). In the previous chapter, the kernels to be evaluated for computing the coefficient of the system matrix are the potential and flux fundamental solutions. They both depend upon the collocation points $\mathbf{x}'$ and the field points $\mathbf{x}$. The kernel $\kappa(\mathbf{x}', \mathbf{x})$ is hence a general asymptotically smooth function in two variables, i.e., the kernels $u^*(\mathbf{x}', \mathbf{x})$ and $q^*(\mathbf{x}', \mathbf{x})$ are singular only when $\mathbf{x}' = \mathbf{x}$, as typically arising in integral formulations of boundary value problems, that can be approximated by a sum of products of two functions $u_i^*(\mathbf{x}')$ and $v_i^*(\mathbf{x})$ in one variable

$$\kappa(\mathbf{x}', \mathbf{x}) = \sum_{i=1}^{k} u_i^*(\mathbf{x}')\, v_i^*(\mathbf{x}) + R_k(\mathbf{x}', \mathbf{x}) \tag{4.4}$$

where $|R_k(\mathbf{x}', \mathbf{x})| \leq \varepsilon_k$ with $\varepsilon_k \to 0$ for $k \to \infty$ is the approximation error. Smoothness properties of the surface Γ are not necessary. More details on this subject are given in [12, 13]. Here it is only mentioned that the asymptotic smoothness of the kernel $\kappa(\mathbf{x}', \mathbf{x})$ with respect to $\mathbf{x}'$ (not with respect to $\mathbf{x}$) represents a sufficient condition for the existence of low rank approximants.

It should be noted that the FMM and panel clustering are also based upon the kernel approximation contained in an integral operator as in (4.1), that is required to be evaluated for each block of elements and collocation points. In contrast, the presented approach consists in a purely algebraic procedure and no expansions are necessary.

Let $\mathbf{C}$ be an $m \times n$ admissible block. It admits the low rank representation

$$\mathbf{C} \simeq \mathbf{C}_k = \mathbf{A} \cdot \mathbf{B}^T = \sum_{i=1}^{k} \mathbf{a}_i \cdot \mathbf{b}_i^T \tag{4.5}$$

where $\mathbf{A}$ is of order $m \times k$ and $\mathbf{B}$ is of order $n \times k$, with $k \ll m$ and $k \ll n$ being the *rank* of the new representation.

The approximating block $\mathbf{C}_k$ satisfies the relation $\|\mathbf{C} - \mathbf{C}_k\|_F \leq \varepsilon \|\mathbf{C}\|_F$, where $\|\cdot\|_F$ represents the *Frobenius norm* and ε is the prescribed accuracy. Sometimes it is useful to represent the matrix using the alternative summation representation, where $\mathbf{a}_i$ and $\mathbf{b}_i$ are the $i-th$ columns of $\mathbf{A}$ and the $i-th$ rows of $\mathbf{B}$, respectively. The approximate representation allows storage savings with respect to the full rank representation and speeds up the matrix-vector product [62].

The low rank blocks are built by computing and storing only *some* of the entries of the original blocks. Such entries allow the representation (4.5) through suitable algorithms, known as adaptive cross approximation (ACA). The ACA algorithms allow to reach the selected collocation matrix accuracy ε adaptively. In contrast to other methods like FMM, panel clustering, etc. the kernel of the integral operator for evaluating the ACA approximants is not replaced by other terms. Moreover, in the proposed algorithm, the calculated rows and columns are sufficient to evaluate the accuracy of the approximation without calculating the whole block. Obviously, the main advantage of the ACA is that the block entries can be easily evaluated by existing code, whereas methods like FMM require a complete recoding.

The algorithm starts by evaluating a random row $\mathbf{C}_{i_k,1:n}$ of the low rank block and finding the location (i_k, j_k) of its *pivot* g_k (the maximum absolute value of the row coefficients). If the pivot is non-zero, the entire column $\mathbf{C}_{1:m,j_k}$ is evaluated, scaled by specific product and divided by the pivot. Hence, the calculated entries are checked with a *stopping criterion*. If this criterion is not fulfilled, the location i_{k+1}, j_k of the column pivot is evaluated and the corresponding row i_{k+1} is calculated and scaled using the previous entries. The entire process is thus repeated till the stopping criterion is satisfied. A record of the already calculated entries avoids finding the same previous pivots.

The algorithm used is shown below.

Algorithm 4.3 Adaptive Cross Approximation (ACA).

$k = 1$; $\mathbf{Z} = \emptyset$; $\mathbf{a}_1 = 0$; $\mathbf{b}_1 = 0$
Repeat
  If $k = 1$ **Then** $i_k = random\,\{i_k \in \mathbb{N},\, k = 1,\, \ldots,\, m\}$
  Else
    If $g_k \neq o$ **Then** $i_k = \arg\max_{i=1,\ldots,m} |(\mathbf{a}_{k-1})_i|,\; i \neq i_1,\, \ldots,\, i_{k-1}$
    Else $i_k = \arg\min\{\mathbf{Z}\}$
    End If
  End If
  $\tilde{\mathbf{b}}_k = \mathbf{C}_{i_k,1:n}$
  Do $l = 1,\, 2, \ldots,\, k$ $\mathbf{b}_k = \tilde{\mathbf{b}}_k - (\mathbf{a}_l)_{i_k}\mathbf{b}_l$
  $\mathbf{Z} = \mathbf{Z} \bigcup \{i_k\}$
  $j_k = \arg\max_{j=1,\ldots,n} |(\mathbf{b}_k)_j|,\; j \neq j_1,\, \ldots,\, j_{k-1}$
  $g_k = (\mathbf{b}_k)_{j_k}$
  If $g_k \neq 0$ **Then**
    $\mathbf{a}_k = \mathbf{C}_{1:m,j_k}$
    Do $l = 1,\, 2, \ldots,\, k-1$ $\tilde{\mathbf{a}}_k = \tilde{\mathbf{a}}_k - (\mathbf{b}_l)_{j_k}\mathbf{a}_l$
    $\mathbf{a}_k = \tilde{\mathbf{a}}_k / g_k$
    $k = k + 1$
  End If
Until the stop criterion is fulfilled or $\mathbf{Z} = \{1,\, 2,\, \ldots,\, m\}$

A schematic presentation of the ACA algorithm is shown in figure 4.4.

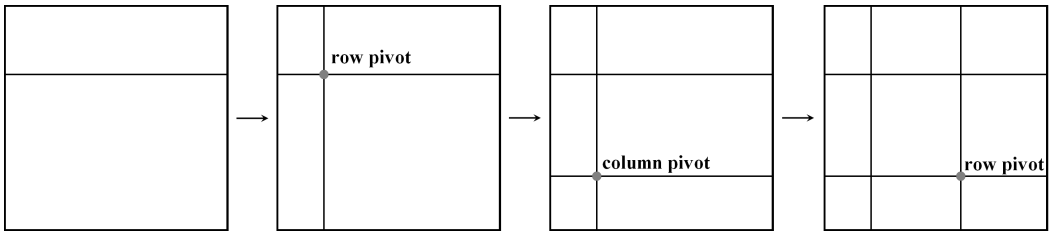


Figure 4.4: A schematic presentation of the ACA algorithm[25].

Stopping criterion

The stopping criterion is based upon the assessment of the convergence of the approximating block in terms of the Frobenius norm [10, 13]. Once the $k-th$ couple $(\mathbf{a}_k, \mathbf{b}_k)$

has been computed the Frobenius norm of the approximation can be computed by the following recursive formula

$$\|\mathbf{C}_k\|_F^2 = \|\mathbf{C}_{k-1}\|_F^2 + 2\sum_{i=1}^{k-1}(\mathbf{a}_k^T\mathbf{a}_i)(\mathbf{b}_i^T\mathbf{b}_k) + \|\mathbf{a}_k\|_F^2\|\mathbf{b}_k\|_F^2 \tag{4.6}$$

where $\mathbf{a}_k$ and $\mathbf{b}_k$ represent the column and row computed at the $k-th$ iteration. A suitable stopping criterion can be expressed as

$$\|\mathbf{a}_k\|_F\|\mathbf{b}_k\|_F \leq \varepsilon\|\mathbf{C}_k\|_F \tag{4.7}$$

that prescribes to stop the iteration when the inequality is satisfied for a required preset accuracy ε.

The difference between the full and the approximated matrices yields the error matrix defined as follows

$$\mathbf{R}_k = \mathbf{C} - \mathbf{C}_k \tag{4.8}$$

where $\mathbf{C}_k$ has been defined in (4.5) and it is the approximate matrix with rank k at the $k-th$ iteration. At the beginning, for $k = 0$, $\mathbf{R}_0 = \mathbf{C}$ and $\mathbf{C}_0 = \mathbf{0}$. At the first iteration the error matrix is

$$\mathbf{R}_1 = \mathbf{R}_0 - \mathbf{a}_1\mathbf{b}_1 \tag{4.9}$$

hence at the $k-th$ iteration

$$\mathbf{R}_k = \mathbf{R}_{k-1} - \mathbf{a}_k\mathbf{b}_k \tag{4.10}$$

Optimised ACA Algorithm

To optimise the ACA algorithm a series of commands have been inserted to avoid drawbacks.

The main problem occurs when $g_k = 0$ for $k = 1, \ldots, m$. In this eventuality the original matrix is formed by all zero coefficients, the rows are never calculated and the entire procedure falls. To solve this problem algorithm (4.3) is modified such that in case $m \neq 1$, only one row and one column with zero coefficients constitute the low rank approximants, whereas when $m = 1$, the low rank block is turned to a full rank block and the single row is evaluated.

A second drawback arises when the low rank block is constituted only by a single row, $m = 1$. In this case the stopping criterion is reached, but the low rank block is basically a full rank block. Hence, the block is simply turned to full rank.

The third problem occurs when the ACA falls ($\mathbf{Z} = \{1, 2, \ldots, m\}$), i.e., the low rank block is located close to the principal diagonal and it is constituted by a few coefficients. This eventuality is solved by substituting the low rank block with a full rank block.

4.1.4 *H*-matrix

The structure of the H-matrices was originally designed to accelerate the building process and the matrix-vector multiplication of discrete integral operators with smooth kernels, such as in the BE formulation. The admissible criterion (4.3) is also used to prove convergence of the ACA algorithm for the generation of low-rank approximants [10, 13].

H-matrix is defined as follows [60].

Let I be an index set. A tree T is called an H-tree (based on I) if the following conditions hold:

1. All verteces of $t \in T$ are subsets of I;

2. $I \in T$;

3. $\#P(t) \neq 1$ for all $t \in T$;

4. If $t \in T$ is not a leaf, $P(t)$ contains disjoint subsets of I and t is the union of its sons, i.e.,

$$t = \bigcup_{p \in P(t)} p \tag{4.11}$$

As afore-mentioned, the H-matrix approach strongly decreases the computational cost of matrix vector multiplication. A conventional product between a $m \times n$ matrix and a $n \times 1$ vector requires $m(2n-1)$ operations. The low rank approximation generates two $m \times k$ and $k \times n$ matrices, instead than one. The final result is achieved by two subsequent matrix-vector products, i.e., the $k \times n$ matrix with the $n \times 1$ vector and the $m \times k$ matrix with the $k \times 1$ vector, obtained with the previous multiplication. Hence the total cost of such an operation is

$$m(2k-1) + k(2n-1) \tag{4.12}$$

which, as evident, is smaller than the conventional operation cost only if

$$k < \frac{2m(n-1)}{[2(m+n)-1]} \tag{4.13}$$

It should be noted that in case of iterative solver this operation (almost linear complexity) is the key to speed up the solution time.

Memory storage is also reduced by using H-matrices since the required memory is $m \times k + k \times n$, instead of $m \times n$ in the standard procedure.

Figure 4.5 shows the first three steps in partitioning of the system matrix using the H-matrix.

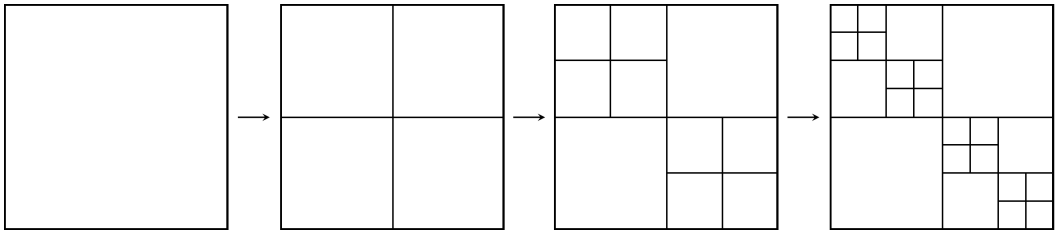


Figure 4.5: Hierarchical matrix.

As afore-mentioned the ACA algorithm (4.3) terminates if the stopping criterion is reached or all the rows have been evaluated ($\mathbf{Z} = \{1, 2, \ldots, m\}$). This last condition is not really convenient because such a block occupies double storage than the corresponding full rank block and the vector matrix product requires $m(2n-1)+m(2m-1)$ operations. Hence, the condition $\mathbf{Z} = \{1, 2, \ldots, m\}$ has been here substituted by considering relation (4.13).

4.2 Boundary Conditions and Right Hand Side Setting

By applying the ACA, the actual setting of the final system for mixed boundary condition problems requires some additional considerations. In this work different types of boundary conditions are considered in such a way that rigid, soft and absorbing surfaces can all be studied in order to simulate a real situation and to perform an eventual parametric analysis. An initial routine selects the matrix that is calculated first based on the boundary conditions that are predominant for that block. If the flux (or potential) is predominant then the matrix $\mathbf{H}$ (or $\mathbf{G}$) is calculated first, otherwise, in the case the boundary condition are in terms of impedance, the ACA algorithm is applied to both the matrices.

In order to speed up significantly the system solution, the "*BlockNode*" pointer suggested by Benedetti *et al.* [14] is used here. The contributions of each block to the solving matrix **A** is stored in the BlockNode pointer and calculated at each step as well as the contribution of the right hand side vector that is, instead, stored in the global vector **F** to save memory.

The code has been implemented using the artificial admittance ζ defined as follows

$$\zeta(\omega) = \frac{q}{u} \tag{4.14}$$

The ACA algorithm is applied to one or both of the matrices **G** and **H** depending upon the boundary conditions that are predominant for each block matrix. Particular care must be taken when not pure Dirichlet, Neumann or mixed Robin conditions are applied. There may be four different cases:

a) BCs mainly in terms of flux (or potential) except for the k^{th} value expressed in terms of potential (or flux).

As an example, one can consider that the boundary conditions are expressed in terms of flux (the first block matrix calculated with ACA is **H**) and at the node k they are expressed in terms of potential. A routine replaces each k^{th} value of each row previously calculated with zero, adds the opposite in sign of the k^{th} column of the **G** block matrix and also adds a zero row with 1 at the k^{th} element (see figure 4.6).

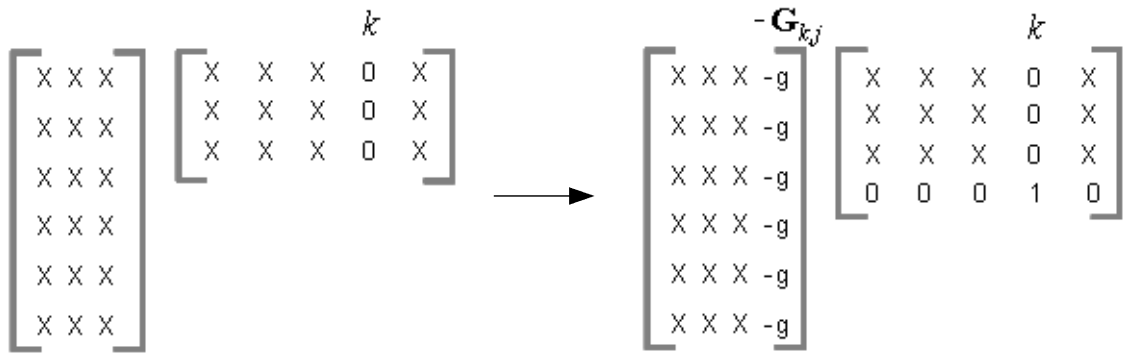


Figure 4.6: Substitution of the k^{th} values of each row with zero, addition of the k^{th} column of the **G** block matrix and of a zero row with *1* at the k^{th} element.

b) BCs mainly in terms of flux except for the k^{th} value expressed in terms of impedance.

Here simply add the k^{th} column of the **G** block matrix not yet calculated multiplied by the artificial admittance ζ opposite in sign, and adds a zero row with 1 at the k^{th} element (see figure 4.7).

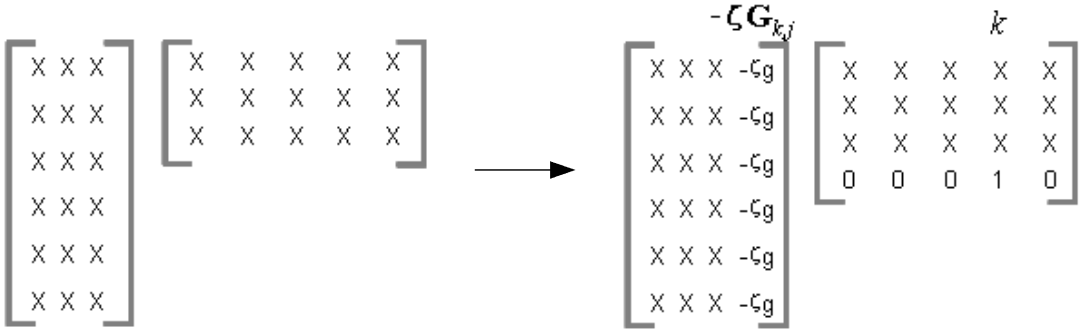


Figure 4.7: Addition of the k^{th} column of the **G** block matrix multiplied by the artificial admittance ζ opposite in sign and of a zero row with *1* at the k^{th} element.

c) BCs mainly in terms of potential except for the k^{th} value expressed in terms of impedance.

In this case multiply the k^{th} row of the **G** block matrix (previously calculated) by the artificial admittance ζ opposite in sign. Then another routine adds the k^{th} column of the **H** block matrix not yet calculated and a zero row with 1 at the k^{th} element (see figure 4.8).

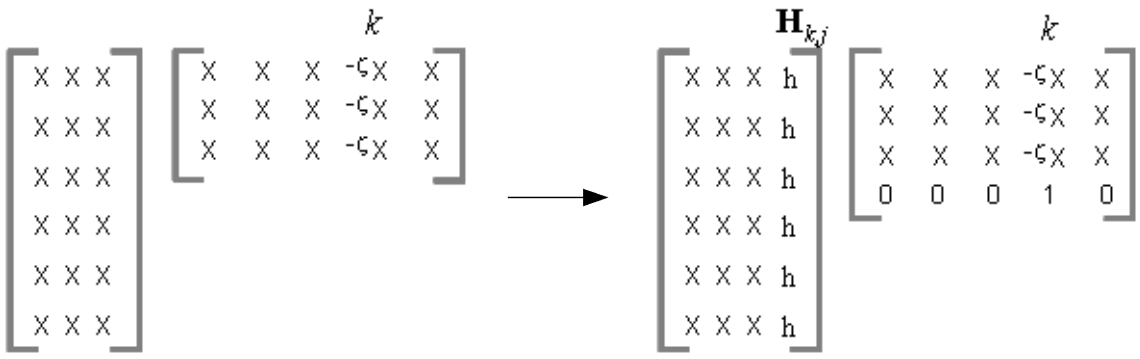


Figure 4.8: Multiplication of the k^{th} row of the **G** block matrix by the artificial admittance ζ opposite in sign, addition of the k^{th} column of the **H** block matrix and of a zero row with *1* at the k^{th} element.

d) BCs mainly in terms of impedance except for the k^{th} value expressed in terms of potential (or flux).

In this case the ACA algorithm acts earlier on the **H** block matrix. If the ACA stop criterion is reached and the k^{th} value is in terms of potential, the k^{th} value of each row calculated is set to zero. The ACA algorithm is finally applied to the **G** block matrix whose columns are multiplied $-\zeta$, and the k^{th} elements of its rows are divided by ζ (see figure 4.9).

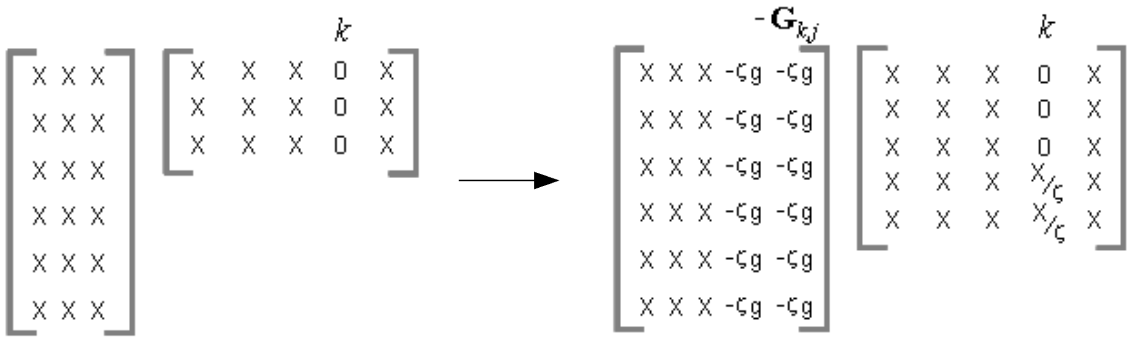


Figure 4.9: Substitution of the k^{th} values of each row with zero, addition of the columns of the **G** block matrix multiplied by the artificial admittance opposite in sign and of its rows where the k^{th} elements are divided by ζ.

Regarding the setting up of the right hand side vector some additional considerations are required as explained next. Recalling the ACA algorithm, the routine that calculates the i^{th} row of one of the block matrices **G** or **H** also calculates the i^{th} row of the other block matrix. Thus, the right hand side contribution of that row for the block matrix analysed is directly calculated.

Now, there are two main cases to analyse.

- BCs mainly in terms of flux (or potential).

Here, one may need to apply the ACA on the matrix **G** (or **H**). In fact, if all the boundary conditions are zero, there is no need to calculate the contribution of the block matrix to the final right hand side and another block matrix can be analysed. Moreover, owing to the fact that the number of entries needed for the ACA is, in most cases, equal for both the block matrix **G** and **H**, it may be convenient to calculate the contribution to the right hand side with a standard procedure (see the next subsection).

- BCs mainly in terms of admittance.

Once the ACA as been applied to the block matrix **H**, the possible contribution to the right hand side vector **F**, due to the presence of the k^{th} value of the boundary conditions

expressed in terms of potential, is easily calculated by multiplying each column of the ACA to the k^{th} value of each row with opposite in sign. Finally, if the ACA algorithm applied to the block matrix **G** is also successfully reached, the contribution to the right hand side of the eventual presence of the boundary condition expressed in terms of flux is clearly calculated.

4.2.1 Optimisation Procedure for the Right Hand Side Vector

In this subsection a possible procedure to optimise the calculation of the right hand side vector is described.

In order to calculate the minimum number of terms four different alternatives which depend upon the boundary conditions need to be analysed:

1. the values of the boundary conditions are all zero;
2. application of ACA algorithm a second time;
3. population of the missing columns;
4. population of the missing rows.

The first case occurs when all the boundary conditions are zero. Thus there is no need to calculate the contribution of the block matrix to the final right hand side and another block matrix can be analysed. The last three options are to optimise the number of the elements of the matrices that still need to be calculated.

Owing to the fact that the number of entries needed for the ACA is, in most cases, equal for both the block matrix **G** and **H**, the number of elements that must be calculated is

$$N_{ACA}^{II} = n_{ACA}^{I} \times m + n_{ACA}^{I} \times n \tag{4.15}$$

where n^I_{ACA} is the number of rows (or columns) calculated in the first application of the ACA.

Moreover, in the case that there are only a few non-zero boundary conditions, say n_{zBC}, only selected columns of the original block matrix are needed and the total number of elements to be calculated is

$$N_{dir1} = N_{zBC} \times m \tag{4.16}$$

The final option corresponds to calculating the remaining contribution of the right hand side block matrix directly and depends on the following numbers

$$N_{dir2} = n \times (m - n^I_{ACA}) \tag{4.17}$$

In conclusion, if the first alternative is not verified, the lower number between N^{II}_{ACA}, N_{dir1} and N_{dir2} drives the choice for calculating the right hand side contribution of each block.

4.3 System Solution

Once the hierarchical representation of the collocation matrix has been established, the solution of the system can be computed either directly, through hierarchical matrix inversion [54], or indirectly, through iterative solvers that exploit the efficient matrix-vector product in low rank format [11]. In the present thesis a GMRES iterative solver [106] with and without a block-diagonal preconditioner is implemented and assessed for H-matrix format for solving the system of equations. The method, proposed by Saad and Schultz (1986) and further developed by many other authors [3, 48, 81, 89], is a Krylov based iterative method for the numerical solution of a system of linear equations, as that formed by BEM. The Arnoldi iteration is used to form a basis for the Krylov

subspace.

Moreover, the dissertation is enlarged with a procedure for evaluating the potential and particle velocity at selected internal points.

4.3.1 GMRES

The GMRES is an iterative method based on the Krylov space [3, 81, 89].

As presented in the previous chapter, the BEM yields to a system of N linear equations that can be written as follows

$$\mathbf{AY} = \mathbf{F} \tag{4.18}$$

where $\mathbf{A}$ is a $N \times N$ square matrix, $\mathbf{F}$ is the right hand side term and $\mathbf{Y}$ is a vector that collects all the unknown of the problem.

The procedure starts with an initial guess $\mathbf{Y}_0$ that produces a residual that can be easily computed

$$\mathbf{r}_0 = \mathbf{F} - \mathbf{AY}_0 \tag{4.19}$$

At the $m - th$ iteration the approximated solution is computed as follows

$$\mathbf{Y}_m = \mathbf{Y}_0 + \mathbf{V}_m\mathbf{X} \tag{4.20}$$

where $\mathbf{X}$ is a $m \times 1$ complex vector and $\mathbf{V}_m$ is a complex basis for the m-order Krylov subspace defined as

$$\mathcal{K}_m = span\left\{\mathbf{r}_0,\, \mathbf{Ar}_0,\, \ldots,\, \mathbf{A}^{m-1}\mathbf{r}_0\right\} \tag{4.21}$$

GMRES approximates the exact solution by the vector $\mathbf{Y}_n \in \mathcal{K}_n$ that minimises the norm of the residual $\mathbf{r}_n = \mathbf{F} - \mathbf{AY}_n$. The vectors $\mathbf{r}_0,\, \mathbf{Ar}_0,\, \ldots,\, \mathbf{A}^{m-1}\mathbf{r}_0$ are almost

linearly dependent, so instead of this basis the Arnoldi iteration is utilised to achieve orthonormal vectors

$$\mathbf{v}_1,\ \mathbf{v}_2,\ \ldots,\ \mathbf{v}_m \tag{4.22}$$

The Arnoldi process produces a $m \times m$ upper Hessenberg matrix $\mathbf{H}_m = \mathbf{V}_m^* \mathbf{A} \mathbf{V}_m$, with $\mathbf{V}_m^*$ complex conjugate of $\mathbf{V}_m$, and satisfies the relationship

$$\mathbf{A}\mathbf{V}_m = \mathbf{V}_{m+1}\tilde{\mathbf{H}}_m \tag{4.23}$$

where $\tilde{\mathbf{H}}_m$ is a $(m+1) \times m$ matrix defined as follows

$$\tilde{\mathbf{H}}_m = \begin{bmatrix} \mathbf{H}_m \\ 0 \cdots 0\ h_{m+1,m} \end{bmatrix} \tag{4.24}$$

where $h_{m+1,m}$ is evaluated by using the matrices $\mathbf{A}$, $\mathbf{V}_{m-1}$ and $\mathbf{H}_{m-1}$.

Now, the residual of the approximated solution (4.20) at the $m-th$ iteration can be written

$$\mathbf{r}_m = \mathbf{F} - \mathbf{A}\mathbf{Y}_m = \mathbf{F} - \mathbf{A}(\mathbf{Y}_0 + \mathbf{V}_m\mathbf{X}) = \mathbf{r}_0 - \mathbf{A}\mathbf{V}_m\mathbf{X} = \mathbf{r}_0 - \mathbf{V}_{m+1}\tilde{\mathbf{H}}_m\mathbf{X} \tag{4.25}$$

Calling $\mathbf{b}_1 = \mathbf{r}_0/\gamma$ with $\gamma = ||\mathbf{r}_0||_2 = \sqrt{\mathbf{r}_0 \cdot \mathbf{r}_0}$, where $\cdot$ is the dot product, yields

$$\mathbf{r}_m = \mathbf{V}_{m+1}(\gamma\mathbf{e}_1 - \tilde{\mathbf{H}}_m\mathbf{X}) \tag{4.26}$$

where $\mathbf{e}_1$ is the canonical vector in the standard basis $\mathbb{R}^{m+1}$.

Due to the fact that $\mathbf{V}_{m+1}$ is an orthonormal matrix, $\mathbf{X}$ gives the solution of the system of equations (4.18) when the residual norm $||\mathbf{r}_n||_2 = ||\gamma\mathbf{e}_1 - \tilde{\mathbf{H}}_n\mathbf{X}||_2$ is minimal

$$\min_{\mathbf{X}\in\mathbb{C}^n} ||\gamma\mathbf{e}_1 - \tilde{\mathbf{H}}_n\mathbf{X}||_2 \tag{4.27}$$

This minimisation process gives to the iterative solver its name. In what follows $\mathbf{X}_j$ indicates the solution at the $j-th$ iteration.

The GMRES steps can be highlighted as follows:

- Do one step of the Arnoldi method;
- find $\mathbf{X}_m$ so that $\mathbf{r}_m$ is minimised;
- compute $\mathbf{Y}_m = \mathbf{Y}_0 + \mathbf{V}_m\mathbf{X}$;
- repeat till the required accuracy have not been obtained.

The algorithm utilised in simulations of the present thesis is shown below. A complete presentation of the GMRES method is beyond the scope of the present thesis. For more information on this subject the reader is referred to [3, 48, 81, 89].

At every iteration, a matrix-vector product must be computed. In all the on-line complex GMRES routines available for FORTRAN, the generation of the whole matrix $\mathbf{A}$ is needed. In the present work the whole matrix is never calculated, resulting in a reduction in memory requirements. The routine adopted is an O(N) procedure taking full advantage from the H-matrix approach [62], instead of $O(N^2)$ for a standard multiplication.

It should be noted that the value of $h_{j+1,j}$ may be zero during the Arnoldi process, which means that the subspace $\mathcal{K}_j$ is invariant under $\mathbf{A}$ and the exact solution has been achieved.

The main GMRES drawback is the storage requirement of the orthogonal basis $\mathbf{V}_m$ and the Hessenberg matrix $\tilde{\mathbf{H}}_m$ that may become prohibitive when the convergence is slow and the size of the problem is large. To eliminate this problem a **Do** loop can be included, that, in case the solution has not reached after a series of iteration,

deletes $\mathbf{V}_m$ and $\tilde{\mathbf{H}}_m$, saves the solution achieved and restarts a new iteration with this solution. Due to the fact that the convergence strongly depends upon $\mathbf{V}_m$ and $\tilde{\mathbf{H}}_m$ already calculated, in the new iteration the convergence is always slower.

Algorithm 4.4 GMRES.

Set *tolerance* and *maxit*

$\mathbf{Y}_0 = \mathbf{F}$

Compute $\mathbf{r}_0 = \mathbf{F} - \mathbf{A}\mathbf{Y}_0$

If $\mathbf{r}_0 = \mathbf{0}$ **Then End**

Else

$\mathbf{v}_1 = \frac{\mathbf{r}_0}{||\mathbf{r}_0||_2}$

$\gamma_1 = \sqrt{\mathbf{r}_0 \cdot \mathbf{r}_0}$

Do $j = 1, \ldots, maxit$

Do $i = 1, \ldots, j$ $h_{ij} = \mathbf{v}_i^T \mathbf{A}\mathbf{v}_j$ **End Do**

$\omega_j = \mathbf{A}\mathbf{v}_j - \sum_{i=1}^{j} h_{ij}\mathbf{v}_j$

$h_{j+1,j} = ||\omega_j||_2$

Do $i = 1, \ldots, j-1$

$$\begin{pmatrix} h_{ij} \\ h_{i+1,j} \end{pmatrix} = \begin{pmatrix} c_{i+1} & s_{i+1} \\ s_{i+1} & -c_{i+1} \end{pmatrix} \begin{pmatrix} h_{ij} \\ h_{i+1,j} \end{pmatrix}$$

End Do

$\beta = \sqrt{h_{jj}^2 + h_{j+1,j}^2}$

$s_{j+1} = \frac{h_{j+1,j}}{\beta}$

$c_{j+1} = \frac{h_{jj}}{\beta}$

$h_{jj} = \beta$

$\gamma_{j+1} = s_{j+1}\gamma_j$

$\gamma_j = c_{j+1}\gamma_j$

If $\{|\gamma_{j+1}| > tolerance \, and \, j < restart\}$ **Then** $v_{j+1} = \frac{\omega_j}{h_{j+1,j}}$

Else

Do $i = j, \ldots, 1$ $\mathbf{X}_i = \frac{1}{h_{ii}} \left(\gamma_i - \sum_{k=i+1}^{j} h_{ik}\mathbf{X}_k \right)$ **End Do**

$\mathbf{Y} = \mathbf{Y}_0 + \sum_{i=1}^{j} \mathbf{X}_i v_i$

End If

End Do

End If

The convergence rate associated with an acoustic simulation depends upon the fre-

quency and the mesh of the geometry. As mentioned in the previous chapter, the wavelength drives the size of each element, hence the number of the elements of a mesh. On the other hand, a given mesh can perform only simulation up to a certain specific frequency f_s. If the frequency is lower than f_s, the convergence rate is high and the solution is achieved after a few iterations, whereas if the frequency is almost f_s the convergence is slow. When the convergence rate is low, as is often the case when dealing with BEM systems, a preconditioner can be computed taking full advantage of the representation in hierarchical format. For $\mathbf{AY} = \mathbf{F}$ system a left preconditioner is an easily invertible matrix $\mathbf{M}$ such that the condition number of the system $\mathbf{M^{-1}A\,y} = \mathbf{M^{-1}F}$ results lower than the original one, improving thus the convergence rate of the iterative solver.

The GMRES residual tolerance set to obtain all the solutions in the thesis is 10^{-5}.

4.3.2 Internal Points

The ACA algorithm can also be used to speed up the calculation of potential and particle velocity at internal points from the boundary values of potential and flux. To achieve this, a cluster tree for the internal points is generated following the procedure seen at the beginning of this section. Thus the hierarchical tree is generated by considering the columns and the rows of the block matrices $\overline{\mathbf{H}}$, $\overline{\mathbf{G}}$, $\overline{\mathbf{H}}'$ and $\overline{\mathbf{G}}'$ (see equations (3.51) and (3.54)). The ACA procedure is applied four times to all the matrices. The name of such a pointer, the values of the parameters η and *cardinality* remain unchanged and hence the same routines as for the boundary points can be applied.

4.4 Numerical Results

In order to demonstrate the efficiency of the proposed method a series of numerical tests have been performed. Results of a parametric study identify the values of two

parameters, i.e., the value of η and the *cardinality*, to achieve the best performance. Comparisons with the standard BEM with a direct solver [45], with LMS Virtual.Lab [82] and with Fast Multipole Method (FMM) for acoustics [1] show that the formulation presented here can significantly reduce the system solution time. All of the numerical simulations were executed on a Xeon(TM) CPU 3.00GHz processor with 2GB of RAM.

Parametric Study

The first analysis presented in this section is to investigate the value of η and the *cardinality*. Two geometries have been tested, i.e., a sphere and an aircraft cabin.

The sphere and cabin surface are discretised with 4764 and 15480 triangular super-parametric constant elements, respectively. The sphere is considered to be pulsating with unitary vibration velocity, sound speed and angular frequency. The geometry of the cabin is shown in figure 4.10. Only half cabin has been modelled. The front panel has been eliminated in the figure to better visualize the internal geometry. A symmetry panel, not shown in the figure, creates a closed surface and it has been set to be hard to generate the other half cabin. For simplicity all the other surfaces within the cabin are assumed to be vibrating. The sound speed and angular frequency have been set equal to 340 m/s and 680 Hz, respectively.

The influence of the cardinality on the total solution time is investigated first.

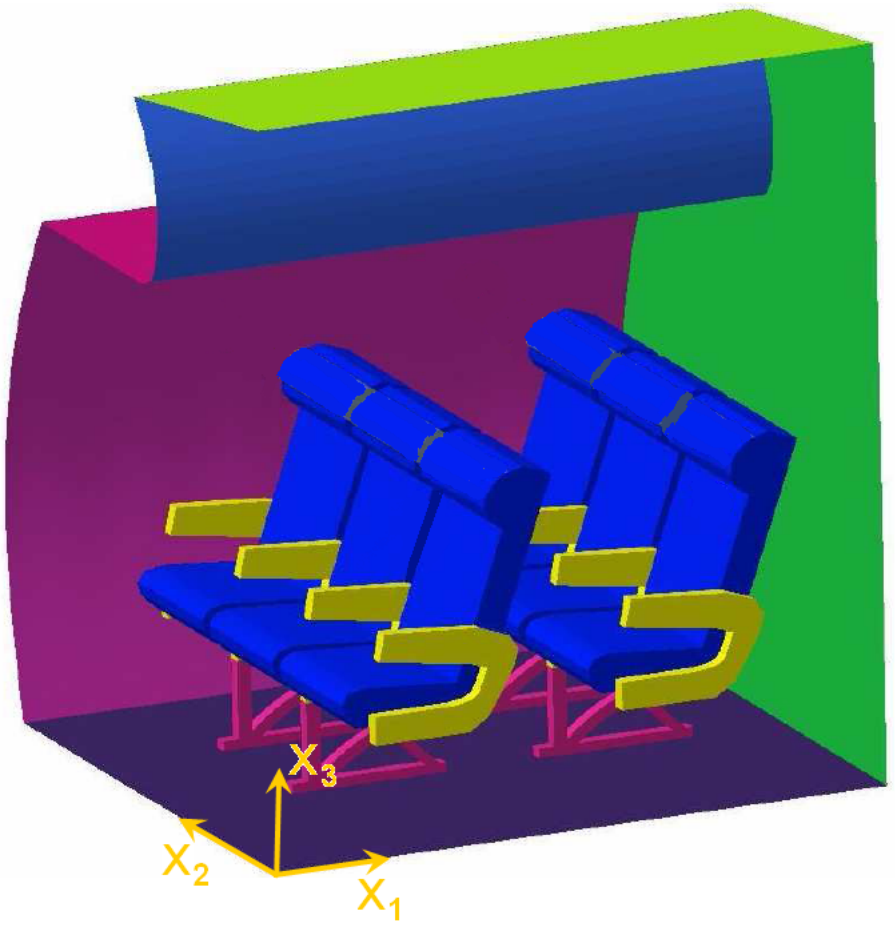


Figure 4.10: Cabin geometry.

Cardinality

A time ratio has been defined by dividing the solution time at different cardinality values by the time achieved at the *cardinality* set to 25. Figures 4.11 and 4.12 show the time ratio trends, for the sphere and the cabin, respectively, of the assembly time, solution time and total time for different *cardinality* values. In both figures, it can be noted that *cardinality* equal to 25 gives the best performance for the solution time, and *cardinality* 50 for the assembly time. In figure 4.11 it is evident that the total time is strongly influenced by the assembly time. This is due to the fact that the GMRES

routine requires only a few iterations to evaluate the solution. On the other hand, in the case of the cabin (figure 4.12), the GMRES requires five iterations to obtain the solution, but as the degrees of freedom are higher than the previous case, so that the solution time influences the total time.

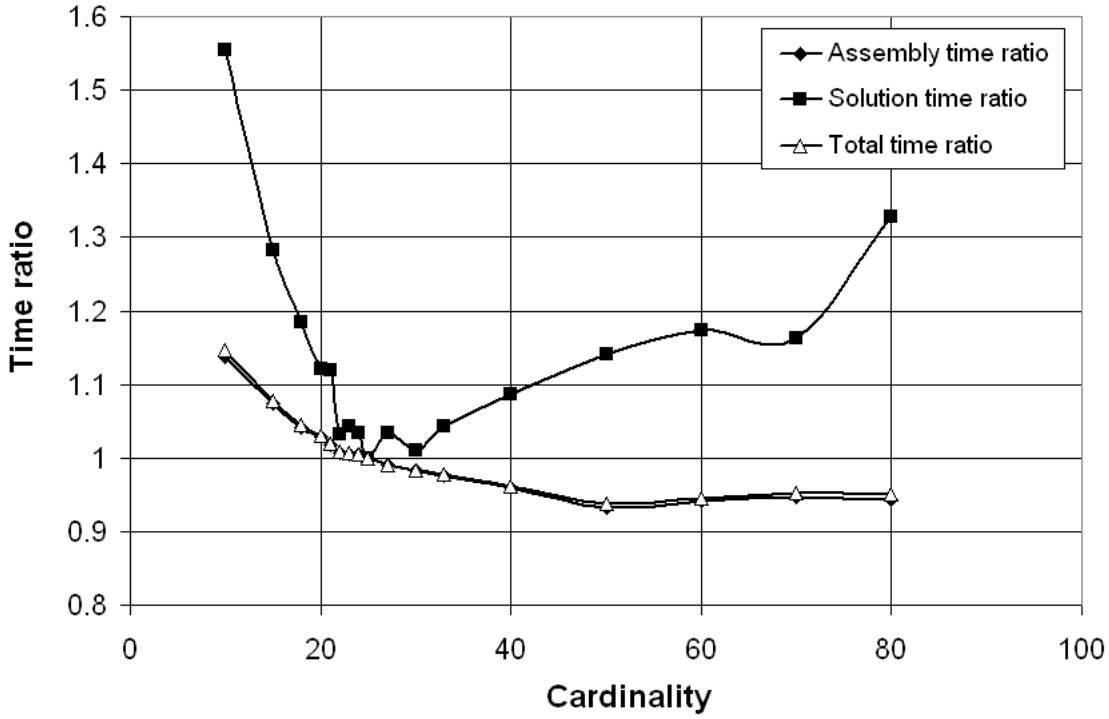


Figure 4.11: Influence on the assembly time, solution time and total time ratios due to the cardinality for a pulsating sphere.

For higher frequencies the assembly time remains almost unchanged, whereas the solution time grows almost linearly (see the analysis below). Therefore, if the assembly time prevails on the solution time, the best choice is to set the cardinality 50, otherwise the best option is 25. In the following simulations the cardinality is set equal to 25 due to the fact that, in general, the geometry is discretised to have the lowest degrees of freedom for the analysed frequency, so that the total solution time is mainly influenced by solution time rather than the assembly time.

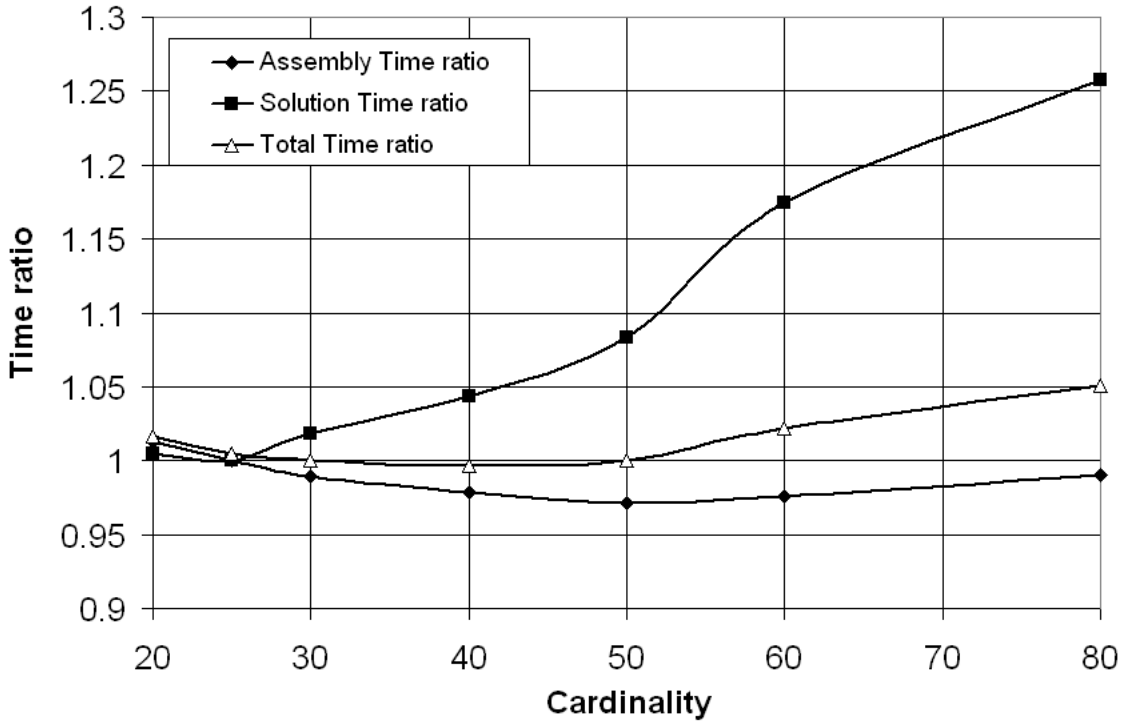


Figure 4.12: Influence on the assembly time, solution time and total time ratios due to the cardinality for an aircraft cabin.

η

Figures 4.13 and 4.14 show the influence of η on the assembly time ratio, the solution time and total time for the sphere and the cabin, respectively. This ratio is obtained by dividing the solution time by the solution time $\eta = 10$. The solution times for both cases highlight that a higher value of η improves the code performance. For $\eta > 4$ the code performances can be improved only in a 5% CPU time acceleration. In the following simulation η is set equal to 10.

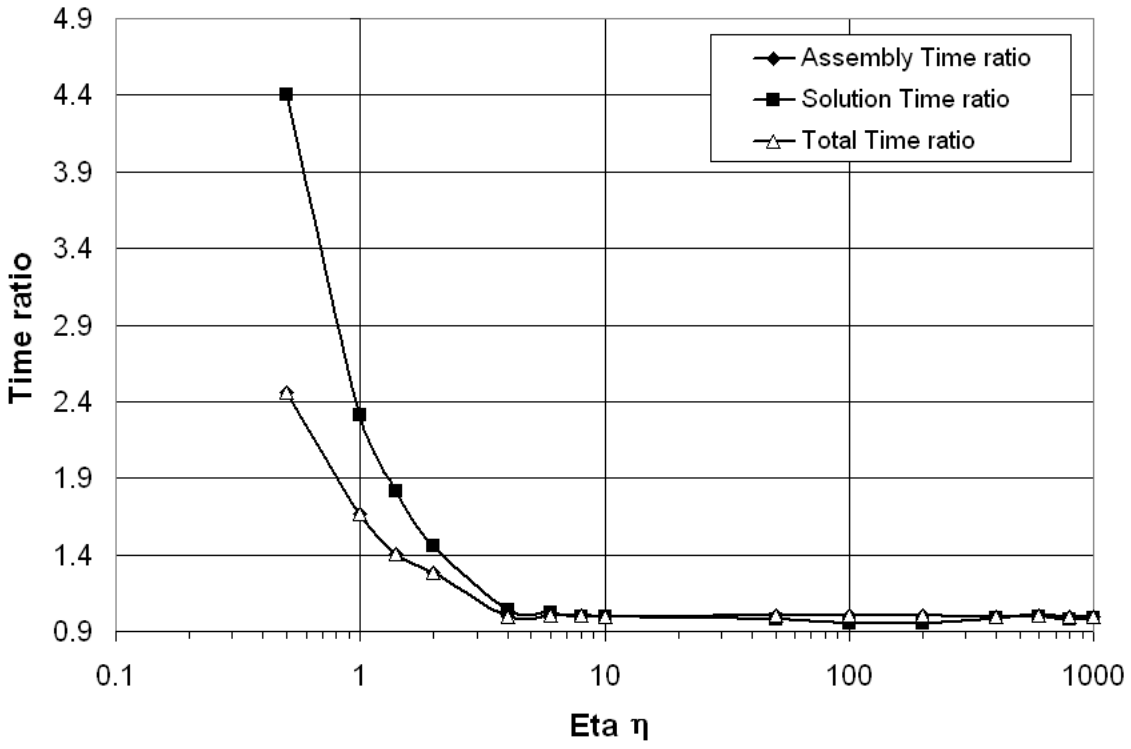


Figure 4.13: Influence on the assembly time, solution time and total time ratios due to η for a pulsating sphere.

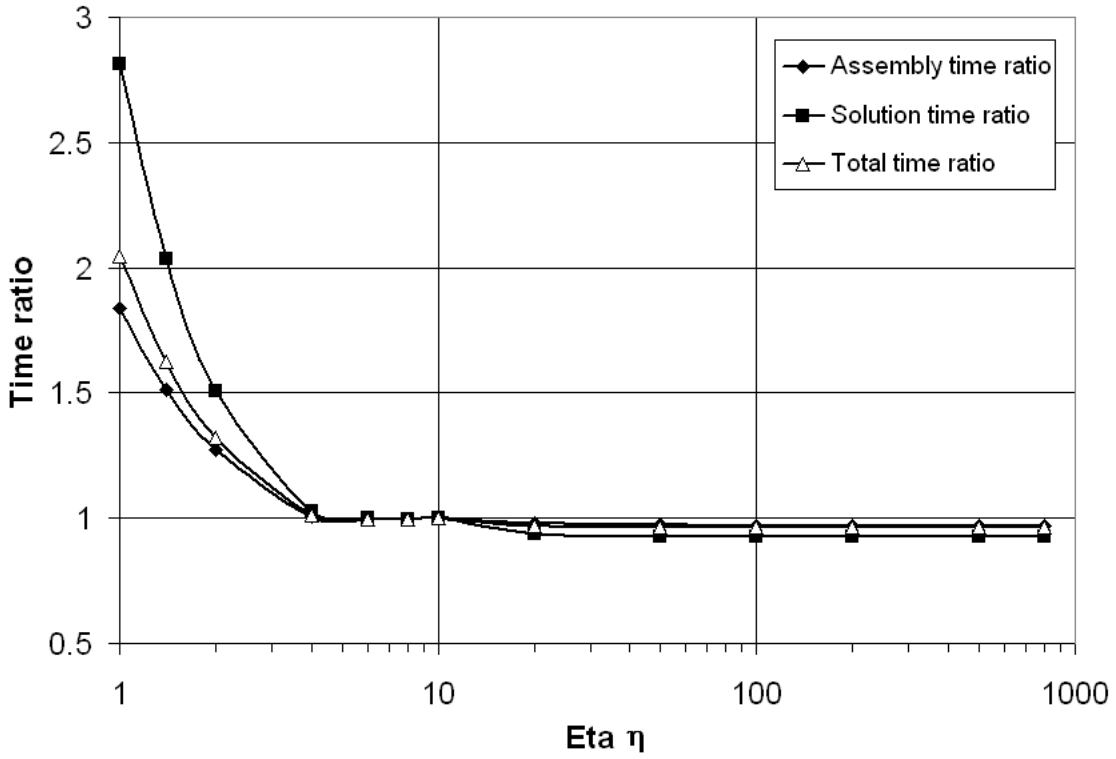


Figure 4.14: Influence on the assembly time, solution time and total time ratios due η for an aircraft cabin.

The main advantage in using η with high value is related to the memory storage requirements of the solving matrix $\mathbf{A}$, as shown in 4.15. The figure shows the block-wise structure of the collocation matrix as generated by the ACA algorithm for a pulsating sphere constituted with 6100 elements for four different values of η (1, 2, 4 and 10). The tone of grey is proportional to the ratio between the memory required for the low rank representation and the memory required for a standard format. Hence, black blocks stand for the full rank block matrix, while almost white blocks are those for which the ACA compression works better.

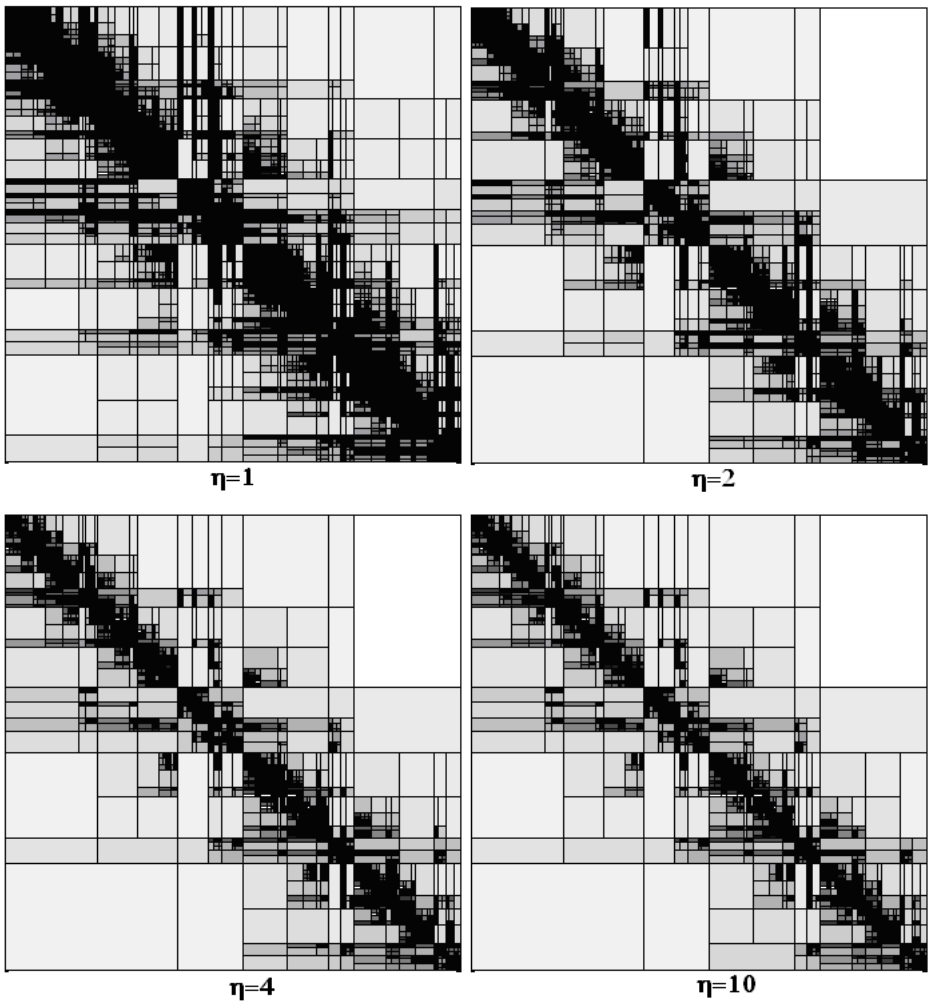


Figure 4.15: Block-wise representation of the ACA generated matrix for $\eta = 1$, $\eta = 2$, $\eta = 4$ and $\eta = 10$.

RABEM vs. SBEM vs. LMS

The problem of the sound radiated by a pulsating sphere with radius r, wave number k and uniform radial velocity all equal to unity is investigated. The acoustic wave velocity and the medium density are set equal to unity. The standard three-dimensional scalar wave propagation formulation using super-parametric (constant unknowns, linear geometry) boundary elements [45], will be referred to as "SBEM", and it is used for

comparison purposes. Table 4.1 compares the two codes speed up ratio (defined as CPU time of SBEM divided by CPU time of RABEM) for setting up the system solution, finding the solution and for the total time for eight different mesh accuracies. The relative percentage error in all the simulations, defined as follows

$$err\,\% = \frac{sol_{SBEM} - sol_{RABEM}}{sol_{SBEM}} \tag{4.28}$$

has been evaluated by comparing the solution at each point obtained by the SBEM code (sol_{SBEM}) with the solution obtained by the RABEM code (sol_{RABEM}) and it is less than 1 %. Comparisons in terms of the speed up ratio are also made with the commercial code LMS Virtual.Lab as shown in table 4.1.

	SBEM/RABEM			LMS/RABEM
dof	Setting up System Solution	Solver	Total	Total
646	0.8	107.9	2.2	0.88
1126	1.0	180.6	3.6	0.45
2112	1.5	611.6	7.8	0.31
3240	2.0	1669.9	18.3	0.33
4764	2.6	4409.8	44.6	0.57
6100	3.2	5562.1	55.4	0.93
8488	4.1	13165.7	132	1.5
10340	5.0	18513.2	175.7	1.8
20232	-	-	-	3.5
28194	-	-	-	10.3

Table 4.1: Speed up ratio between the RABEM, SBEM and LMS.

The comparison with SBEM demonstrates that the RABEM formulation is effective in the population of the linear system when more than 2000 degrees of freedom mesh is studied. However, the GMRES routine is effective even considering a limited number of elements.

Comparison of RABEM and LMS for a rigid sphere (same medium characteristic as seen in the first example) scattered by a plane waves with unit amplitude and zero

phase is shown in figure 4.16.

It must be pointed out that no attempt has been made to optimise the general BEM routines of integration etc. in the RABEM and they remain the same as in the standard BEM (SBEM).

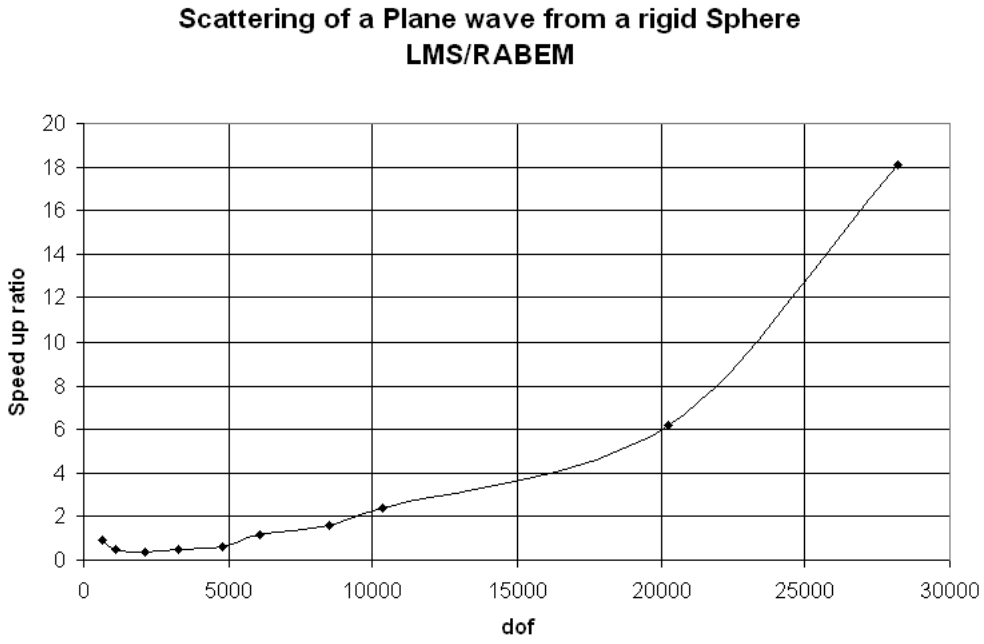


Figure 4.16: Speed up ratio for a scattered rigid sphere by a plane wave - LMS/RABEM.

Internal Points

To demonstrate the speed up that can be achieve when the ACA is applied at selected internal points, the CPU time of the RABEM and standard code is compared for the 3240 dof pulsating sphere and for four sets of internal points: 546, 2184, 4368 and 10374. Once again the speed up ratio is defined as the ratio of CPU times obtained by SBEM over RABEM. Figure 4.17 shows the resulting acceleration during the procedure for calculating the internal point potential. The RABEM CPU time required depends

upon the location of such internal points as well as the dof of the boundary mesh. The standard procedure is invariant to the location, while the rank of the approximated matrices decreases as the points are further away from the boundary of the problem.

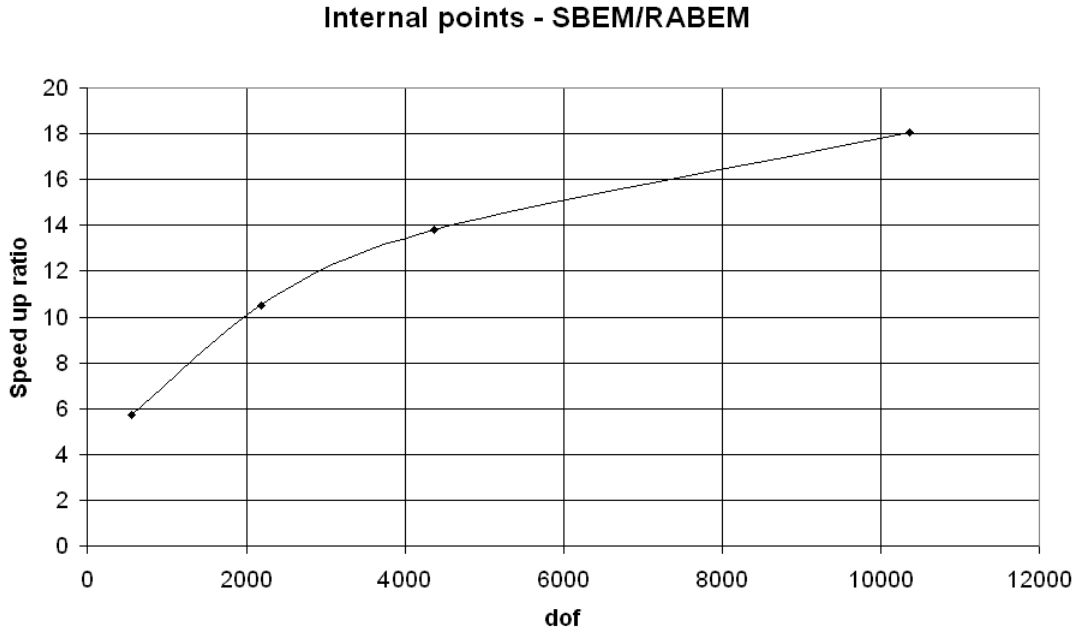


Figure 4.17: Speed up ratios relates to four different groups of internal points for a pulsating sphere discretised with 3240 super-parametric triangular elements.

Frequency Variation

The variation of the computational time with respect to varying frequency is studied in the problem of pulsating sphere. The example tested in the first above (with the same boundary conditions) is studies for 8 angular frequencies (1, 2, 4, 8, 12, 16, 20, 30 rad/s). The mesh has 10340 super-parametric (constant unknowns, linear geometry) triangular elements. Figure 4.18 shows the ratios obtained by dividing the CPU times for different angular frequencies with the CPU time for the angular frequency of 1 Hz/rad. As evident, the CPU time increases almost linearly.

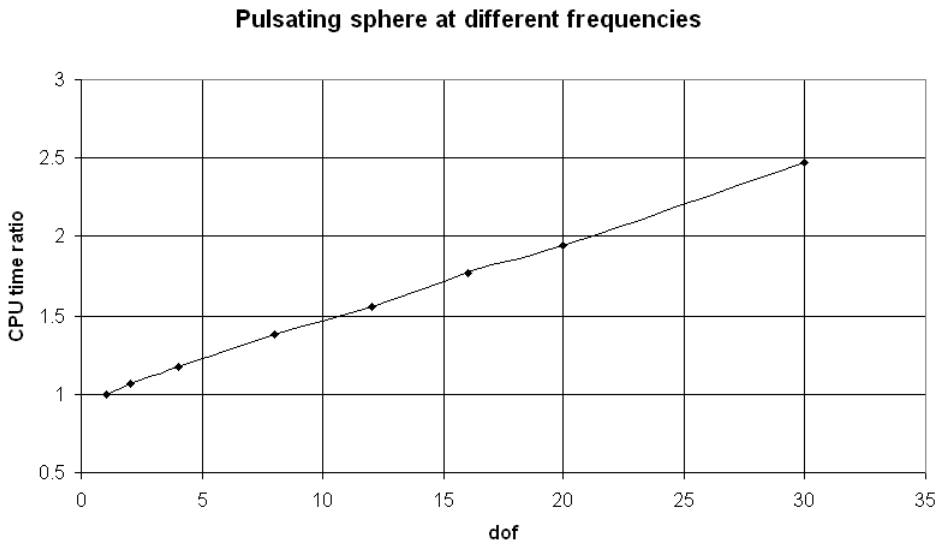


Figure 4.18: CPU time ratios for different angular frequencies for a pulsating sphere meshed with 10340 triangular elements.

A Row of Seats in an Aircraft Cabin

Another example to which the RABEM has been applied is a row of three seats of an aircraft cabin as shown in figure 4.19. The surface of the seats has been divided into 27,284 super-parametric triangular elements. The maximum extensions along the x_1, x_2, x_3 axes are 694, 1563 and 960 millimetres, respectively. The sizes of the smallest and the largest triangles are 3.58E-03 and 2.38E-02 millimetre, respectively, so the maximum frequency that can be applied is around 1.3-1.5 kHz. In the simulation performed all the surfaces have been set as hard and a monopole with unit complex potential amplitude has been inserted at the centre of the left seat with a distance of 7.4 and 21.8 cm from the cushion and the back of the seat, respectively. The speed up ratio related to the Fast Multipole Method FMM and for the RABEM without preconditioner (RABEM) and with a block diagonal preconditioner (RABEMpdb) are displayed in the figure 4.20 for nine different frequencies (100, 200, 400, 600, 800, 900,

1000, 1100 and 1200 Hz). As evident, RABEM is faster than the FMM code [131] for higher frequencies. In particular for frequencies lower than 400Hz FastBEM is slightly faster, but as the frequency increases the speed up ratio grows up almost linearly up to 2.6 for 1.2 kHz. In this example the RABEMpdb is never faster than RABEM.

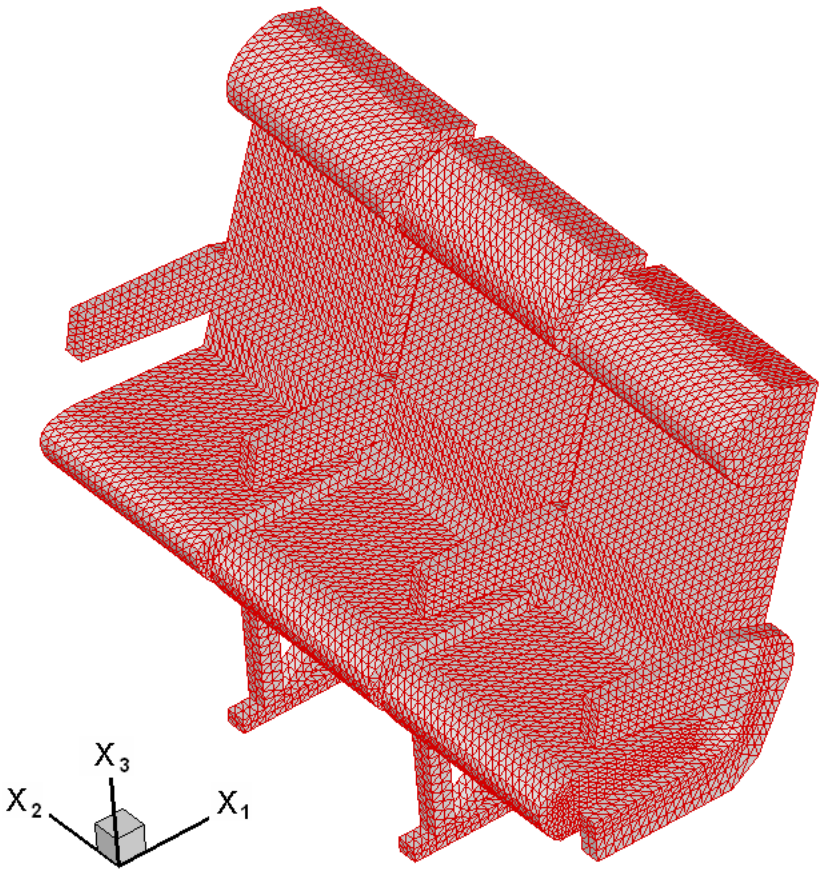


Figure 4.19: Surface of an airplane seat row meshed with 27,284 triangular elements.

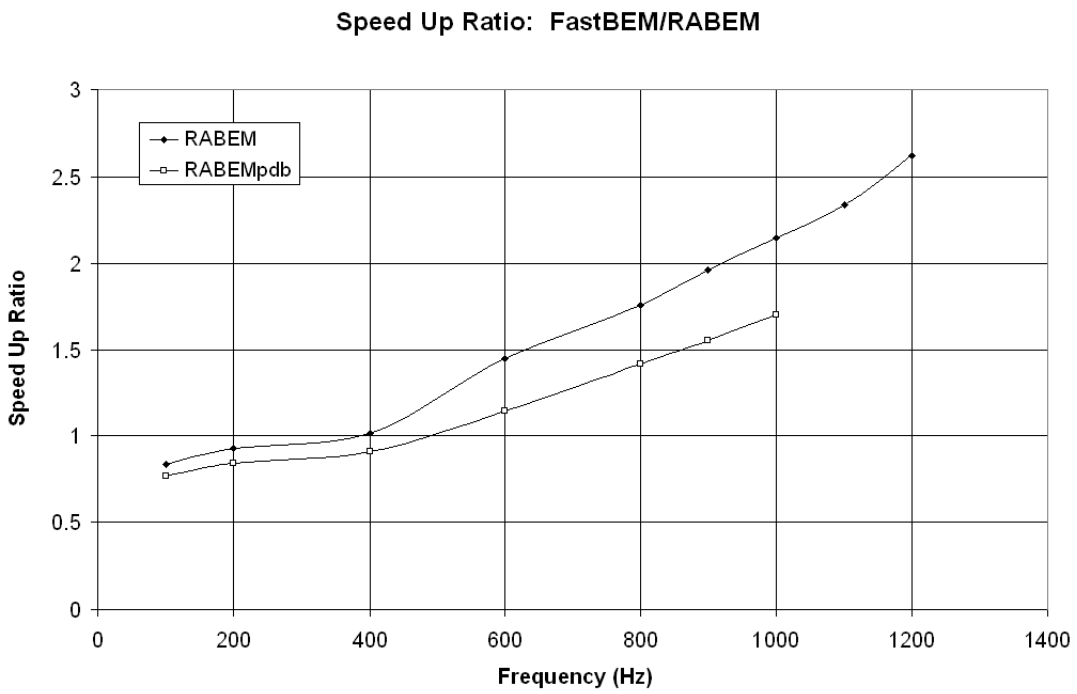


Figure 4.20: Comparison between the unpreconditioned, the diagonal preconditioned and block diagonal preconditioned GMRES for an airplane seat row meshed with 27,284 triangular elements.

The same geometry has been simulated by Virtual.Lab LMS for a frequency of 100Hz. The RABEM code solved it 4.2 times faster than LMS.

Finally, in figure 4.21 the solution in terms of real part of the potential for the 100Hz frequency is displayed.

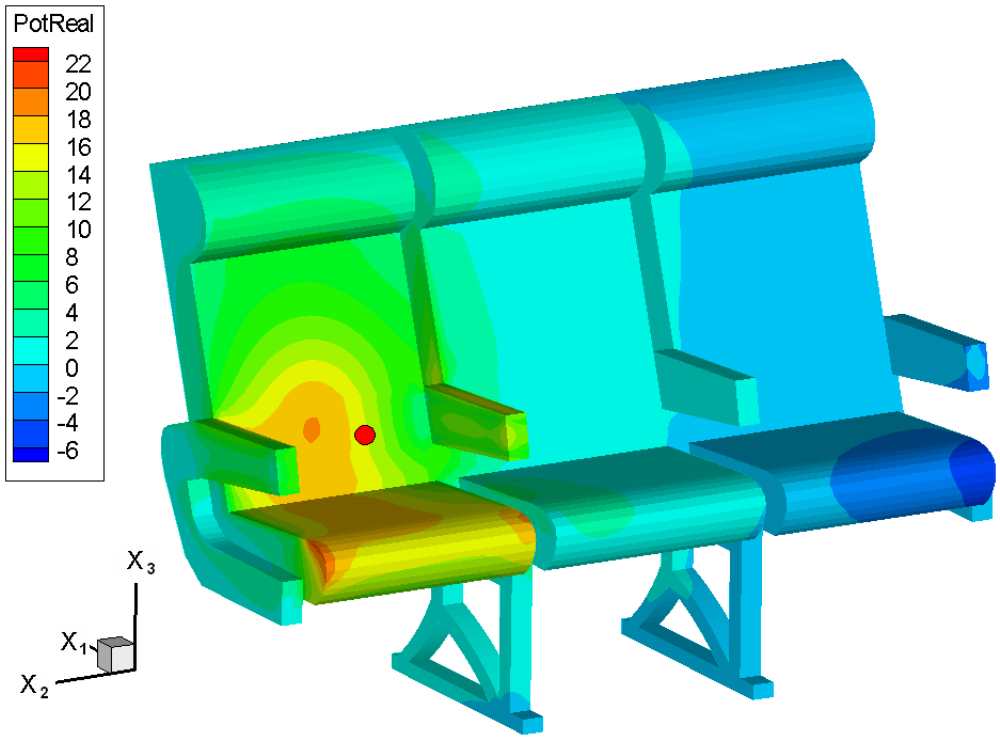


Figure 4.21: Real part of the potential for the aircraft seats when a monopole acts at 100Hz.

Airplane Approaching an Airport

Aircraft traffic is a profoundly irritating factor for people who live in the proximity of airports and hence there is a need to investigate the noise pollution in these areas (see figure 4.22). In this part a series of simulations that tests the sound pressure levels is used to demonstrate the application of RABEM to large scale industrial problems. The problem of reducing the noise level inside residential houses close to airport is beyond the scope of this thesis and more details of this subject can be found in the literature [38, 67].



Figure 4.22: Qantas Boeing 747 approaching runway 27L at London Heathrow Airport, England [128].

Simulations involving 53074 elements (see figure 4.23) of a model representing the Dassault Falcon airplane is presented first. The total length of the aircraft is 18.5 m and the wing span is 22.46 m. The highest frequency applied has been 180 Hz. The sizes of the smallest and the largest triangles are 1.02E-02 and 0.23 mm, respectively, so the maximum frequency that can be applied is around 185 Hz. In the simulations performed all the surfaces have been set as hard and two monopole sources with unit complex potential amplitude have been inserted just in front of the compressors of two engines. Figure 4.24 shows the sound pressure level for 25Hz.

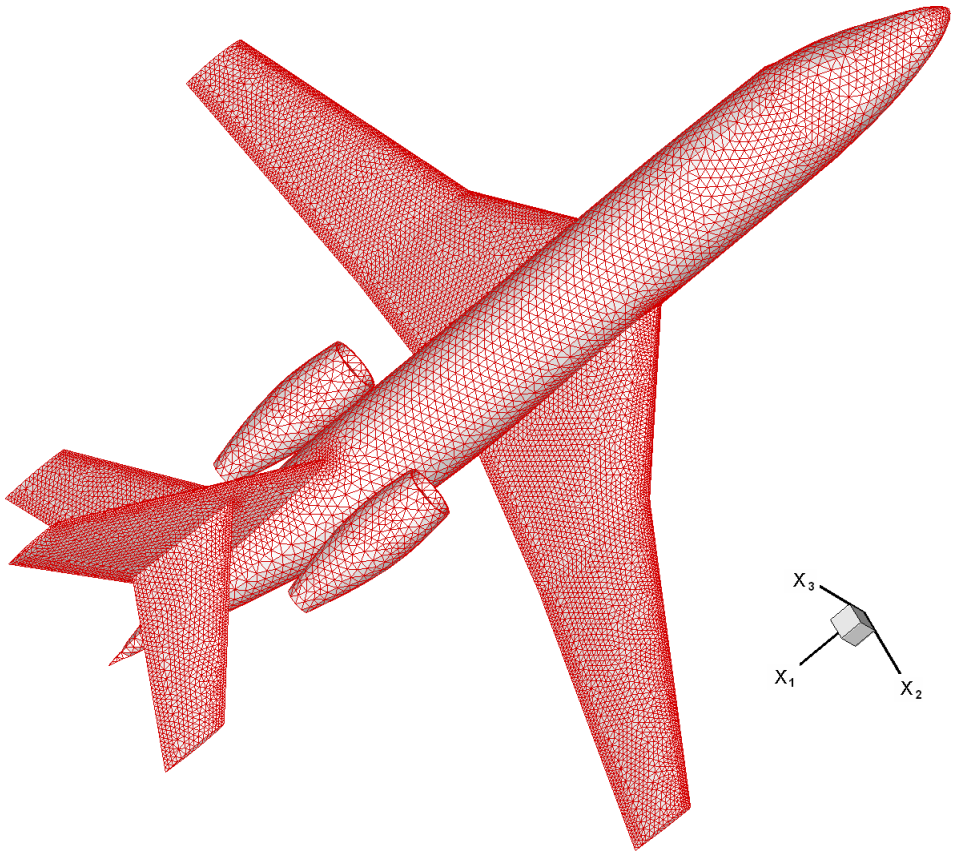


Figure 4.23: 53,074 triangular elements Dassault Falcon mesh.

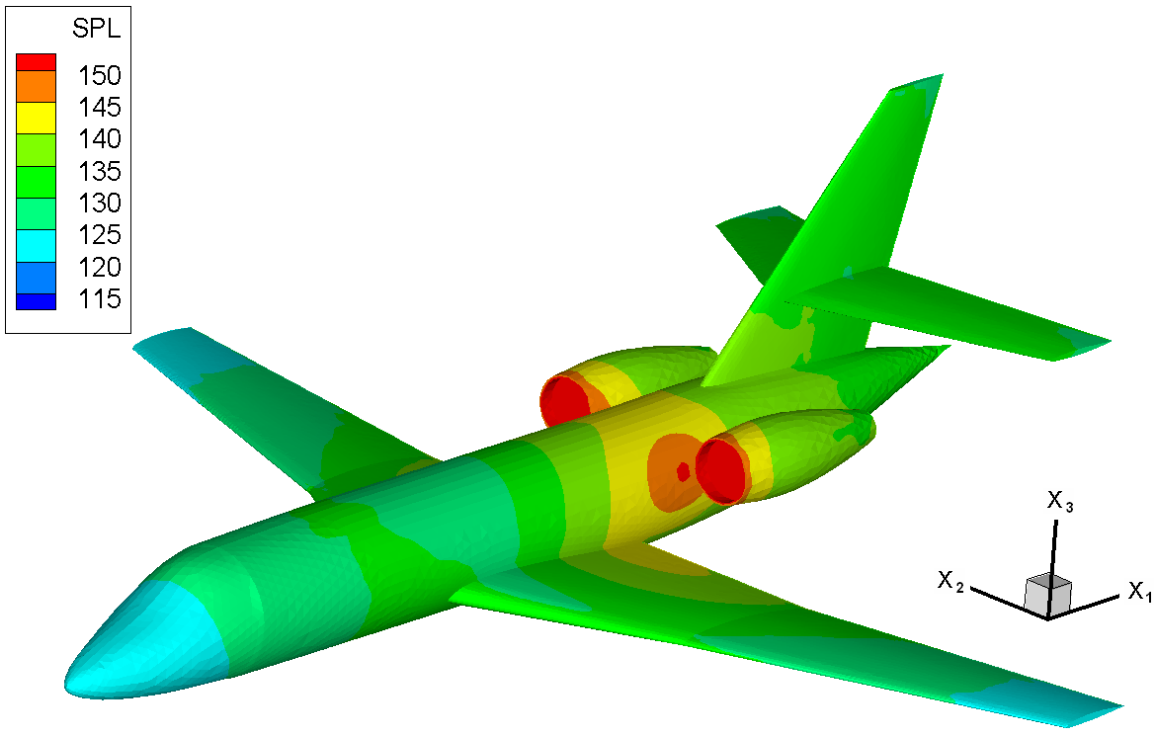


Figure 4.24: Sound pressure level at 25Hz generated by a Dassault Falcon.

The sound pressure level generated by the Dassault Falcon approaching an airport is shown in figures 4.25 and 4.26. Seven simulations are presented considering the aircraft at seven different altitudes from the ground (250, 200, 150, 125, 100, 75, 50 m) for 100 Hz. The perceived noise (A-weighting curve is utilised) goes from around 80 dBA to around 110 dBA when the aircraft altitude is between 150 m and 20 m.

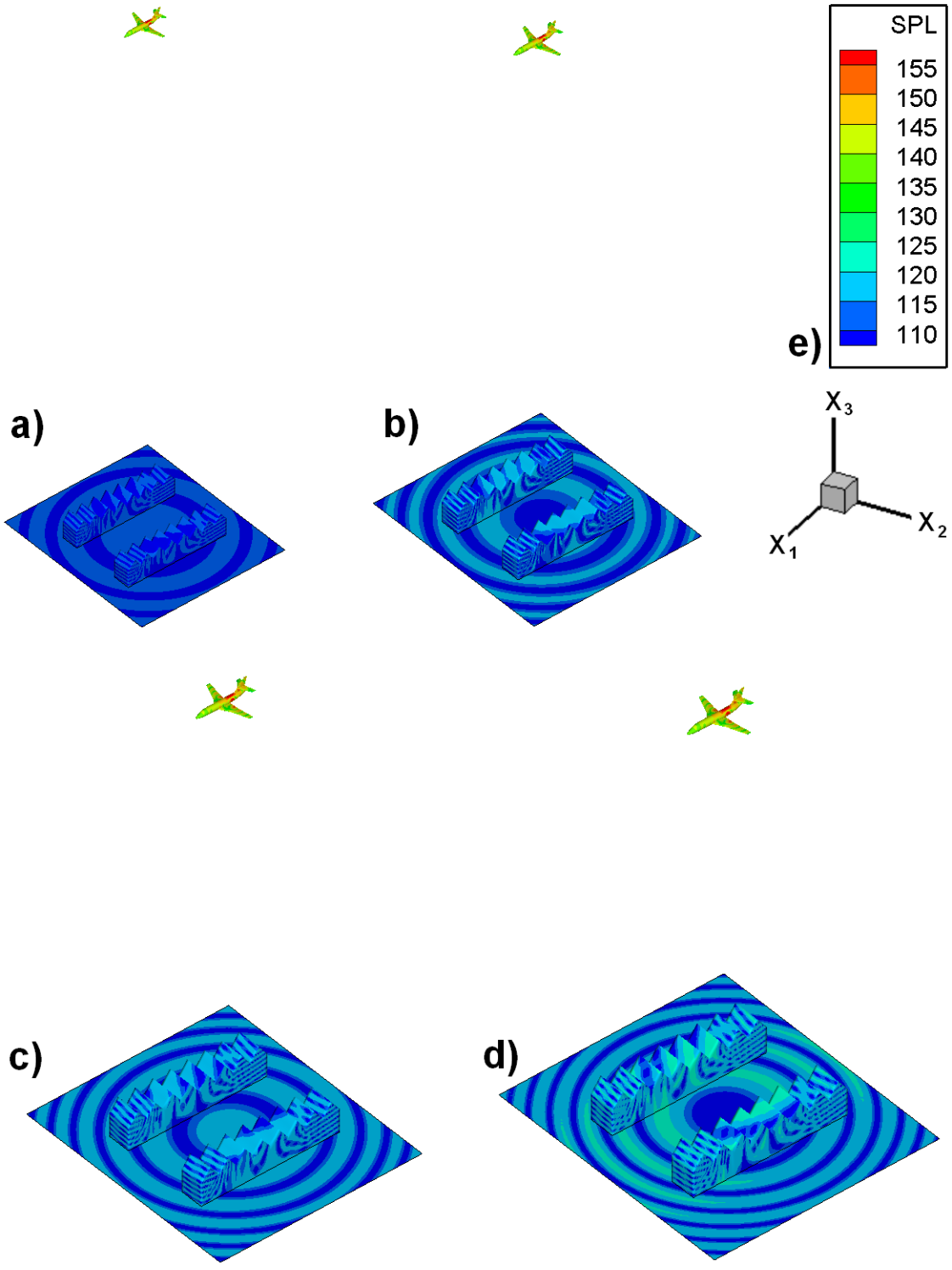


Figure 4.25: Sound pressure level at 100Hz generated by a Dassault Falcon approaching in an airport at different altitudes: a) 250 m; b) 200 m; c) 150 m; d) 125 m.

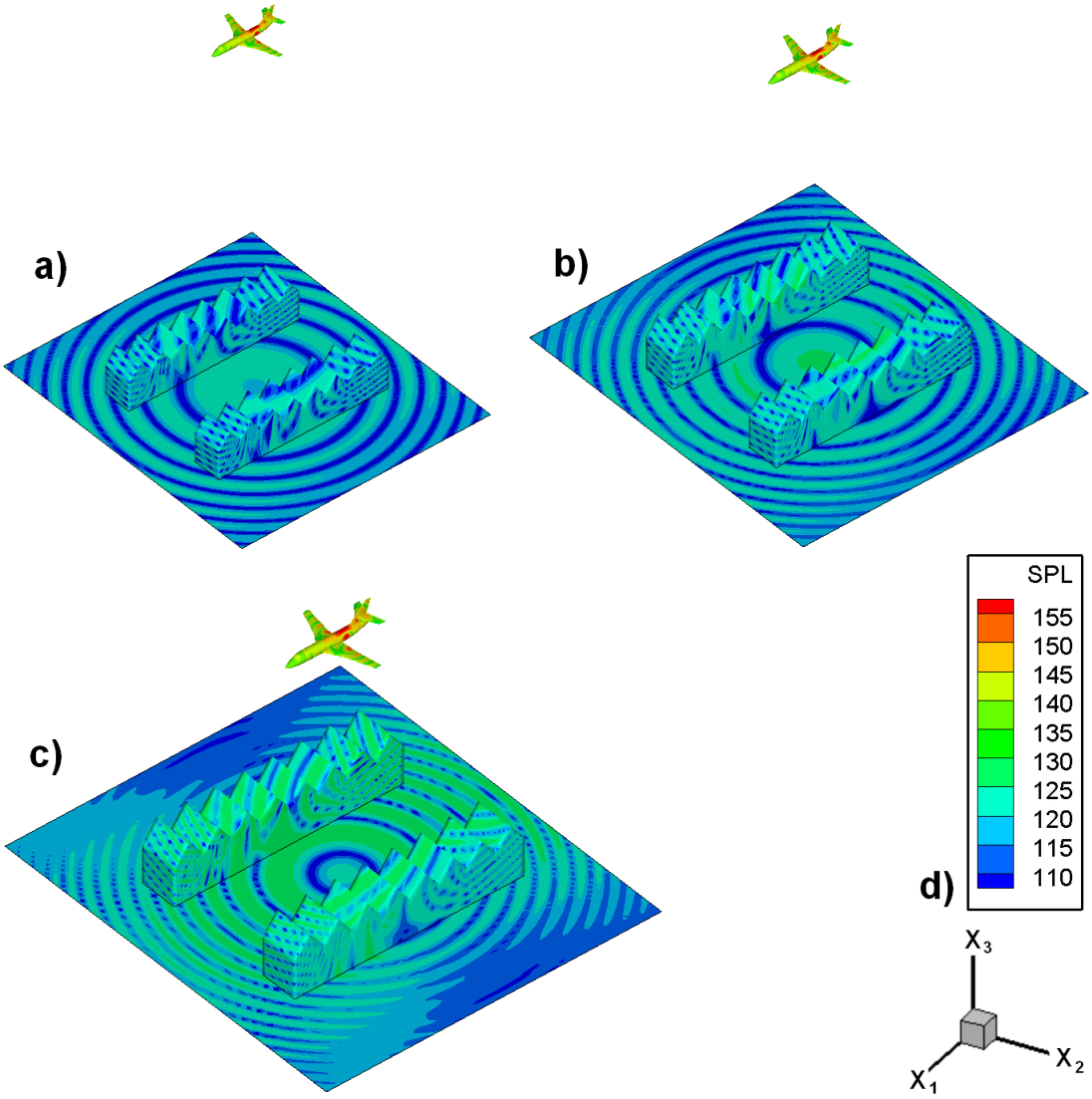


Figure 4.26: Sound pressure level at 100Hz generated by a Dassault Falcon approaching in an airport at different altitudes: a) 100 m; b) 75 m; c) 50 m.

4.5 Summary

A new hierarchical adaptive cross approximation technique coupled with GMRES for 3D boundary element solution of acoustic problems has been presented in this chapter. The solution of linear system of equations is accelerated by calculating only a few entries of the original matrix. The whole matrix has been divided into two groups of blocks (*low* and *full rank*) based on size and distance between a group of collocation points and a group of boundary elements. The latter blocks are represented entirely, whereas the former blocks are approximated with a predefined accuracy that is adaptively achieved. The process leading to the subdivision in sub-blocks and to their further classification is based on a preliminary hierarchical partition, i.e., *cluster tree*, of the matrix index set aimed at grouping subsets of indices corresponding to contiguous nodes and elements. The cluster tree generates the further classification of the matrix blocks, i.e., *block tree*. The low rank format can be applied to those blocks, called *admissible*, that are populated by integrating over a cluster of elements whose distance, suitably defined, from the cluster of collocation nodes is above a certain threshold. An admissible block can be represented in low rank format. Such representation constitutes an approximation of the discrete integral operator based, from the analytical point of view, on a suitable expansion of the kernel of the continuous integral operator. The ACA is a purely algebraic procedure and no expansions of the kernel are necessary as in other popular techniques. This feature makes the procedure particularly appealing since it is not necessary to modify or rewrite the routines for the boundary integration in previously developed codes. Moreover, ACA approximates adaptively a low rank block with *a priori* selected accuracy, so that the resulting accuracy is always comparable to standard codes. The conventional ACA algorithm has been slightly modified to avoid possible problems. The whole procedure takes advantage of the $\mathcal{H}$-Matrix format that accelerates the system solution. Different types of boundary conditions have been im-

plemented into the ACA solution algorithm. The right hand side vector evaluation has been accelerated by implementing a proposed procedure. The ACA and the H-Matrix format are also employed for the post processing steps required to evaluate the potential and particle velocity values at the internal points. The GMRES with and without a block-diagonal preconditioner has been tested for a series of numerical examples. The superparametric formulation with constant unknowns and linear geometry elements is utilised. A parametric analysis is investigated first. Then two simple benchmark problems of the pulsating sphere and of the scattering of a plane wave from a rigid sphere have been investigated. Large scale applications involving a row of three seats representing the seats in an aircraft cabin and noise emanating from engines of the Dassault Falcon aircraft have been also presented. The tests carried out have shown that the new assembly and solution technique can achieve CPU times of almost $O(N)$ for low frequency and $O(N \log N)$ for high frequency problems.

Chapter 5

Active Noise Attenuation in a Control Volume

The origins of Active Noise Control (ANC) can be traced back to the pioneering works of Paul Lueg [84] in 1933 and Conover [37] in 1956.

In the free field, Nelson *et al.* [93] claimed that a significant global noise reduction (at least 10 dB power attenuation) can be achieved only if the separation distance between the sources that generate either the primary noise and the control field, both simulated with a monopole, is less than one-tenth of the wavelength of the disturbance. In the case where the control source is placed at half wavelength from the primary source, no reduction can be accomplished. In an enclosed space Nelson *et al.* [92] investigated and developed a computer simulation of ANC and verified their models experimentally for harmonic sound fields. They established that a disturbance can be globally reduced for resonance frequencies and the control source does not require to be separated by less than one half wave-length from the primary noise source as for the free field case, even for considerable number of sources. Ross [103], Hesselm [70] and Berge *et. al* [17] applied the ANC theory to reduction of noise emanating from transformers. They reported that a 20 dB reduction can be easily achieved even for

unsophisticated audio equipment for discrete frequencies of less than 100Hz, but at higher frequencies the noise attenuation level is not acceptable. It was also established that the level of noise attenuation depends upon the direction of observation, since transformers generate noise from extended surfaces that would require several control sources to obtain a global noise reduction.

Early works on the development of local active noise control approach are due to the theoretical and experimental study of Joseph *et. al* [75] and the numerical work of David and Elliot [44]. It was reported [44] that a 10 dB reduction zone can be obtained for frequencies above the Schroeder frequency and for uniform and diffuse primary noise, and the reduction can be larger, up to one tenth of the wavelength, if the cancellation point is further from the secondary source. Moreover, the sound pressure level away from the cancellation point is almost unaffected. The local ANC approach has been further developed by Garcia-Bonito and Elliot [50]. In their work the primary source is a diffuse enclosed sound field, the secondary source is modelled as a rigid sphere with a vibrating segment and the listener's head is assumed to be a rigid sphere. Rafaely *et al.* [99] presented laboratory results for a headrest system. They asserted that a useful performance can be achieved only in the case where the system cancels the pressure at a "virtual microphone" close to the user's ears, that project the quiet area away from the physical microphone. Moreover, they proved that the performance is maintained significant also including the natural movement of the user's head. In the subsequent work Garcia-Bonito and Elliot [51] demonstrated that the reduction zone can be enlarged by cancelling the pressure and the secondary particle velocity at two different points.

In this chapter noise in a 3D free field is attenuated by a local ANC approach and simulated using BEM for monotone frequencies. In the last two decades the ANC has been studied using the BEM by many authors, for example: [8, 41, 56, 124]. These studies are focused on attenuating the offending noise in a global sense. In the study

[41] the secondary sources are not monopoles or point sources as in previous works, but extended vibrating surfaces in free space. The BEM is used to find the total radiated power from a pulsating sphere and from vibrating surfaces within a box and minimised by using the secondary source vibration surface velocity. The Guang-Hann [56] work is focused on the reduction of noise generated in the airport. The method of the images is used to create the ground and a new fundamental solution is calculated by including the impedance of such a surface. The secondary sources have finite dimensions, fixed locations and sizes. The effort of Yang and Tseng [124] is mainly focused on the optimal position of loudspeakers in 2D and 3D cases. The indirect BEM is used to simulate the sound propagation while the sequential quadratic programming (SQP) was selected as optimiser. Bai and Chang [8] performed the ANC of a noise radiated in enclosures with known normal specific acoustic impedance. The total time average acoustic potential energy is selected as the cost function to be minimised and used to optimise the positions and the amplitudes of the secondary sources.

The main idea of the present study is to minimise the square modulus of the potential and the square modulus of the total particle velocity in one direction in a control volume rather than cancelling those quantities at discrete points. This procedure aims to extend the noise reduction volume into a larger zone than for the standard point cancellation procedure for a free field ANC. A diffuse primary field has been created by 72 plane waves with a probabilistic uniform distribution amplitude and plots of all the simulations are obtained from the average result of 20 samples. The results demonstrate the efficiency of the new technique using three control volumes with different sizes. Also described are some critical aspects when an ANC system is set. Finally, results are presented for attenuating the unwanted noise using two control sources.

5.1 Noise Attenuation by Using a Single Control Source

This section presents a novel approach for attenuating an unwanted noise in a prescribed volume. The approach consists of reducing the noise in an area of interest, here called a control volume (CV) and denoted as D. It is shown that our approach can yield a more extended noise attenuation area compared to the conventional point cancellation strategy [50, 51] for local ANC simulations.

To reduce the noise level within D, the integral of the square modulus of the total potential $U(\mathbf{X}_D)$ at the points in the volume D is used as the cost function to be minimised, that is

$$f_c(\mathbf{X}_D) = \int_D |U(\mathbf{X}_D)|^2 dD \tag{5.1}$$

with $\mathbf{X}_D \in D$ and where $U(\mathbf{X}_D)$ is given by (3.51).

As evident, for a given primary noise distribution, the above cost function is minimised by the secondary source field that is generated by a 3D object with hard boundary conditions (i.e., $q = 0$) everywhere except for a vibrating portion of the surface (i.e., $q \neq 0$) (see figure 5.1).

The optimum vibration velocity of the secondary source surface $\bar{\mathbf{q}}_s(\mathbf{x}_v)$ can be evaluated using a constant α that relates the optimum secondary field solution to a solution obtained by any velocity of secondary source vibrating surface $\mathbf{q}_s(\mathbf{x}_v)$ as follows

$$\bar{\mathbf{q}}_s(\mathbf{x}_v) = \alpha \mathbf{q}_s(\mathbf{x}_v) \tag{5.2}$$

where $\mathbf{x}_v$ refers to the points of the secondary vibrating surface.

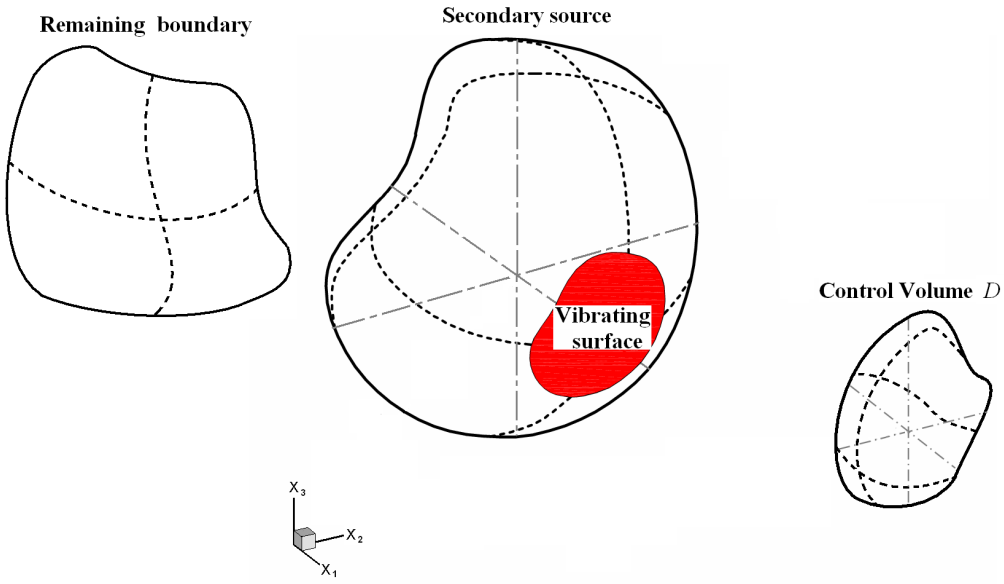


Figure 5.1: The problem configuration including vibrating surface, secondary source and control volume.

The potential U and particle velocity U' at any point of the domain (including the boundary points) is generated by both the primary and the secondary fields. Due to the linearity of the wave equation, each of these fields can be evaluated separately, and summed together as follows

$$\begin{aligned} U &= U_p + \alpha U_s = (U_{pR} + iU_{pI}) + (\alpha_R + i\alpha_I)(U_{sR} + iU_{sI}) \\ U' &= U'_p + \alpha U'_s = (U'_{pR} + iU'_{pI}) + (\alpha_R + i\alpha_I)(U'_{sR} + iU'_{sI}) \end{aligned} \tag{5.3}$$

where the subscripts $_p$ and $_s$ refers to the primary and secondary quantities, respectively, and the subscripts $_R$ and $_I$ refer to the real and imaginary parts, respectively.

Substituting relations (5.3) into the cost function (5.1) yields the following expression

$$f_c(\mathbf{X}_D) = \int_D [(U_{pR} + \alpha_R U_{sR} - \alpha_I U_{sI})^2 + (U_{pI} + \alpha_I U_{sR} + \alpha_R U_{sI})^2] dD \tag{5.4}$$

The complex constant α is determined by minimising the cost function (i.e., setting the cost function derivative with the respect to α_R and α_I equal to zero). Hence, a system with two equations is obtained where the solution α can be written as follows

$$\alpha = \left(-\frac{\bar{c} + \bar{d}}{\bar{a} + \bar{b}}, \frac{\bar{f} - \bar{g}}{\bar{a} + \bar{b}} \right) \tag{5.5}$$

where the constants values in the above expression are shown in table 5.1. It should be noted that each term of table 5.1 is integrated in the control volume.

	$\bar{a}$	$\bar{b}$	$\bar{c}$	$\bar{d}$	$\bar{f}$	$\bar{g}$
$\int_D (U_{\times\times} U_{\times\times})\, dD$	U_{sR}^2	U_{sI}^2	$U_{pR} U_{sR}$	$U_{pI} U_{sI}$	$U_{pR} U_{sI}$	$U_{pI} U_{sR}$

Table 5.1: Values of the terms in equation (5.5).

In order to obtain the value of α, the system of equations (3.48) is solved first for the primary field and again for the secondary source field with any prescribed values of the boundary conditions at the vibrating surface. Therefore, each terms in equation (5.5) are evaluated by equation (3.51) applied to the primary and secondary fields, separately.

The solution (5.5) represents the optimum noise attenuation that can be achieved since the second derivative of f_c with respect to α is always positive, hence

$$\frac{\partial^2}{\partial \alpha_R^2} \int_D |U(\mathbf{X}_D)|^2 dD = \frac{\partial^2}{\partial \alpha_I^2} \int_D |U(\mathbf{X}_D)|^2 dD = 2 \int_D (U_{sR}^2 + U_{sI}^2) dD \tag{5.6}$$

5.2 Results for a Single Control Source

In this section ANC is simulated by the BEM for a single secondary source. A local strategy is here employed and results demonstrate that such an approach results in a

more extended noise reduction area compared with the conventional point cancellation strategy. Regarding the goal of the present thesis, such a control source can be inserted in the headrests of the cabin rows of seats as shown in figure 5.2.

Next, the mathematical model of the primary noise and the secondary source are presented. In the second subsection the plots of the novel strategy are presented.

All the figures are plotted using a grid of 101×101 points and three different values of reduction: 6, 10, 20 dB.



Figure 5.2: SEAT headrest with two speakers.

5.2.1 Primary Noise and Secondary Source Model

The primary offending noise is considered to be diffused and it is generated by plane waves with homogeneous direction of propagation [50]. The primary noise potential at each point of coordinate $\mathbf{X}$ is given by equation [50, 51, 99]

$$U_p(\mathbf{X}) = \sum_{j=1}^{j_{max}} \sum_{l=1}^{l_{max}} (a_{jl} - ib_{jl}) \mathbf{e}^{ik\hat{e}_k \cdot \mathbf{X}} \tag{5.7}$$

where i is the imaginary unit, k is the wave-number, $\hat{e}_k$ is the plane wave versor and $\cdot$ is the operator of the scalar product. The values of j_{max} and l_{max} are 6 and 12, respectively, used to generate 72 plane waves distributed in all directions of the space which create a diffuse primary noise. The values of a_{jl} and b_{jl} are randomly chosen from a uniform distribution.

The secondary source field is created according to [50, 51] by a sphere of radius 0.08 m with a constant active segment of 120^o. Therefore for a free space simulation the boundary (Γ) is divided by the secondary (Γ_s) vibrating surfaces and the residual 240^osegment surface has been considered to be infinitely hard (Neumann BCs with q=0) as shown in figure 5.3.

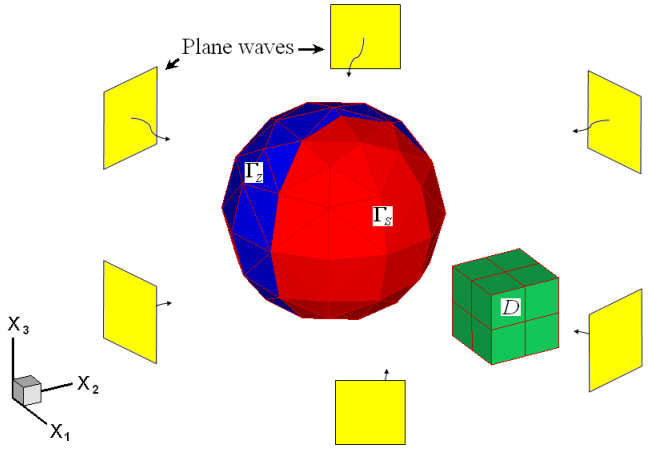


Figure 5.3: Mathematical model of the problem: Γ_S vibrating surface, Γ_z case of the speaker, D control volume, primary noise plane waves.

The sphere that models the loudspeaker is discretised by 62 nodes and 120 triangular super-parametric (linear geometry and constant unknowns) elements. The vibrating segment has the x_1x_3-plane and the x_1x_2-plane as symmetry planes (see figure 5.3) and it can have different extensions along the latter plane. Figure 5.4 shows the vibrating segments of two spheres with 120^0 and 90^0 degree.

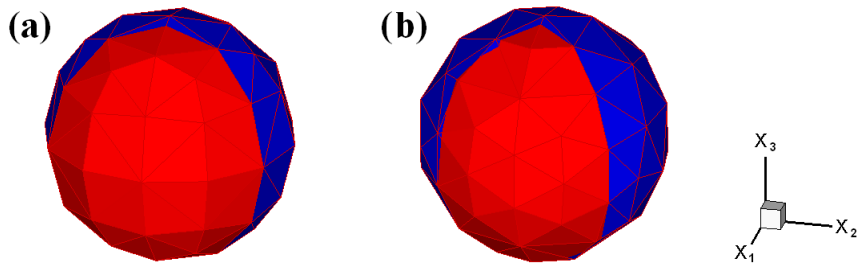


Figure 5.4: Spheres with active segments of 120^0 (a) and 90^0 (b) degree.

The noise attenuation is obtained from the average result of 20 samples. Such simulations are quite time consuming since calculating α for 20 samples needs the knowledge of the primary and the secondary field solutions as well as the value of the potential at the internal points that constitute the CV. However, it should be noted that the system matrix (3.48) and the internal point matrices (3.51) are evaluated only once, since they depend upon the geometry of the problem that is never modified.

Due to the diffuse distribution of the primary field of equation (5.7), at each point of the field the reduction in decibels (dB) is provided by dividing the average square modules of the controlled field by the average squared modulus of the diffuse primary field and taking the $\log 10$ of this ratio multiplied by 10, as follows

$$Reduction(\mathbf{X}) = 10 \log_{10} \frac{\sum_{j=1}^{20} |U(\mathbf{X})|_j^2}{\sum_{j=1}^{20} |U_p(\mathbf{X})|_j^2} \tag{5.8}$$

5.2.2 Results for Different CV Dimensions

A preliminary validation of the developed code is presented in appendix A. The results obtained by the point cancellation strategy for four frequencies (109, 273, 546, 1092 Hz) are shown in figure 5.5 to be compared with the results of the proposed strategy for

three CVs with different dimensions. The integral over the CV is represented using 8 node brick cells. The Legendre-Gauss quadrature rule is subsequently used to evaluate the integral (5.1), [111, 125].

The first CV (*small*) has dimensions of $5 \times 8 \times 4$ *cm* along the x_1, x_2, x_3-axes, respectively. The two diagonal points are located at (17, -4, -2) and (22, 4, 2) from the centre of the sphere. The mesh used for the CV is composed of 24 nodes and 6 elements. The second CV (*medium*) has a volume 8 times the first. The two diagonal points are located at (15, -8, -4) and (25, 8, 4) from the centre of the sphere. The mesh is composed of 140 nodes and 72 elements. The last CV (*large*) has a volume 27 times the first. The two diagonal points are located at (13, -12, -6) and (25, 12, 6) from the centre of the sphere. The CV is meshed with 270 nodes and 160 elements. Table 5.2 presents the characteristics of the CVs.

Figures 5.6, 5.7 and 5.8 show the average total potential field in the x_1, x_2-plane when the noise attenuation is achieved by using the small, the medium and the large CVs, respectively. The secondary field is generated by a rigid sphere with an active segment of 120^0 degree and radius of 8 cm. All of them are compared with the case of a single point cancellation that is shown in figure 5.5. From figure 5.5, it can be seen that a more homogeneous distribution of the noise attenuation is possible by using the formulation here introduced.

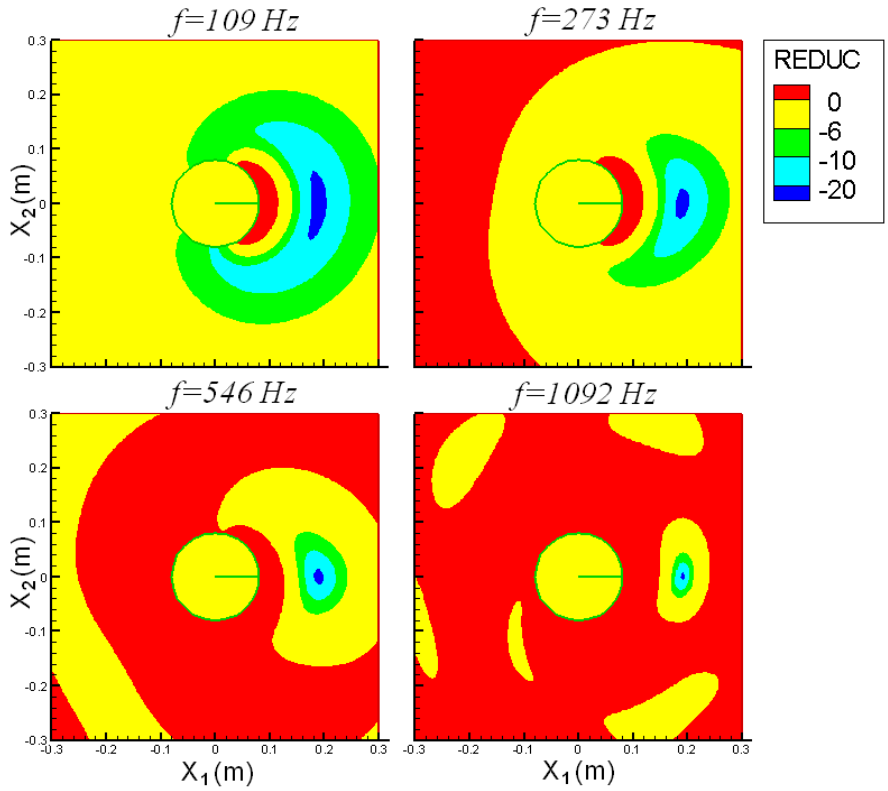


Figure 5.5: Average noise reduction area generated by a rigid sphere with an active segment of 120^0 degree and by the point cancellation strategy at the point (19.4, 0.0, 0.0) *cm*.

CV classification	Dimens. *(cm)* x_1	x_2	x_3	Location of diagonal points x_1	x_2	x_3	x_1	x_2	x_3	Number nodes	Number elements
S *small*	5	8	4	17	-4	-2	22	4	2	24	6
M *medium*	10	16	8	15	-8	-4	25	8	4	140	72
L *large*	15	24	12	13	-12	-6	28	12	6	270	160

Table 5.2: Characteristics of the CVs.

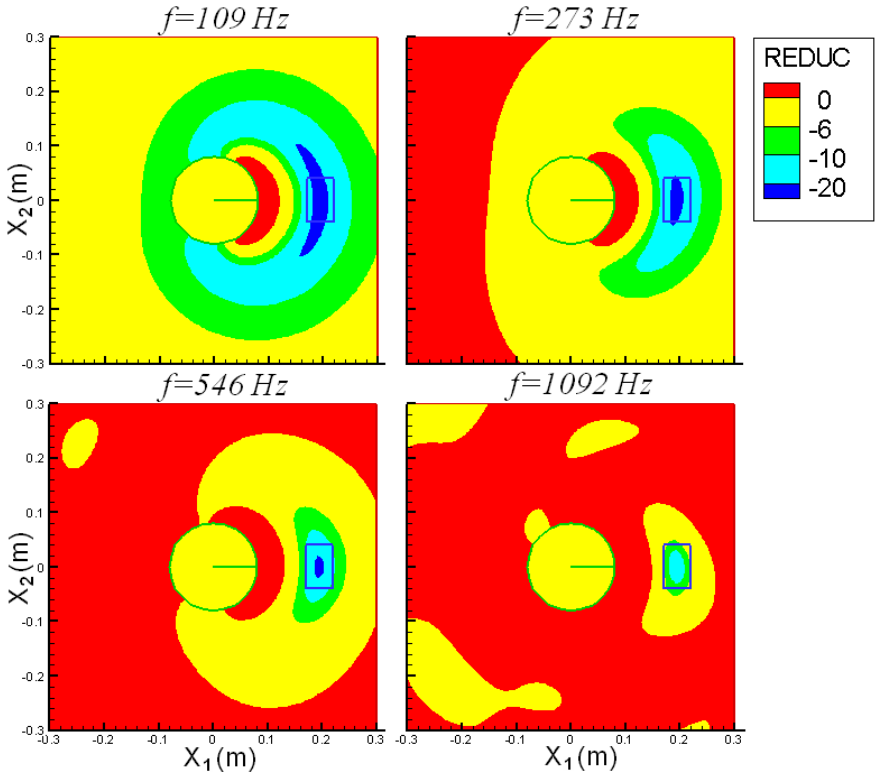


Figure 5.6: Average noise reduction area generated with the small CV.

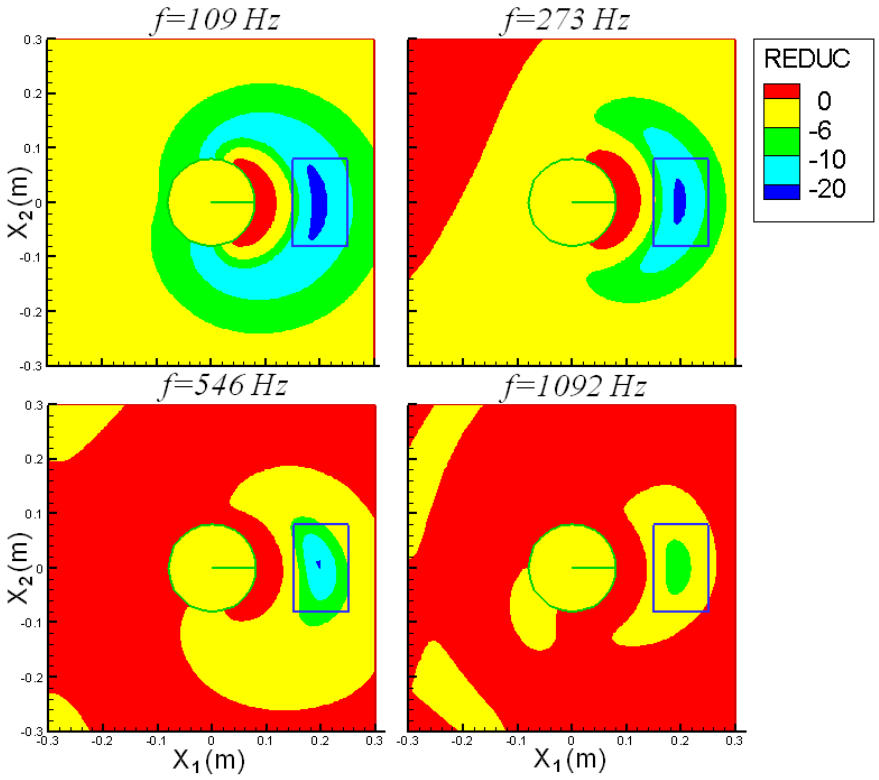


Figure 5.7: Average noise reduction area generated with the medium CV.

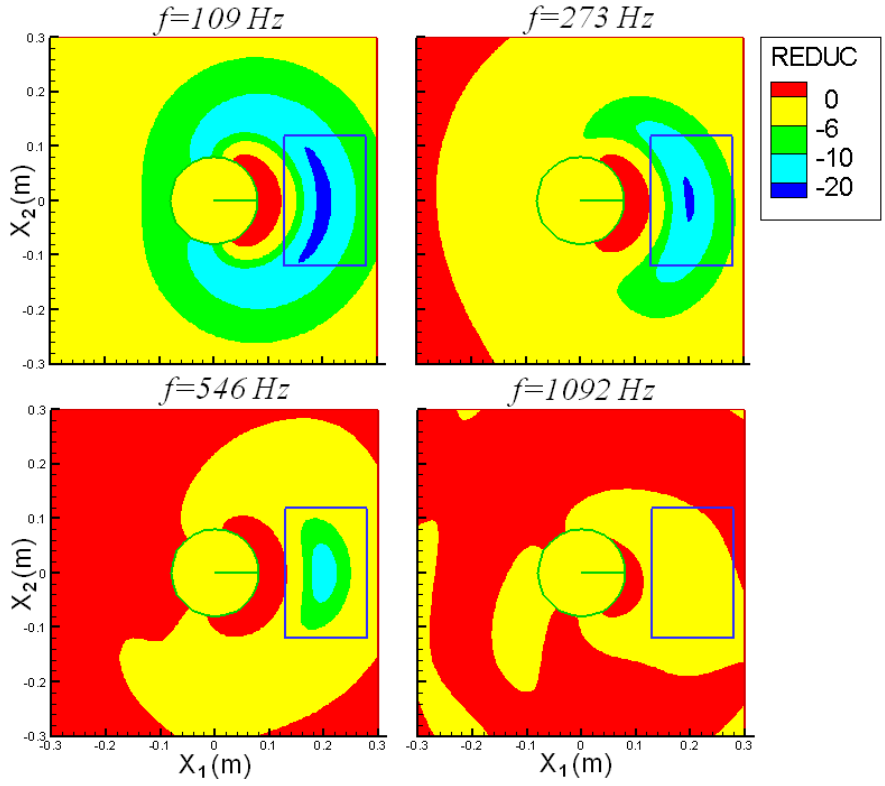


Figure 5.8: Average noise reduction area generated with the large CV.

5.3 Faulty ANC System

The ANC can be practically realised utilising an adaptive feed-forward system, whose scheme is shown in figure 5.9. A primary disturbance is evaluated by a microphone that sends the reference signal to the control system which elaborates this information and creates the optimum control field by, for example, a loudspeaker. The second microphone evaluates the effectiveness of the control response and sends the signal to the control system that adapts the response on the basis of the residual disturbance. An ANC system is often modified over the time by a series of parameters, such as microphone and loudspeaker age, temperature and humidity of air, presence of people, etc. A robust controlling system should be able to adapt the controlled field in case of

variations of the environment.

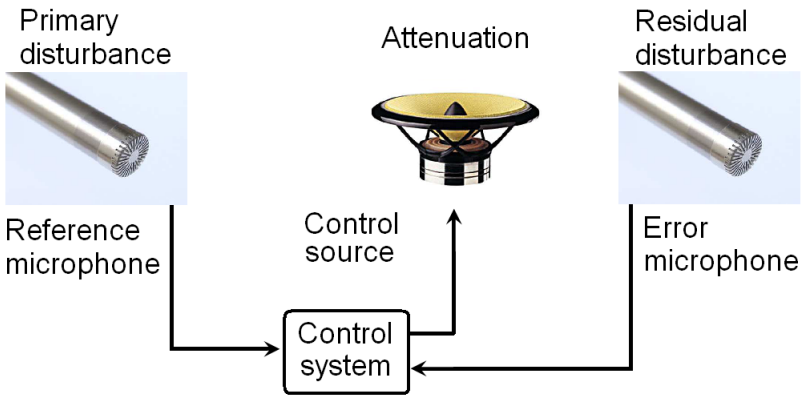


Figure 5.9: Adaptive feed-forward ANC system.

The control system is a composed of a microprocessor that mainly performs additions and multiplications in a small amount of time. A profound evolution of the ANC is due to the development of the digital signal processor (DSP) that is particularly conceived for the required operations of a control system. Modern control systems are very fast and can provide the control response in a few milliseconds. However, some other delays are due to other various components, e.g., analog-to-digital and digital-to-analog conversion process, time required by loudspeakers to generate sound waves once the signal is arrived, etc. All these delays, namely *group delay*, are around a few milliseconds. During this period of time the wave can travel between 1 and 10 metres. In fact, considering the speed of sound 343 m/s and a group delay of 6 milliseconds, a sound wave covers approximately $343 \times 0.006 \approx 2m$. This is the minimum distance between the reference microphone and the control source. Hence, the ANC has this physical problem to attenuate the sound pressure level for random disturbances. Only periodic disturbance can therefore be controlled. A complete presentation of this field is beyond the scope of the present thesis and more information on this subject can be found in [91, 112].

In this section, we are only interested in analysing the effect on the noise reduction area due to an ANC system that does not furnish the optimum secondary amplitude and phase. In general, the adaptive method is implemented to limit these defects. However, it is possible that the adaptive control does not work properly and amplitude or phase do not have optimum values.

A preliminary trend of the effects of amplitude and phase variations is shown in figure 5.10. In particular, in 5.10-a the secondary source has optimum values and the noise is completely cancelled, whereas in 5.10-b and 5.10-c the secondary amplitude and phase are varied 20% and $\pi/10$, respectively, from their optimal values. It can be noted that the variation of the phase produces a greater effect on the total field than a variation in the amplitude.

Figures 5.11 and 5.12 show the effects on the noise reduction area due to a variation of the amplitude and phase, respectively. The optimum potential amplitude and phase are varied at a point situated 0,194 m from the centre of the sphere along the x_1-axes. All the plane-waves of the primary diffuse noise have unitary amplitude, thus only a single sample is shown, and the secondary field is generated by a rigid sphere with an active segment of 120^0 degree and radius of 8 cm. The variations are calculated in percentage ($\pm 5\%$,$\pm 10\%$, $\pm 20\%$) from the optimum value that maximises the noise reduction level for a medium size CV for a frequency of 109 Hz. The phase is varied with respect to π.

As evident, varying the potential amplitude does not affect much the noise attenuation and a 20 dB reduction is achieved also for $\pm 20\%$ variations. On the contrary phase variation modifies deeply the overall acoustic field and the noise is reduced by a few dB when the percentage variation is 20%.

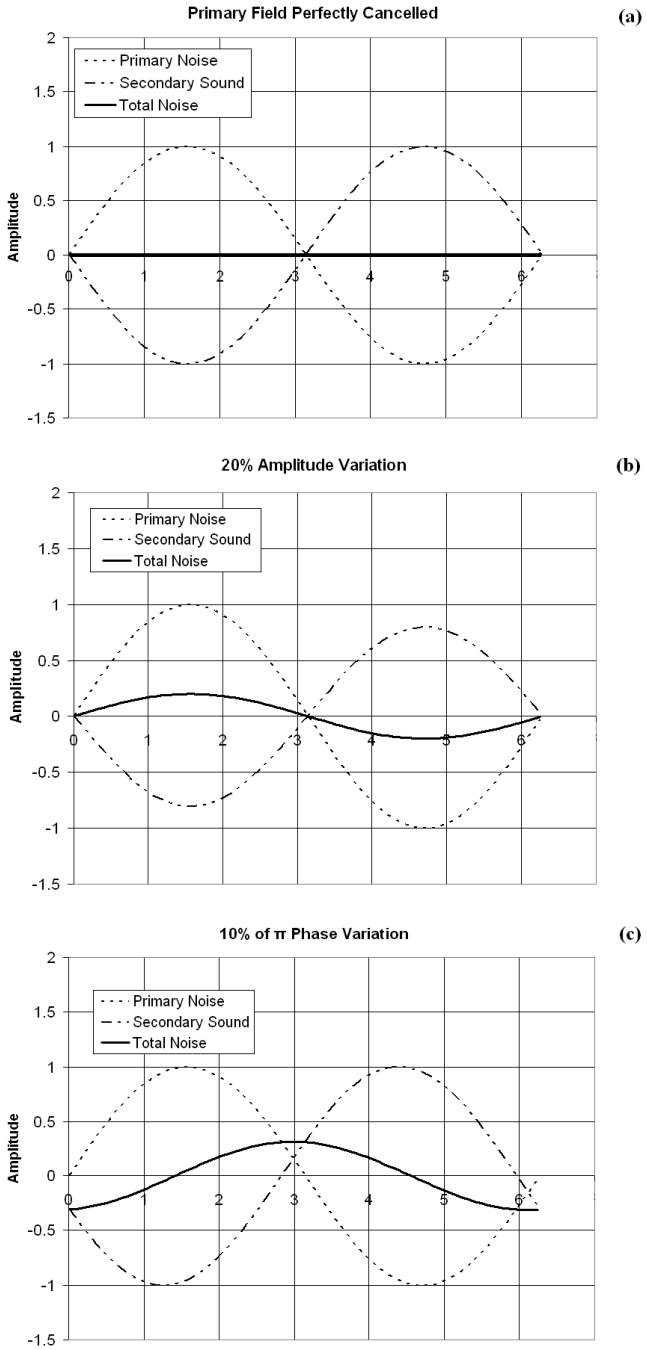


Figure 5.10: Superposition (continuous line) of a primary sinusoidal field with a secondary source without variations (a); with a variation of 20% of the potential amplitude (b) and 10% π of the phase (c).

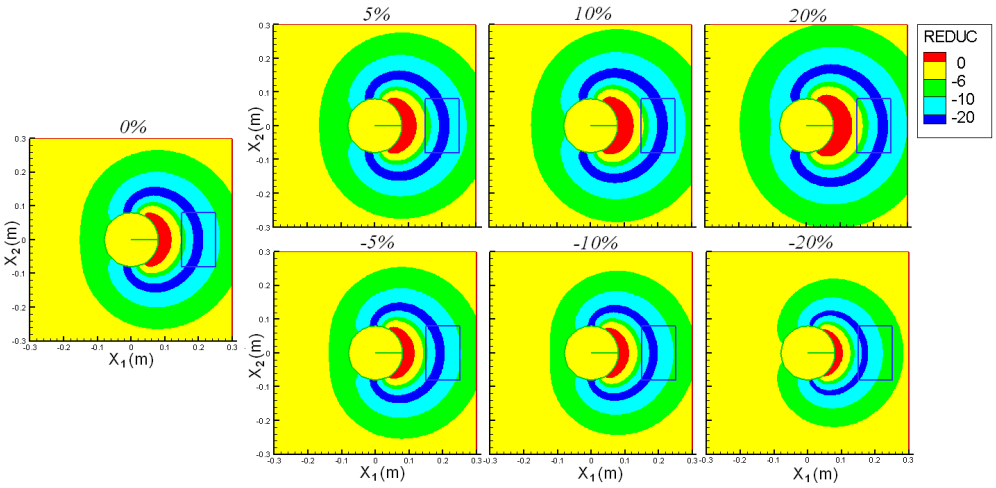


Figure 5.11: Noise reduction area when the secondary field is varied in percentage (±5%, ±10%, ±20%) from its optimal value that minimises the noise level.

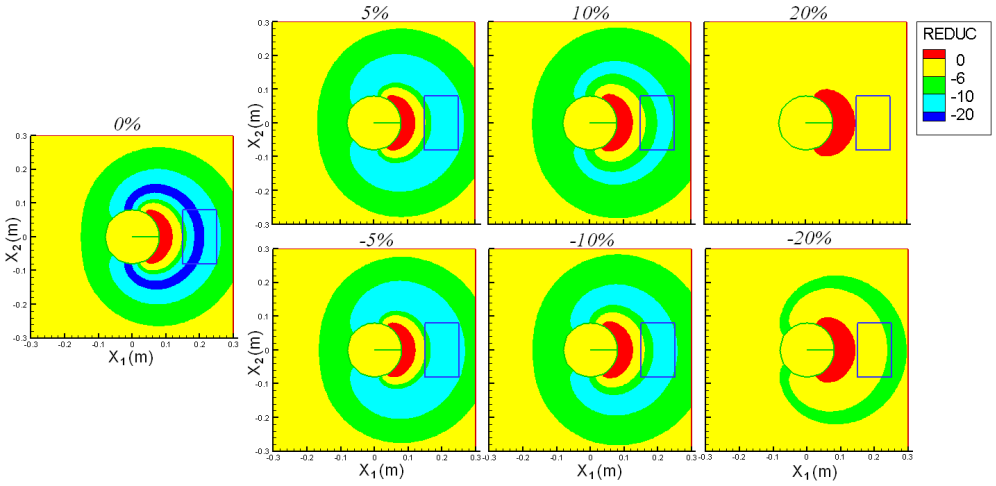


Figure 5.12: Noise reduction area when the secondary field is varied in percentage (±5%, ±10%, ±20% π) from its optimal value that minimises the noise level.

5.4 Noise Attenuation Using Two Control Sources

In the previous sections the noise has been attenuated using a single secondary source. Herein the addition of a second secondary source proves that a higher noise attenuation level can be achieved.

In the circumstances studied in the present thesis, a second loudspeaker can be placed in the panel above the passenger head or on the back of facing passenger seat or, in the case of spacious seat (i.e. business class) in the headrest, close to the previous loudspeaker. The importance of the two speaker locations on the overall noise reduction is highlighted with three different configurations in the next section.

5.4.1 Mathematical Model

The addition of the second control source requires another cost function that should be minimised contemporaneously with equation (5.1). Such a cost function can be written as follows

$$f_{c2}(\mathbf{X}_D) = \int_D |U_1'(\mathbf{X}_D)|^2 dD \tag{5.9}$$

where U_1' is the component along the x_1-direction of the particle velocity.

The second loudspeaker is also modelled as a hard 3D object with a vibrating surface. Its optimal vibration velocity $\bar{\mathbf{q}}_{s2}(\mathbf{x}_v)$ is evaluated by a second constant β as for the previous case

$$\bar{\mathbf{q}}_{s2}(\mathbf{x}_v) = \beta \mathbf{q}_{s2}(\mathbf{x}_v) \tag{5.10}$$

The total potential and the total component of the total particle velocity along one direction at a generic point ($\mathbf{X}$) are evaluated, respectively, as in expression (5.3) by adding an extra term that refers to the second control source as follows

$$
\begin{aligned}
U &= U_p + \alpha U_{s1} + \beta U_{s2} \\
U' &= U'_p + \alpha U'_{s1} + \beta U'_{s2}
\end{aligned}
\tag{5.11}
$$

where the subscripts $_{s1}$ and $_{s2}$ refer to the first and the second control source, respectively.

Expressions in (5.11) are substituted into the cost functions (5.1) and (5.9) that are minimised by α and β (i.e., the cost function derivatives with the respect to α_R, α_I, β_R and β_I are set equal to zero). A system with four equations and four unknowns (α_R, α_I, β_R and β_I) is obtained whose solution is displayed below. The solution of such system can be simplified, as shown below, by considering the primary field as constant at the CV points [87].

Each term of the α and β requires solution of (3.48) and application of equations (3.51) and (3.54) three times, first for the primary field, by considering both the secondary sources as rigid surfaces, and again twice for the two secondary sources, acting independently, for any initial value of the vibrating velocity ($\mathbf{q}_{s1}$ and $\mathbf{q}_{s2}$) and by considering the other secondary source as a rigid sphere.

The solution for the standard procedure in terms of α_R, α_I, β_R and β_I can be written as follows

$$
\begin{aligned}
\alpha_R = -\frac{U_{pI}(l_1 + l_2 - d_1 - d_2 + d_7 - d_8) + U_{pR}(l_3 + l_4 - d_3 + d_4 - d_5 - d_6) + }{m_1 + m_2 + m_3 + m_4 + m_5 + m_6 + m_7 + m_8 + } \\
\frac{+U'_{1pI}(b_4 - b_1 + g_1 - b_6 - b_7 + g_3) + U'_{1pR}(g_2 - b_2 - b_3 + b_5 - b_8 + g_4)}{+2(-bc_1 - bc_2 - bc_3 + bc_4 + bc_5 - bc_6 - bc_7 - bc_8)}
\end{aligned}
\tag{5.12}
$$

$$\alpha_I = -\frac{\begin{array}{c}U_{pI}(l_3+l_4-d_3+d_4-d_5-d_6)-U_{pR}(l_1+l_2-d_1-d_2+d_7-d_8)+\\ m_1+m_2+m_3+m_4+m_5+m_6+m_7+m_8+\\ +U'_{1pI}(g_2-b_2-b_3+b_5-b_8+g_4)-U'_{1pR}(b_4-b_1+g_1-b_6-b_7+g_3)\end{array}}{+2(-bc_1-bc_2-bc_3+bc_4+bc_5-bc_6-bc_7-bc_8)} \quad (5.13)$$

$$\beta_R = -\frac{\begin{array}{c}U_{pI}(c_6-c_1-c_2-c_5+h_1+h_2)+U_{pR}(c_3-c_4-c_7-c_8+h_3+h_4)+\\ m_1+m_2+m_3+m_4+m_5+m_6+m_7+m_8+\\ +U'_{1pI}(f_1+f_3-a_1-a_4+a_6-a_7)+U'_{1pR}(f_2+f_4-a_2+a_3-a_5-a_8)\end{array}}{+2(-bc_1-bc_2-bc_3+bc_4+bc_5-bc_6-bc_7-bc_8)} \quad (5.14)$$

$$\beta_I = -\frac{\begin{array}{c}U_{pI}(c_3-c_4-c_7-c_8+h_3+h_4)-U_{pR}(c_6-c_1-c_2-c_5+h_1+h_2)+\\ m_1+m_2+m_3+m_4+m_5+m_6+m_7+m_8+\\ +U'_{1pI}(f_2+f_4-a_2+a_3-a_5-a_8)-U'_{1pR}(f_1+f_3-a_1-a_4+a_6-a_7)\end{array}}{+2(-bc_1-bc_2-bc_3+bc_4+bc_5-bc_6-bc_7-bc_8)} \quad (5.15)$$

where U'_{1pI} and U'_{1pR} are the real and imaginary parts of component along the x_1-direction of the primary particle velocity, respectively. All the other quantities in the above solutions are reported in table 5.3.

$\int_D (U_{\times\times}U_{\times\times}$ $U_{\times\times}U_{\times\times})\,dD$	1	2	3	4
$a_\times$	$U'_{s1I}U_{s1I}U_{s2I}$	$U'_{s1R}U_{s1I}U_{s2I}$	$U'_{s1I}U_{s1R}U_{s2I}$	$U'_{s1R}U_{s1R}U_{s2I}$
$b_\times$	$U'_{s2I}U_{s1I}U_{s2I}$	$U'_{s2R}U_{s1I}U_{s2I}$	$U'_{s2I}U_{s1R}U_{s2I}$	$U'_{s2R}U_{s1R}U_{s2I}$
$c_\times$	$U'_{s1I}U'_{s2I}U_{s1I}$	$U'_{s1R}U'_{s2R}U_{s1I}$	$U'_{s1R}U'_{s2I}U_{s1I}$	$U'_{s1I}U'_{s2R}U_{s1I}$
$d_\times$	$U'_{s1I}U'_{s2I}U_{s2I}$	$U'_{s1R}U'_{s2R}U_{s2I}$	$U'_{s1R}U'_{s2I}U_{s2I}$	$U'_{s1I}U'_{s2R}U_{s2I}$
$f_\times$	$U'_{s2I}U^2_{s1I}$	$U'_{s2R}U^2_{s1I}$	$U'_{s2I}U^2_{s1R}$	$U'_{s2R}U^2_{s1R}$
$g_\times$	$U'_{s1I}U^2_{s2I}$	$U'_{s1R}U^2_{s2I}$	$U'_{s1I}U^2_{s2R}$	$U'_{s1R}U^2_{s2R}$
$h_\times$	$U'^2_{s1I}U_{s2I}$	$U'^2_{s1R}U_{s2I}$	$U'^2_{s1I}U_{s2R}$	$U'^2_{s1R}U_{s2R}$
$l_\times$	$U'^2_{s2I}U_{s1I}$	$U'^2_{s2R}U_{s1I}$	$U'^2_{s2I}U_{s1R}$	$U'^2_{s2R}U_{s1R}$
$m_\times$	$U'^2_{s2I}U^2_{s1I}$	$U'^2_{s2R}U^2_{s1I}$	$U'^2_{s2I}U^2_{s1R}$	$U'^2_{s2R}U^2_{s1R}$
$bc_\times$	$U'_{s1I}U'_{s2I}$ $U_{s1I}U_{s2I}$	$U'_{s1R}U'_{s2R}$ $U_{s1I}U_{s2I}$	$U'_{s1R}U'_{s2I}$ $U_{s1R}U_{s2I}$	$U'_{s1I}U'_{s2R}$ $U_{s1R}U_{s2I}$
$\int_D (U_{\times\times}U_{\times\times}$ $U_{\times\times}U_{\times\times})\,dD$	5	6	7	8
$a_\times$	$U'_{s1I}U_{s1I}U_{s2R}$	$U'_{s1R}U_{s1I}U_{s2R}$	$U'_{s1I}U_{s1R}U_{s2R}$	$U'_{s1R}U_{s1R}U_{s2R}$
$b_\times$	$U'_{s2I}U_{s1I}U_{s2R}$	$U'_{s2R}U_{s1I}U_{s2R}$	$U'_{s2I}U_{s1R}U_{s2R}$	$U'_{s2R}U_{s1R}U_{s2R}$
$c_\times$	$U'_{s1R}U'_{s2I}U_{s1R}$	$U'_{s1I}U'_{s2R}U_{s1R}$	$U'_{s1I}U'_{s2I}U_{s1R}$	$U'_{s1R}U'_{s2R}U_{s1R}$
$d_\times$	$U'_{s1I}U'_{s2I}U_{s2R}$	$U'_{s1R}U'_{s2R}U_{s2R}$	$U'_{s1R}U'_{s2I}U_{s2R}$	$U'_{s1I}U'_{s2R}U_{s2R}$
$f_\times$	-	-	-	-
$g_\times$	$U'_{s2I}U^2_{s2I}$	$U'_{s2R}U^2_{s2I}$	$U'_{s2I}U^2_{s2R}$	$U'_{s2R}U^2_{s2R}$
$h_\times$	-	-	-	-
$l_\times$	$U'^2_{s2I}U_{s2I}$	$U'^2_{s2R}U_{s2I}$	$U'^2_{s2I}U_{s2R}$	$U'^2_{s2R}U_{s2R}$
$m_\times$	$U'^2_{s1I}U^2_{s2I}$	$U'^2_{s1R}U^2_{s2I}$	$U'^2_{s1I}U^2_{s2R}$	$U'^2_{s1R}U^2_{s2R}$
$bc_\times$	$U'_{s1R}U'_{s2I}$ $U_{s1I}U_{s2R}$	$U'_{s1I}U'_{s2R}$ $U_{s1I}U_{s2R}$	$U'_{s1I}U'_{s2I}$ $U_{s1R}U_{s2R}$	$U'_{s1R}U'_{s2R}$ $U_{s1R}U_{s2R}$

Table 5.3: Values of the terms in equations. (5.12-5.15).

5.5 Results for Two Control Sources

In this section the adoption of a system with two control sources is investigated. The importance of the control source locations is described next. A simplified procedure and a strategy utilising different cost functions are presented. As for the single source, results are obtained from the average results of 20 samples and for four frequencies (i.e., 109, 273, 546, 1092 Hz).

5.5.1 Standard Procedure

In this subsection the control sources and CV are located at different places and three different configurations are tested (see figure 5.13).

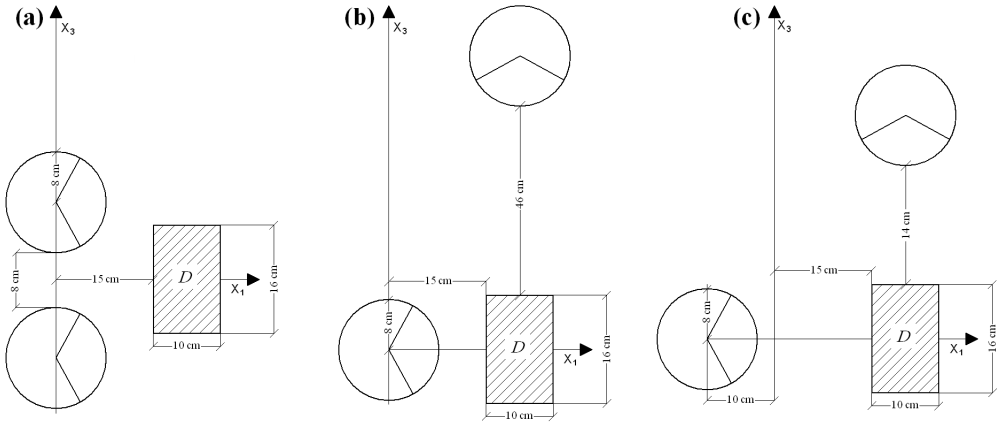


Figure 5.13: The three configurations tested: (a) configuration 1, (b) configuration 2, (c) configuration 3.

In the first configuration (figure 5.13-a) the vibrating segments of both sources are directed towards the x_1-axes and the CV is placed between them. In the second configuration (figure 5.13-b) the vibrating segments are directed towards the centre of the CV and one of them is placed at a larger distance from this point. Finally, the last configuration (figure 5.13-c) is similar to the second, but both of them are placed at the same distance from the centre of the CV. The point at which the value of the primary field has been calculated and maintained constant is at 19.4 *cm* from the origin in all of the three configurations.

Figures 5.14, 5.15 and 5.16 show the average total potential field in the x_1x_2-plane and x_1x_3-plane, ((a) and (b) in each figure, respectively) due to a primary diffuse field and two secondary fields generated by two rigid spheres with an active segment of 120^0

degree and radius of 8 *cm* when the noise attenuation is achieved in the medium size CV.

It can be noted that the best noise attenuation level is reached with the second configuration for the initial two lowest frequencies. As the frequency increases the third configuration provides a higher noise attenuation level. Moreover, the first configuration should be avoided since a considerable noise reduction is reached only in the symmetry plane between the two sources. This effect occurs because the two sources create two parallel acoustic fields so that they interact reciprocally and the noise is essentially created by them. This configuration highlights that the location of the secondary sources is a basic design consideration.

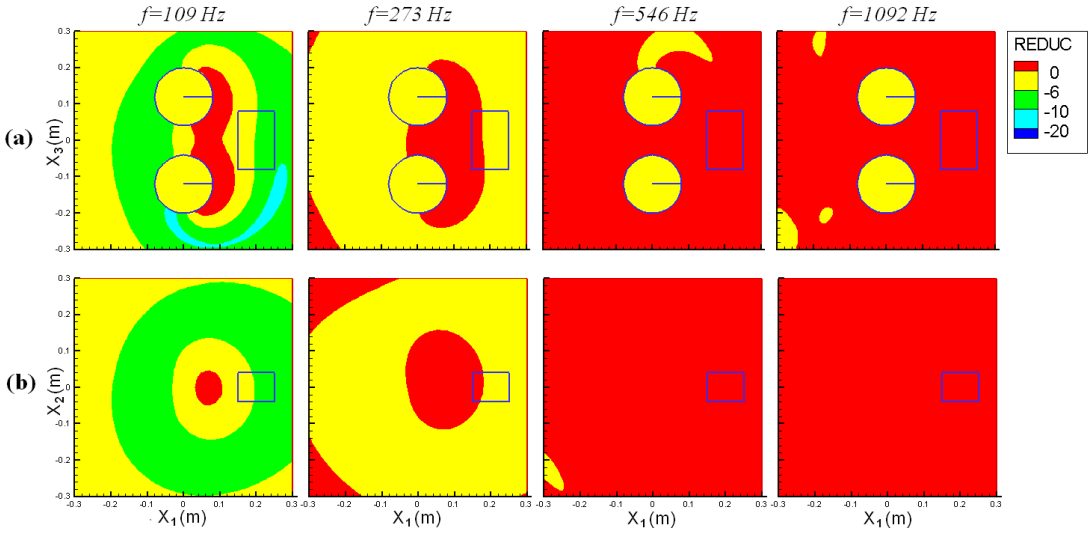


Figure 5.14: Average noise reduction area for the first configuration.

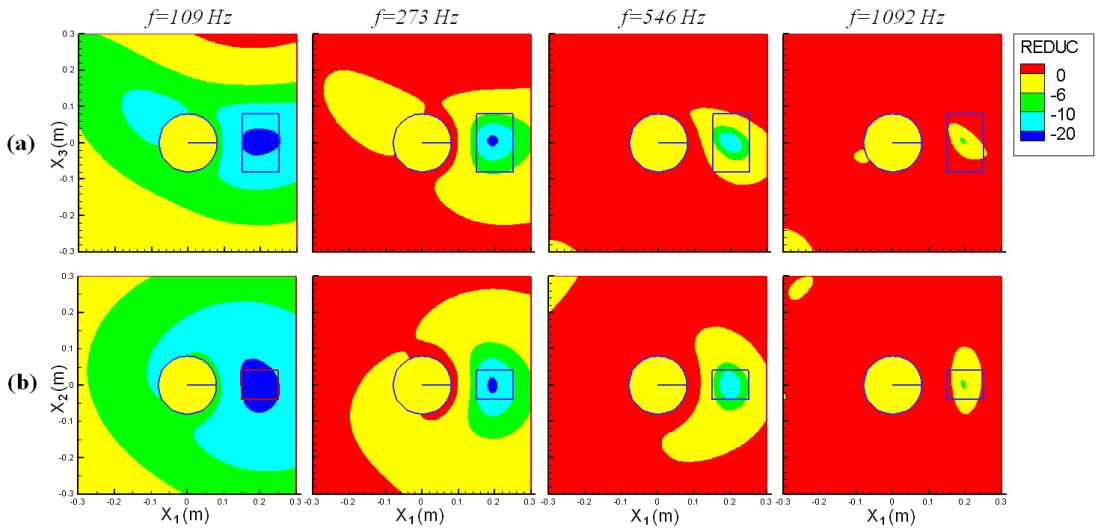


Figure 5.15: Average noise reduction area for the second configuration.

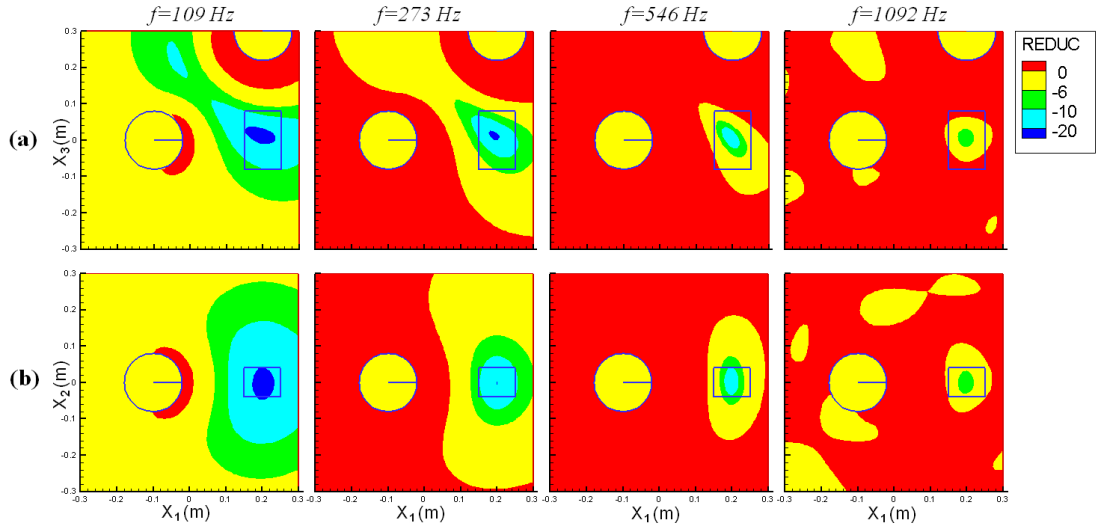


Figure 5.16: Average noise reduction area for the third configuration.

5.5.2 Simplified Procedure

This subsection presents the results of a simplified procedure employing two loudspeakers.

The optimisation of the two control source vibration velocities (i.e., evaluation of α and β) requires the knowledge of many terms as reported in equations (5.12)-(5.15). To decrease the number of such terms, the total particle velocity in the cost function (5.9) is substituted by the component created only by the two secondary fields. Hence, the primary field is assumed to be constant inside the CV. With reference to the solutions (5.12)-(5.15), the terms U'_{1pI} and U'_{1pR} are set to zero and the related terms are eliminated, resulting in a reduction of the computational effort.

The average total potential field in the x_1x_2-plane and x_1x_3-plane, when the potential and only the secondary components along the x_1-direction are minimised in a CV, is shown in figure 5.17. The second control source has same characteristic of the first one. The second configuration of figure 5.13 is utilised.

Comparing figures 5.17 and 5.15 highlights a greater noise reduction area which is now attached to the closer source. This suggests that minimising the secondary source particle velocity components instead of the total speeds up the computational time without decreasing the extension of the noise reduction area.

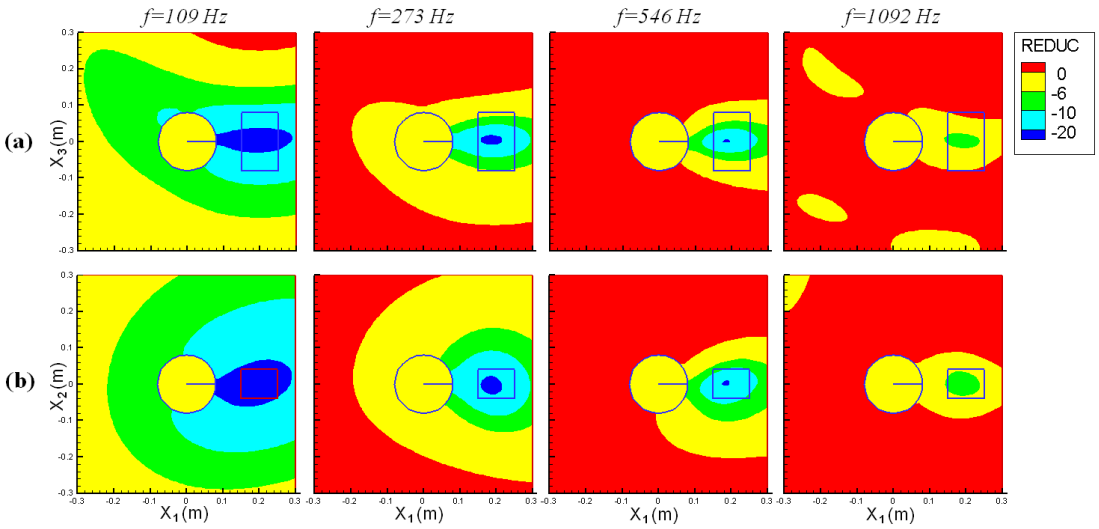


Figure 5.17: Average noise reduction area of the simplified procedure.

5.5.3 Modified Procedure

This subsection presents the results when the component along the x_1-direction of the particle velocity in the cost function (5.9) is substituted by the component along the x_2-direction.

Figure 5.18 shows the average total potential field in the x_1x_2-plane and x_1x_3-plane following the above described procedure. The second configuration of figure 5.13 is utilised.

As evident, changing the component of the particle velocity decreases the noise reduction within the CV, hence this approach has to be avoided. This happens because the distance of one secondary source from the CV is greater than the other and thus the former source has a predominant role on the noise attenuation level. Moreover, the third configuration does not suffer from this problem because the two sources have approximately the same distance from the CV.

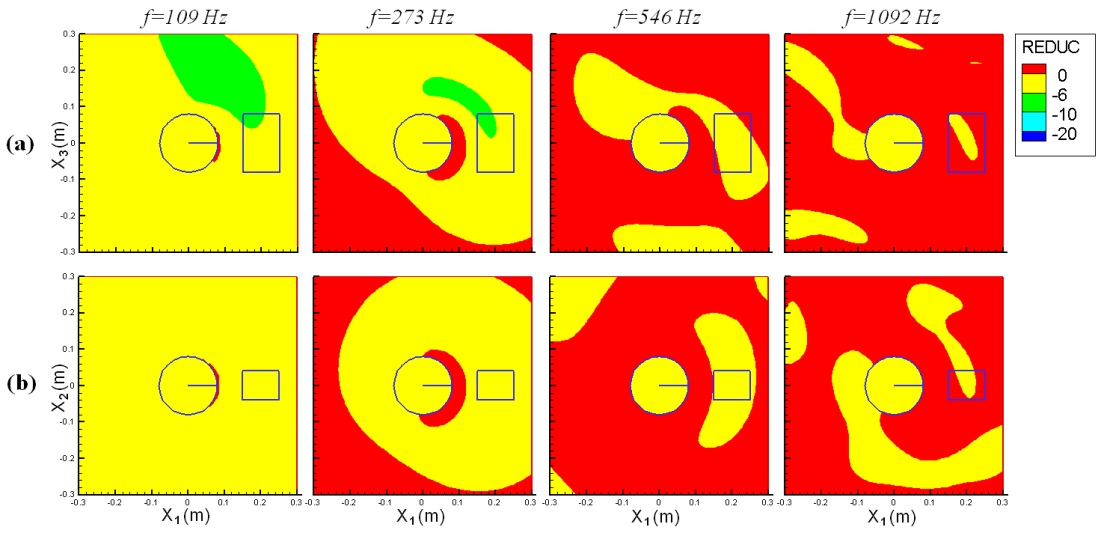


Figure 5.18: Average noise reduction area when the component of the particle velocity is along the x_2-direction instead of the x_1-direction.

5.6 Practical Aspects of the Proposed Control Volume Approach

This section presents a few theoretical ideas on practical aspects to realise the proposed strategy in an ANC system.

As evident, such a strategy can be fully realised only if the sound field is perfectly known at every CV point. This means to place several reference microphones close to the user's head area to predict the noise level. Nevertheless, such a system is unfeasible for a practical application, especially inside an aircraft cabin, and a different approach is thus required.

A possibility to overcome this drawback consists on hypothesizing that the primary field is constant at the control volume points. This hypothesis is supported by the consideration that the characteristic wavelength that an ANC system can control, is larger than the control volume dimensions. On the contrary, the secondary source can be considered to have its effective response.

In substance, under this hypothesis an adaptive feed-forward ANC system requires a single reference microphone that, in case of single control source, could be located behind the loudspeaker, and a single error microphone to be placed close to the ear (see Rafaely *et al.* [99]). The secondary field generated by the loudspeaker at the CV points (i.e., polar diagram) can be evaluated for a standard passenger-seat configuration by a common acquisition system for acoustic measurement and without any primary disturbance. Finally, the error microphone can adaptively adjust the loudspeaker response by a single attainment.

In the case of two loudspeakers, the proposed hypothesis yields excellent results. In fact, a constant primary disturbance at the CV points means a particle velocity equal to zero at the same points. As seen in the subsection 5.5.2, this procedure does not reduce the quiet zone. Thus, only a single further error microphone is required for evaluating

the secondary particle velocity along a single direction only and to adapt the response of the control source.

The effectiveness of the proposed CV approach would need to be tested experimentally in the future.

Summary

A new local ANC approach, which consists on attenuating a primary noise in a specific area, here called a *control volume* (CV) has been presented in this chapter. The 3D acoustic modelling is based on the BEM for monotone frequencies.

A first strategy adopts a single control source, which, regarding the goal of the present thesis, can be inserted in the headrest of the passenger seat. The primary noise has been considered to be diffuse and it has been generated by 72 planewaves with random amplitude uniformly distributed, whereas the secondary field has been created by a 3D sphere with a vibrating portion. A suitable cost function has been minimised to drive the optimal vibration velocity of the control source surface. Three control volumes with different sizes have been tested and their results compared with the conventional cancelling point strategy. The variations of phase and amplitude of the control source optimal response have been also analysed, highlighting that local ANC depends more upon on controlling phase than amplitude. The last part of the chapter regards a second strategy for the local ANC that adopts two control sources. The second secondary source could be located in the ceiling of the cabin or on the back of facing passenger seat or in any available and convenient positions. The locations of the control sources and the CV assume a fundamental role and three different configurations suggest appropriate places. The second control source complicates the evaluation of the optimal secondary responses, but a simplified procedure demonstrated that an extended noise attenuated zone can be also achieved using a few terms. A different cost function

has been considered, but a higher noise reduction level has not been achieved.

The results of BEM simulation suggested that the proposed method generated wider and more homogeneous quiet zone compared to the conventional point cancellation approach.

A few practical aspects on the proposed method conclude the chapter.

Chapter 6

A Sensitivity Formulation for Three Dimensional Active Noise Control

In the last few decades Active Noise Control (ANC) has been widely explored as discussed in Chapter 5. Early research into global noise reduction in a free space involved the use of secondary loudspeakers placed close to the primary sources (Conover [37], Nelson *et al.* [93], Ross [103], Hesselman [70], Berge *et al.* [17]). In an enclosed space, a global noise reduction is achieved only for frequencies close to resonance, the secondary source can be located everywhere in enclosures except at nodal points (Nelson *et al.* [92]). Elliot *et al.* [50, 51, 99] demonstrated the feasibility of a system that attenuates the noise in a local sense.

Only recently, techniques aimed at maximising the noise reduction level by the optimisation of the actuator locations have been explored. Haftka and Adelman [63] and Chen *et al.* [29] represent early efforts in this area where the primary noise is reduced by using piezo patches. The two techniques are based on randomized searching method such as integer programming methods or simulated annealing methods. Ruckman and Fuller [105] in their investigation adopted an approach where structural control actuator locations are optimised over a subset selection (only a discrete number of locations is

permitted). The work of Baek and Elliot [7] represents one of the first studies to find the optimum location of speakers for the ANC using genetic algorithms and simulated annealing methods. Martin and Roure [88] applied a mixed method using a selective search algorithm for the optimum location of the actuators and a genetic algorithm to determine the optimum location of the error sensors. Seyedin and Abedi [110] simulated the sound propagation in a room with reflecting surfaces and obtained the optimum locations of an anti-noise source, which is a monopole constrained at one of the four walls.

There have been several studies reported on the computation of the shape design sensitivity analysis for the acoustic problems using the BEM (see for instance [36, 77, 78, 79, 85]). A direct differentiation approach has been shown to be more accurate and to overcome the inaccuracy of the finite difference method (FDM).

An early application of the BEM to a sensitivity analysis [41] for the ANC, minimises the total radiated power from a pulsating sphere and from vibrating surfaces within a box using the secondary source vibration surface velocity. The study of Yang and Tseng [124] is mainly focused on the optimal position of loudspeakers in 2D and 3D cases. The indirect BEM is used to simulate the sound propagation while the sequential quadratic programming (SQP) was selected as optimiser. Bai and Chang [8] reduced a noise radiated in enclosures with specific acoustic impedances. The total time average acoustic potential energy is selected as the cost function to be minimised and used to optimise the positions and the amplitude of the secondary sources. However, all the above studies use the so-called zero order optimisation, hence they do not require the evaluation of the derivative of the BEM system solution with respect to the design variable.

On the contrary, the first order optimisation methods necessitate the first derivative of the cost function and therefore of the BEM system solution with respect to the design variable. Consequently, the problem requires the solutions of two systems of equations,

one for the direct problem and another for the sensitivities. The computational effort can be large and represents the main drawback of the sensitivity analysis. In recent years, only a few strategies have been proposed to overcome this difficulty. Prasad and Kane [59] demonstrated the superiority of employing preconditioned iterative equation solvers in reanalysis and sensitivity analysis. Fritze *et al.* [49] proposed a coupled FE and BE analysis in structural–acoustic optimisation analyses for passive noise control of large scale models. Nemitz and Bonnet [94] utilised a sensitivity based boundary element formulation accelerated by the fast multipole method to solve the problem of inverse scattering of scalar waves.

In this chapter a new BEM formulation for the optimisation of a local ANC is presented. The noise attenuation strategy is based upon the formulation presented in Chapter 5 where the noise, simulated in a 3D field, is reduced within a fixed enclosure, called a control volume (CV), with a fixed secondary source. Here, the three main original contributions are:

i) first order derivative sensitivity analysis applied to a local ANC approach solved with the BEM;

ii) optimisation of the noise attenuation area location, of the control source location and, overall, orientation;

iii) reduction of the computational cost of the proposed analysis utilising a Hierarchical Adaptive Cross Approximation (ACA) technique coupled with the GMRES (RABEM code).

The BEM is applied to the three dimensional (3D) Helmholtz equation [45, 123] for monotone frequencies both to determine the solution of the direct problem and to evaluate the sensitivities by an implicit differentiation approach. The direct solution and the sensitivities are used to solve the optimisation problems. A superparametric formulation with linear-constant elements has been used. The Adaptive Cross Approximation

(ACA) is used to generate both the system matrix and the right hand side vector, the H-matrix format is used for the storage requirements and the GMRES is used to solve the linear systems of equations. The same strategy is also used to evaluate the potential at selected internal points, the differential of the system matrix and of the potential with respect to the design variables. Several examples are presented to demonstrate the accuracy of the proposed procedure. They include:

i) optimum CV location in an infinite unbounded domain;

ii) optimum secondary source location inside a room;

$iii - iv$) optimum secondary source orientation inside a box and a room;

v) optimum secondary source locations at different frequencies in an aircraft cabin.

6.1 Optimisation

In this chapter the ANC has been approached by attenuating an unwanted noise in a confined region, called a control volume (CV), as presented in Chapter 5. The two goals of this study are to optimise both the location and the orientation of the secondary source by keeping the CV fixed (see figure 6.1), and to optimise the CV location by fixing the control source (see figure 6.2).

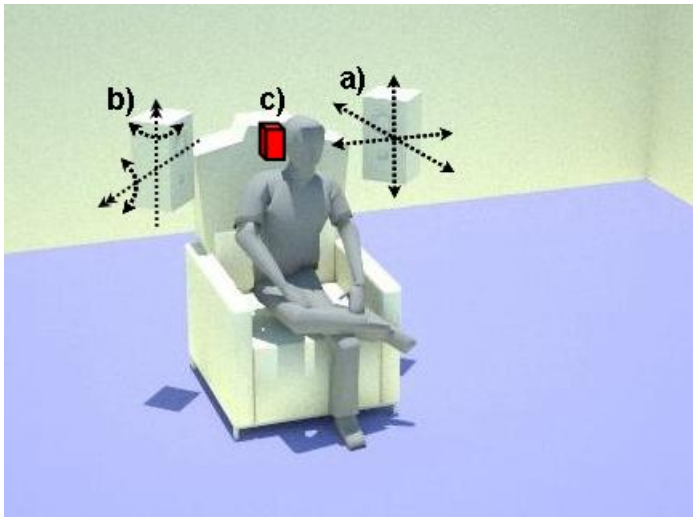


Figure 6.1: Optimisation process applied to the control source: a) optimum location; b) optimum orientation; c) fixed control volume.

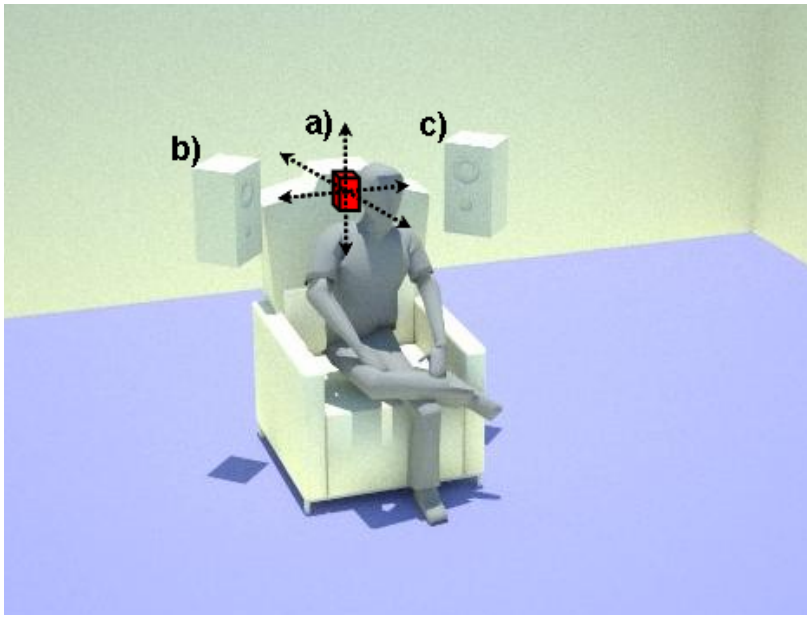


Figure 6.2: Optimisation process applied to the control volume: a) optimum CV location; b-c) fixed control sources.

Let us recall the Helmholtz equation (3.4) to describe the acoustic field

$$\nabla^2 u(\mathbf{x}) + k^2 u(\mathbf{x}) = \frac{1}{c^2} b \tag{6.1}$$

where u is the acoustic potential, $k = \omega/c$, with ω angular frequency and c sound velocity, is the wave-number; b is refers to the presence of sources, such as monopole or plane-wave within the domain Ω with strength $b(\mathbf{X^s})/c^2$.

The total field is generated by the unwanted primary noise and the control source fields. Due to the linearity of the Helmholtz equation, the primary and secondary fields are evaluated separately and summed together to obtain the resulting field as in the following expression

$$\begin{aligned} U &= U_p + \alpha U_s = (U_{pR} + iU_{pI}) + (\alpha_R + i\alpha_I)(U_{sR} + iU_{sI}) \\ U' &= U'_p + \alpha U'_s = (U'_{pR} + iU'_{pI}) + (\alpha_R + i\alpha_I)(U'_{sR} + iU'_{sI}) \end{aligned} \tag{6.2}$$

where α is a constant utilised to drive the optimum control field as seen in Chapter 5, the subscripts $_p$ and $_s$ refer to the primary and the secondary results, respectively, and the subscripts $_R$ and $_I$ refer to the real and imaginary parts, respectively.

The optimisation problem will minimise the square modulus of the potential $U(\mathbf{X}'_D)$ within the CV in space as D

$$f_c(\mathbf{a},\, \mathbf{b}) = \int_D |U(\mathbf{X}'_D)|^2 dD \tag{6.3}$$

where $\mathbf{a} \equiv a_l = (a_1,\, a_2,\, a_3)$ and $\mathbf{b} \equiv b_m = (b_1,\, b_2,\, b_3)$ are the position vectors of the CV and the secondary source, respectively, (see figure 6.3). The controlling field is generated by a 3D object with hard boundary conditions everywhere except for a vibrating portion of the surface. The CV location is optimised by assuming that its shape and orientation remain fixed from the initial location to the final and that the secondary source is unmoved. Hence, the design variable is $\mathbf{a}$ with $\mathbf{b}$ fixed. On the contrary during the optimum control source location/orientation optimisation procedure the design variable

is **b** with **a** fixed.

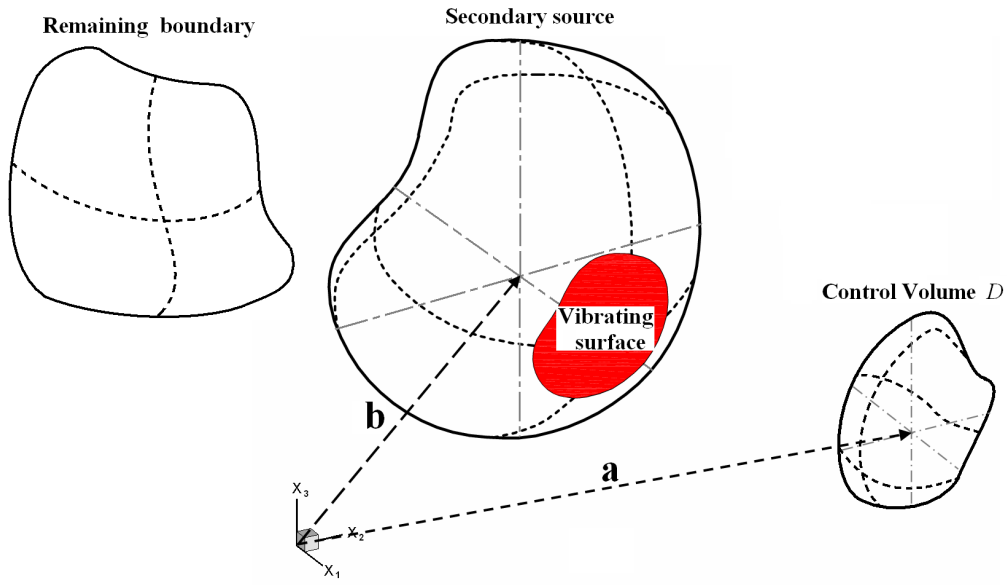


Figure 6.3: Geometry of the problem: secondary source with the vibrating surface, remaining boundary, CV, position vectors of the CV $\mathbf{a} \equiv a_l = (a_1, a_2, a_3)$ and of the secondary source $\mathbf{b} \equiv b_m = (b_1, b_2, b_3)$.

The optimisation problems can be solved iteratively and the final solution is achieved if the difference between the cost functions ($f_c(\mathbf{a})$ or $f_c(\mathbf{b})$) at two consecutive design variables is below a prescribed positive tolerance ε

$$\mid f(\mathbf{a}^{k+1}) - f(\mathbf{a}^k) \mid < \varepsilon \tag{6.4}$$

where k and $k+1$ represent the iteration numbers of two consecutive iterations.

The design variable vector $\mathbf{a}$ (or $\mathbf{b}$) at the $k+1$ iteration can be evaluated by the value of the vector at the $k-th$ iteration as follows

$$\mathbf{a}^{k+1} = \mathbf{a}^k + \mathbf{\Delta a}^k \tag{6.5}$$

where $\mathbf{\Delta a}^k$ is a variation of the current point and it can be represented as

$$\mathbf{\Delta a}^k = \alpha_k \, \mathbf{d}^k \tag{6.6}$$

where $\mathbf{d}^k$ is the desirable *search direction* to seek the optimum solution and α_k is the *step size*, a positive scalar quantity, that indicates the step in that direction. In practice, the optimisation process is converted into two subproblems, i.e., one related to evaluation of the best direction to modify the design variables and the second associated to the detection of the step length. These two quantities are iteratively updated to evaluate the optimum design variable until the condition (6.4) is fulfilled.

The optimisation procedure adopted here is based upon the Broyden-Fletcher-Goldfarb-Shanno (BFGS) variant of the Davidon-Fletcher-Powell (DFP) method [6, 98], that is a first order method and it is described in appendix B.

Hence, at each iteration the derivative of the cost function (6.3) with respect to each single component m of a design variable (either $\mathbf{a}$ or $\mathbf{b}$) is required and it is evaluated using equation (6.2) as follows

$$f_{c,m}(\mathbf{a},\, \mathbf{b}) = \frac{\partial f_c(\mathbf{a},\, \mathbf{b})}{\partial m} = \int_D \frac{\partial}{\partial a_m}[(U_{pR}+\alpha_R U_{sR}-\alpha_I U_{sI})^2+(U_{pI}+\alpha_I U_{sR}+\alpha_R U_{sI})^2]dD \tag{6.7}$$

where the Leibniz Integral Rule has been used. The two additional terms, that are generated if the limits of integration are functions of the design variable, have not been included in equation (6.7) because the CV geometry is not modified by the differentiation process.

Manipulating equation (6.7) yields the following explicit expression

$$f_{c,m}(\mathbf{a},\,\mathbf{b}) = 2\int_D [(U_{pR} + \alpha_R U_{sR} - \alpha_I U_{sI})(U_{pR,m} + \alpha_{R,m} U_{sR} + \alpha_R U_{sR,m} - \alpha_{I,m} U_{sI} - \alpha_I U_{sI,m}) + (U_{pI} + \alpha_I U_{sR} + \alpha_R U_{sI})(U_{pI,m} + \alpha_{I,m} U_{sR} + \alpha_I U_{sR,m} - \alpha_{R,m} U_{sI} - \alpha_R U_{sI,m})]dD \tag{6.8}$$

where $\alpha_{R,m}$ and $\alpha_{I,m}$ are evaluated by considering the value of α that provides the optimum secondary response for given $\mathbf{a}$ and $\mathbf{b}$.

Therefore, the optimisation process can be updated if the sensitivities, i.e., the partial derivative of the primary and secondary potentials with respect to the position vector $\mathbf{a}$ or $\mathbf{b}$ at every CV point, are evaluated at every iteration.

6.2 Implicit Differentiation of the Boundary Integral Equation

The sensitivities involved in equation (6.8) can be determined by differentiating the discretised form of the classic boundary integral equation collocated at the boundary point $\mathbf{x}'_j$, as

$$c(\mathbf{x}'_j)u(\mathbf{x}'_j) + \sum_{i=1}^{N} u_i \int_{-1}^{+1}\int_{-1}^{+1} q^*(\mathbf{x}'_j, \mathbf{x}(\eta_k)) J_i d\eta_1 d\eta_2 = \sum_{i=1}^{N} q_i \int_{-1}^{+1}\int_{-1}^{+1} u^*(\mathbf{x}'_j, \mathbf{x}(\eta_k)) J_i d\eta_1 d\eta_2 + \sum_{t=1}^{NP} P_t(\mathbf{x}'_j, \mathbf{X}^s_t) \tag{6.9}$$

where $k = 1,\, 2,\; j = 1, \ldots N$ with N number of boundary nodes; u_i and q_i are the potential and the flux at the element i, respectively; η_1, η_2 are the local coordinates, J_i is the Jacobian of the $i-th$ integration element and $P_t(\mathbf{x}'_j, \mathbf{X}^s_t)$ refers to the presence of

the $t-th$ extra source located at $\mathbf{X}_t^s$. Finally, $u^*(\mathbf{X}', \mathbf{x})$ and $q^*(\mathbf{X}', \mathbf{x})$ are the potential and the flux (normal to the boundary surface Γ) fundamental solutions, respectively.

The BEM problem is solved by utilising the boundary conditions (BCs) and evaluating the remaining unknowns at the boundary points.

The differentiation of equation (6.9) with respect to the $m-th$ design variable can be written as follows

$$c(\mathbf{x}'_j)u_{,m}(\mathbf{x}'_j) = -\sum_{i=1}^{N} u_{i,m} \int_{-1}^{+1}\int_{-1}^{+1} q^*(\mathbf{x}'_j, \mathbf{x}(\eta_k))J_i d\eta_1 d\eta_2 - \sum_{i=1}^{N} u_i \int_{-1}^{+1}\int_{-1}^{+1} q^*_{,m}(\mathbf{x}'_j, \mathbf{x}(\eta_k))J_i d\eta_1 d\eta_2 + \sum_{i=1}^{N} q_{i,m} \int_{-1}^{+1}\int_{-1}^{+1} u^*(\mathbf{x}'_j, \mathbf{x}(\eta_k))J_i d\eta_1 d\eta_2 + \sum_{i=1}^{N} q_i \int_{-1}^{+1}\int_{-1}^{+1} u^*_{,m}(\mathbf{x}'_j, \mathbf{x}(\eta_k))J_i d\eta_1 d\eta_2 + \sum_{t=1}^{NP} P_{t,m}(\mathbf{x}'_j, \mathbf{X}_t^s) \quad (6.10)$$

where $c_{,m}(\mathbf{x}'_j)$ and $J_{,m}$ are zero as the design variables do not affect smoothness and size of the boundary elements and of the CV.

The value of the potential at any internal point $\mathbf{X}'_j$ can be easily obtained in terms of the boundary values of potential u_i and flux q_i value at the boundary elements i and it is given by

$$U(\mathbf{X}'_j) + \sum_{i=1}^{N} u_i \int_{-1}^{+1}\int_{-1}^{+1} q^*(\mathbf{X}'_j, \mathbf{x}(\eta_k))J_i d\eta_1 d\eta_2 = \sum_{i=1}^{N} q_i \int_{-1}^{+1}\int_{-1}^{+1} u^*(\mathbf{X}'_j, \mathbf{x}(\eta_k))J_i d\eta_1 d\eta_2 + \sum_{t=1}^{NP} P_t(\mathbf{X}'_j, \mathbf{X}_t^s) \quad (6.11)$$

whose derivative can be written as follows

$$U(\mathbf{X}'_j)_{,m} = -\sum_{i=1}^{N} u_{i,m} \int_{-1}^{+1}\int_{-1}^{+1} q^*(\mathbf{X}'_j, \mathbf{x}(\eta_k)) J_i d\eta_1 d\eta_2 -$$
$$\sum_{i=1}^{N} u_i \int_{-1}^{+1}\int_{-1}^{+1} q^*_{,m}(\mathbf{X}'_j, \mathbf{x}(\eta_k)) J_i d\eta_1 d\eta_2 + \sum_{i=1}^{N} q_{i,m} \int_{-1}^{+1}\int_{-1}^{+1} u^*(\mathbf{X}'_j, \mathbf{x}(\eta_k)) J_i d\eta_1 d\eta_2 +$$
$$\sum_{i=1}^{N} q_i \int_{-1}^{+1}\int_{-1}^{+1} u^*_{,m}(\mathbf{X}'_j, \mathbf{x}(\eta_k)) J_i d\eta_1 d\eta_2 + \sum_{t=1}^{NP} P_{t,m}(\mathbf{X}'_j, \mathbf{X}^s_t) \quad (6.12)$$

Equation (6.10) can be collocated at each boundary point in order to build a final system of equations in terms of the unknown sensitivities. After imposing the boundary conditions, such a system can be solved and the sensitivities at any internal point can be determined by equation (6.12). It must be pointed out that the above relations can be evaluated if both the derivatives of the fundamental solutions and the derivatives of r and of its components with respect to the design variables are obtained. Such terms are outlined in the next section.

6.3 Sensitivity Analysis

Let us recall the potential and flux fundamental solutions given, respectively, by equations (3.16) and (3.18)

$$u^*(\mathbf{X}', \mathbf{x}) = \frac{1}{4\pi r} \mathbf{e}^{-ikr}$$

$$q^*(\mathbf{X}', \mathbf{x}) = \frac{\partial u^*}{\partial r}\frac{\partial r}{\partial n} = -\frac{1}{4\pi r^2}(1 + ikr)\mathbf{e}^{-ikr} r_{,n}$$

where r is the distance between the boundary point $\mathbf{x}$ and the internal (or boundary) collocation point $\mathbf{X}'$ (or $\mathbf{x}'$), $r = |\mathbf{x} - \mathbf{X}'|$ (or $r = |\mathbf{x} - \mathbf{x}'|$), and i is here the imaginary unit.

The sensitivities of the fundamental solutions can be evaluated as follow

$$u^*_{,m}(\mathbf{X}', \mathbf{x}) = \frac{\partial u^*}{\partial r}\frac{\partial r}{\partial m} = -\frac{1}{4\pi r^2}(1 + ikr)\mathbf{e}^{-ikr} r_{,m} \tag{6.13}$$

$$q^*_{,m}(\mathbf{X}', \mathbf{x}) = \frac{\partial q^*}{\partial r}\frac{\partial r}{\partial m} = \frac{1}{4\pi r^3}[(2 + 2ikr - k^2 r^2) r_{,n} r_{,m} - (r + ikr^2) r_{,nm}]\mathbf{e}^{-ikr} \tag{6.14}$$

where the partial derivatives of r and $r_{,n}$ with respect to the design variables ($r_{,m}$ and $r_{,nm}$) can be calculated using the chain rule. Their expressions depend upon the type of optimisation problem under analysis, i.e., optimum control volume location or optimum secondary source location or optimum secondary source orientation.

6.3.1 Optimum Control Source and Control Volume Locations

In case of optimisation of the control source location the value of $r_{,m}$ is evaluated as follows

$$r_{,m} = \frac{\partial r}{\partial r_j}\frac{\partial r_j}{\partial m} = \frac{r_j}{r}(\pm\delta_{jm}) = \pm\frac{r_m}{r} \tag{6.15}$$

where $j = 1, 2, 3$ refers to the coordinate system, δ_{jm} is Kronecker delta, $r_j = x_j - x'_j$ is the single component of r along the j-axes and r_m is the component along the direction m. The sign of the expression (6.15) depends upon the element over which the integral is calculated. In particular, if the element belongs to the secondary source, m coincides with the direction of x_j and the sign of (6.15) is positive, whereas if the collocation point is on the secondary source boundary, m coincides with the direction of x'_j and (6.15) is negative.

Now, the second derivative of r with respect to n and m is given by the following relation

$$r_{,nm} = \frac{\partial}{\partial m}\frac{\partial r}{\partial n} = \pm\left(\frac{n_m}{r} - \frac{r_m(r_j n_j)}{r^3}\right) \tag{6.16}$$

where the sign follows the previous rule seen in (6.15), hence $r_{,nm}$ has positive/negative sign when $r_{,m}$ is positive/negative.

In case of optimisation of the control volume location, the problem is solved by equations (6.15) and (6.16) that, since $r_j = x_j - X'_j$, have always negative signs.

6.3.2 Optimum Control Source Orientation

In case of optimisation of the control source orientation, the derivatives of the fundamental solution are evaluated by relations (6.13) and (6.14). The formulation presented in subsection 6.3.1 is not applicable for evaluating the optimum orientation of the control source. Next, the procedure for dealing with orientation is described.

To solve the problem the control source geometry is fixed, thus it has been modelled, according to [50], as a rigid sphere with a 120° degree vibrating segment (see figure 6.4). The origin of the local coordinate system coincides with the centre of the sphere (with coordinates c_j, with $j = 1, 2, 3$) and x_1 is the axial symmetry axes from the centre of the vibrating segment.

It is worth noting that rotation and translation are two rigid movements that have different aspects. In fact, the final location of an object that is translated does not depend upon the sequence of the translating directions, whereas its final orientation (at least in 3D) depends upon the succession of rotations. Herein, with reference to figure 6.4, the secondary source is rotated with respect to a local coordinate system, always parallel to the global system, whose origin coincides with the centre of the sphere. The first rotation is around the x_2-local axes and the second around the x_3-local axes. The same final secondary orientation can be obtained with different series of rotations, but in general they require evaluating of a new local coordinate system with respect to the

rotated sphere.

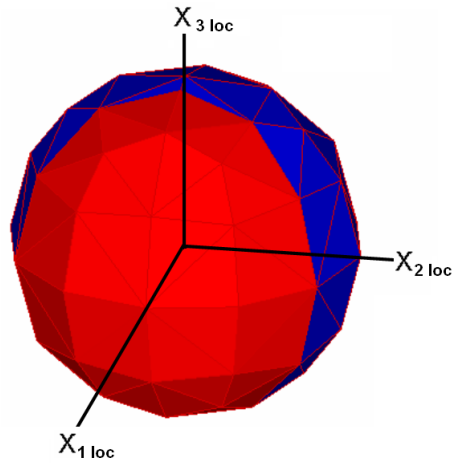


Figure 6.4: Secondary source modelled as a rigid sphere with a 120° active segment.

First, the procedure to find the optimum orientation of the secondary source around the x_2-local axes is introduced. As evident, the components along the x_1-local and x_3-local axes of each node are affected, while the component along the x_2-local axes remains unchanged. The design variable is the angle φ, i.e., the rotation around the x_2-local axes (see figure 6.5).

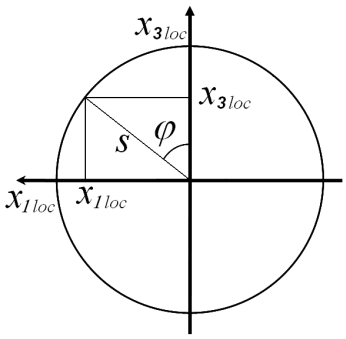


Figure 6.5: Secondary source section: the x_1 and x_3-local axes

The distance s between each node and x_2-local axes (at the origin of the circumference in figure 6.5) can be easily evaluated using the components of the node at the spherical surface in the global system, x_{1g} and x_{3g}.

$$s = \sqrt{x_{1loc}^2 + x_{3loc}^2} = \sqrt{(x_{1g} - c_1)^2 + (x_{3g} - c_3)^2} \tag{6.17}$$

where x_{1loc} and x_{3loc} are coordinates of each secondary node in the local system. It should be noted that s is located on a sphere section parallel to the $x_1 - x_3$ plane.

The value of the angle φ as shown in figure 6.5 can be calculated by using trigonometry algebra. Hence, in the global system the node coordinates can be written as follows

$$\begin{aligned} x_{1g} &= c_1 + x_{1loc} = c_1 + s\sin\varphi \\ x_{3g} &= c_3 + x_{3loc} = c_3 + s\cos\varphi \end{aligned} \tag{6.18}$$

The partial derivatives of the coordinates are given by

$$\begin{aligned} x_{1g,\varphi} &= s\cos\varphi = x_{3loc} \\ x_{3g,\varphi} &= -s\sin\varphi = -x_{1loc} \end{aligned} \tag{6.19}$$

Hence, the partial derivative of the distance $r = |\mathbf{x} - \mathbf{x}'|$ between the collocation point $\mathbf{x}'$ and the element node of the secondary surface $\mathbf{x}$ can be evaluated as follows

$$r_{,\varphi} = \frac{\partial}{\partial\varphi}\sqrt{r_j^2} = \frac{r_j r_{j,\varphi}}{r} \tag{6.20}$$

where $r_{j,\varphi}$ with $j = 1\,, 2\,, 3$ is the derivative of the component r_j along the j-axes with respect to the design variable φ. It should be noted that $r_{j,\varphi}$ coincides with $x_{jg,\varphi}$ when the element node belongs to the secondary source boundary, whereas it coincides with $-x_{jg,\varphi}$ when the point source is on the secondary surface.

The derivative of $r_{,n}$ with respect to φ can be written as follows

$$r_{,n\varphi} = \frac{\partial}{\partial \varphi}\frac{\partial r}{\partial n} = \frac{n_j r_{j,\varphi} + n_{j,\varphi} r_j}{r} - \frac{r_{,n} r_{,\varphi}}{r^2} \tag{6.21}$$

where $n_{j,\varphi}$ indicates the derivative of the component n_j along the j-axes with respect to the design variable φ that for a spherical secondary source can be evaluated as follows

$$n_{1,\varphi} = n_3; \qquad n_{2,\varphi} = 0; \qquad n_{3,\varphi} = -n_1 \tag{6.22}$$

As is evident, the value $n_{j,\varphi}$ vanishes when an element does not belong to the secondary surface.

Such an approach can be easily extended to the rotation around the x_3-local axes of the spherical secondary source. The new design variable θ is defined as the rotational angle around the x_3-local axes as shown in figure 6.6.

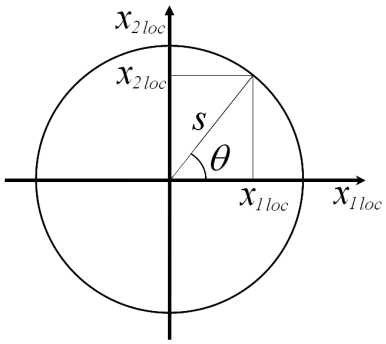


Figure 6.6: Secondary source section: the x_1 and x_2-local axes

The distance s is now on the sphere section which is parallel to the $x_1 - x_2$ plane and it can be written as follows

$$s = \sqrt{x_{1loc}^2 + x_{2loc}^2} = \sqrt{(x_{1g} - c_1)^2 + (x_{2g} - c_2)^2} \tag{6.23}$$

The component along the x_1-local and x_2-local axes of the sphere surface in the global system can be evaluated as follows

$$x_{1g} = c_1 + x_{1loc} = c_1 + s\cos\theta$$
$$x_{2g} = c_2 + x_{2loc} = c_2 + s\sin\theta \tag{6.24}$$

and the partial derivatives of r is evaluated as in (6.20).

The value of $r_{,n\theta}$ is given by equation (6.21), where the component of n, under the hypothesis of spherical secondary source, are

$$n_{1,\theta} = -n_2; \qquad n_{2,\theta} = n_1; \qquad n_{3,\theta} = 0 \tag{6.25}$$

6.4 Equation Assembly

The equation (6.9) can be collocated at the node of each element ($j = 1, \ldots N$) to give the following system matrix (equation (3.48))

$$\mathbf{Hu} = \mathbf{Gq} + \mathbf{p} \tag{6.26}$$

where $\mathbf{H}$ and $\mathbf{G}$ contain integrals of the fundamental solutions on the boundary elements, $\mathbf{u}$ and $\mathbf{q}$ contain potentials and fluxes on the boundary, respectively. Finally, the vector $\mathbf{p}$ is generated by the NP sources within the domain Ω.

The boundary conditions can be easily accounted in (6.26), hence the following system of algebraic equations is achieved

$$\mathbf{AY} = \mathbf{BJ} + \mathbf{p} = \mathbf{F} + \mathbf{p} \tag{6.27}$$

where $\mathbf{Y}$ is the vector containing the unknown boundary potentials and fluxes, $\mathbf{J}$ is a vector collecting the prescribed BCs, $\mathbf{A}$ and $\mathbf{B}$ are two coefficient matrices which are non-symmetric and densely populated, and they are composed by the columns of the matrices $\mathbf{H}$ and $\mathbf{G}$ that correspond to the unknowns and the prescribed BCs,

respectively. Finally, $\mathbf{F}$ is obtained by multiplying the matrix $\mathbf{B}$ with the vector $\mathbf{J}$.

The collocation method can be also applied to (6.10) to give the following system of equations

$$\mathbf{H}_{,m}\mathbf{u} + \mathbf{H}\mathbf{u}_{,m} = \mathbf{G}_{,m}\mathbf{q} + \mathbf{G}\mathbf{q}_{,m} + \mathbf{p}_{,m}(\mathbf{X}^{\mathbf{s}}) \tag{6.28}$$

where $\mathbf{H}$, $\mathbf{G}$, $\mathbf{u}$ and $\mathbf{q}$ are known after the solution of the direct problem (6.27), $\mathbf{H}_{,m}$ and $\mathbf{G}_{,m}$ have been outlined in section 6.2 and they involve the second and fourth integrals of equation (6.10), and $\mathbf{u}_{,m}$ and $\mathbf{q}_{,m}$ are the unknown sensitivities, i.e., the derivative of potential and flux with respect to the $m-th$ design variable. The sensitivity boundary conditions are easily gathered from the boundary conditions of the direct problem, i.e., $\mathbf{u}_{,m} = 0$ at the boundary points where $\mathbf{u}$ is given or $\mathbf{q}_{,m} = 0$ where $\mathbf{q}$ is assigned. Finally, $\mathbf{p}_{,m}$ is a vector created by the partial derivatives of the NP sources within the domain Ω with respect to m. As seen in (6.26) and (6.27), equation (6.28) can be rearranged after imposing the boundary conditions

$$\mathbf{A}\mathbf{Y}_{,m} = \mathbf{A}_{,m}\mathbf{Y} + \mathbf{B}_{,m}\mathbf{J} + \mathbf{p}_{,m} \tag{6.29}$$

As evident the term related to $\mathbf{B}\mathbf{J}_{,m}$ is not included in the above system of equations since the derivative of the prescribed BCs with respect to the design variables $\mathbf{J}_{,m}$ is zero.

The potential and its derivative with respect to the design variable at the internal points are evaluated utilising equations (6.11) and (6.12). The internal point potential is given by

$$\mathbf{U} = -\overline{\mathbf{H}}\mathbf{u} + \overline{\mathbf{G}}\mathbf{q} + \mathbf{P} \tag{6.30}$$

where $\overline{\mathbf{H}}$ and $\overline{\mathbf{G}}$ involve integrals of the fundamental solution with source point coinci-

dent with any internal point and $\mathbf{P}$ refers to the effects of the NP extra sources. The vector $\mathbf{U}_{,m}$ of the potential derivatives at the internal points is written as follows

$$\mathbf{U}_{,m} = -\overline{\mathbf{H}}\mathbf{u}_{,m} - \overline{\mathbf{H}}_{,m}\mathbf{u} + \overline{\mathbf{G}}\mathbf{q}_{,m} + \overline{\mathbf{G}}_{,m}\mathbf{q} + \mathbf{P}_{,m} \tag{6.31}$$

Equations (6.30) and (6.31) provide the terms to evaluate the cost function (6.3) and its derivative (6.8) with respect to $\mathbf{a}$ or $\mathbf{b}$.

In general, the procedure that yields the optimum secondary source location and orientation requires calculation of all the matrices in equations (6.26-6.31) and solving the two systems of equations (6.27) and (6.29) at every iteration. In fact, the secondary source is part of the geometry of the problem and a variation of its location modifies the solution of both the primary and the secondary fields. On the contrary, the optimum control volume location depends only upon the position of the CV points and, therefore, the boundary solution of the direct problem does not need to be updated and the boundary sensitivities are zero.

6.5 Numerical Aspects

6.5.1 Matrix Update

In this paragraph some implementation aspects of the formulation for the optimum secondary source location/orientation are illustrated.

The two systems of equations (6.27) and (6.29) are different at each secondary source location, hence at each iteration they are assembled and solved twice, for the primary and for the secondary fields (as is evident, in the case of optimum control source rotation the primary field is evaluated only once). Nevertheless, not all the coefficients of the matrices $\mathbf{H}$, $\mathbf{G}$, $\mathbf{H}_{,m}$, and $\mathbf{G}_{,m}$ are calculated at each step.

Consider that the element coefficients referring to the secondary source are located

at the beginning of the matrices and those referred to the remaining boundary of the domain at the end. Hence the matrices $\mathbf{H}$, $\mathbf{G}$, $\mathbf{H}_{,m}$, and $\mathbf{G}_{,m}$ can be divided into four parts as shown in figure 6.7 on the basis of the position of the source points and of the integration elements.

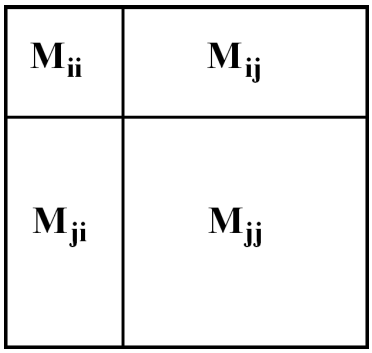


Figure 6.7: Matrix division.

The $\mathbf{M_{ii}}$ and $\mathbf{M_{ij}}$ parts of figure 6.7 refer to the effect on the secondary source generated by itself and by the remaining part of the boundary, respectively, while the $\mathbf{M_{ji}}$ and $\mathbf{M_{jj}}$ parts collect the integrals when the source point is placed anywhere except on the secondary source and the integration element moves both on the secondary source ($\mathbf{M_{ji}}$) and on the remaining boundary ($\mathbf{M_{jj}}$), respectively.

As evident, $\mathbf{M_{ii}}$ and $\mathbf{M_{jj}}$ remain unchanged for a new secondary source location/orientation, whereas the matrices $\mathbf{H}_{,m}$, and $\mathbf{G}_{,m}$ have zero coefficients in such portions. Hence, at each iteration the $\mathbf{H}$, $\mathbf{G}$, $\mathbf{H}_{,m}$, and $\mathbf{G}_{,m}$ matrices are evaluated only at the $\mathbf{M_{ji}}$ and $\mathbf{M_{ij}}$ portions for both the primary and secondary fields.

6.5.2 Rapid Solver

Due to the fact that the BEM system matrix is non-symmetric and fully populated, the solutions of the two systems (6.27) and (6.29) are time consuming, especially in

optimisation and identification problems where the solution is required many times. Moreover, each term of the cost function (6.3) and its derivative (6.8) requires evaluation of the internal point quantities by equations (6.30) and (6.31) that can considerably increase the solution time in the case of large sized control volumes. To accelerate the CPU time for all simulations the Adaptive Cross Approximation (ACA) in conjunction with the H-matrix format and the iterative solver GMRES is utilised as presented in Chapter 4. The proposed method (RABEM) has been applied to accelerate the matrix assembly time, the boundary solution steps (6.27) and (6.29) and the evaluation of $\overline{\mathbf{H}}$, $\overline{\mathbf{G}}$, $\overline{\mathbf{H}}_{,m}$ and $\overline{\mathbf{G}}_{,m}$ in (6.30 - 6.31).

Comparisons between the proposed strategy and the standard procedure can be found in many papers (see for instance [13, 14, 22]). It must be pointed out that the singularities of the kernels involved in the sensitivity problem are of the same order of the singularities as the kernels involved in the direct approach [85]. Such a point guarantees a sufficient condition for the low rank representation of the matrices $\mathbf{H}_{,m}$ and $\mathbf{G}_{,m}$ of (6.26). Moreover, the programming path for the application of the ACA is the same for the two system of equations, i.e., the direct system and the sensitivities system.

6.6 Numerical Examples

In this section five different examples are presented to test the proposed procedure. The secondary field is created by a hard ($q = 0$) spherical speaker (with radius equal to 8 cm except in the last example where it has been reduced to 4 cm) with a 120° vibrating segment (with constant q) and meshed with 120 constant elements (see figure 6.4).

The optimum secondary source location is obtained in terms of the coordinates of the sphere's centre.

The reduction is calculated as suggested by Bermudez *et al.* [18] and it can be

written as follows

$$Attenuation(\mathrm{X}') = -10\log_{10}\left(\frac{f_c(\mathrm{X}')_{op}}{f_c(\mathrm{X}')_0}\right) \tag{6.32}$$

where $f_c(\mathrm{X}')_{op}$ and $f_c(\mathrm{X}')_0$ are the values of the optimised cost function (6.3) and of the cost function without secondary source at the internal point X', respectively.

The integral over the CV is represented using 8 node brick cells. The Legendre-Gauss quadrature rule is subsequently used to evaluate the integral (6.3), [111, 125].

The geometry of the second example has been taken from Seyedin and Abedi [110] whose data are used as reference.

For internal problems the optimisation routine [98] has been modified to avoid the possibility of the boundary related to the design variables going outside the geometry along the iteration path.

The five numerical examples are summarized in table 6.1 where design variables, example number and geometry are indicated. It should be noted that the procedure for secondary source optimum orientation is validated with the two examples.

Design variables	**Example**	**Geometry**
Optimisation of CV location	1^{st}	Unbounded domain
Optimisation of sec. sour. location	2^{nd}	$4\ m \times 3\ m \times 2.5\ m$ room
Optimisation of secondary source orientation	3^{rd}	$1\ m \times 0.5\ m \times 0.5\ m$ box
	4^{st}	$4\ m \times 3\ m \times 2.5\ m$ room
Optimis. of sec. sour. location at different freq.	5^{st}	Airplane cabin

Table 6.1: Numerical examples.

The proposed procedure would be time consuming if a standard BEM code was utilised. As described in Chapter 4 the code based on the H-matrix ACA GMRES formulation is up to 175 times faster than a standard BEM base code for a mesh with

more than 10340 elements. Furthermore, the increased computational efficiency of the proposed fast procedure is also confirmed in evaluation of the potential and particle velocity at the internal points.

6.6.1 CV optimum location

The first example consists of finding the optimum location of the CV centre in an infinite domain immersed in a diffuse primary noise (see figure 5.3). The primary noise potential at each point of coordinate $\mathbf{X}$ is given by equation (5.7)

$$U_p(\mathbf{X}) = \sum_{j=1}^{j_{max}} \sum_{l=1}^{l_{max}} (a_{jl} - ib_{jl}) \mathbf{e}^{ik\hat{e}_k \cdot \mathbf{X}} \tag{6.33}$$

where i is the imaginary unit, k is the wave-number, $\hat{e}_k$ is the plane wave versor and $\cdot$ is the operator of the scalar product. The values of j_{max} and l_{max} are 6 and 12, respectively, used to generate 72 plane waves distributed in all directions of the space which create a diffuse primary noise. The values of a_{jl} and b_{jl} are randomly chosen from a uniform distribution. The origin of the global coordinate system coincides with the sphere centre. The CV has dimensions of $10 \times 16 \times 8$ cm in the x_1, x_2, x_3 axes, respectively. It has been meshed by 140 nodes and 72 8-nodes brick elements.

It must be pointed out that the optimum CV location depends on the frequency under analysis and on the random distribution of the primary noise.

In the present example the optimisation procedure is performed at 1092 Hz and along only the x_1-axes. Figure 6.8 shows a series of CV location for different iterations of the optimisation procedure. In particular, the CV in a) is the initial guess position, b) is the location of the CV at the first iteration and c) the final optimum CV location.

Figure 6.9 shows the variation of the cost function versus the x_1-coordinate of the CV centre for four different frequencies (109, 273, 546, 1092 Hz) . The same primary field composed by 72 plane waves of the previous example have been used at the different

frequencies. It can be noted that the higher the frequency, the higher the number of local minima and the lower the noise attenuation level. As evident, from figure 6.9, some local minima may occur and a unique optimum CV location valid for all frequencies cannot be evaluated. The present results have been compared to the results obtained in [44, 99] in appendix C.

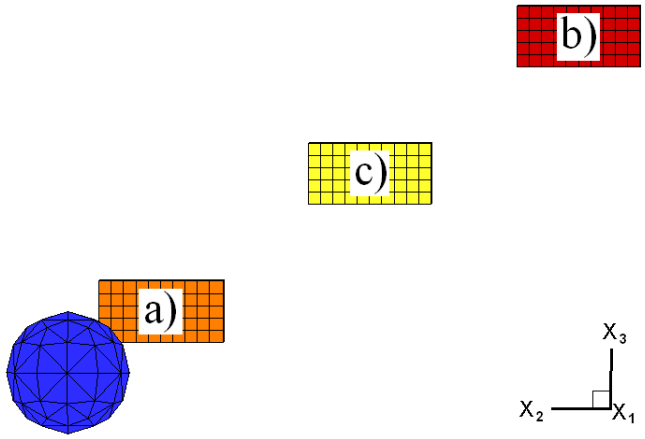


Figure 6.8: Example 1. Different locations of the CV at a frequency of 1092 Hz: a) initial guess; b) first iteration; c) second iteration.

6.6.2 Optimisation of the secondary source location

In the second example the location of the secondary speaker is optimised inside a room with dimension (in metres) 4×3×2.5 and discretised by 5902 nodes and 11800 super-parametric (linear geometry, constant unknown) elements. The walls are modelled as hard, hence the sound is not absorbed and remains inside the room all the time. The primary noise is generated by a vibrating surface placed from (2.6, 3.0, 2.0) to (3.0, 3.0, 2.2) in one of the walls, i.e., a noisy air gate is simulated. The reduction of the noise is requested in a cubic CV with opposite vertexes (0.5, 0.5, 0.8) and (2.5, 1.5, 2.0)

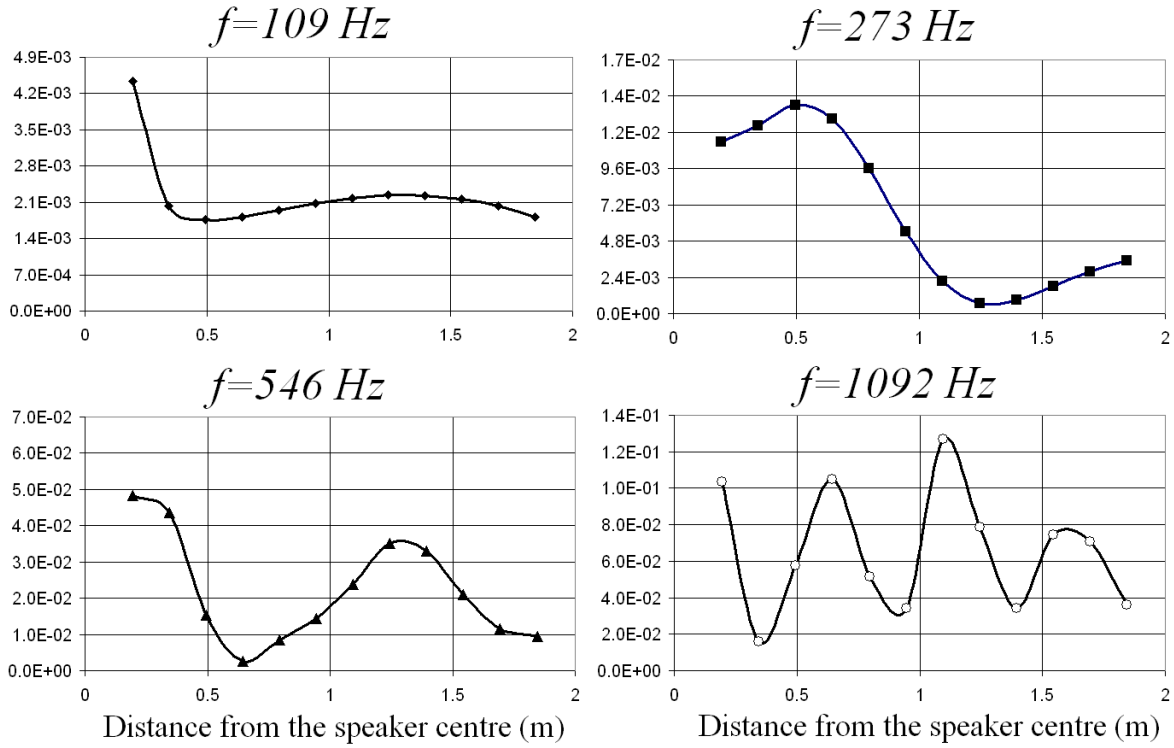


Figure 6.9: Example 1. The cost function f_c for four different frequencies.

composed by 2640 point and 2090 linear brick elements. The frequency, used in this example and in the next one, is 78 Hz close to the first resonance frequency (85 Hz).

Figure 6.10 shows the geometry of the room, the coordinate system, the location of the CV (the box on the left) and the primary noise, which is displayed in red.

In [110] the secondary source is modelled as a monopole moving on the walls of the room. The best position (2.5, 3.0, 1.9) allows a maximum noise reduction of 17.9 dB. In the present contribution a higher level of noise reduction is achieved and the best position of the secondary source is evaluated to be in front of the source of noise.

Such a location is not the only optimum value since, as reported in [92], in closed space the optimum location can be at several positions inside the enclosure, especially for not damped environment.

Table 6.2 shows the optimum locations of the centre of the secondary source for four orientations of the vibrating segment with respect to the x_1 axes (0, $\pi/2$, π, $3\pi/2$:

where the secondary source is rotated around the x_3-axes and the vibrating segment is initially orientated along the x_1-axes) and initial guess at the point (2.0, 2.9, 0.1).

Initial orient. (rad)	Final opt. pos. (x_1, x_2, x_3)	Attenuation (dB)	N iter.
0	2.60, 2.78, 1.96	35.20	12
$\pi/2$	2.69, 2.80, 2.00	41.41	22
π	2.65, 2.81, 1.98	36.82	12
$3\pi/2$	2.74 2.81, 1.98	39.66	17

Table 6.2: Example 2. Optimum location of the secondary source centre, level of noise attenuation (dB) and number of iterations for four different initial orientation values (0, $\pi/2$, π, $3\pi/2$) in radians.

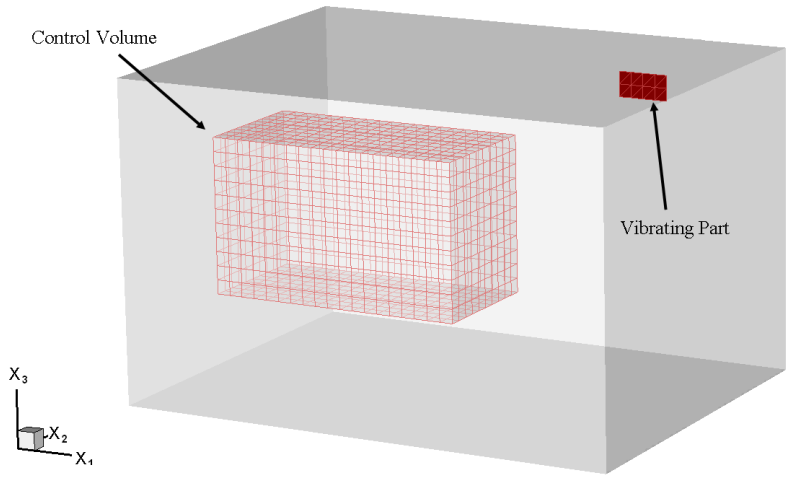


Figure 6.10: Example2. Room geometry, CV and primary noise locations.

The best reduction is achieved when the initial orientation is $\pi/2$ so that the directions of the vibrating segment and the primary noise are the same. Figure 6.11 shows the different locations assumed by the secondary source at each iteration. In particular the bottom position (a) is the initial guess, then the secondary source is moved to better locations (b) between the initial guess and the primary noise position, hence in a subsequent iteration (c) it is almost at the optimum location, that is clearly marked.

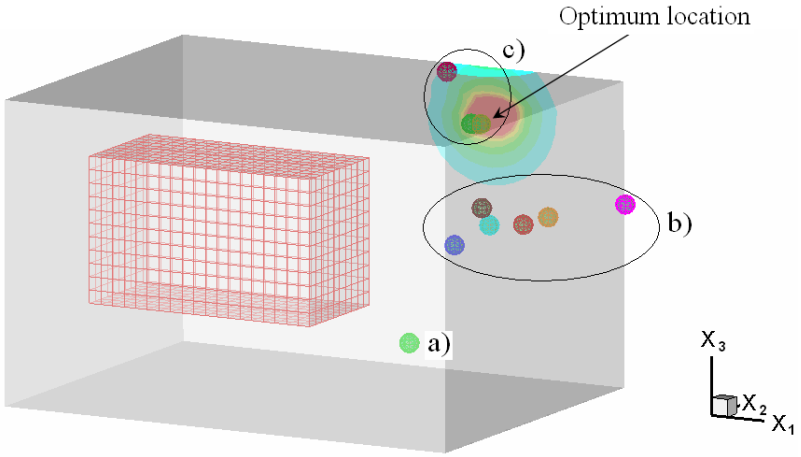


Figure 6.11: Example 2. Different locations of the secondary source in the optimisation procedure.

Figures 6.12 and 6.13 depict the sound pressure level distribution inside the room and in the CV in absence of the secondary source (a) and in presence of the optimum secondary source (b).

As evident, the SPL is very low inside the CV where a reduction up to 60 dB is achieved at some points. The SPL in the room is reduced in average of 10-15 dB.

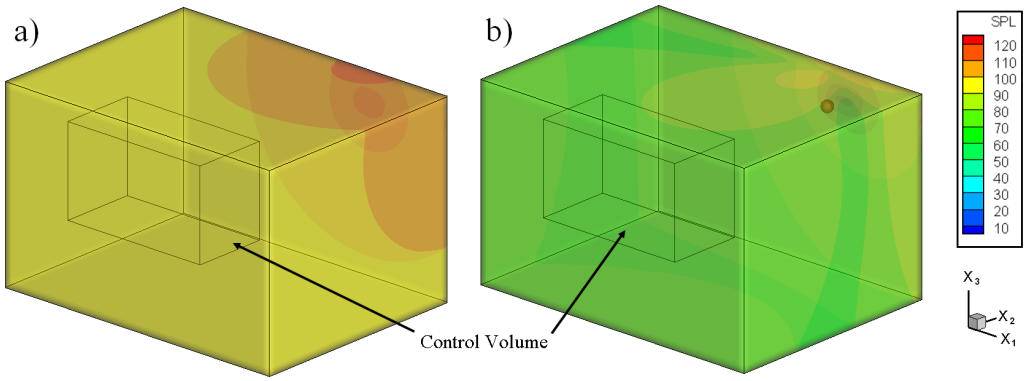


Figure 6.12: Example 2. SPL distribution (dB) inside a 4×3×2.5 m room of a) the pure primary noise, and b) the total field generated by the primary noise and the speaker.

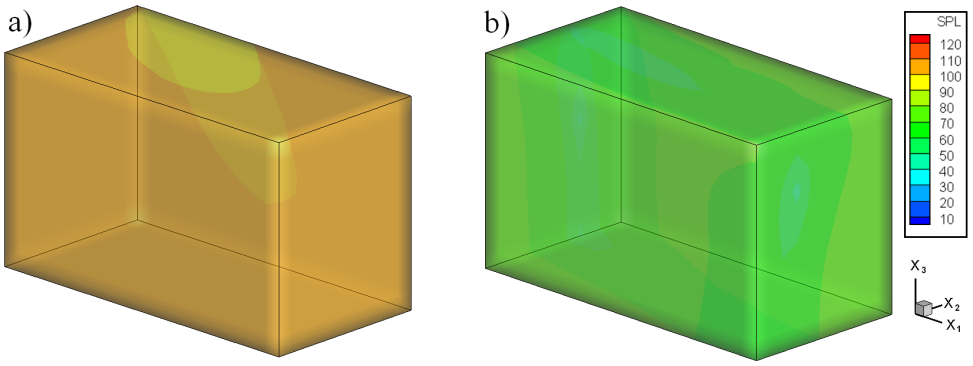


Figure 6.13: Example 2. SPL distribution (dB) inside a 2×1×1.2 m CV of a) the pure primary noise, and b) the total field generated by the primary noise and the speaker.

6.6.3 Optimisation of the secondary source orientation

This example concerns the optimal orientation of the secondary source. A box with dimensions 1×0.5×0.5 (in metres) contains a small cubic (0.3×0.3×0.3 m) CV, with the two opposite corners (0.1, 0.05, 0.05) and (0.4, 0.35, 0.35). The primary noise is generated, as in the last example, by a vibrating portion of a wall of the box, with opposite corners (0.8, 0.5, 0.3) and (0.9, 0.5, 0.4) (see figure 6.14). The frequency chosen is 320 Hz, close to the first resonance frequency (340 Hz). The centre of the secondary source is located in front of the source of noise at the point (0.8, 0.3, 0.4) and the vibrating surface is orientated along the negative x_2-axes. At this position the cost function value is $f_c = 6.85\,10^{-9}$. The geometry of the problem as depicted in figure 6.14, where the CV, the secondary source and the vibrating surface of the wall can be easily distinguished.

Figures 6.15 and 6.16 show the SPL contour plot in the whole box and inside the CV, respectively, for two different orientations of the secondary source: a) initial guess ($\theta = -\pi/2$, $\phi = 0$), b) optimal configuration ($\theta = 1.585$, $\phi = 0.315$ rad). The final cost function is $f_c = 1.52\,10^{-9}$. A reduction of 6.54 dB is achieved inside the CV.

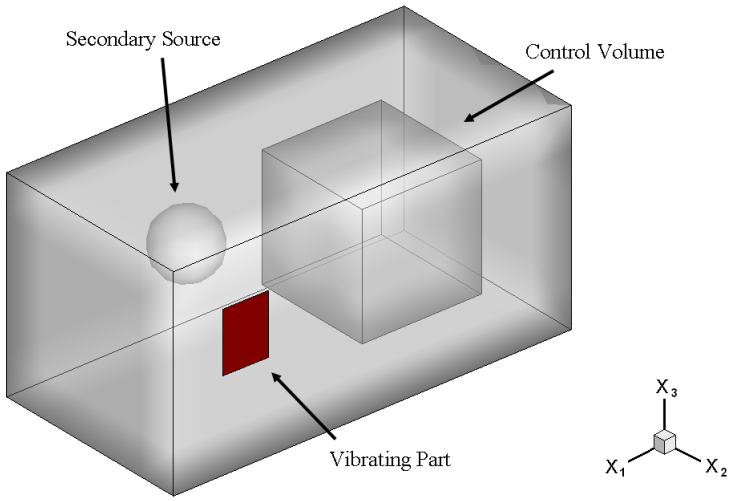


Figure 6.14: Example 3. Geometry of the problem.

This example shows that the orientation of the secondary source influences the level of noise; its optimum value may reduce considerably the SPL inside the CV.

A second example (example 4) of optimisation of the secondary source orientation has been performed. The secondary source centre is located at (2.65, 2.81, 1.98) in the same room of example 2; such a location has been obtained as optimum position with the source orientation equal to π and the vibrating segment pointing as the x_1-axes. Table 6.3 shows the initial guess and the final orientation (in radians) of the source, the attenuation achieved and the number of required iterations.

Initial rotation θ,φ	Final optimum orientation	Attenuation (dB)	N iterations
0.0, 1.5	0.0, 2.13	38.02	6
0.0, 3.0	0.2, 2.135	38.17	6
1.5, 4.0	0.0, 2.13	38.02	6
2.35, 0.0	1.59, -0.23	40.52	4

Table 6.3: Example 4. Optimisation of the speaker's orientation for different initial guesses.

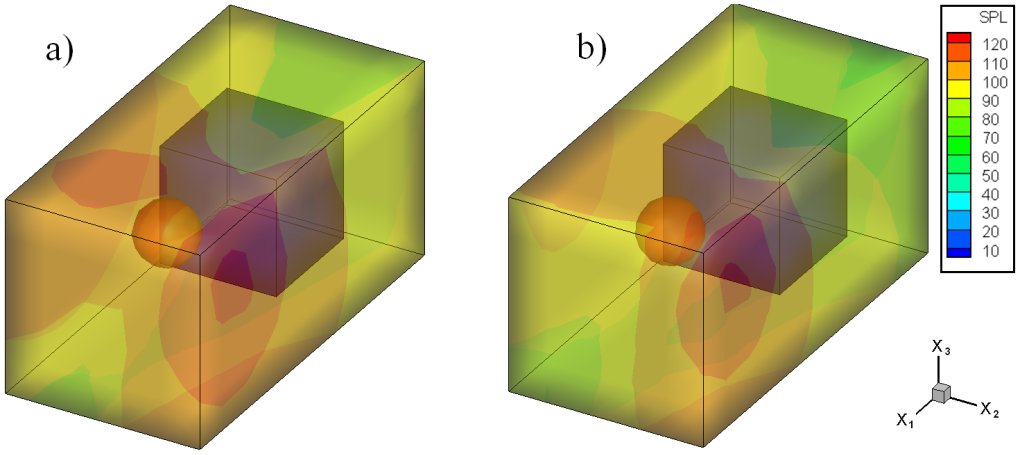


Figure 6.15: Example 3. SPL distribution (dB) inside the box of the total field generated by the primary noise and the speaker a) initial guess, and b) optimal value.

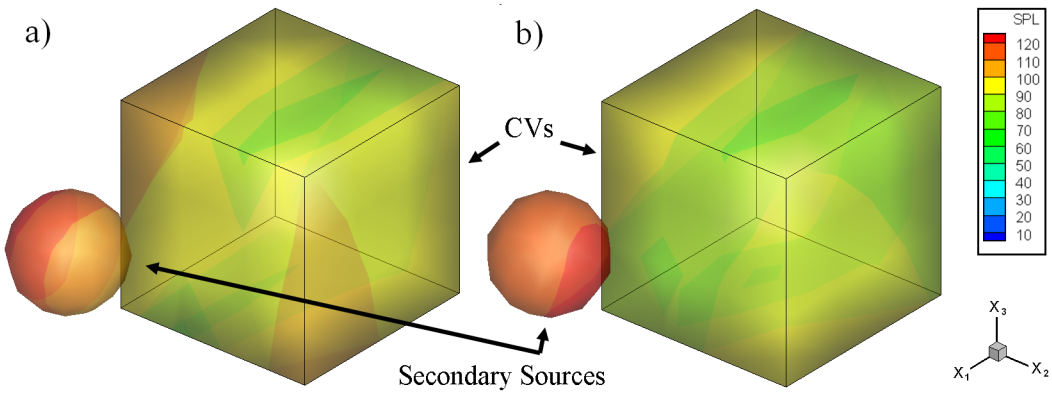


Figure 6.16: Example 3. SPL distribution (dB) inside the CV of the total field generated by the primary noise and the speaker: a) initial guess, and b) optimal value.

It can be noted that the first, second and third analysis achieve approximately the same optimum, whereas the fourth attempt gives a different local minimum with higher attenuation. Nevertheless, the reduction in dB for all is the same if a tolerance of 2 dB is considered.

Finally, it should be noted that the reduction level in all the four final orientations is higher than the value obtained from the optimal location analysis of the previous case when the initial orientation is π.

6.6.4 Optimisation of the secondary source location in a large-scale engineering problem

A series of simulations to evaluate the optimal secondary source location for seven different frequencies (70, 100, 130, 160, 170, 180, 200 Hz) inside an airplane cabin is presented in this section.

In figure 6.17 the model representing the aircraft cabin is depicted. Due to the geometrical and loading symmetry, half cabin is considered. A symmetric plane is considered. A monopole is positioned at (2.0, 4.0, -0.5) to simulate the noise inside the cabin. The initial guess of the secondary source is located at (0.76, 1.24, 1.0). A detailed view of one of the rows, the CV and secondary source locations are all depicted in figure 6.18. The secondary source vibrating surface is highlighted in red.

The cabin is included in a cuboid of dimensions $2\times1.9\times2.3$ whereas each line of seats is 0.5×1.35 m with height 1.054 m. The headrest is 0.46 m long (along the x_2-axes) and the control volume is a $0.2\times0.32\times0.2$ m cuboid, so that it covers most of the headrest extension. The secondary field is generated by a rigid sphere with radius 4 cm and an active segment of 120^0 degree headed in the negative x_2 direction, kept constant along the optimisation procedure. The cabin is meshed by 3914 nodes and 7699 constant elements in order to be able to deal with up to 250 Hz. In fact, 10 elements per wavelength are guaranteed at such a frequency. All the surfaces are assumed to be hard. The integration in the CV is performed by subdividing it into 160 cuboid linear elements.

The seven frequencies tested cover the frequency range (50-200 Hz) of a typical jet noise [83].

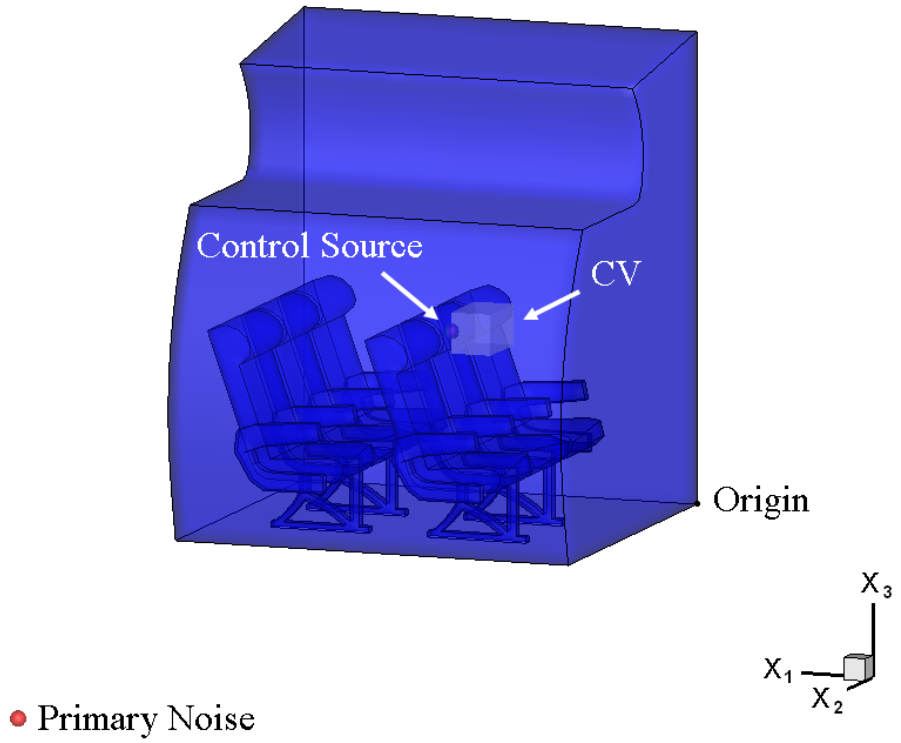


Figure 6.17: Example 5. Geometry of the cabin: Origin of the coordinate system, CV, secondary source and primary noise (monopole outside the cabin) locations.

Figure 6.19 shows a few secondary source locations at different iterations of the optimisation procedure at 70 Hz, where the initial position (a), locations of a first group of iterations (b), a location of the last iteration (c), and the final optimum location (d) are displayed. The final placement is on the top of the seat row, close to the front panel.

Figure 6.20 shows the SPL distribution at 70 Hz when the secondary source is located at the optimum position (-0.532, -0.187, 0.396). The presence of extended zones of quiet is related to the large value of the wavelength (equal to 4.86 m) in comparison with the size of the cabin.

The SPL and the optimum secondary source locations, highlighted with red circles, are displayed in figure 6.21 for the following frequencies: a) 100 Hz; b) 130 Hz; c) 160 Hz; d) 170 Hz; e) 180 Hz; f) 200 Hz.

Table 6.4 reports the optimum location of the centre of the secondary source (re-

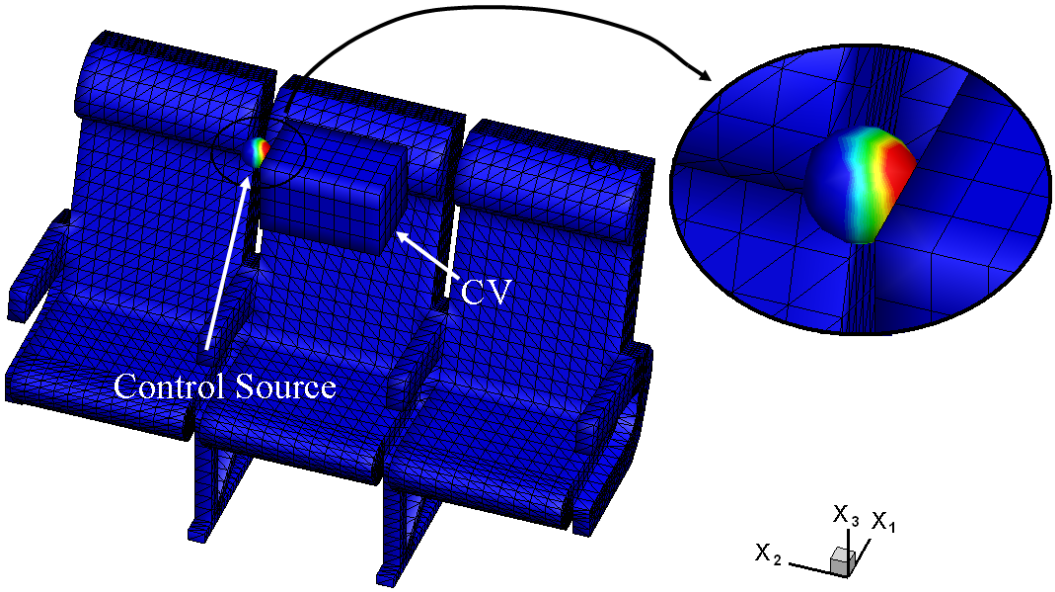


Figure 6.18: Example 5. Particular of the seat of the cabin: row and CV meshes, secondary source with the vibrating segment.

ferred to a coordinate system which is parallel to the global one and centred at the initial location of the secondary source), the initial and optimal reductions in dB. For each frequency the optimal reduction is about double the initial one.

Freq. (Hz)	Optimum loc.	Initial reduction (dB)	Optimal reduction (dB)
70	(-0.54, -0.19, 0.40)	7.69	17.37
100	(0.15, -0.53, 0.96)	7.31	11.95
130	(0.06, 0.14, -0.06)	6.60	11.48
160	(-0.09, 0.57, -0.03)	7.75	19.29
170	(-0.12, 0.60, -0.05)	8.53	18.44
180	(-0.05, 0.22, -0.02)	9.05	16.40
200	(-0.05, 0.21, -0.03)	9.26	16.02

Table 6.4: Example 5. Optima secondary source locations for seven different frequencies (70, 100, 130, 160, 170, 180, 200 Hz) and the corresponding reduction at the initial and optima locations, respectively.

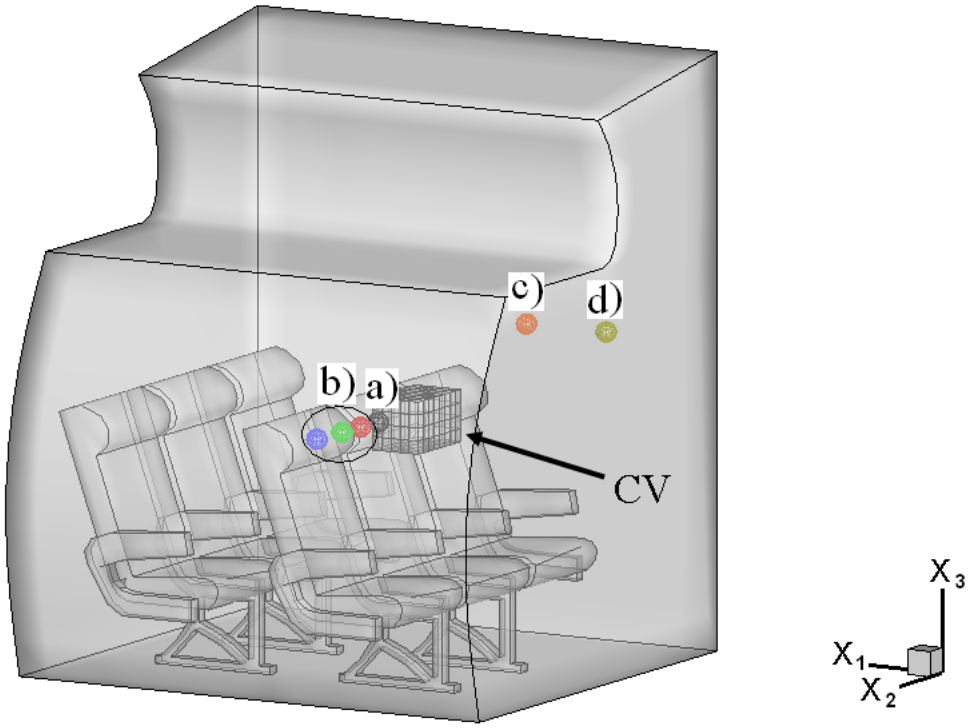


Figure 6.19: Example 5. A few different secondary source locations at optimisation procedure iterations at 70 Hz: a) initial guess; b) locations of a first group of iterations; c) next to the last iteration; d) final optimal position.

Considering all examples, it can be noted that in an infinite domain the solution depends upon the diffuse primary noise characteristic, whereas for a distinctive noise at a certain frequency the optimum location and orientation of the secondary source have distinguished optimum values.

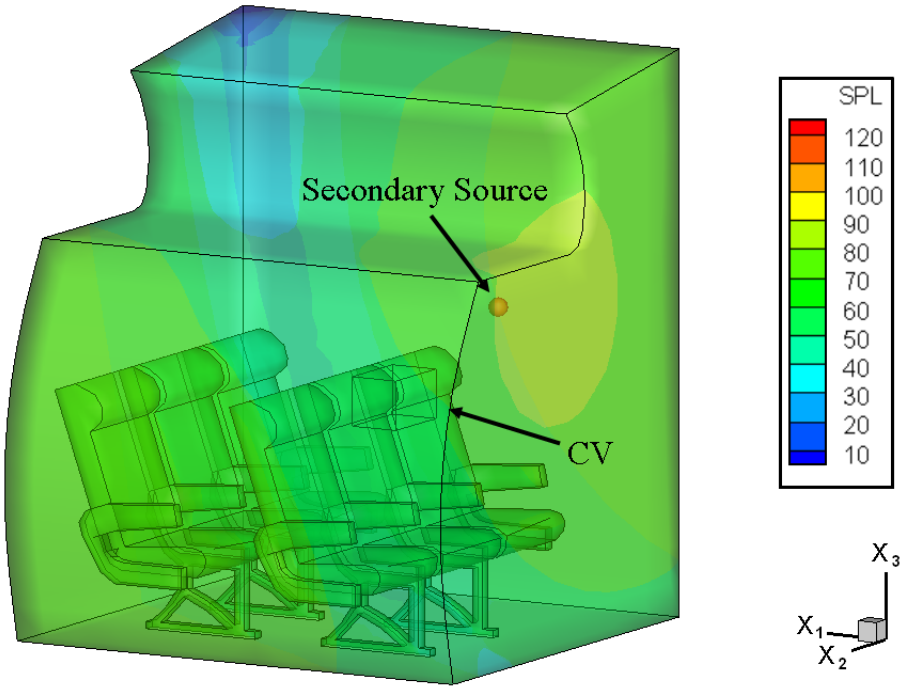


Figure 6.20: Example 5. SPL and optimum secondary source location at 70 Hz.

Summary

In this chapter a sensitivity analysis in active noise control has been developed. The 3D acoustic propagation problem has been modelled by the Helmholtz equation and numerically solved by coupling the ACA, the H-matrix format and the GMRES solver with the BEM (RABEM code). The optimisation procedure is performed by applying a first order method. The sensitivities are determined by the implicit differentiation approach. The noise reduction has been achieved by attenuating the unwanted primary sound inside a control volume with the aid of a secondary acoustic source. Three optimisation problems have been presented. The first refers to the optimum location of the CV, the second and the third find the optimum secondary source location and orientation, respectively, to obtain the highest noise reduction among all the possible admissible configurations. Five examples have been presented in order to demonstrate the efficiency of the procedure. An example is performed with reference to a real large-

scale engineering problem, i.e., the best location of the loudspeaker for a local ANC strategy inside an aircraft cabin.

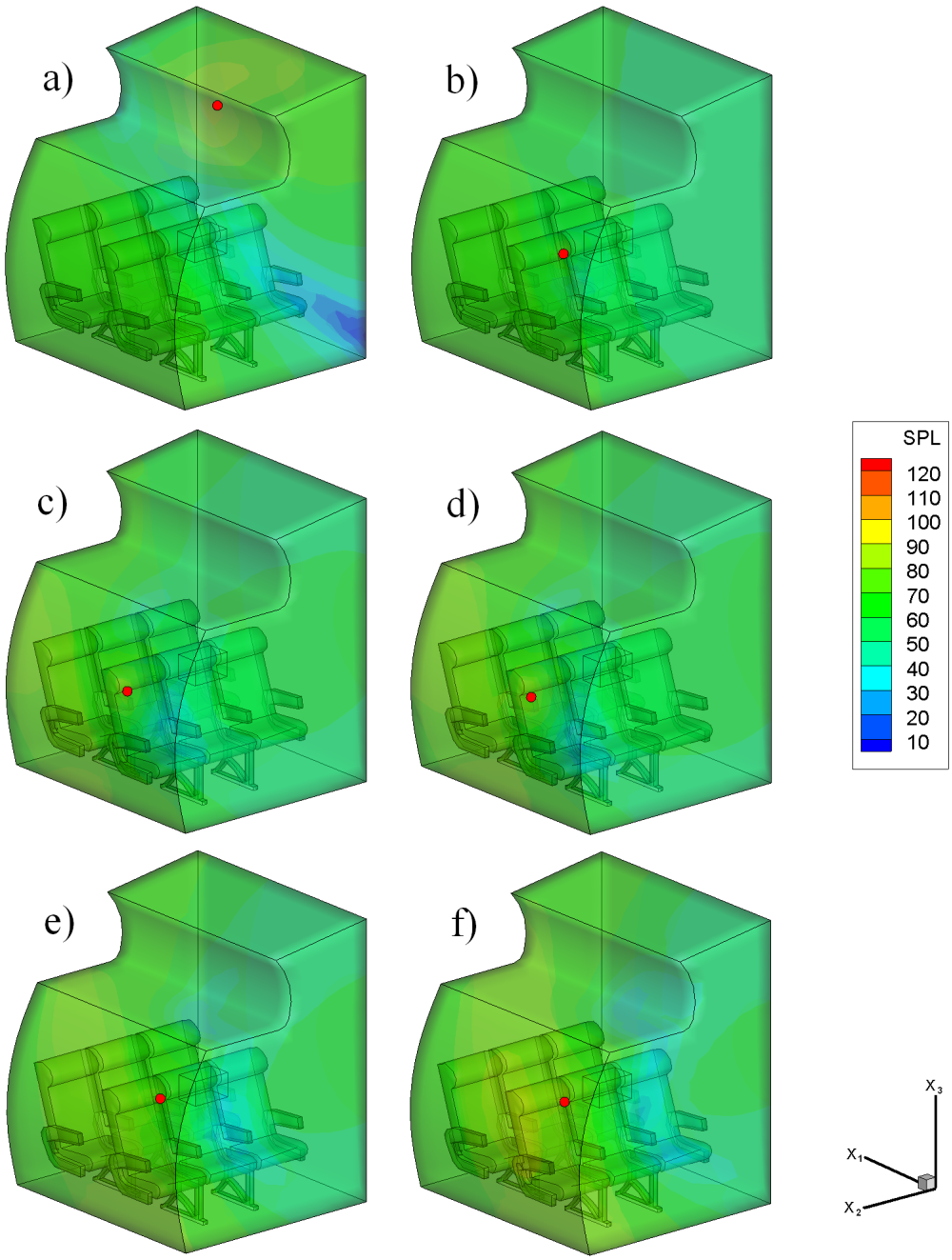


Figure 6.21: Example 5. SPL and optima secondary source locations, highlighted in red, for the six frequencies: a) 100 Hz, b) 130 Hz, c) 160 Hz, d) 170 Hz, e) 180 Hz, f) 200 Hz.

Chapter 7

Passive Noise Control

Passive Noise Control is the most popular noise control strategy because it is simple, cheap and easy to implement. As mentioned in Chapter 2, disturbing noise can strongly affect a person's social behaviour and psychologists are studying the consequences of extended exposure to unwanted noise on the human mind, i.e., psychoacoustics. In this regard modern aircraft are surely quieter than their predecessors, but better performances can be still achieved. Many studies are focused towards this goal (see for instance [38, 42, 96, 114]).

Computer simulations help in identifying locations and materials that could be utilised for such a purpose and strongly reduce practical costs of experimental tests. Nevertheless, the complex shape of the cabin does not allow an analytical approach and it requires numerical procedures. Additionally, the presence of unequally distributed absorbing materials on the cabin surfaces complicates the investigation and an high performance approach is necessary.

This chapter presents some results obtained inside the project "Smart tEchnologies for stress free Air Travel (SEAT)" under the 6^{th} Framework Programme. The work reported in this chapter includes contributions from Dr. Vincent Marant (Acusttel), Dr. Vincenzo Mallardo (Imperial College), Mr. Lucas Li (Imperial College). The main

goal is to numerically investigate the acoustic performance of a new textile which was utilised inside the project. This textile is a nanofibre web with excellent absorptive properties in the low frequency range and it can be used as upholstery to reduce the noise in the aircraft cabin. For this reason the analysis has been focused on the frequency range 8-1000 Hz.

All the numerical results are obtained by LMS Virtual.Lab commercial code [82] and a few of them are compared with the RABEM code. The direct BEM is utilised for all the simulations and the LMS results are given in terms of pressure/velocity. The value at any internal point can be determined in the post-processing step on the basis of the knowledge of the solution on the boundary as explained in Chapter 3. The mesh used is composed of parametric linear quadrilateral/triangular elements and it has been set to have at least four elements per wavelength.

The numerical simulations have been aimed at reducing the effort of the experimental tests of the project and to evaluate the practical influence of the nanofibre and different headrest geometries on the sound distribution inside an aircraft cabin. First, some experimental tests performed by Acusttel (one of the partners of the project) have been recovered. Second, various textile properties, diverse locations of the nanofibre and different headrest geometries have been investigated, and, third, a sensitivity analysis on the new headrest shape is presented.

The current results refer to a specific signal spectrum related to one of the common flight operations of an aircraft. The geometry under investigation is similar to an actual aircraft cabin. The absorbing properties of the panels of the cabin are determined on the basis of both the scientific literature [38] and the experimental results obtained by Acusttel [86].

7.1 Experimental Tests

The experimental tests were performed at Thales laboratory (Toulouse, France) by Acusttel during the SEAT project. An aircraft cabin mock-up (see figure 7.1) was set up and subjected to different acoustic sources. Some microphones were located to measure the sound pressure level (SPL) in proximity to the passenger's ears.

The mock-up is constituted by two lines of three rows (see figure 7.2). The cabin is edged by a Plexiglas and a plywood panel in the rear and front parts, respectively, and the cabin entrance is located at the front panel (see figure 7.1-b). The structure of the floor is built in wood and covered with carpet and all the remaining surfaces (lateral panels and storage ceiling) are plywood.

In order to create a diffuse acoustic field, the noise was generated by a dodecahedral speaker located in the middle of the corridor at 1.42 m from the floor and at 0.37 m from the rear plane (point A in figure 7.2). The experiments were performed with different acoustic signals reproducing various phases of a common flight, e.g., boarding, take-off, cruise, landing. Three spectrum signals are given in figure 7.3-7.5. The final primary field is generated by scaling these signals by an amplification factor that depends on the dodecahedral speaker.

Two microphones were located in each row at the headrests of the seats (see figure 7.1-a and dots of figure 7.2). As afore-mentioned the SEAT project is focused on the economy class, hence the data are referred to the seat 7-9 and 12-14.

The acquisition system, including microphones, analyser and wires, is of class I, i.e., the most precise possible. The sample frequency was 51200 Hz and the acquisition was real-time and simultaneous in several microphone positions. Finally, the microphone calibration was checked before and after the tests.



(a) (b)

Figure 7.1: Experimental mock-up: a) microphones at the seat headrests; b) front panel [86].

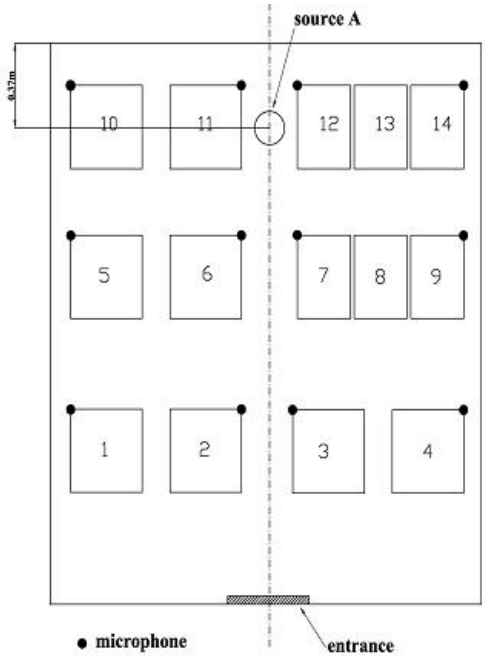


Figure 7.2: Thales mock-up [86].

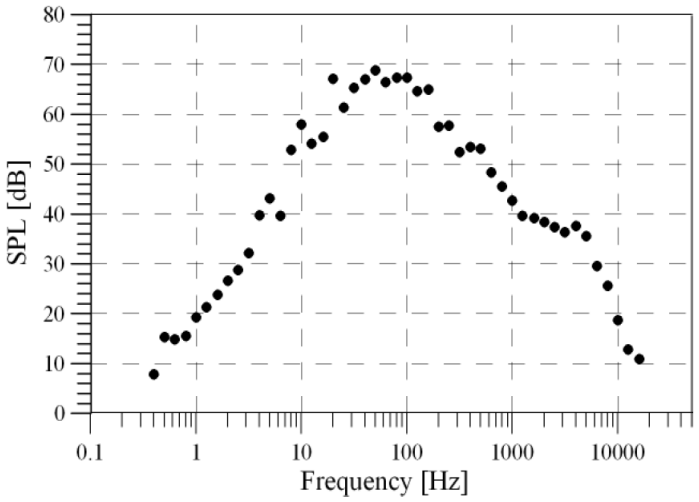


Figure 7.3: Experimental signal spectrum: takeoff.

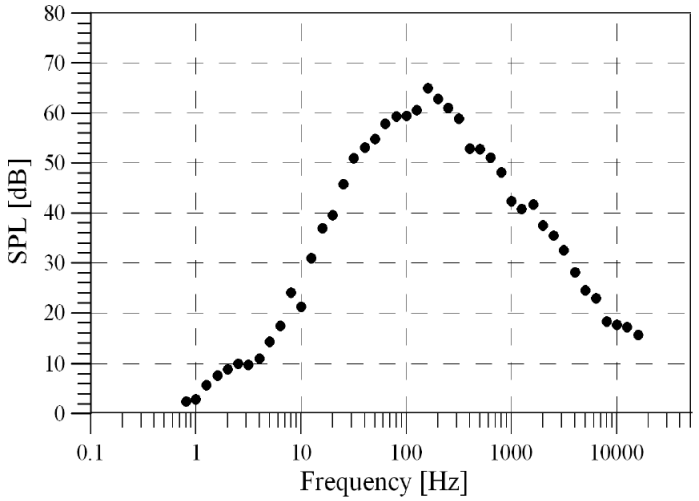


Figure 7.4: Experimental signal spectrum: landing.

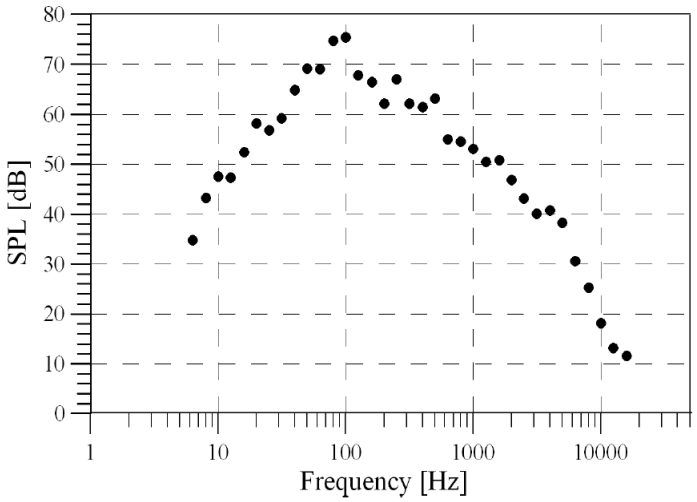


Figure 7.5: Experimental signal spectrum: cruise.

7.2 Cabin Model

The model of the analysed cabin consists of two lines of three seats (with passengers) surrounded by the aircraft fuselage. The initial geometric model (figure 7.6) have been developed during the SEAT project and have been modified and meshed to perform the acoustic simulations with LMS[1] and RABEM. In order to reduce the computational effort of each simulation, the geometry has been simplified, i.e., eliminating the passengers (the experimental results are available without passengers) and utilising only half cabin. Furthermore, two panels, one at the front (which is not included in the figures to show the results) and one at the rear of the cabin, were added to the model in order to obtain an "internal closed surface" to be correctly described by a numerical approach.

The frequencies investigated are between 8 and 1000 Hz since the afore-mentioned nanofibres provide better performance in this range compared with a standard uphol-

[1]The BEM models were developed with Abaqus by Dr. V. Mallardo (Imperial College) and later modified by L. Li (Imperial College), a fourth year student of the Aeronautics Department under the supervision of the author of this thesis.

stery textile. In other frequencies the new textile in conjunction to seat filling does not offer any further absorbing property, since the absorbing coefficient is already undoubtedly high in a standard aircraft seat. Thus no simulation has been performed above 1000 Hz.

The surfaces have been meshed with linear either quadrilateral (quad) or triangular (tri) elements. Figures 7.7-a and 7.7-b show the meshes adopted in the simulations. The former is composed by 9876 nodes and has been utilised for frequencies up to 100 Hz, whereas the latter is for the range 125-1000 Hz and it is constituted by 13806 nodes. Both meshes are sufficient to guarantee at least 4 elements per wavelength. Two triangular meshes (with about 20200 and 32280 nodes, respectively) have been also used to verify the accuracy of the results with regard to 1000 Hz frequency. The front panel, not present in the experimental tests, has been added in the numerical model to obtain a closed surface for the BEM simulations.

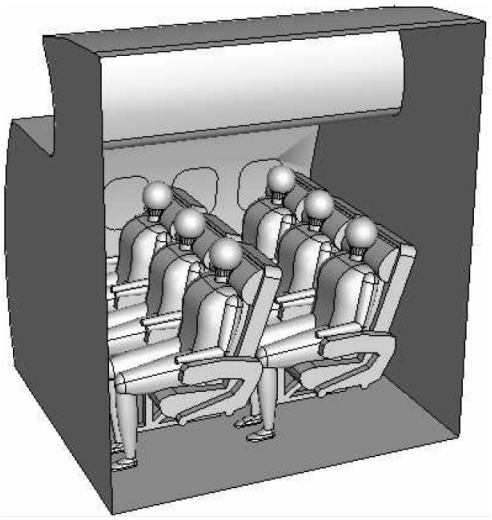


Figure 7.6: Initial cabin model [86].

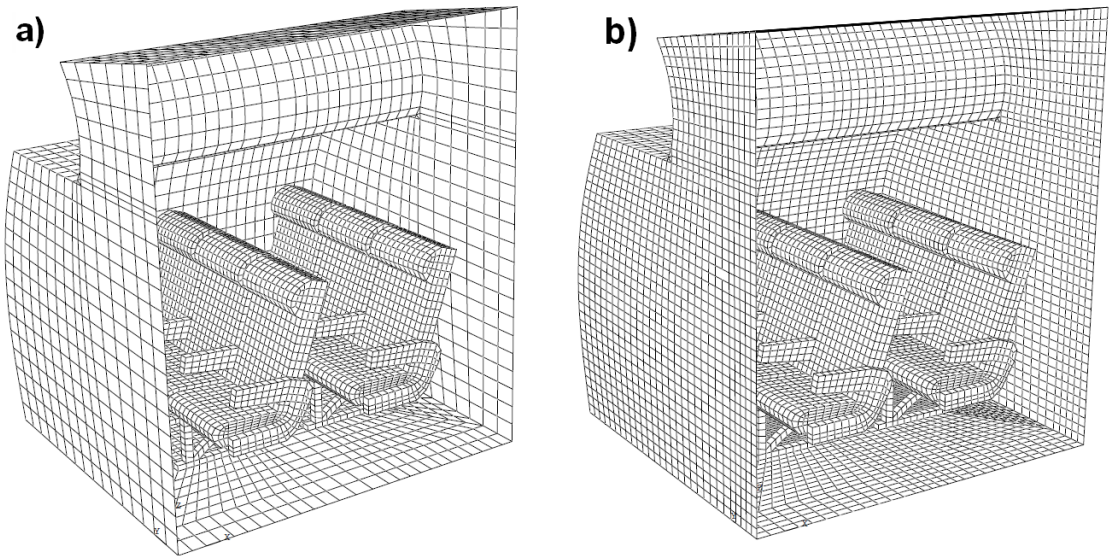


Figure 7.7: Final cabin models [86].

7.2.1 Microphones

Four microphones have been located at same positions of the experimental tests (A, B, C, D in figure 7.8). Table 7.1 lists their locations in mm with respect to the origin placed in the low corner of the corridor (see figure 7.8).

Microphone	x_1	x_2	x_3
A	818	1723	1045
B	818	311	1045
C	1618	1723	1045
D	1618	326	1045

Table 7.1: Microphone coordinates in the mathematical model [86].

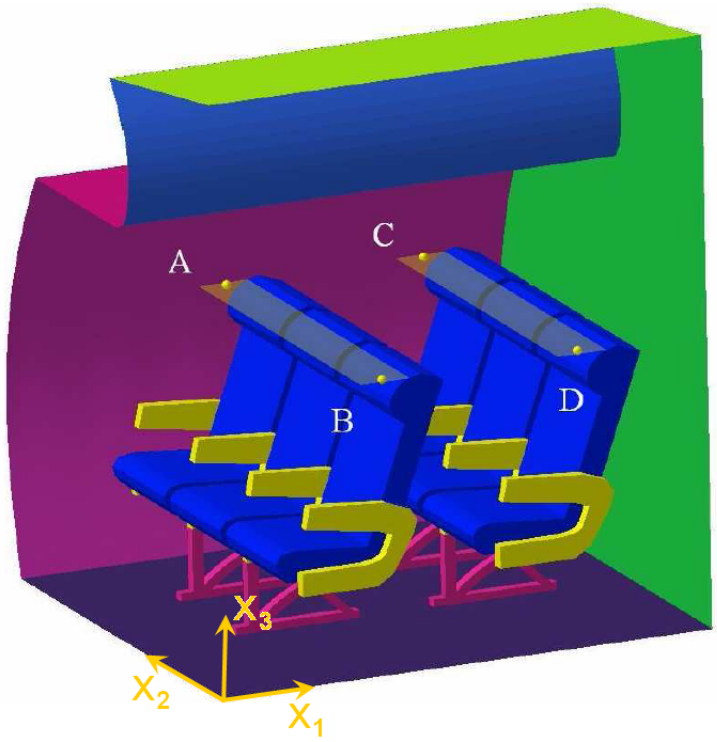


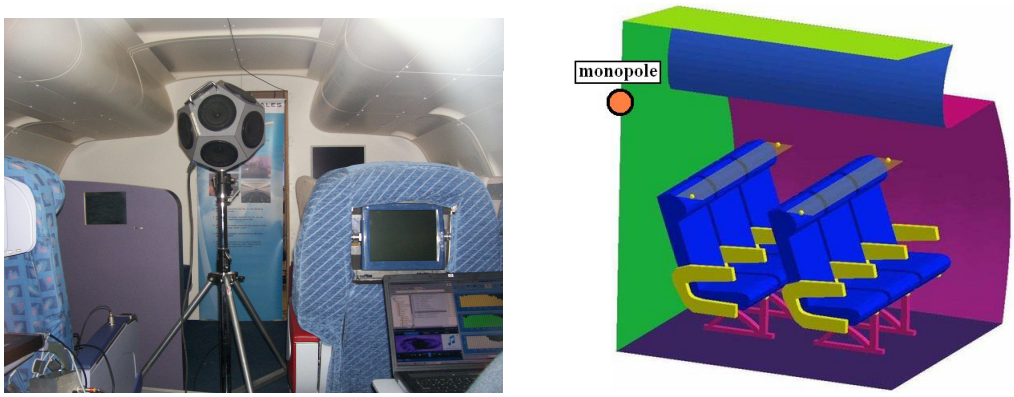
Figure 7.8: Location of the four microphones in the model [86].

7.2.2 Noise Source

As explained in the previous section, during the experiments the primary noise was created by different acoustic signals, but in the simulations, the numerical response has been tested for a specific signal, i.e., the take off signal, whose spectrum is shown in figure 7.3. It should be noted that such signal is not periodic, thus PNC fits well with our purpose.

The noise source (figure 7.9-a) has been simulated as a monopole source (figure 7.9-b) and its amplitude has been set on the basis of the experimental tests. In fact, the signal of figure 7.3 is amplified by the dodecahedral speaker and in the present analysis the amplification factor has been considered to be constant at various frequencies. This constant has been calibrated using the nearest microphone to the monopole (microphone

D in figure 7.8). As evident, a perfect match between the numerical and experimental tests for each microphone has not been achieved, due to the different shape of the experimental/numerical cabin and different boundary conditions.



a) b)

Figure 7.9: Noise source: a) experimental dodecahedral speaker; b) numerical monopole [86].

In most applications the signal frequency content (or the frequency spectrum) is investigated. There are two primary reasons for obtaining frequency information about a signal. First, the response of the ear and the sensation of sounds in humans is strongly dependent on frequency as described in the Chapter 2. Second, the physical processes of sound emission, propagation, diffraction and transmission are all frequency dependent. Thus the required numerical response of the mock-up at different frequencies has been obtained by a multifrequency BEM analysis. The LMS software provides the numerical response in terms of pressure/velocity and the central frequency of each octave band is used to represent the behaviour of the entire octave. The amplitude of the numerical monopole (unique value common to all frequencies under investigation) was set on the basis of the experimental tests that were also utilised to calibrate the numerical model.

It should be noted that, in the experimental model, the dodecahedral speaker was located in the middle of the corridor, therefore, in the numerical model, it has been

possible to take into account the symmetry with respect to the vertical plane and use only half cabin.

7.2.3 Boundary Condition Setting

The cabin internal panels and seats have all been modelled as absorbing surfaces with different impedance values and the whole geometry has been subdivided into the following surfaces: left, front and rear panels, floor, ceiling, seats, armrests and seat supports.

With the exception of the seat supports, that have been considered to be rigid, i.e., Neumann BCs with $q = 0$, all the other surfaces are absorbing materials and their impedance is characterized as in the equation (3.6)

$$z = \frac{p}{v} \tag{7.1}$$

where p and v are the pressure and normal velocity (with respect to the surface), respectively. Such an impedance is in general a complex number. In the literature the materials are characterized by the absorption coefficient α with the following relations

$$\alpha = 1 - ||r_p||^2$$

$$z = z_0 \frac{1 + r_p}{1 - r_p} \tag{7.2}$$

where z_0 is the impedance of the air and r_p the reflection coefficient. It should be noted that α also takes the transmission coefficient into account, and it is a real number. Consequently, the impedance z cannot be uniquely determined. This problem could be solved by fixing the impedance phase. Figure 7.10 shows the trends of the absorbing coefficient α for phase equal to zero at various values of the real part of the impedance z_R. In spite of such a simplified assumption, z_R can assume two different values for

a given value of α, but only the part of the curve which is after the peak is to be considered physically meaningful [38].

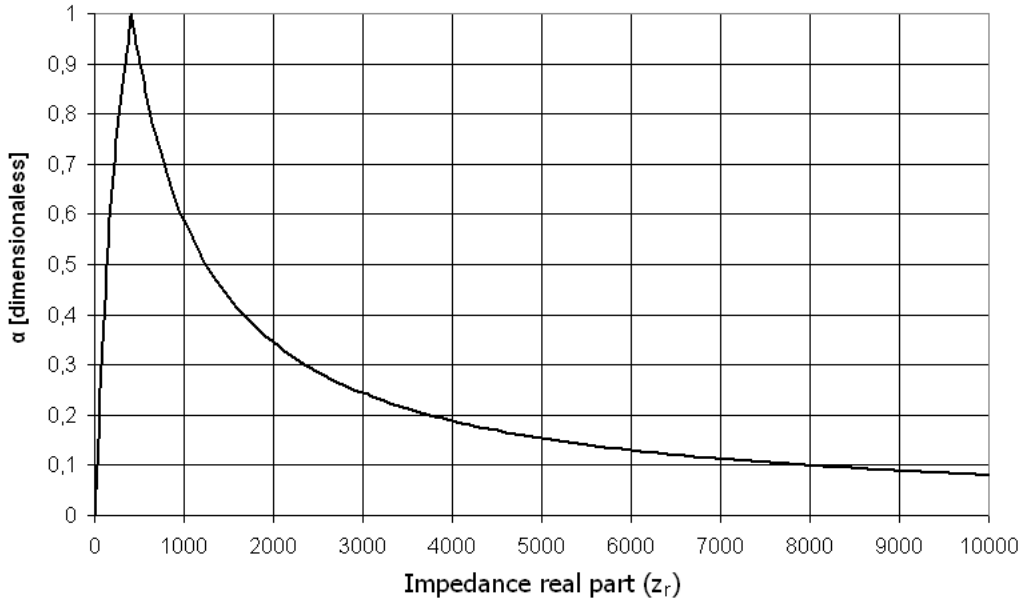


Figure 7.10: Relation between the absorbing coefficient α and the real part of the impedance z.

Some absorption coefficients of the mock-up were determined experimentally (in particular the value referring to the typical seat textile). The remaining impedance values have been gathered from the scientific literature (see for instance [38], pp. 944-945 and [67] Chapters 21, 24) and then assessed by a parametric comparison (whose final results are shown in the next section) between numerical and experimental results.

7.2.4 Nanofibres

The numerical results presented in the next section are due to a new textile, called "nanofibre". Such a textile was produced by Aitex (Instituto Tecnologico Textil, Spain,

one of the SEAT project partner) utilising a special apparatus, the Nanospider, protected by the patent number WO 2005/024101 [73]. The experimental tests of Acusttel on the material demonstrated to be particularly absorptive also at low frequencies (up to three times) compared with textiles typical adopted in aircraft cabins (see figure 7.12). Such a performance is rather unusual and opens new possibilities in the passive noise control for low frequencies.

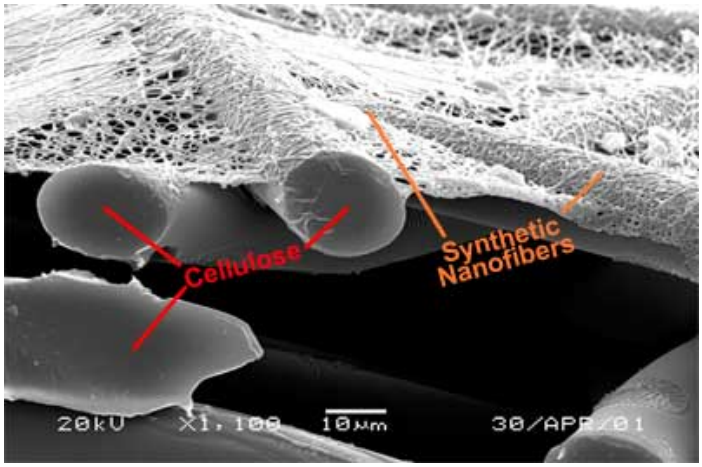


Figure 7.11: A microscope view of the nanofibre [129].

7.2.5 Bubble Concept

The SEAT project developed a new idea that strongly reduces the noise level perceived by a passenger, i.e., the *bubble concept*. Two absorbing panels have been inserted in the seat headrests laterally to the passenger's head as depicted in figure 7.13. Numerical analyses (presented in the next section) have been aimed at measuring the influence of the bubble concept on the cabin noise level including a parametric analysis with different orientation of the two caps.

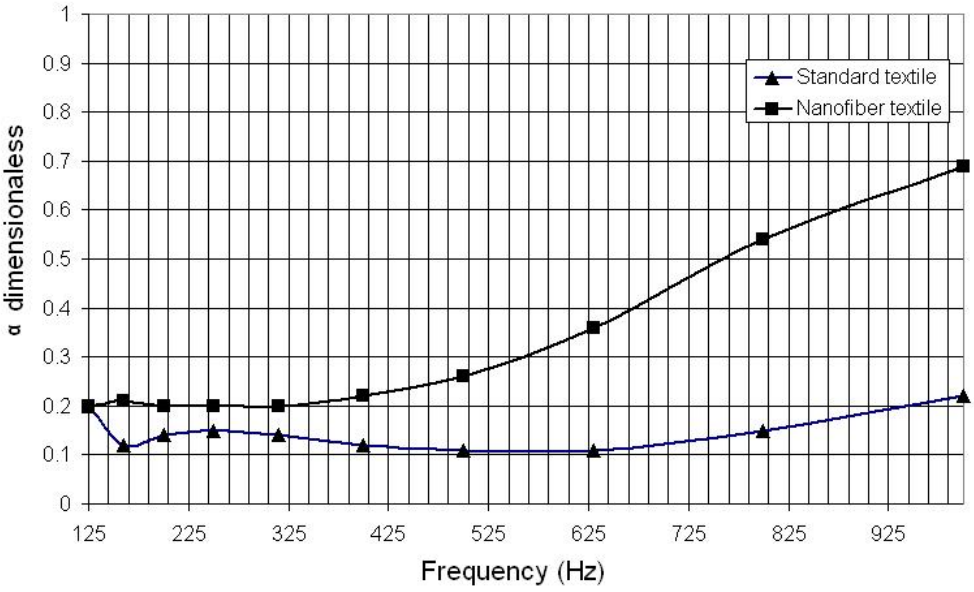


Figure 7.12: Acoustic performance of the nanofibre textile compared with a typical textile [86].

In order to include the bubble concept, two new meshes (one for the frequencies up to 100 Hz, the other one for the range 125-1000 Hz) are utilised (see figure 7.14) for all first group simulations and they are composed of around 12000 (figure 7.14-a) and 20000 (figure 7.14-b) nodes, respectively.

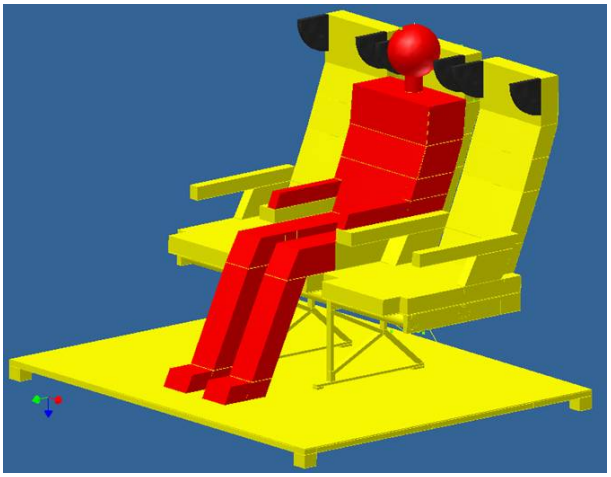


Figure 7.13: Bubble concept [86].

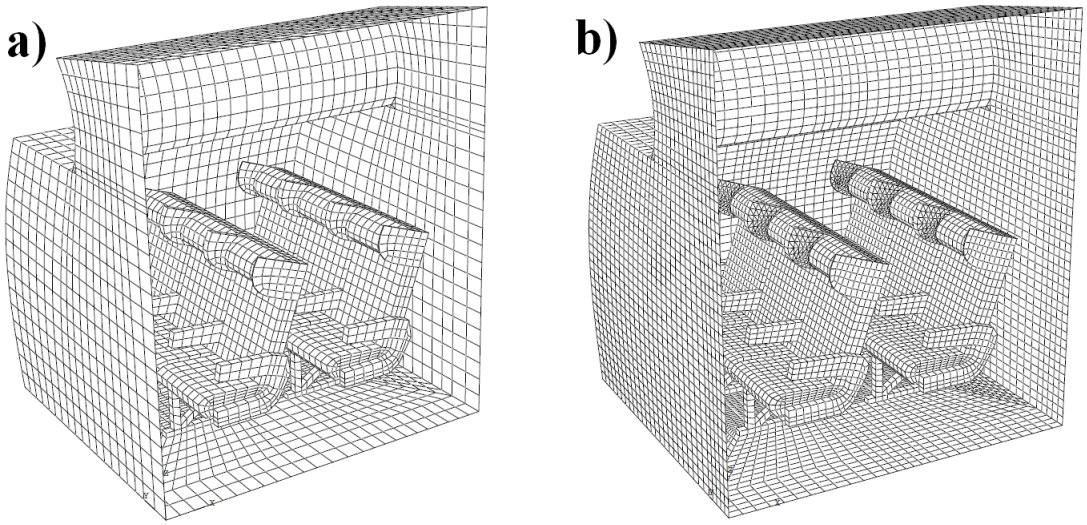


Figure 7.14: Model with lateral caps located at the headrests: coarse mesh (a), fine mesh (b) [86].

7.3 Numerical Results for the SEAT Project

In this section three groups of numerical results are presented. The first group has been obtained to assess the optimal boundary conditions which better match the experimental results at the microphone locations (see figure 7.8), the second group evaluates the influence on the noise reduction level of the nanofibres and the bubble concept, and the last group presents results for different orientations of the two lateral caps. For the second group two different signals have been adopted: *i*) the takeoff signal of the experimental test and *ii*) a typical white noise. In the third group a typical white noise is the disturbing noise.

These results have been utilised in the SEAT project and have been aimed on determining the best positions to locate the nanofibre textile and the best headrest shape.

7.3.1 Comparison with the Experimental Results

In order to obtain numerical results directly comparable to further experimental tests (not included in the present thesis) with the insertions of nanofibres and the bubble concept, the differences between the experimental tests and the numerical model have been minimised.

A numerical parametric study has been performed to evaluate the result sensitivities with respect to the boundary conditions and, in particular, to the impedance of each surface of the cabin. For the sake of simplicity such an analysis is here omitted and in tables 7.2, 7.3 and 7.4 only the main results are summarized for various frequencies. The signal tested at the microphones refers to a typical takeoff noise.

The comparison between experimental and numerical results using the above boundary conditions are depicted in figure 7.15. Over the range 125-1000 Hz the error is acceptable (from 0 to 15%), but it increases in the low frequency range 31.5-100 Hz (no experimental results are available over the range 8-25 Hz). The higher differences in the low frequency range are related to the fact that the low frequency response is mainly driven by the geometry of the model and not by the boundary conditions (region 1 of figure 2.8). In fact, the numerical model has some geometrical differences with the mock-up cabin (for instance the number of rows) which influence the comparison and in the low frequency range only slight differences in the numerical results have been observed when the impedance values are varied.

Absorbing coefficient value (α)									
Frequency (Hz)	*8*	*10*	*12.5*	*16*	*20*	*25*	*31.5*	*40*	*50*
Floor	0.002	0.003	0.005	0.01	0.015	0.02	0.025	0.03	0.05
Rear panel	0.002	0.004	0.007	0.01	0.014	0.018	0.02	0.03	0.04
Front panel	0.1	0.1	0.1	0.1	0.1	0.1	0.1	0.1	0.15
Ceiling	0.001	0.003	0.005	0.005	0.01	0.01	0.01	0.02	0.03
Armrests	0.001	0.001	0.002	0.002	0.003	0.004	0.005	0.005	0.005
Seats	0.05	0.05	0.05	0.05	0.05	0.065	0.075	0.075	0.1

Table 7.2: Values of the absorption coefficient over the range 8-50 Hz [86].

Absorbing coefficient value (α)									
Frequency (Hz)	*63*	*80*	*100*	*125*	*160*	*200*	*150*	*315*	*400*
Floor	0.09	0.12	0.15	0.25	0.275	0.3	0.325	0.35	0.375
Rear panel	0.05	0.1	0.15	0.2	0.23	0.26	0.3	0.34	0.37
Front panel	0.2	0.3	0.6	0.9	0.95	0.95	0.95	0.95	0.95
Ceiling	0.05	0.07	0.1	0.15	0.175	0.2	0.225	0.25	0.275
Armrests	0.006	0.008	0.01	0.02	0.021	0.023	0.025	0.029	0.036
Seats	0.14	0.175	0.21	0.49	0.51	0.53	0.56	0.61	0.69

Table 7.3: Values of the absorption coefficient over the range 63-400 Hz [86].

Absorbing coefficient value (α)				
Frequency (Hz)	*500*	*630*	*800*	*1000*
Floor	0.4	0.45	0.5	0.6
Rear panel	0.4	0.45	0.5	0.6
Front panel	0.95	0.95	0.95	0.95
Ceiling	0.3	0.325	0.35	0.375
Armrests	0.05	0.06	0.08	0.1
Seats	0.8	0.817	0.84	0.88

Table 7.4: Values of the absorption coefficient over the range 500-1000 Hz [86].

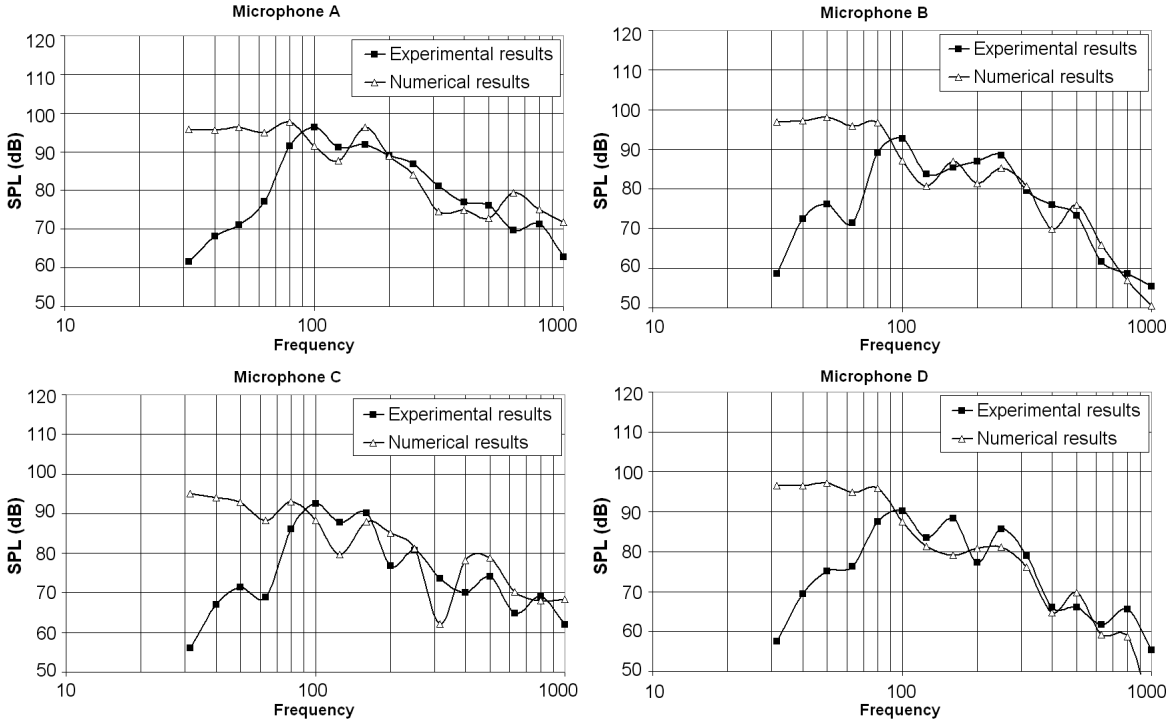


Figure 7.15: Comparison between experimental and numerical results at the microphones [86].

7.3.2 Noise Reduction Acting on Seat Covers and on Headrest Shape

In this subsection a sensitivity analysis of the noise reduction level in the cabin due to different textiles in the seat covers and to the bubble concept is presented. The analysis drew on the excellent absorption properties, even in the low frequency range, of the nanofibre utilised in the SEAT project.

All the simulations have been performed with reference to the same position of the noise source used in the experimental tests. Two new textiles, 10% and 20%, respectively, more absorptive along the entire frequency range have been investigated and compared at the microphone locations. The latter textile has been also adopted to

investigate the noise reduction for the bubble concept.

The new values of α have been chosen because the Acusttel data, as reported in figure 7.12, refers to the upholstery and do not include the internal layers of a typical aircraft seat (particular absorbing) as required for a complete and accurate analysis. The absorbing coefficient of the whole seats including all the layers (not evaluated by Acusttel) is already very high ($\alpha \backsimeq 1$) at high frequencies, whereas at low frequencies is quite low. Thus, inserting nanofibres does not provide a higher absorbing coefficient at high frequencies. Hence, 10% and 20% have been chosen to find a compromise between the nanofibre and the internal layer characteristics.

The noise reduction is depicted in figure 7.16 with regards to the experimental signal (takeoff phase). It is clear that the seat textile influences the noise level in the cabin and the presence of the caps located laterally to the headrests guarantees the best noise control. As could be expected, the passive noise control is more effective for frequencies higher than 400 Hz where a reduction of 8 dB can be achieved.

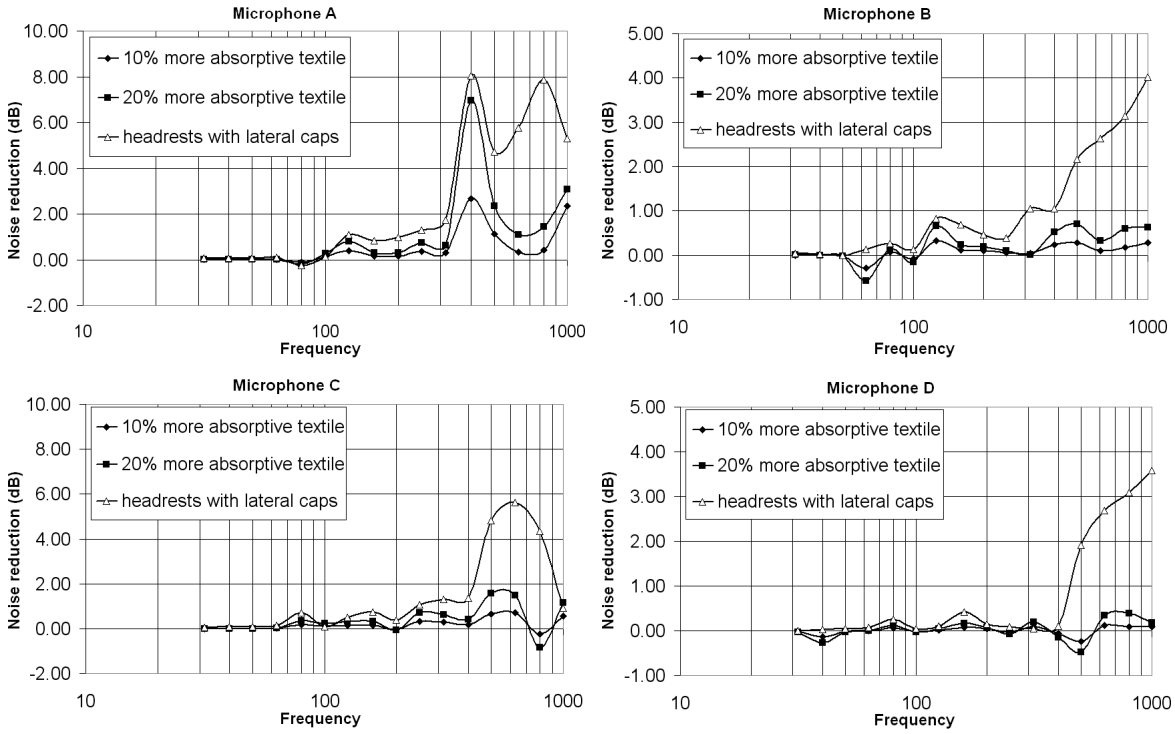


Figure 7.16: Noise reduction at the microphone locations: 10% more absorptive textile; 20% more absorptive textile; headrests with lateral caps [86].

Comparisons have also been performed in the overall range of frequencies. The total SPL can be determined by applying the root mean square average of the responses at various frequencies. Over the range 8-1000 Hz the noise reduction due to different textiles is negligible. The performance improves if the comparison is performed over the range 125-1000 Hz (see figure 7.17). As frequency range increases, the noise reduction increase and the whole response is considerably improved. For instance, in the 500-1000 Hz range the overall comparison is depicted in figure 7.18.

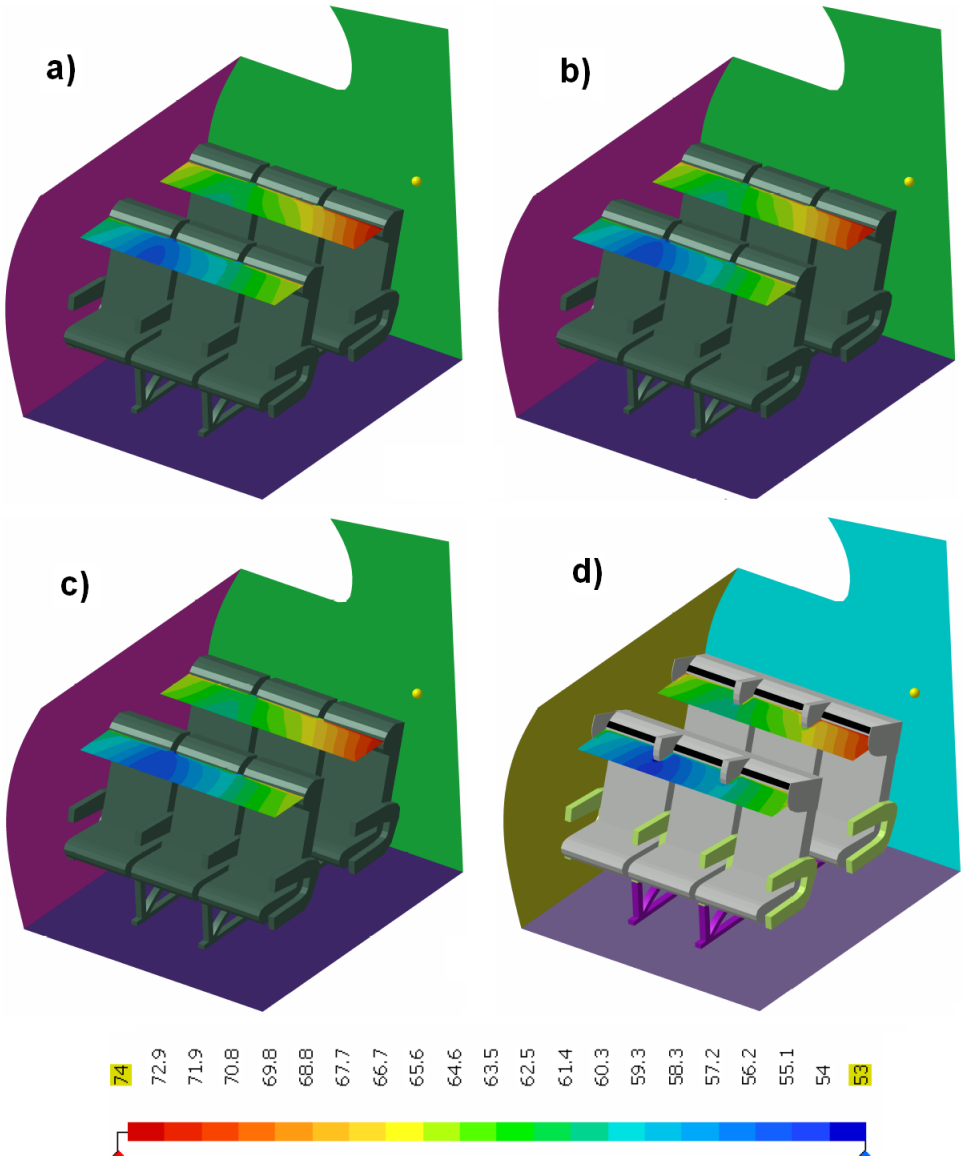


Figure 7.17: SPL for the experimental signal over the range 125-1000 Hz: a) standard textile; b) 10% more absorptive textile; c) 20% more absorptive textile; d) headrests with lateral caps [86].

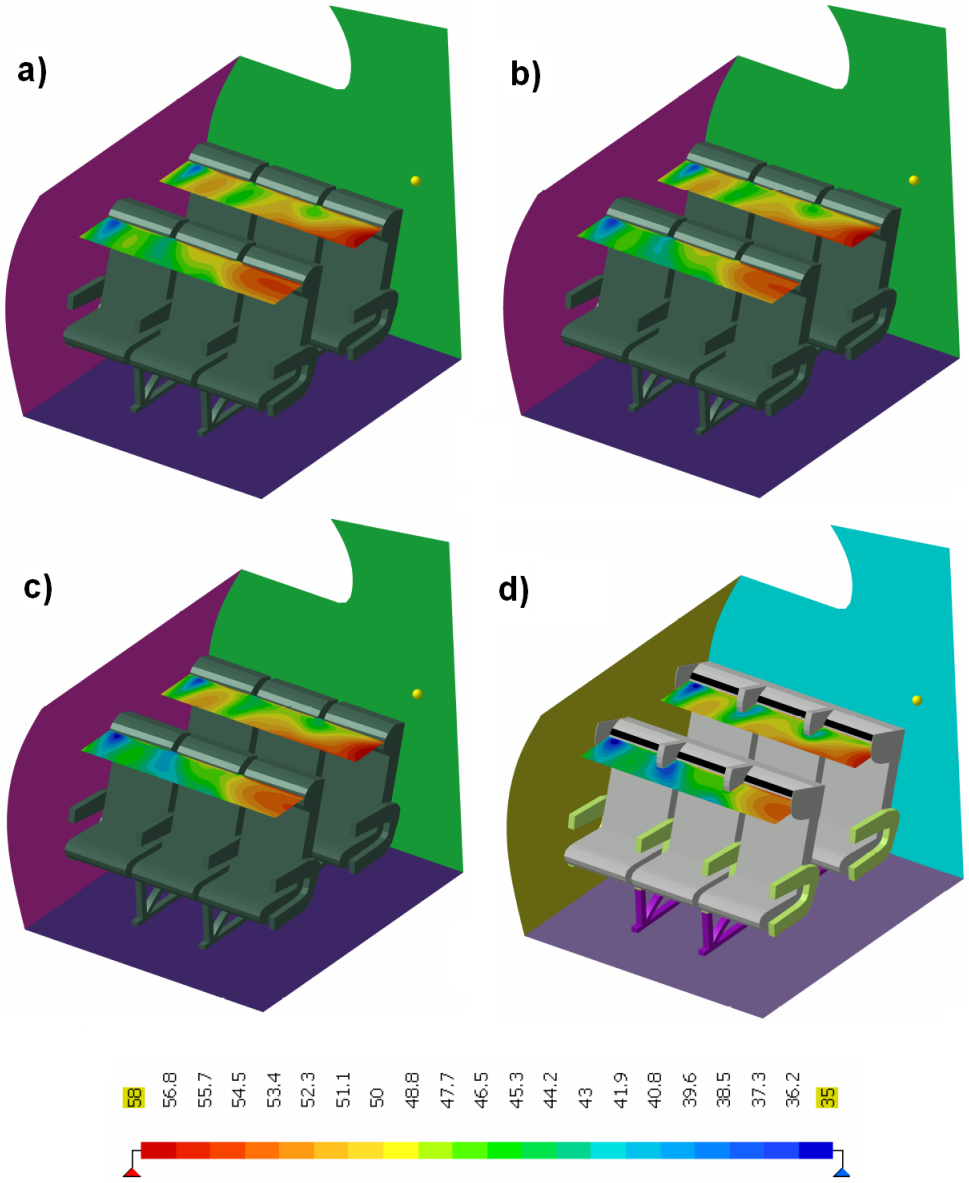


Figure 7.18: SPL for the experimental signal over the range 500-1000 Hz: a) standard textile; b) 10% more absorptive textile; c) 20% more absorptive textile; d) headrests with lateral caps [86].

The noise reduction corresponding to the experimental signal can be better visualized by investigating some points close to the passengers' ears at the points indicated in figure 7.19. Tables 7.5 and 7.6 report the SPL at these points for the four different configurations, i.e., standard textile (first column: S.T.), 10% (second column: 10%)

and 20% more absorptive textile (third column: 20%), headrest with caps (last column: Caps). The noise reduction goes up to 1.5 dB (around 3% of the initial SPL) over the range 125-1000 Hz and up to 2.5 dB (around 5% of the initial SPL) over the range 500-1000 Hz. As evident, the noise reduction at the points located close to the loudspeaker (F1 and F2) is negligible as this locations are directly illuminated by the acoustic source.

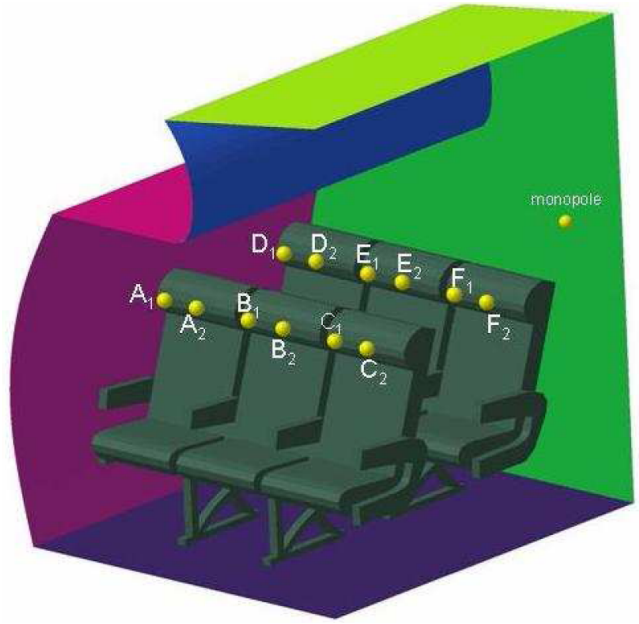


Figure 7.19: Location of the point close to the passengers' ears [86].

	S.T.	10%	20%	Caps
A_1	63.1	62.8	62.6	62.1
A_2	60.6	60.4	60.1	59.7
B_1	60.5	60.1	59.6	59.1
B_2	62.3	62.0	61.7	61.4
C_1	65.5	65.3	65.1	64.5
C_2	67.4	67.2	67.1	66.7
D_1	67.5	67.3	67.1	66.8
D_2	65.2	65.1	65.0	64.7
E_1	66.4	66.3	66.1	65.9
E_2	68.1	68.0	67.9	66.1
F_1	71.3	71.2	71.1	70.9
F_2	73.8	73.8	73.7	73.5

Table 7.5: SPL in dB at the passengers' ears over the range 125-1000 Hz [86].

	S.T.	10%	20%	Caps
A_1	44.9	44.3	43.1	43.0
A_2	50.5	49.8	48.6	47.9
B_1	50.6	49.6	48.0	46.3
B_2	52.0	51.3	50.2	50.2
C_1	57.2	56.7	55.9	54.3
C_2	57.8	57.6	57.3	56.8
D_1	46.7	46.7	46.9	46.9
D_2	54.6	54.3	53.9	52.9
E_1	51.2	50.9	50.7	50.7
E_2	53.2	52.9	52.4	51.9
F_1	53.2	53.0	52.5	52.1
F_2	57.5	57.5	57.5	55.6

Table 7.6: SPL in dB at the passengers' ears over the range 500-1000 Hz [86].

The acoustic performance of the aircraft cabin has been also tested for a typical white noise, with amplitude 0.01 kg/sec^2, generated from a monopole located as for the experimental tests. Comparison over the entire range 8-1000 Hz does not show any

noise reduction, but focusing the results on higher frequencies demonstrates that adopting high absorption textiles and the bubble concept may improve the noise reduction properties of the system. In figures 7.20 and 7.21 the SPL is depicted at the level of the passengers' ears over 125-1000 Hz and 500-1000 Hz, respectively.

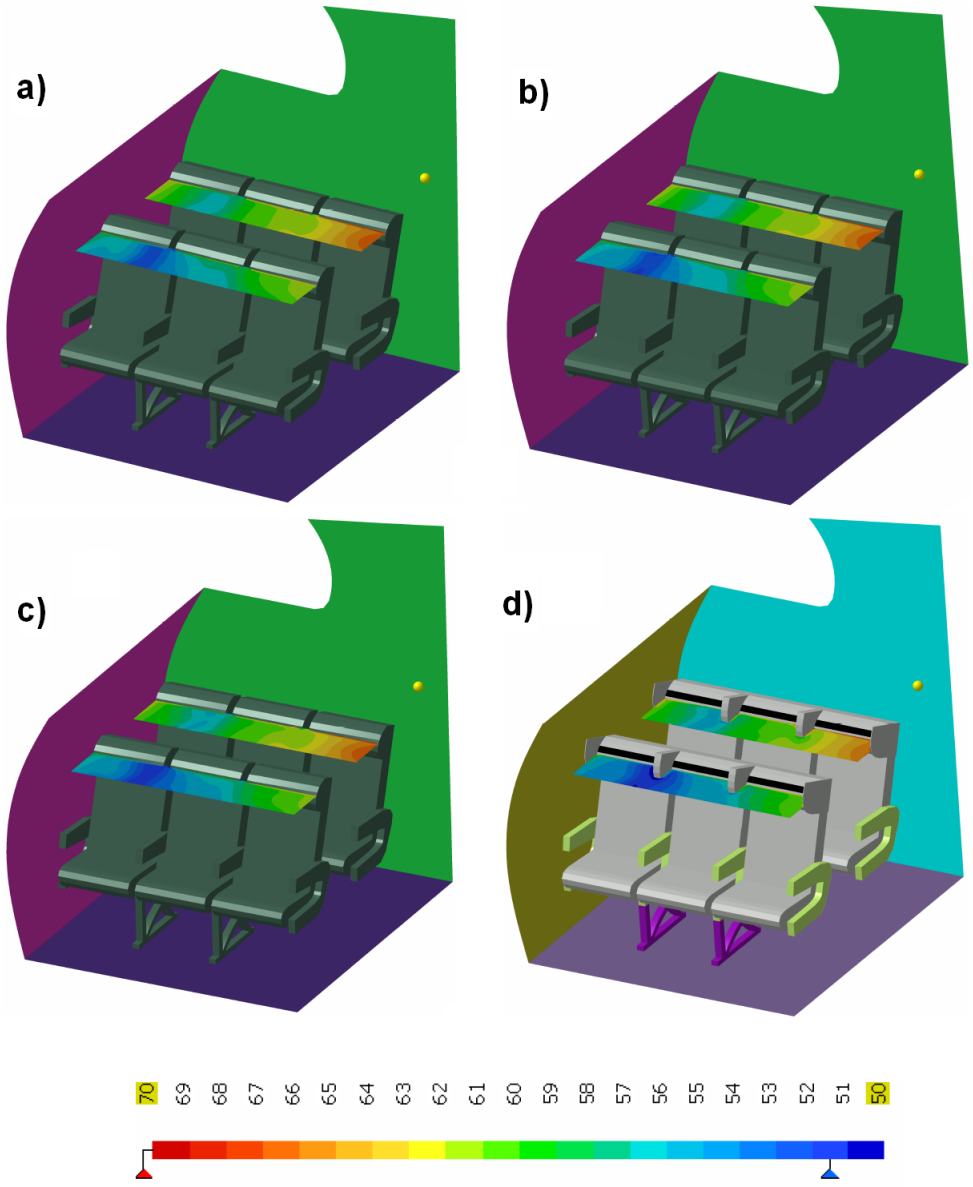


Figure 7.20: SPL for the white noise over the range 500-1000 Hz: a) standard textile; b) 10% more absorptive textile; c) 20% more absorptive textile; d) headrests with lateral caps [86].

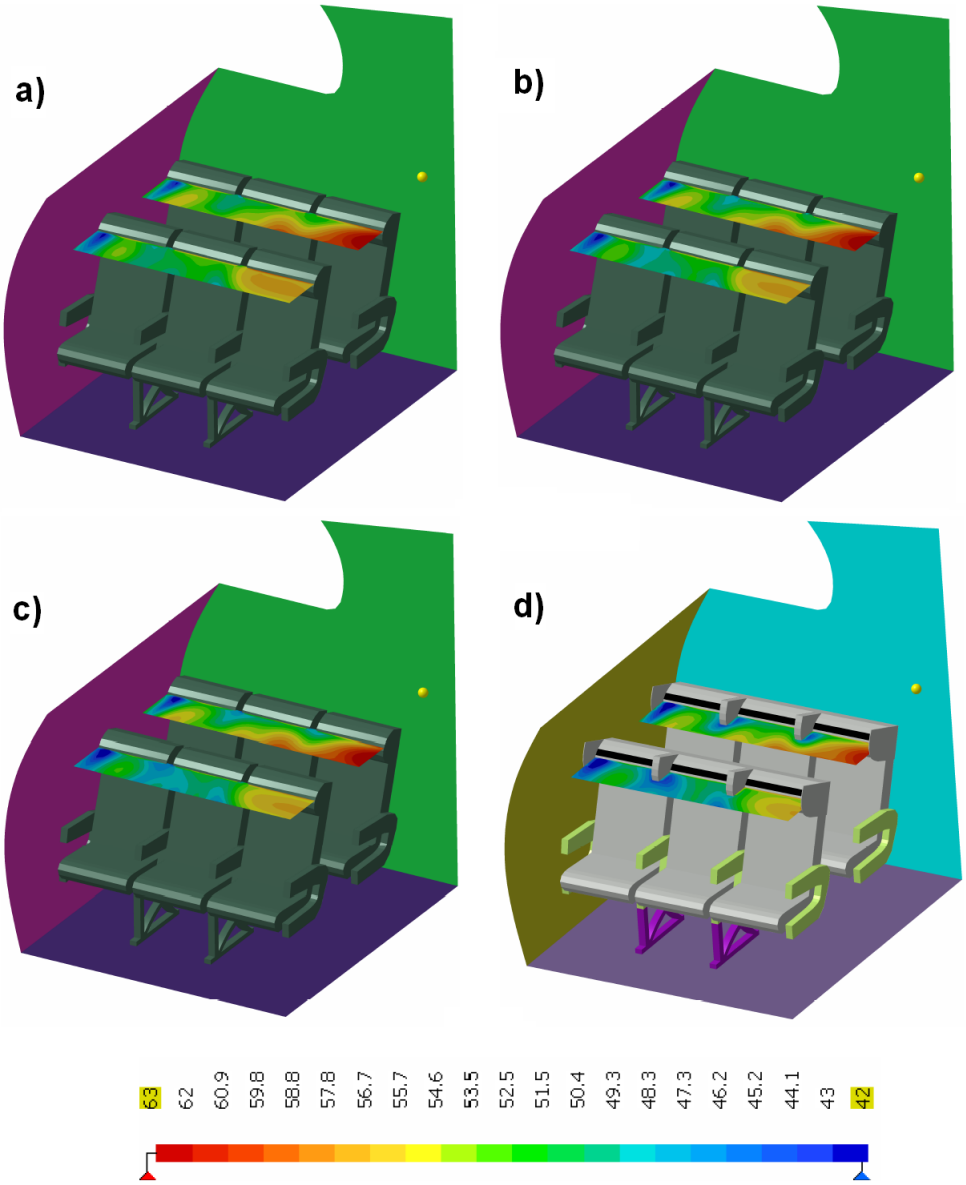


Figure 7.21: SPL for the white noise over the range 500-1000 Hz: a) standard textile; b) 10% more absorptive textile; c) 20% more absorptive textile; d) headrests with lateral caps [86].

7.3.3 Bubble Caps Sensitivities

The idea presented in this subsection is to introduce a new design of the bubble concept caps. The block shaped cushion of the previous section is substituted by two plate cushions whose cross-sectional shape is shown in figure 7.22. This strategy permits sound wave to pass between two caps of consecutive headrests increasing the wet area, and to orientate the two caps with different angles.

In order to create the discretised boundary surfaces, two caps have been added to the two meshes without caps (figure 7.7). Such strategy permits the generation of each discretized geometry varying only the angle of the caps and this avoids to generate various meshes for different angles. The thickness of the caps is reduced to 5 mm, but it can be enlarged without any problems. The top and bottom corners of the caps are jointed to the headrests.

The results of the analysis in terms of SPL and noise reduction percentage are shown in table 7.7. A positive angle variation means that the caps are orientated outward of the headrest, while a negative angle inward. A significant reduction is achieved at all microphone locations and for each new configuration. It can be noted that even for a variation of 0^o there is a considerable noise reduction, especially at the outer locations, confirming the improvement due to the new design.

The combined SPL distribution is shown in figure 7.23.

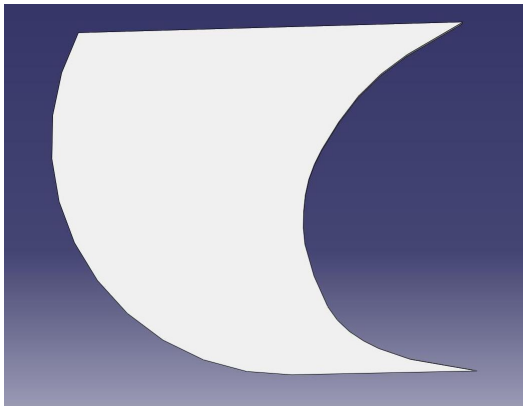


Figure 7.22: Design of the new cap for the bubble concept.

Micr.	Prev.	0^odeg	%	5^odeg	%	10^odeg	%	-5^odeg	%	-10^odeg	%
A	79.0	75.0	5.1	75.0	5.1	74.0	6.3	75.0	5.1	75.0	5.1
B	74.0	74.0	0.0	73.0	1.4	73.0	1.4	73.0	1.4	73.0	1.4
C	73.0	67.0	8.2	68.0	6.8	68.0	6.8	67.0	8.2	68.0	6.8
D	71.0	70.0	1.4	69.0	2.8	69.0	2.8	70.0	1.4	69.0	2.8

Table 7.7: SPL in dB at the passengers' ears over the range 500-1000Hz.

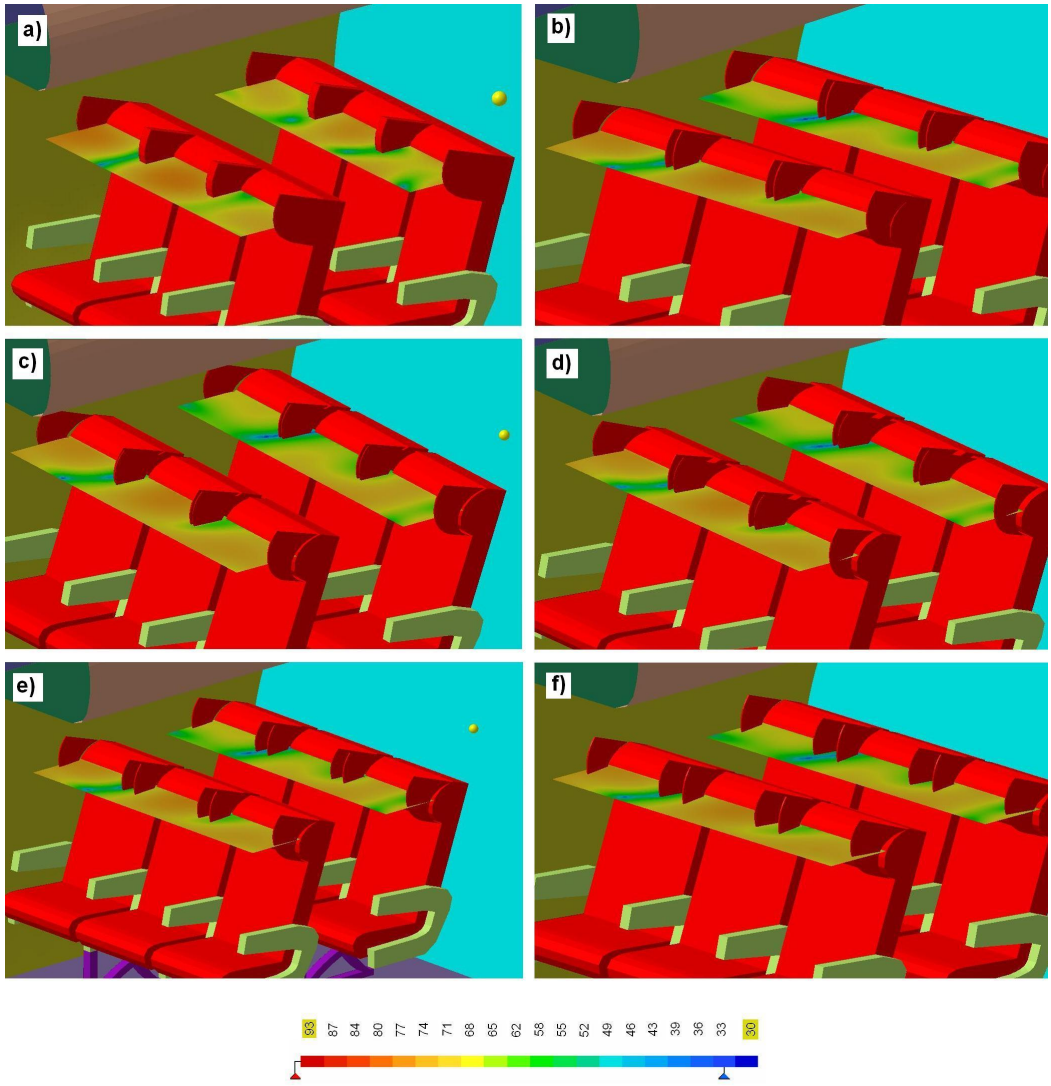


Figure 7.23: SPL for the experimental signal over the range 8-1000 Hz: a) SEAT project configurations; b) separated caps; c) 5^o degree ; d) 10^o degree; e) -5^o degree; f) -10^o degree.

Summary

This chapter presents a series of passive noise control (PNC) analyses in the aircraft cabin adopting different seat textiles and a new headrest shape. The investigation draws on a new nanofibre textile with excellent acoustic absorption properties even over the low frequency range (below 1000 Hz). Some experimental tests have been carried out on a mock-up cabin with different signals reproducing various flight operations. The numerical model has been calibrated in order to comply with the experimental results. Many variables, e.g., geometry, material absorption coefficients, etc., have influence on the model response. On the basis of the values given in the literature, a parametric analysis has been carried out to match the acoustic impedance of the panels utilising the numerical results and the experimental tests.

Groups of simulations have been performed to evaluate the influence on the noise reduction level of the nanofibre insertions and the new headrest shapes. Two different signals have been used: the first signal is coincident with one of the signals used in the experiments whereas the second signal is a typical white noise. Both signals have confirmed that the passive approach with the new textile inserted in all seat surfaces is capable of reducing noise over a frequency range of 125-1000 Hz. The sensitivity analysis of the headrest shapes highlights that lateral caps can be really efficient in reducing noise inside aircraft cabins. The bubble concept is an effective practical approach since lateral caps can be inserted more easily (with limited additional costs and weights) than other absorbing materials in various surfaces of the cabin.

Chapter 8

Conclusion and Future Work

This chapter presents the final conclusions and recommendations for future research. These conclusions are based on the formulations developed and tested in previous chapters, by which the main objectives outlined in Chapter 1 were achieved.

8.1 Conclusions

The work presented in this thesis concerned the development of the Boundary Element Method for active and passive noise control.

Solving acoustic problems involving large scale geometries is a computationally intensive process. Thus, considerable attention was given to developing new solution techniques that would improve the efficiency of the BEM for large scale acoustic problems. A new formulation was also developed for attenuating noise in a control volume rather than cancelling the offending noise at discrete points. A novel sensitivity formulation was presented for the optimisation in a local ANC strategy. The sensitivity BEM was used to find the optimum locations and orientations of the secondary source and the optimum locations of the control volume. Finally, a series of numerical simulations for a PNC approach proved the efficiency of a new noise absorbing textile utilised as

upholstery in an aircraft cabin.

The conclusions of the work are summarized below.

i) Two discretisation strategies involving constant and quadratic elements were investigated. Although using quadratic elements would result in fewer elements overall and hence less solution time (up to 35 time faster for the meshed used in the analysis), the formulation for constant elements was preferred due to the simplicity of its integration process.

ii) A technique based on the Adaptive Cross Approximation (ACA), the Hierarchical matrix (H-matrix) format and the GMRES solver was developed and implemented in an in-house code called RABEM (Rapid Acoustic Boundary Element Method). Based on the tests carried out, the following conclusions can be made:

- two parameters, i.e., the *cardinality* and η are required to optimise the solution time. In particular, the cardinality influences the speed up ratio more than 50% and η up to 450 %. Moreover, η is also responsible for minimising the memory storage. A correct value of these two parameters is thus fundamental;
- the technique can also be used to speed up standard acoustic BEM code with a direct solver. For a pulsating sphere with radius, wave number and uniform radial velocity all equal to unity discretised with 10,340 elements, RABEM is 5 times faster than the standard code in the assembly time, 18,513 times faster in the solution time and overall (total solution time) 175 times quicker. In addition, the ACA was applied for the evaluations of potential and particle velocity at selected internal points. RABEM is 18 time faster than the standard code for calculating the potential at 10,500 internal points for a pulsating sphere discretised with 3,240 triangular elements;

- RABEM was also compared with Virtual.Lab (LMS [82]) and shown to be 10 and 18 times faster for a pulsating sphere and a rigid sphere scattered by a plane wave, respectively. Both spheres were discretised with 28,194 elements;
- RABEM was also compared with FastBEM(R), a code using the BEM Fast Multipole Method [1], for a row of three seats of an aircraft cabin discretised with 27,284 elements and perturbed by a monopole close to one of the seats for nine different frequencies (100, 200, 400, 600, 800, 900, 1000, 1100 and 1200 Hz). It was noted that RABEM is up to almost three times faster than FastBEM for frequencies higher than 400 Hz and for frequencies below this value RABEM is only 20% slower than FastBEM. Moreover, RABEM with a block diagonal preconditioner has been also compared, but it has never found to be faster than the code without preconditioner.

iii) In chapter 5 a new local active noise control (ANC) approach has been presented. The main conclusions of this chapter are as follows:

- the proposed procedure permits to generate a wider and more homogeneous quiet zone compared to the conventional point cancellation strategy;
- variations of secondary amplitude and phase for the optimal values suggest that the phase assumes a predominant role in the setting of a DSP system;
- the quiet zone can be enlarged by adding a second control source. In this case the locations of the two secondary sources and the control volume are an important aspect in the final design of the ANC system;
- a simplified procedure, obtained considering the primary noise constant in the control volume, proved to speed up the evaluation of the optimal secondary fields utilising two control sources without reducing the noise atten-

uated zone;

- the component of the particle velocity in the second cost function should be chosen with particular care, since an incorrect choice can significantly reduce the quiet zone.

iv) The sixth chapter presented new optimisation formulations for local ANC. The strategy of chapter 5 for ANC that reduce the primary noise within a fixed enclosure, the control volume, with a fixed secondary source was adopted. The main conclusions are:

- the optimisation process can effectively evaluate the location of the noise attenuation area (control volume), the location and, overall, orientation of the secondary source;
- the solution for the sensitivity problem was accelerated by applying the Hierarchical Adaptive Cross Approximation (ACA) technique coupled with GMRES.

v) In the chapter 7 a PNC analysis for reducing the noise level inside an airplane cabin has been presented. Experimental tests and numerical simulations have been performed to apply the analysis to a realistic situation. The investigation arises from the excellent noise absorbing properties at low frequencies of a new textile, the nanofibre, that has been utilised within the SEAT project. The main conclusions are:

- the numerical simulations proved that the nanofibers can provide a significant noise reduction, especially over a frequency range of 125-160 Hz. At higher frequencies of more than 300 Hz, the new textile can provide up to 7 dB reductions;

- inserting lateral caps greatly improves the nanofiber absorbing performances, mainly at the passenger's ear level;
- the shape of the lateral caps can be optimised to increase the wet area and to orientate the two caps with different angles. This strategy permits to considerably reduce the SPL perceived by the airplane passengers.

In summary, the boundary element method has proved to be an efficient and robust method for large scale acoustic analyses and modelling of active and passive noise control.

8.2 Future Research

Future work in the noise control area simulated with fast solvers based on the BEM is suggested in this section and it can be summarized as follows:

1. RABEM can be further accelerated by substituting the standard BEM based routines, that furnishes the ACA the system matrix columns and rows, with faster routines taken from other existing codes, for instance LMS Virtual.Lab, or possibly utilising a coupled ACA-FMM formulation;

2. RABEM can deal with problems without any size limitations by modifying its structure. RABEM has been implemented to store the system matrix into the computer RAM. This limits the size of the problems that can be solved since memory difficulties may occur for problems with more than 50 thousand degrees of freedom. A possible solution consists of creating a code based on the solver that provides the iterative solution by direct evaluation of the matrix-vector product without storing the system matrix. Such a code requires the evaluation of the system matrix at each solver iteration, but the classification of the matrix into

low and full rank blocks should be performed only once at the beginning of the procedure;

3. RABEM capability can be improved by using computer clusters or supercomputers and if integrated with a graphic interface;

4. the effectiveness of the proposed CV strategy would need to be validated experimentally;

5. the performances of local ANC formulation should be validated by using an aircraft cabin model that includes the presence of passengers;

6. the sensitivity analysis can be extended to optimise the location of microphones, and to evaluate the best shapes of both the control volume and the secondary source by adopting suitable cost functions;

7. the sensitivity analysis presented in the sixth chapter can be repeated including the presence of a second secondary source, even though a simplifying procedure should be required to reduce the computational effort;

8. the PNC performance inside an aircraft cabin can be increased by improving the absorbing properties of carpets, curtains and by inserting noise absorbing patches in different locations along of the fuselage walls;

9. a sensitivity analysis can be formulated for the PNC to evaluate the optimum locations inside an aircraft cabin of noise absorbing materials that provide the highest noise attenuation level with a limited addition of extra-weigh.

Appendix A

Preliminary Validations

A.1 Preliminary Validation: Garcia-Bonito Results

In the papers of Elliot and Garcia-Bonito [50, 51] a series of interesting results are achieved and here they are reproduced by using a FORTRAN code based on the RABEM.

The active segment has been considered to have a uniform vibrating surface. In fact, their model idealizes a loudspeaker using the Legendre polynomial and the spherical Hankel function, as follows

$$U(r,\theta) = \sum_{m=0}^{\infty} A_m P_m(\cos\theta) h_m^{(2)}(kr) \tag{A.1}$$

where $P_m(\cos\theta)$ is the Legendre polynomial of order m, $h_m^{(2)}(kr)$ is the spherical Hankel function of second kind of order m and A_m is the complex pressure amplitude that has to be calculated [90].

Equation (A.1) is replaced by a constant function without producing any considerable differences.

Figure A.1 shows the noise reduction area for a 45^0 degree active segment that

vibrates with a uniform distribution (a) and with a distribution as seen in the above equation (b). The primary noise field is created by 72 planewaves with unitary amplitude. It can be seen there are not many differences between the two distributions.

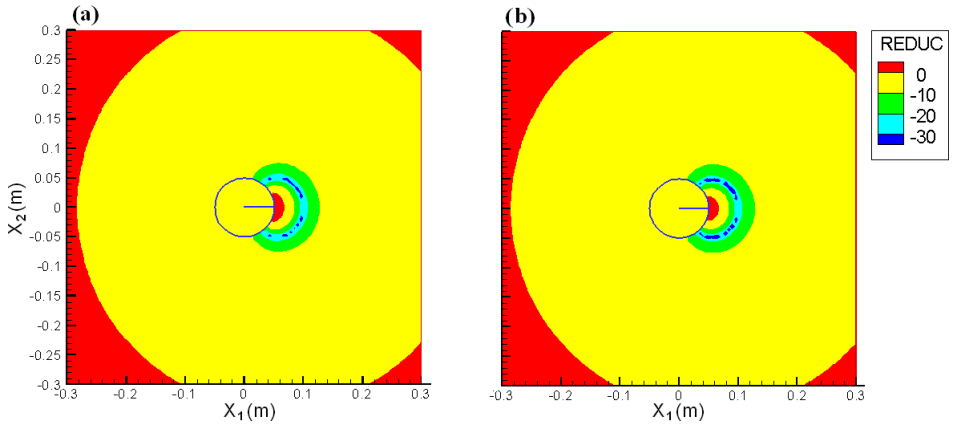


Figure A.1: Noise reduction area generated by a rigid sphere with an active segment of 45^0 degree considered to be uniform (a) and produced by a function of Legendre polynomial and the spherical Hankel function (b).

Figure A.2 shows the average potential field due to a primary diffuse field and a secondary field generated by a rigid sphere with a vibrating segment of different sizes with kd=0.5, where k is the wave-number and d is the distance between the centre of the sphere and the cancellation point. It can be noted that these results are absolutely comparable with those achieved by Elliot and Garcia-Bonito [50].

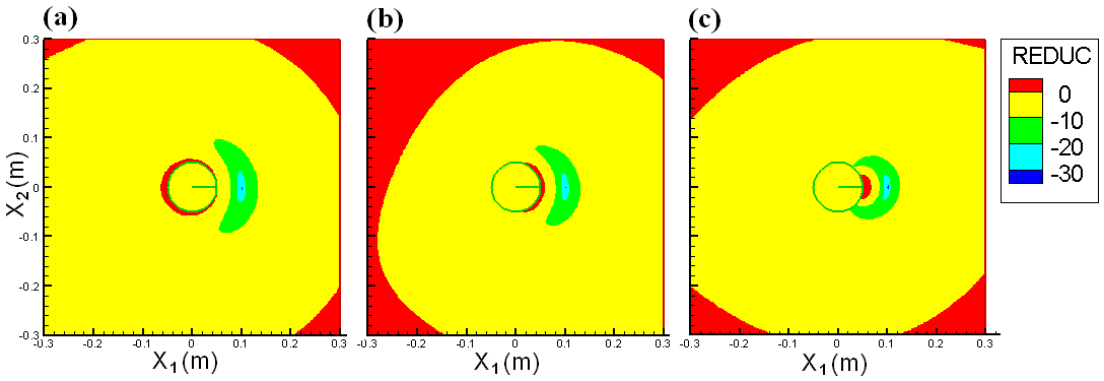


Figure A.2: Average noise reduction area generated by a rigid sphere with a vibrating segment of different sizes when kd=0.5: (a) 360^0, (b) 180^0, (c) 45^0.

Figure A.3 exhibits another comparison with Elliot and Garcia-Bonito study [50] for different values of kd and in particular the average total potential field in the x_1x_2 plane due to a primary diffuse field and the secondary field when the sphere has an active segment is 90^0 degree, radius of 5 cm and the cancellation point is 7.5 cm from the centre of the sphere.

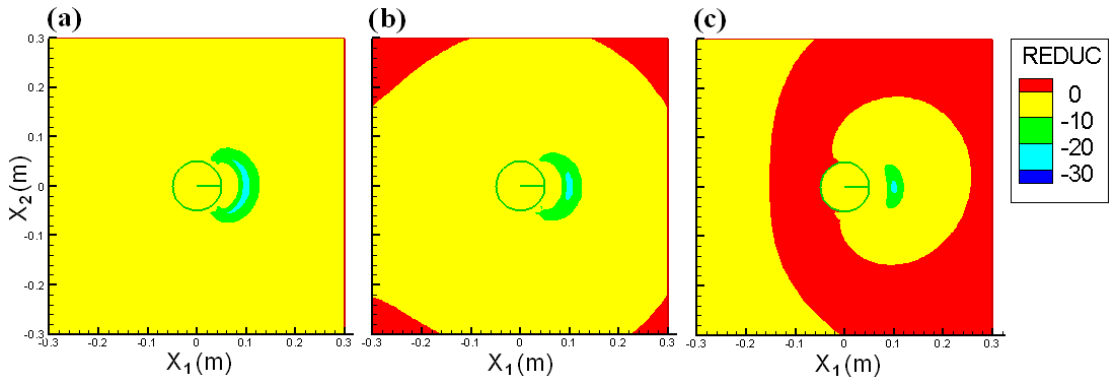


Figure A.3: Average noise reduction area generated by a rigid sphere with different values of kd: (a) $kd = 0.2$, (b) $kd = 0.5$, (c) $kd = 1.0$.

Finally, comparison with the Elliot and Garcia-Bonito work [51] for a secondary spherical source with radius 8 cm, vibrating segment of 120^0 degree, cancelling point at 19 cm from the centre of the sphere is shown in figure A.4.

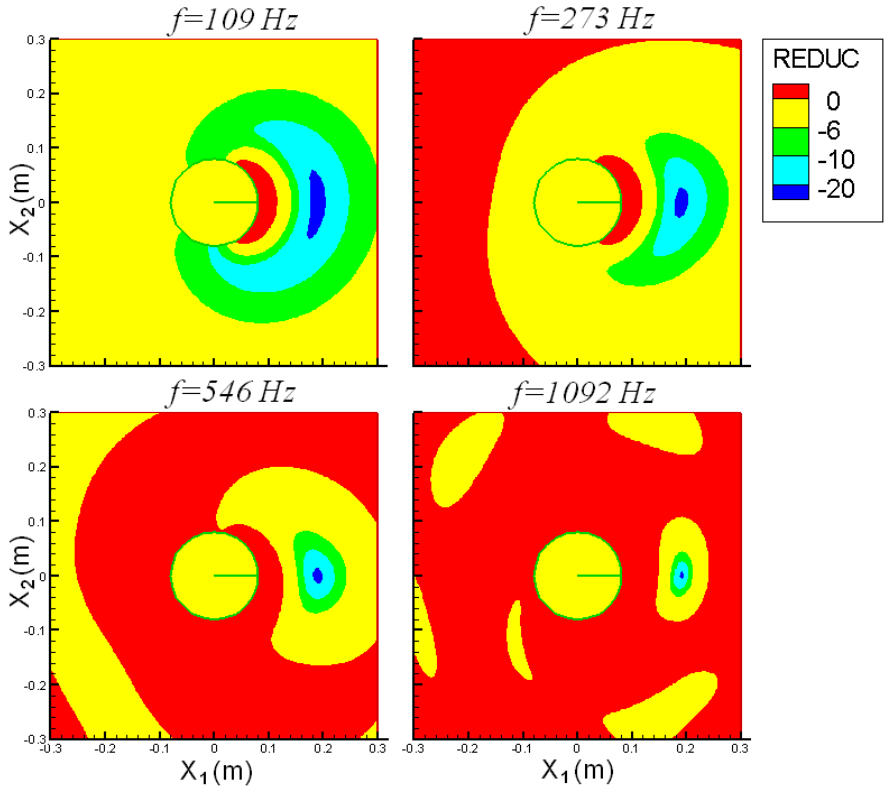


Figure A.4: Average noise reduction area generated by a rigid sphere with an active segment of 120^0 degree and by the point cancellation strategy at the point (19.4, 0.0, 0.0) cm.

The asymmetry in figure A.4 is due to the fact that the primary field is generated randomly and only 20 samples have been used.

A.2 Integration Process Validation

In what follows the results that validate the integration procedure are presented.

The integral over the CV is represented using 8 node brick cells. The Legendre-Gauss quadrature rule is subsequently used to evaluate the integral (5.1), [111, 125]. The number of cells that constitutes the CV depends upon the CV size and the frequency that is analysed. A control volume with a volume of 3,125 $10^{-8}m^3$ and meshed with 2 brick elements is used in the integral of equation (5.1). Over the range of frequencies used here (109-1092 Hz), such a CV can be considered infinitesimal and its behaviour is the same of a single point for a sound propagation point of view. Figure A.5 presents the comparison between four different frequencies (109, 273, 546, 1092 Hz) when a primary noise is cancelled at one point (a) and within the infinitesimal CV (b). The primary field is generated by a single wave with unitary amplitude and the secondary by a rigid sphere with an active segment of 120^0 degree and radius 8 cm.

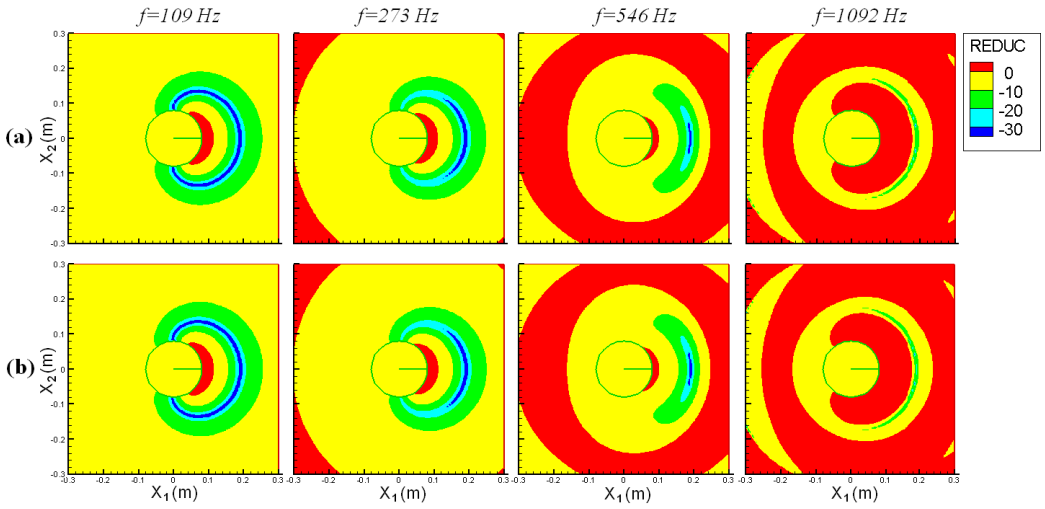


Figure A.5: Integration Process Validation: a) minimisation obtained by a CV of volume equal to 3,125 $10^{-8}m^3$; b) cancellation point strategy.

Appendix B

Optimisation Methods

The optimisation procedure used in chapter 6 is based upon a Quasi Newton Method. In this appendix optimisation methods are briefly reviewed focusing on the method utilised for evaluating the optimum location/orientation of the control source and the optimum location of the control volume, i.e., the Broyden-Fletcher-Goldfarb-Shanno (BFGS) variant of the Davidon-Fletcher-Powell (DFP) method.

In general, an optimisation process is performed by evaluating an optimum value of a design variable $\mathbf{x}$ that minimises a suitable cost function $f(\mathbf{x})$, similar to that in equation (6.3), where the design variables were $\mathbf{a}$ and $\mathbf{b}$, subjected to equality and inequality constraints. The general optimisation problem can be formalized as follows

$$\text{Minimise } f(\mathbf{x}), \qquad h_i(\mathbf{x}) = 0,\ i = 1, \dots p, \qquad g_j(\mathbf{x}) < 0,\ j = 1, \dots q \tag{B.1}$$

where $\mathbf{x} = (x_1, x_2, \dots, x_n)$, $h_i(\mathbf{x})$ and $g_j(\mathbf{x})$ are the equalities and inequalities, respectively. At the side of these implicit constraints related to the value of the cost function, there are explicit constraints directly connected to the bound of the design variables, i.e., $\mathbf{x}_s \leq \mathbf{x} \leq \mathbf{x}_l$, where $\mathbf{x}_s$ and $\mathbf{x}_l$ are the smallest and largest allowed values for the

design variable, respectively.

The optimum design problems can be divided into three categories:

1. **Linear constrained** problems that are solved by linear programming technique, also well-known as Simplex Method. The optimal solution always exists for the problem and at least two constraints are active.

2. **Non-linear unconstrained** problems without any equalities or inequalities or explicit constraints that bound the design variables.

3. **Non-linear constrained** problems that are the most common types of problems, that comprehend a significant variety of aspect of human life, e.g., engineering, finance, science, etc.

Non-linear unconstrained problems are quite rare in practical engineering applications. Nevertheless, they are studied since they are essential in understanding the most common non-linear constrained problems. In addition, a numerical approach to solve constrained problems is to convert them into a sequence of unconstrained problems.

B.1 Non-linear Optimisation Problem

In many practical problems, the function to be minimised is non-linear as in the case presented in chapter 6. Many researchers formulated strategies to solve these kind of optimisation problems.

B.1.1 A General Algorithm

The necessary and sufficient conditions for the point $\mathbf{x}^*$ to be a local minimum are, respectively, that the partial derivative of the cost function satisfies the conditions

$$\frac{\partial f(\mathbf{x}^*)}{\partial x_i} = 0 \qquad \text{with}\, i = 1, \ldots n \tag{B.2}$$

and the Hessian matrix, defined as follows,

$$\mathbf{H}(\mathbf{x}^*) = \left[\frac{\partial^2 f(\mathbf{x}^*)}{\partial x_i \partial x_j}\right] \tag{B.3}$$

is positive semi-definite or positive definite at the point $\mathbf{x}^*$.

Many numerical methods provide iteratively an approximated solution and the optimum value of the design variable that minimise the cost function is obtained if the difference between the cost function at two consecutive iterations is below a certain prescribed positive tolerance ε

$$\mid f(\mathbf{a}^{k+1}) - f(\mathbf{a}^k) \mid < \varepsilon \tag{B.4}$$

where k and $k+1$ represent the iteration numbers of two consecutive iterations.

The design variable vector at the $k+1$ iteration can be evaluated by the value of the vector at the $k-th$ iteration as follows

$$\mathbf{x}^{k+1} = \mathbf{x}^k + \mathbf{\Delta x}^k \tag{B.5}$$

where $\mathbf{\Delta x}^k$ is a variation of the current point and it can be decomposed into two parts

$$\mathbf{\Delta x}^k = \alpha_k \, \mathbf{d}^k \tag{B.6}$$

where $\mathbf{d}^k$ is the desirable *search direction* to seek the optimum solution and α_k is the *step size*, a positive scalar quantity that indicates the step in that direction. In practice, the optimisation process is converted into two subproblems, i.e., one related on evaluating the best direction to modify the design variables and the second associated to the detection of the step length.

Several methods have been developed to obtain these two pieces of information. Here, we are only interested in pointing out the basic concepts related to the evaluation

of the search direction and the step size.

B.1.2 Search Direction and Step Size

The linear Taylor's expansion at the point $\mathbf{x}^{k+1}$ to first order furnishes

$$f(\mathbf{x}^{k+1}) = f(\mathbf{x}^k) + (\mathbf{x}^{k+1} - \mathbf{x}^k) \cdot \nabla f(\mathbf{x}^k) \tag{B.7}$$

that can be manipulated by equation (B.6) to yield the following equation

$$f(\mathbf{x}^{k+1}) - f(\mathbf{x}^k) = \alpha_k \mathbf{d}^k \cdot \nabla f(\mathbf{x}^k) \tag{B.8}$$

Considering equation (B.4) and the fact that α_k is positive produce the inequality well known as the *descent condition* that can be now written

$$\mathbf{d}^k \cdot \nabla f(\mathbf{x}^k) < 0 \tag{B.9}$$

Any small variation of the design variable in a direction that satisfies the inequality of equation (B.9) will decrease the cost function. Most numerical optimisation methods are based on this concept and they are the so-called *descent method*.

The optimum step size that minimises the cost function in a preset direction would accomplish the equation

$$\frac{\partial f(\mathbf{x}^{k+1})}{\partial \alpha} = \frac{\partial f(\mathbf{x}^{k+1})}{\partial \mathbf{x}} \frac{\partial (\mathbf{x}^{k+1})}{\partial \alpha} = \nabla f(\mathbf{x}^{k+1}) \cdot \mathbf{d}^k = 0 \tag{B.10}$$

which mean that the two vectors $\nabla f(\mathbf{x}^{k+1})$ and $\mathbf{d}^k$ must be orthogonal.

In general the condition (B.10) cannot be evaluated analytically in most practical applications and a numerical approach is required. Moreover, the step size evaluation is the simplest of the two subproblems and any further details towards this goal are beyond the scope of this thesis and more details can be found in the literature [6, 98].

B.2 Quasi-Newton Method

Evaluating the search direction is much more complicated than evaluating the step size and several algorithms have been developed to deal with difficulty. They can be classified into three categories: *i*) zeroth, *ii*) first and *iii*) second order methods. In particular, the last category is also well-known as Newton method.

A method belongs to the category in relation to the order of derivative utilised. Thus a zeroth order method uses only function values, a first order method the first function derivative and function values, a second order method the second and first function derivative and function values. The greater expense of the computation aspects in higher order methods is justified by the accuracy and the convergence that are, generally, improved.

The Broyden-Fletcher-Goldfarb-Shanno (BFGS) variant of the Davidon-Fletcher-Powell (DFP) method is a first order method and belongs to the variable metric methods that are sometime called quasi-Newton methods, whose main advantage is that they store and update information from previous iterations to speed up the convergence.

To explain the basic concept of the variable metric method, the Taylor's expansion at the point $\mathbf{x}^{k+1}$ to second order is required

$$f(\mathbf{x}^{k+1}) = f(\mathbf{x}^k) + (\mathbf{x}^{k+1} - \mathbf{x}^k) \cdot \nabla f(\mathbf{x}^k) + \frac{1}{2}(\mathbf{x}^{k+1} - \mathbf{x}^k) \cdot \mathbf{H} \cdot (\mathbf{x}^{k+1} - \mathbf{x}^k) \qquad \text{(B.11)}$$

which yields

$$\nabla f(\mathbf{x}^{k+1}) = \nabla f(\mathbf{x}^k) + \mathbf{H} \cdot (\mathbf{x}^{k+1} - \mathbf{x}^k) \qquad \text{(B.12)}$$

or in a different form

$$\mathbf{x}^{k+1} = \mathbf{x}^k - \mathbf{H}^{-1} \cdot \left(\nabla f(\mathbf{x}^{k+1}) - \nabla f(\mathbf{x}^k)\right) \tag{B.13}$$

The variable metric methods are also called quasi Newton methods because instead of the inverse of the Hessian matrix $\mathbf{H}^{-1}$ an approximated matrix $\mathbf{A}^k$ is utilised

$$\mathbf{H}^{-1} \simeq \mathbf{A}^k \tag{B.14}$$

This last matrix is iteratively updated and at the subsequent iteration $k+1$ the matrix $\mathbf{A}^{k+1}$ can be evaluated by the previous matrix $\mathbf{A}^k$ plus a correction term

$$\mathbf{A}^{k+1} = \mathbf{A}^k + \mathbf{R}^k \tag{B.15}$$

There are several methods that have been developed to evaluate such a term. One of this is DFP method. This method provides the correction term as follows

$$\mathbf{R}^k = \frac{(\mathbf{x}^{k+1} - \mathbf{x}^k) \otimes (\mathbf{x}^{k+1} - \mathbf{x}^k)}{(\mathbf{x}^{k+1} - \mathbf{x}^k) \cdot (\nabla f^{k+1} - \nabla f^k)} - \frac{\left[\mathbf{A}^k \cdot \left(\nabla f^{k+1} - \nabla f^k\right)\right] \otimes \left[\mathbf{A}^k \cdot \left(\nabla f^{k+1} - \nabla f^k\right)\right]}{(\nabla f^{k+1} - \nabla f^k) \cdot \mathbf{A}^k \cdot (\nabla f^{k+1} - \nabla f^k)} \tag{B.16}$$

where the symbol $\otimes$ indicates the outer product. The BFGS variant of such a method simply adds an extra term to the previous equation that can be written as follows

$$\left[\left(\nabla f^{k+1} - \nabla f^k\right) \cdot \mathbf{A}^k \cdot \left(\nabla f^{k+1} - \nabla f^k\right)\right] \mathbf{u} \otimes \mathbf{u} \tag{B.17}$$

where $\mathbf{u}$ has the following definition

$$\mathbf{u} = \frac{(\mathbf{x}^{k+1} - \mathbf{x}^k)}{(\mathbf{x}^{k+1} - \mathbf{x}^k) \cdot (\nabla f^{k+1} - \nabla f^k)} - \frac{\mathbf{A}^k \cdot \left(\nabla f^{k+1} - \nabla f^k\right)}{(\nabla f^{k+1} - \nabla f^k) \cdot \mathbf{A}^k \cdot (\nabla f^{k+1} - \nabla f^k)} \tag{B.18}$$

More details in this regard are beyond the scope of this thesis and can be found in the literature [6, 98].

Appendix C

Benchmark Results for the Optimum Location of the Control Volume

For the sake of completeness the cost function obtained by the proposed procedure is compared with the results depicted in [44, 99]. The regular trend of their quiet zone could appear to be in contrast with the oscillatory behaviour of the herein obtained cost functions. The approach in [44] is based upon an idealized model that creates a pure tone diffuse field homogeneous in all the directions, whereas in the present contribution the diffuse field is created by a finite number of planewaves. The distribution of the primary waves plays a fundamental role in the optimum CV location.

In figure C.1 primary diffuse disturbance created by 72 planewaves is depicted for four different frequencies (109, 273, 546, 1092 , all in Hz) in a plane of dimension (in m) 1×1 meshed with 931 nodes. The same plane has been used to display in figure C.2 the secondary field amplitude created by a rigid sphere with an active segment of 120^0 degree and radius 8 cm.

Now, for such a primary diffuse field the cost function trends are shown in figure 6.9. The troughs and crests of these trends represent the optimum and worst locations of the CV along the x_1-axis for the four frequencies, respectively.

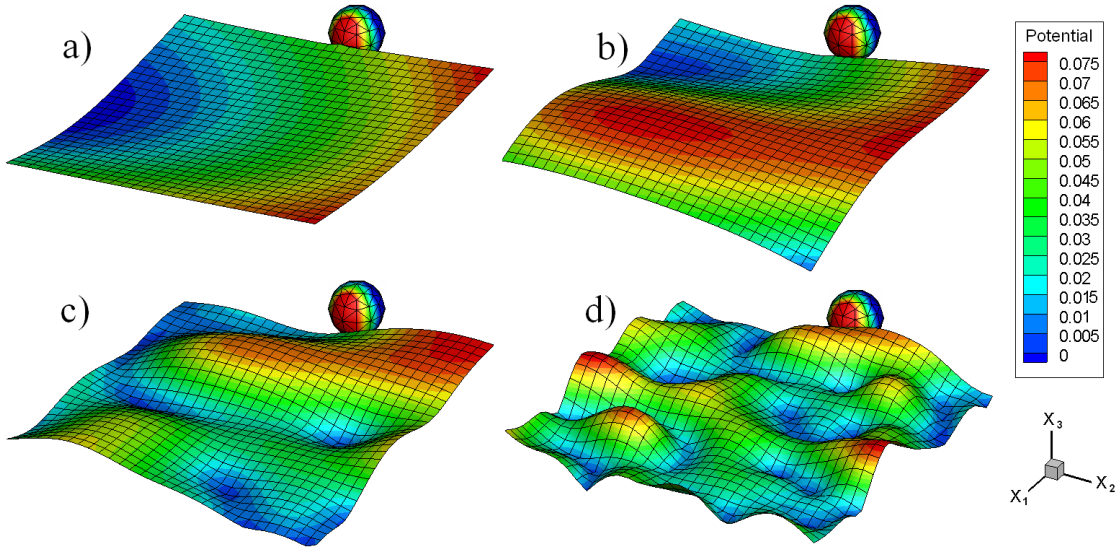


Figure C.1: Primary diffuse noise amplitude created by 72 planewaves distributed in all directions of the space for four different frequencies: a) 109Hz; b) 273 Hz; c) 546Hz; d) 1092 Hz.

Figure C.3 shows for each frequency the total (primary and secondary fields) potential amplitude distribution for one local optimum value (a trough in figure 6.9), whereas figure C.4 shows the same quantity at one of the worst values.

As evident the best CV positions are located where the total fields form a sufficient flat noise reduction distribution, whereas the worst CV locations are placed between two contiguous zones of high noise level. In particular figures C.4-b) and C.4-d) show that a low attenuation CV location can be also placed further away from the secondary source due to the diffuse distribution of the primary noise, highly in contrast with [44, 99] results.

It should be pointed out that figures C.1, C.2, C.3 and C.4 have been obtained by multiplying the resulting potential for a constant factor, different for each figure, in order to better visualize their variations.

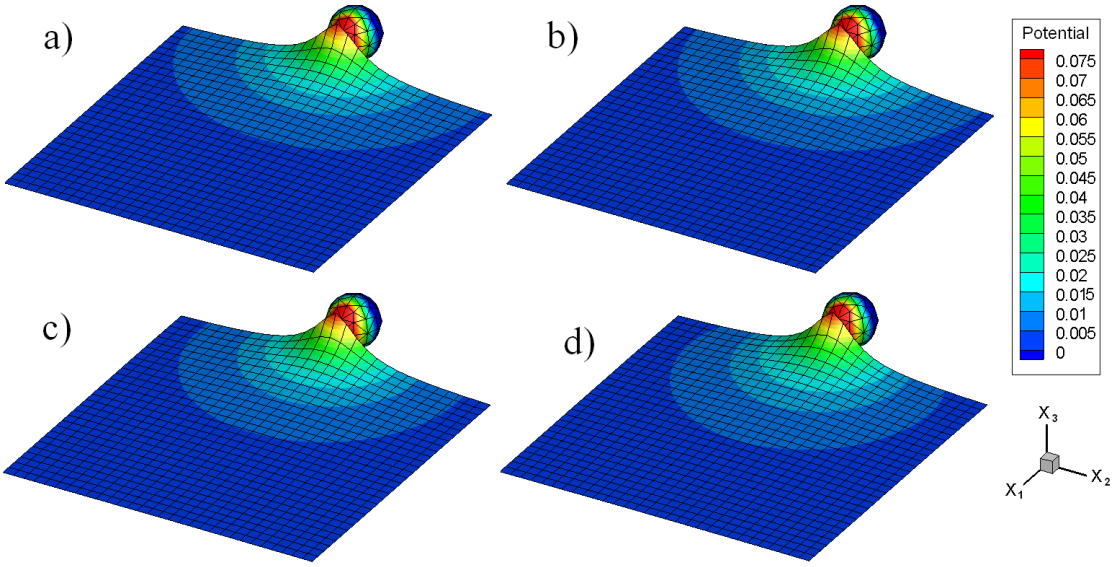


Figure C.2: Secondary field amplitude created by a rigid sphere with an active segment of 120^0 degree and radius 8 cm for four different frequencies: a) 109Hz; b) 273 Hz; c) 546Hz; d) 1092 Hz.

In conclusion, the noise attenuated zone depends upon the primary field characteristics and the optimum control volume location is not predictable as in the case of a pure tone diffuse field homogeneous in all the directions as in [44, 99] .

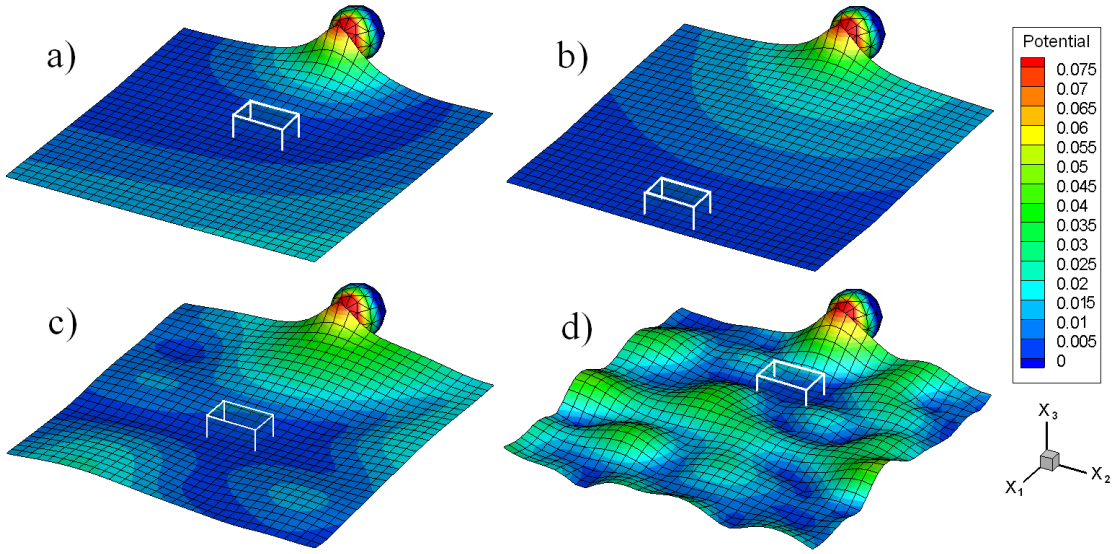


Figure C.3: Total amplitude potential for the optimum CV x_1-locations corresponding to the trough of the cost function in figure 6.9: a) 109Hz; b) 273 Hz; c) 546Hz; d) 1092 Hz.

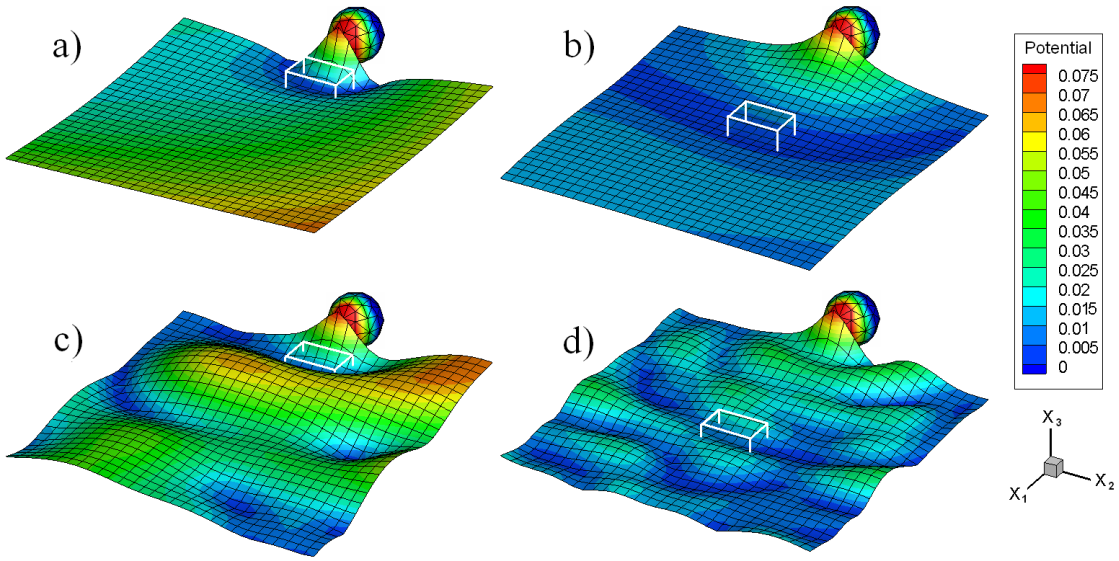


Figure C.4: Total amplitude potential of the worst CV x_1-locations corresponding to the crests of the cost function in figure 6.9: a) 109Hz; b) 273 Hz; c) 546Hz; d) 1092 Hz.

Bibliography

[1] Advanced CAE Research FastBEM Acoustics(R) software (2009): http://www.fastbem.com.

[2] R.M. Alford, K.R. Kelly, D.M. Boore. Accuracy of Finite-Difference Modeling of The Acoustic Wave Equation. *Geophysics* **39**, 834, 1974.

[3] S. Amini, N.D. Maines. Preconditioned Krylov Subspace methods for Boundary Element solution of the Helmholtz Equation. *International Journal for Numerical Methods in Engineering*, **41**, 875-898, 1998.

[4] P.R.S. Antunes, S.S. Valtchev. A meshfree numerical method for acoustic wave propagation problems in planar domains with corners and cracks. *Journal of Computational and Applied Mathematics*, **234**(9), 2646-2662, 2010.

[5] S. Aoki, K. Amaya, M. Urago, A. Nakayama. Fast Multipole Boundary Element Analysis of Corrosion Problems. *CMES: Computer Modeling in Engineering & Sciences*, **6**(2), 123-132, 2004.

[6] J.S. Arora. *Introduction to optimum design*. New York: McGraw-Hill, 1989.

[7] K.H. Baek, S.J. Elliott. Natural Algorithms For Choosing Source Locations In Active Control Systems. *Journal of Sound and Vibration*, **186** (2), 245-267, 1995.

[8] M.R. Bai, S. Chang. Active Noise Control of Enclosed Harmonic Fields by Using BEM-Based Optimization Techniques. *Applied Acoustics*, **48** (1996) 15-32.

[9] A. Baines. *Storia degli Strumenti Musicali*. Biblioteca Universale Rizzoli, 1974.

[10] M. Bebendorf. Approximation of boundary element matrices. *Numerische Mathematik*, **86**, 565-589, 2000.

[11] M. Bebendorf. Hierarchical LU decomposition-based preconditioners for BEM. *Computing*, **74**, 225-247, 2005.

[12] M. Bebendorf, R. Grzhibovskis. Accelerating Galerkin BEM for linear elasticity using adaptive cross approximation. *Mathematical Methods in the Applied Sciences*, **29**, 1721-1747, 2006.

[13] M. Bebendorf, S. Rjasanow. Adaptive low-rank approximation of collocation matrices. *Computing*, **70**(1), 1-24, 2003.

[14] I. Benedetti, M. H. Aliabadi, G. Daví. A fast 3D dual boundary element method based on hierarchical matrices. *International Journal of Solids and Structures*, **45**(7-8), 2355-2376, 2007.

[15] I. Benedetti. *A fast Hierarchical 3D Dual Boundary Element Method for the analysis of damaged structures with bonded piezoelectric sensors*. PhD Thesis, Università degli Studi di Pisa, 2008.

[16] W. Benthien, A. Schenck. Nonexistence and nonuniqueness problems associated with integral equation methods in acoustics. *Computers & Structures*, **65**(3), 295-305, 1997.

[17] T. Berge, O. Pettersen, S. Sorsdal. Active cancellation of transformer noise: Field measurements. *Applied Acoustics*, **23**, 309-320, 1988.

[18] A. Bermùdez, P. Gamallo, R. Rodrìguez. Finite element methods in local active control of sound. *SIAM Journal on Control and Optimization*, **43**, 437-465, 2004.

[19] S. Borm, L. Grasedyck, W. Hackbush. Introduction to Hierarchical matrices with applications. *Engineering Analysis with Boundary Elements*, **27**, 405-422, 2003.

[20] Ph. Bouillard, S. Suleaub. Element-Free Galerkin solutions for Helmholtz problems: formulation and numerical assessment of the pollution effect. *Comput. Methods Appl. Mech. Engrg.* **162**, 317-335, 1998.

[21] R. Bragard, F.J. De Hen. *Gli Strumenti Musicali nell'Arte e nella Storia dai Primordi ai Nostri Giorni*. Bramante Editrice, 1984.

[22] A. Brancati, M.H. Aliabadi, I. Benedetti. Hierarchical Adaptive Cross Approximation GMRES Technique for Solution of Acoustic Problems Using the Boundary Element Method. *CMES: Computer Modeling in Engineering & Sciences*, **43**(2), 149-172, 2009.

[23] C.A. Brebbia. *The boundary element method for engineers*. Wiley, New York, 1978.

[24] C.A. Brebbia. *Recent Advances in Boundary Elements*. Pentech Press, London, 1978.

[25] A. Buchau, W.M. Rucker, O. Rain, V. Rischmuller, S. Kurz, S. Rjasanow. Comparison between different approaches for fast and efficient 3-D BEM computations. IEEE transactions on magnetics, **39**(1), 1107-1110, 2003.

[26] A.J. Bullmore. A comparison of simple analytical models for representing propeller aircraft structural and acoustic responses. 1988.

[27] A. J. Burton, G. F. Miller. The application of integral equation methods to the numerical solution of some exterior boundary-value problems. *Proceedings of the Royal Society of London*, **323**, 201-210, 1971.

[28] J. Carrier, L. Greengard, V. Rokhlin. A fast adaptive multipole algorithm for particle simulations. *SIAM J. Sci. Statist. Comput.* **9**, 669-686, 1988.

[29] G.S. Chen, R.J. Bruno, M. Salama. Optimal placement of active: passive members in truss structures using simulated annealing. *American Institute of Aeronautics and Astronautics Journal*, **29**(8), 1327-1334, 1991.

[30] I.L. Chen, J.T. Chen, S.R. Kuo, M.T. Liang. A new method for true and spurious eigensolutions of arbitrary cavities using the CHEEF method. *J. Acoust. Soc. Am.*, **109**, 982- 999, 2001.

[31] J.T. Chen, J.H. Lin, S.R. Kuo, S.W. Chyuan. Boundary Element Analysis for the Helmholtz Eigenvalue Problems with a Multiply Connected Domain. *Proceedings: Mathematical, Physical and Engineering Sciences*, **457**, 2521-2546, 2001.

[32] J.T. Chen, F.C. Wong. Dual formulation of multiple reciprocity method for the acoustic mode of a cavity with a thin partition. *J. Sound Vib.*, **217**, 75-95, 1998.

[33] J.T. Chen, L.W. Liu, H.K. Hong. Spurious and true eigensolutions of Helmholtz BIEs and BEMs for a multiply connected problem. *Proceedings: Mathematical, Physical and Engineering Sciences*, **459**(2036), 1891-1924, 2003.

[34] J.T. Chen, S.R. Lin, J.J. Tsai. Fictitious frequency revisited. *Engineering analysis with boundary elements*, **33**(11), 1289-1301, 2009.

[35] W.C. Chew, J.M. Song, T.J. Cui, S. Velamparambil, M.L. Hastriter, B. Hu. Review of Large Scale Computing in Electromagnetics with Fast Integral Equation Solvers. *CMES: Computer Modeling in Engineering & Sciences*, **5**(4), 361-372, 2004.

[36] R.D. Ciskowski, C.A. Brebbia. *Boundary Element Methods in Acoustics.* Computational Mechanics Publications Elsevier Applied Science, 1991.

[37] W.B. Conover. Fighting noise with noise. *Noise Control*, **2**, 78-82, 1956.

[38] M.J. Crocker. *Handbook of acoustic.* John Wiley & Sons, 1998.

[39] J. M. Crotty. A block equation solver for large unsymmetric matrices arising in the boundary integral equation method. *International Journal for Numerical Methods in Engineering*, **18**(7), 997-1017, 1982.

[40] T.A. Cruse, F.J. Rizzo. *Boundary integral equation method: computational applications in applied mechanics.* AMD-Vol. II, A.S.M.E., 1975.

[41] K.A.Cunefare, G.H.Koopmann. A boundary element approach to optimization of active noise control sources on three-dimensional structures. *ASME J. Vibr. Acoust.*, **113,** 387–394, 1990.

[42] I. Dandaroy, J. Vondracek, R. Hund, D. Hartley. Passive interior noise reduction analysis of King Air 350 turboprop aircraft using boundary element method/finite element method (BEM/FEM). *J. Acoust. Soc. Am.*, **118**(3), 1888-1889, 2005.

[43] G. Dassios, G. Kamvyssas. Point source excitation in direct and inverse scattering: The soft and the hard small sphere. *IMA Journal of Applied Mathematics* **55**(1), 67-84, 1995.

[44] A. David, S.J. Elliot. Numerical Studies of Actively Generated Quiet Zones. *Applied Acoustics*, **41**, 63-79, 1994.

[45] J. Dominguez. *Boundary Elements in Dynamics.* Computational Mechanics Publications, 1993.

[46] U . Emborg. Cabin noise control in the Saab 2000 highspeed turboprop aircraft. *Proc. ISMA* **23**, 13–25, 1998.

[47] H. Fletcher, W.A. Munson. Loudness, its definition, measurement and calculation. *Journal of the Acoustical Society of America*, **5**, 82-108, 1933.

[48] V. Frayssé, L. Giraud, S. Gratton. A Set of GMRES Routines for Real and Complex Arithmetics. *Tech. Rep. TR/PA/97/49*, CERFACS, 1997.

[49] D. Fritze, S. Marburg, H.J. Hardtke. FEM–BEM-coupling and structural–acoustic sensitivity analysis for shell geometries. *Computers and structures*, **83**, 143-154, 2005.

[50] J. Garcia-Bonito, S.J. Elliot. Local Active Control of Diffracted Diffuse Sound Fields. *J. Acoust. Soc. Am.*, **98**, 1017-1024, 1995.

[51] J. Garcia-Bonito, S.J. Elliot. Active Cancellation of Acoustic Pressure and Particle Velocity in the Near Field of a Source. *Journal of Sound and Vibration*, **221**, 85-116, 1999.

[52] K. Giebermann. Multilevel approximation of boundary integral operators. *Computing*, **67**, 183-207, 2001.

[53] S.A. Goreinov, E.E. Tyrtyshnikov, N.L. Zamarashkin. A theory of pseudoskeleton approximations. *Linear algebra and its applications*, **261**, 1-21, 1997.

[54] L. Grasedyck, W. Hackbusch. Construction and arithmetics of H- matrices. *Computing*, **70**, 295-334, 2003.

[55] L. Grasedyck. Adaptive recompression of H-matrices for BEM. *Computing*, **74**, 205-223, 2005.

[56] C. Guang-Hann. *Determination of Secondary Sources in Noise Cancellation with Boundary Element Method*, PhD Thesis, Iowa State University, 1992 .

[57] G.H. Golub, C.F. VanLoan. *Matrix computations*. The Johns Hopkins University Press, 1989.

[58] L. Greengard, V. Rokhlin. A fast algorithm for particle simulations, *J. Comput. Phys*. **73**, 325-348, 1987.

[59] K. Guru Prasad, J.H. Kane. Shape reanalysis and sensitivities utilizing preconditioned iterative boundary solvers. *Structural Optimization*, **4**, 224-235, 1992.

[60] W. Hackbush. A sparse matrix arithmetic based on H-matrices. Part I: introduction to H-matrices. *Computing*, **63**, 89-108, 1999.

[61] W. Hackbush, B.N. Khoromskij. A sparse matrix arithmetic. Part II: application to multidimensional problems. *Computing*, **64**, 21-47, 2000.

[62] W. Hackbusch, Z. Nowak. On the fast matrix multiplication in the boundary element method by panel clustering. *Numerische Mathematik*, **73**, 207-243, 1989.

[63] R.T. Haftka, H.M. Adelman. Selection of actuator locations for static shape control of large space structures by heuristic integer programming. *Computers and Structures* **20**, 575-582, 1985.

[64] C.H. Hansen, S.D. Snyder. *Active control of noise and vibration*. Spon, 1997.

[65] I. Harari. Finite element formulations for exterior problems: application to hybrid methods, non-reflecting boundary conditions, and infinite elements. International Journal For Numerical Methods In Engineering, **40**, 2791-2805, 1997.

[66] I. Harari, T.J.R. Hughes. A cost comparison of boundary element and finite element methods for problems of time-harmonic acoustics. *Comput. Methods Appl. Mech. Engrg.*, **97**, 77-102, 1992.

[67] C.M. Harris. *Manuale dei Controllo del Rumore*. Tecniche Nuove, Milano 1983.

[68] X. He, K.M. Lim, S.P. Lim. Fast BEM Solvers for 3D Poisson-Type Equations. *CMES: Computer Modeling in Engineering & Sciences*, **35**(1), 21-48, 2008.

[69] Z.C. He, G.R. Liu, Z.H. Zhong, S.C. Wu, G.Y. Zhang, A.G. Cheng. An edge-based smoothed finite element method (ES-FEM) for analyzing three-dimensional acoustic problems. *Comput. Methods Appl. Mech. Engrg.*, **199**, 20-33, 2009.

[70] N. Hesselman. Investigation of noise reduction in a 100 KVA transformer tank by means of active methods. *Applied Acoustics*, **11**, 27-34, 1978.

[71] V. Jayachandran, S.M. Hirsch, J.Q. Sun. On the numerical modelling of interior sound fields by the modal function expansion approach. *Journal of Sound and Vibration*, **210**(2), 243-254,1998.

[72] V. Jayachandran, N.E. Meyer, M.A. Westervelt, J.Q. Sun. Piezoelectrically driven speakers for active aircraft interior noise suppression. *Appl. Acoust.*, **57**(3), 263-277, 1999.

[73] O. Jirsak, F. Sanetrnik, D. Lukas, V. Kotek, L. Martinova, J. Chaloupek. A method of nanofibres production from a polymer solution using electrostatic spinning and a device for carrying out the method. WO/2005/024101, 2005.

[74] S. Johansson, I. Claesson. Active Noise Control in Propeller Aircraft. *Conference for the Promotion of Research in IT at New Universities and at University Colleges in Sweden*, Ronneby, Sweden, 111-120, 2001.

[75] P. Joseph, S.J. Elliot, P.A. Nelson. Near field Zone of Quiet. *Journal of Sound and Vibration*, **172**, 605-627, 1994.

[76] J.H. Kane, K. Kumar. An Arbitrary Condensing, Noncondensing Solution Strategy for Large Scale, Multi-Zone Boundary Element Analysis. *Comp. Methods Appl. Mech. Eng.*, **79**, 219-244, 1990.

[77] J.H. Kane, S. Mao, G.C. Everstine. A boundary element formulation for acoustic shape sensitivity analysis. *Journal of the Acoustical Society*, **90**(1), 561-573, 1991.

[78] B. U. Koo. Shape design sensitivity analysis of acoustic problems using a boundary element method. *Computers & Structures*, **65**(5), 713-719, 1997.

[79] B.U. Koo, J.G. Ih, B.C. Lee. Acoustic shape sensitivity analysis using the boundary integral equation. *J. Acoust. Soc. Am.*, **104**(5), 2851-2860, 1998.

[80] S.R. Kuo, W. Yeih, Y.C. Wu. Applications of the generalized singular-value decomposition method on the eigenproblem using the incomplete boundary element formulation. *J. Sound Vib.* **235**, 813-845, 2000.

[81] C.Y. Leung, S.P. Walker. Iterative solution of large three dimensional BEM elastostatic analyses using the GMRES technique. *International Journal for Numerical Methods in Engineering*, **40**, 2227-2236, 1997.

[82] LMS International. *User's Manual SYSNOISE Rev 8B*. Leuven, 2008.

[83] H.Y. Lu. Effect of Excitation on Coaxial Jet Noise. *AIAA Journal*, **21**(2), 214-220, 1983.

[84] P. Lueg. Process of Silencing Sound Oscillations. German Patent DPR No. 655 508.

[85] V. Mallardo, M.H. Aliabadi. A BEM sensitivity and shape identification analysis for acoustic scattering in fluid-solid problems. *International Journal for Numerical Methods in Engineering* **41**(8), 1527-1541, 1998.

[86] V. Mallardo, M.H. Aliabadi, A. Brancati, V. Marant. Noise control in the aircraft cabin. (in press)

[87] W.J. Mansur, F.C. Araújo, J.E.B. Malaghini. Solution of BEM systems of equations via iterative techniques. *International Journal for Numerical Methods in Engineering*, **33**(9), 1823-1841, 1992.

[88] T. Martin, A. Roure. Active Noise Control Of Acoustic Sources Using Spherical Harmonics Expansion and a Genetic Algorithm: Simulation and Experiment. *Journal of Sound and Vibration* **212** (3), 511-523, 1998.

[89] M. Merkel, V. Bulgakov, R. Bialecki, G. Kuhn. Iterative solution of large-scale 3D-BEM industrial problems. *Engineering Analysis with Boundary Elements*, **2**, 183-197, 1998.

[90] P. M. Morse, K.U. Ingard. *Theoretical Acoustic*. McGraw Hill, New York, 1968.

[91] P. A. Nelson. *Active control of sound.* Academic, 1992.

[92] P.A. Nelson, A.R.D. Curtis, S.J. Elliot, A.J. Bullmore. The active minimization of harmonic enclosed sound fields: part i, ii, iii. *Journal of Sound and Vibration*, **117**, 1-58, 1987.

[93] P.A. Nelson, A.R.D. Curtis, S.J. Elliott, A.J. Bullmore. The Minimum Power Output of Free Field Point Sources and The Active Control of Sound. *Journal of Sound and Vibration*, **116**(3), 397-414, 1987.

[94] N. Nemitz, M. Bonnet. Topological sensitivity and FMM-accelerated BEM applied to 3D acoustic inverse scattering. *Engineering Analysis with Boundary Elements*, **32**(11), 957-970, 2008.

[95] A.D. Pierce. *Acoustic: an introduction to its Physical Principles and Applications.* McGraw Hill, New York, 1981.

[96] L.D. Pope, E.G. Wilby, C.M. Willis, W.H. Mayes. Aircraft interior noise models: Sidewall trim, stiffened structures, and cabin acoustics with floor partition, *Journal of Sound and Vibration*, **89**(3), 371-417, 1983.

[97] R. Profeta. *Storia e Letteratura degli Strumenti Musicali*. Marzocco, 1942.

[98] W.H. Press. *Numerical recipes: the art of scientific computing*. Cambridge University Press, 2007.

[99] B. Rafaely, S.J. Elliott, J. Garcia-Bonito. Broadband performance of an active headrest. *Journal of the Acoustical Society of America*, **106**(2), 787-793, 1999.

[100] K. Renji, P.S. Nair, S. Narayanan. Critical and Coincidence Frequencies of Flat Panels. *Journal of Sound and Vibration*, **205**(1), 19-32, 1997.

[101] R.H. Rigby, M. H. Aliabadi. Out-of-core solver for large, multi-zone boundary element matrices. *International Journal for Numerical Methods in Engineering*, **38**(9), 1507-1533, 1995.

[102] V. Rokhlin. Rapid solution of integral equations of classical potential theory. *J. Comput. Phys.* **60**, 187-207, 1983.

[103] C.F. Ross. Experiments on the active control of transformer noise. *Journal of Sound and Vibration*, **61**, 473-480, 1978.

[104] T. D. Rossing. *The science of sound*. Addison Wesley, 2002.

[105] C.E. Ruckman, C.R. Fuller. Optimizing Actuator Location in Active Noise Control System using Subset Selection. *Journal of Sound and Vibration* **172** (5), 605-627, 1995.

[106] Y. Saad, M.H. Schultz. GMRES: A generalized minimal residual algorithm for solving nonsymmetric linear systems. *SIAM J. Sci. Stat. Comput.*, **7**(3), 856-869, 1986.

[107] C. Sachs. *Storia degli Strumenti Musicali*. Arnoldo Mondadori Editori, 1980.

[108] H.A. Schenck. Improved Integral Formulation for Acoustic Radiation Problems. *Journal of the Acoustical Society of America*, **44**, 41-58, 1968.

[109] A.F. Seybert, T.K. Rengarajan. The use of CHIEF to obtain unique solutions for acoustic radiation using boundary integral equations. *J. Acoust. Sot. Am.*, **81**, 1299-1306, 1987.

[110] S.A. Seyedin, M.H. Abedi. Optimizing Secondary Source Location in Acoustic ANC Systems. *Information and Communication Technologies ICTTA '06*, **1**, 1953-1957, 2006.

[111] I.M. Smith, D.V. Griffiths. *Programming the finite element method*. Second Edition. John Wiley & Sons.

[112] S.D. Snyder. *Active Noise Control Primer*. Springer-Verlag Inc, New York, USA, 2000.

[113] S. Suleau, Ph. Bouillard. One-dimensional dispersion analysis for the element-free Galerkin method for the Helmholtz equation. *Int. J. Numer. Methods Eng.* **47**, 1169–1188, 2000.

[114] Z. Sun, J. Sun, C. Wang, Y. Dai. Dynamic vibration absorbers used for increasing the noise transmission loss of aircraft panels. *Appl. Acoust.*, **48**(4), 311-321, 1996.

[115] G.R.G. Tai, R.P. Shaw. Helmholtz equation eigenvalues and eigenmodes for arbitrary domains. *J. Acoust. Soc. Am.*, **56**, 796-804, 1974.

[116] S. Temkin. *Elements of Acoustic*. Wiley, New York, 1981.

[117] L.L.Thompson. A review of finite element methods for time-harmonic acoustics. *J. Acoust. Soc. Amer.*, **119**, 1315-1330, 2006.

[118] E.E. Tyrtyshnikov. Mosaic-skeleton approximations. *Calcolo*, **261**, 1-21, 1996.

[119] O. Von Estorff, S. Rjasanow, M. Stolper, O. Zalesk. Two efficient methods for a multifrequency solution of the Helmholtz equation. *Computing and Visualization in Science*, **8**, 159-167, 2005.

[120] H.T. Wang, G. Hall, S.Y. Yu, Z.h. Yao. Numerical Simulation of Graphite Properties Using X-ray Tomography and Fast Multipole Boundary Element Method. *CMES: Computer Modeling in Engineering & Sciences*, **37**(2), 153-174, 2008.

[121] H.T. Wang, Z.H. Yao. A New Fast Multipole Boundary Element Method for Large Scale Analysis of Mechanical Properties in 3D Particle-Reinforced Composites. *CMES: Computer Modeling in Engineering & Sciences*, **7**(1), 85-96, 2005.

[122] H.T. Wang, Z.H. Yao. A Rigid-fiber-based Boundary Element Model for Strength Simulation of Carbon Nanotube Reinforced Composites. *CMES: Computer Modeling in Engineering & Sciences*, **29**(1), 1-14, 2008.

[123] L.C. Wrobel, M.H. Aliabadi. *The Boundary Element Method*. Two volumes set. New Jersey: UK John Wiley, 2002.

[124] T.C. Yang, C.H. Tseng. Effective Optimization-Based Approach for Designing Active Noise Control System in Enclosures. *Finite Elements in Analysis and Design*, **15**, 303-316, 1994.

[125] O.C. Zienkiewicz. *The finite element method for solid and structural mechanics.* Elsevier Butterworth-Heinemann, 2005.

[126] http://clerccenter.gallaudet.edu/Clerc_Center/Information_and_Resources/Info_to_Go/Hearing_Loss_Information/Hearing_Loss_For_Older_Children.html, November 2009.

[127] http://en.wikipedia.org/wiki/File:Acoustic_weighting_curves.svg, April 2010.

[128] http://en.wikipedia.org/wiki/File:Qantas_b747_over_houses_arp.jpg, May 2010.

[129] http://www.amsoil.com/products/ea_filters/EaA.aspx, May 2010.

[130] http://www.decimin.com/Images/mass%20low-1.jpg, November 2009.

[131] http://www.ips.it/scuola/concorso/kant/musgre.htm, November 2009.

[132] ISO Standard 2631. Mechanical vibration and shock – Evaluation of Human Exposure to Whole-Body Vibration.

[133] ISO Standard 226:2003. Acoustics – Normal Equal Loudness Level Contours.

[134] IEC 61672 : 2003. Electroacoustics - sound level meters.